Stony Brook University

Preparation and Comprehensive Characterization of Poly(diiododiacetylene) and Spectroscopic Studies of Its Reactions with Lewis Bases

A Dissertation Presented

by

Liang Luo

to

The Graduate School

in Partial Fulfillment of the

Requirements

for the Degree of

Doctor of Philosophy

in

Chemistry

Stony Brook University

May 2009

Stony Brook University

The Graduate School

Liang Luo

We, the dissertation committee for the above candidate for the

Doctoral of Philosophy degree, hereby recommend

acceptance of this dissertation.

Nancy S. Goroff – Dissertation Advisor

Associate Professor, Department of Chemistry

Iwao Ojima – Chairperson of Defense

Distinguished Professor, Department of Chemistry

Andreas Mayr – Third Member of Defense

Professor, Department of Chemistry

Philip B. Allen – Outside Member of Defense

Professor, Department of Physics, Stony Brook University

This dissertation is accepted by the Graduate School

Lawrence Martin

Dean of the Graduate School

Abstract of the Dissertation

Preparation and Comprehensive Characterization of Poly(diiododiacetylene) and Spectroscopic Studies of Its Reactions with Lewis Bases

by

Liang Luo

Doctor of Philosophy

in

Chemistry

Stony Brook University

2009

Conjugated polymers have attracted great interest for their electronic and optical properties. Poly(diiodiacetylene), or PIDA, is a conjugated polymer containing the poly(diacetylene) (PDA) backbone but with only iodine atom substituents. The monomer diiodobutadiyne **1** can be aligned in the solid state with designed hosts **2** – **10** by hydrogen bonds, between oxalamide or urea groups, and weak Lewis acid-base interactions (halogen bonds), between iodoalkynes and nitriles or pyridines. If the alignment of diynes in the co-crystals favors the topochemical polymerization in a co-crystal, the co-crystal starts out pale blue, but turns shiny and metallic-colored as the polymerization progresses. The development of a crystallization methodology which greatly improves the yield of PIDA to above 50% now allows the full characterization of the polymer by X-ray diffraction, solid-state ^{13}C MAS-NMR, Raman, ESR, and electron absorption spectroscopy. Comparison of a series of hosts reveals an odd-even effect in the topochemical polymerization, based on the alkyl chain length of the host. The topochemical polymerization can also be observed in water suspensions of micron-sized **10·1** co-crystals; the

size distribution of these microcrystals, and the resulting polymer chains, can be controlled by sonication. Extensive rinsing of the crystals in organic solvents separates the polymer from the soluble host. Once isolated, PIDA nanofibers disperse in organic solvents to form blue suspensions. Adding Lewis bases to the blue suspension leads first to rapid disappearance of these absorption peaks attributed to PIDA, followed by generation of free iodine atoms. The resulting solid material gives a Raman scattering spectrum consistent with graphitic carbon. The base-treated material has a much higher conductivity than initial PIDA samples, but maintains a nanofibrous morphology. Additional studies have examined the topochemical polymerization of diiodooctatetrayne as an approach to novel carbon-rich conjugated polymers.

Table of Contents

List of Figures

List of Schemes

List of Tables

Acknowledgments

The whole work in the dissertation is guided by my research advisor, Prof. Nancy S. Goroff. Without her invaluable guidance, enthusiastic support, and continuous encouragement, I could not have developed confidence in my abilities as a chemist, and for that I am truly grateful. The extensive knowledge and creative thinking of Dr. Goroff have been the source of inspiration for me throughout this work. In addition, her cheerful, attractive personality has distinguished her from the community, making her a perfect example of the scientist that I could learn from in my life. I felt extremely fortunate and very proud to have her as my Ph. D. advisor.

I would also like to express my gratitude to the other members in my academic committee. I sincerely appreciate my committee chair, Prof. Iwao Ojima, and the third member, Prof. Andreas Mayr, for their help and encouragement throughout my advancement in the Ph. D. program. Their comments and suggestions on my academic meetings and seminars are really helpful, and I have greatly benefited from their recommendation letters. I would also like to thank Prof. Philip B. Allen of Physics at Stony Brook, who kindly served as my outside committee member. Before that I have already benefited from his helpful discussions on some optical problems.

I am especially indebted to Prof. Joseph W. Lauher and Prof. Frank W. Fowler for their help and support over the years. They have been teaching me knowledge and techniques on both organic chemistry and crystallography since I started my research. My TA experience in CHE 321 and 322 with them is also memorable and beneficial to my future career.

I need to acknowledge Christopher Wilhelm, who conducted all the MAS NMR experiments discussed in the dissertation. Besides that, Chris provided many helpful comments in our daily discussions. I also thank Aiwu Sun, Lei Li, Li Cui, and Lu Zhou for training me when I started my lab work. In addition, many thanks are due to help from other previous and present Goroff

group members, including Zachary Katsamanis, Audra Selvagio, David Connors, Raquel Campo, Rosemarie Salerno, Allison Black, and Daniel Resch. I greatly enjoyed the time I spent together with them.

Many of my research projects are performed with the help of many other research groups, without which my dissertation could not have been completed. I must thank Prof. Clare P. Grey and her group members for helping in MAS NMR; Prof. Nicole S. Sampson and Prof. Daniel P. Raleigh for providing UV/Vis spectrometers; Prof. Peter J. Tonge and Allison Stelling for helping me in measuring Raman of the suspensions; Dr. James Quinn and Dr. Susan Van Horn for helping me in electron microscopy; Prof. Gary Halada, Samrat Chawda, and Christopher Young for helping me in measuring Raman of the solid samples; Prof. Benjamin S. Hsiao and Yimin Mao for helping me in measuring DSC, TGA, and light scattering; Prof. Peter Khalifah and his group members for helping me in X-ray diffractions; Prof. Richard J. Gambino for helping me to carry out impedance studies. I also obtained a lot of help from outside Stony Brook, including Dr. Xuefeng Guo and Prof. Colin Nuckolls at Columbia University for conductivity measurements, and Prof. Seth R. Marder and his group members at Georgia Tech. In our collaboration with Center for Nanophase Materials Sciences at Oak Ridge National Laboratory, I got great help from Dr. Kai Xiao, Dr. Karren L. More, Dr. Jane Y. Howe, Dr. Ilia Ivanov, and other members in Dr. David B. Geohegan's group. I am greatly grateful for their kind help.

I would like to thank our NMR specialist and adjunct professor, Dr. James Marecek for his kind assistance in NMR spectroscopy and many valuable discussions about my research projects. I also need to thank Prof. Dale Drueckhammer and Prof. Kathlyn A. Parker for teaching me advanced organic chemistry in CHE 504 and organic synthesis in CHE 503. In addition, their

nice organization and participation of combined organic group (COG) meetings are quite beneficial to all the students in organic chemistry. Acknowledgement is also made to Prof. Stephen A. Koch, who taught me inorganic chemistry in CHE 511 and gave continuous help in crystallography to me over the years.

A lot of my research work could not have been carried out without the help from people in 7th floor of Chemistry Building. Acknowledgments are made to all the members in Lauher and Fowler group, Ojima Group, Parker Group, and ICB&DD member Dr. Bela Ruzsicska. Many thanks are also due to all my friends in Stony Brook, who never hesitated when I asked for help.

During my staying at Stony Brook, I received numerous kind help from our stuff members. I would like to express my special appreciation to Ms. Diane Godden, Ms. Katherine Hughes, and Ms. Pat Marinoccio for their warm-hearted assistance in a variety of my personal matters.

I dedicate this thesis to my parents and fiancée, for their love and continuous support.

Chapter 1. Introduction

1.1. Conjugated polymers

π-Conjugated polymers are polymers that contain extensively delocalized π electrons and that conduct electricity or act as electrical semiconductors. The extensive delocalization of π electrons is responsible for an array of remarkable characteristics in these polymers, such as non-linear optical behavior,[1] electronic conductivity,[2] and multi-photon absorption.[3] Classic conjugated polymers are listed in Figure 1.1.

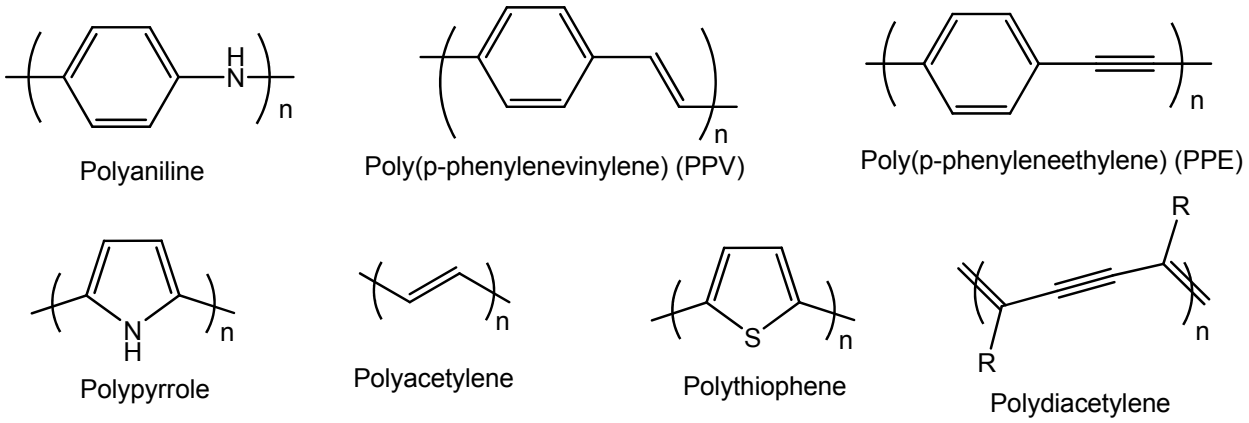

Figure 1.1. Classic conjugated polymers.

1.1.1. History

Interest in studying π-conjugated polymers has continued for several decades. The first report on conjugated polymers dates back to the mid 1800s, when a medical doctor Henry Letheby first reported the electrochemical and chemical oxidation products of aniline in acidic media.[4] In 1963, D. E. Weiss and coworkers reported high conductivity in oxidized iodine-doped polypyrrole, achieving a conductivity of as high as 1.0 $S \cdot cm^{-1}$. In a series of papers published in 1963, they first described the effects of doping with iodine on conductivity, the conductivity type of iodine-doped polypyrrole, and electron spin resonance of polypyrrole.[5-7]

In 1977, Alan J. Heeger, Alan MacDiarmid and Hideki Shirakawa reported metallic conductivity in iodine-doped polyacetylene.[8] Heeger, MacDiarmid and Shirakawa eventually received the 2000 Nobel Prize in Chemistry *"for the discovery and development of conductive polymers"*.[9] There followed extensive research and development in the semiconducting and conducting properties of a large family of conjugated polymers, which resulted in the development of organic polymeric electronics, such as light emitting diodes,[10] solar cells,[11] and transistors.[12]

1.1.2. Theory

The essential structural characteristic of all conjugated polymers is their quasi-infinite π system extending over a large number of recurring monomer units. This feature results in materials with directional conductivity, strongest along the axis of the chain. The band gap between the π-bonding orbitals and π-antibonding orbitals determines the optical and electronic properties of conjugated polymers.[13]

The simplest form of conjugated polymers, polyacetylene $(CH)_n$, can be used as a model to explain the band structure of infinite π systems, as shown in Figure 1.2. For butadiene (n = 1), there are 4 π orbitals. In octatetraene (n = 2), the energy of the 8 molecular orbitals (MO)s can be considered as plus and minus perturbations on the energy of the 4 butadiene MOs for the two halves of the molecule. The 12 MOs for n = 3 can similarly be thought of, to the first order, as four sets of three, each set containing the three linear combinations of ψ for the three butadiene units in the molecule. At the infinite polyene (or plyacetylene), each of the four sets contains an infinite number of MOs. A collection of all MOs in a given set from the same monomer MO is called a band. Increased conjugation brings the HOMO and LUMO orbitals closer together and decreases the band gaps, the energy separation between valence band (highest-lying filled band)

and conduction band (lowest-lying empty band). In some cases of infinite π systems, some bands may overlap with their neighboring bands, as shown in second case in Figure 1.2. [13]

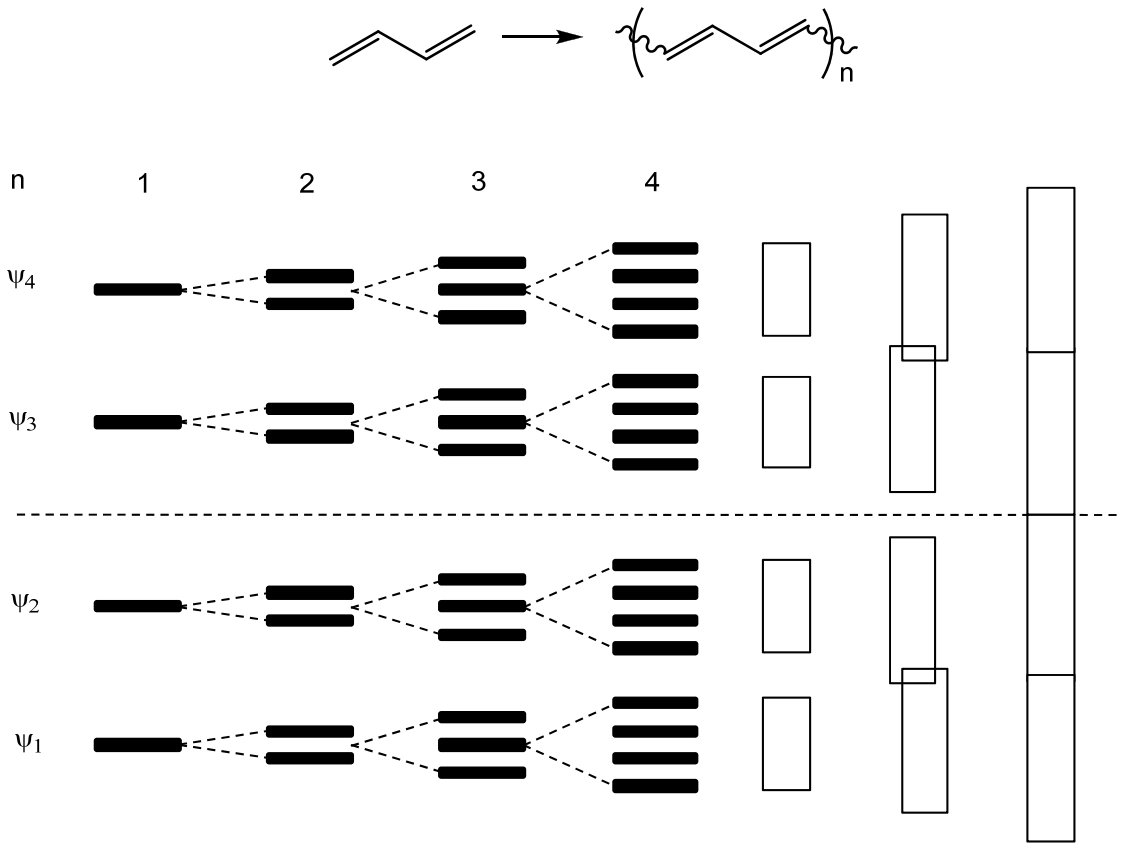

Figure 1.2. Evolution from π MOs in finite polyacetylenes to bands in an infinite π system.[13]

The band structure makes clear predictions about the nature of an electronic material. An insulator has a very large band gap, while a semiconductor has a small but finite band gap. A metal has a zero band gap, because of an incompletely filled band or the overlap of two bands. Although in polyacetylene the π-electrons are delocalized and band gap is zero, pure polyacetylene is a semiconductor. The alternating single-double bond structure of polyacetylene opens a gap in the electronic structure in its ground state. The conducting polymers can be achieved by a chemical treatment known as doping. All conducting organic polymers are in fact doped forms of otherwise semiconducting or insulating conjugated polymers. Doping either oxidizes or reduces conjugated polymers so that it will introduce positive charge (p-type) or

negative charge (n-type) to conjugated polymers, resulting in sufficient charge carriers to make the materials conducting.

From the point view of the band structure, doping introduces orbitals into the band gap. Figure 1.3 exhibits the evolution of the band structure during p-type doping of a polyacetylene. Removing an electron from the pristine polymer generates a partially delocalized radical cation, called polaron, and leaves a hole in the top of the valence band (*ii*). Several orbitals in the valence band have dropped in energy, leaving a singly occupied band orbital in the gap. A similar thing happened in the conduction band, producing an empty orbital in the gap (*iii*). Structure in *iii* after relaxation to form the polaron bands (*iv*), which in some cases can merge with the valence and conduction bands (*v*) to produce a conducting polymer.[13]

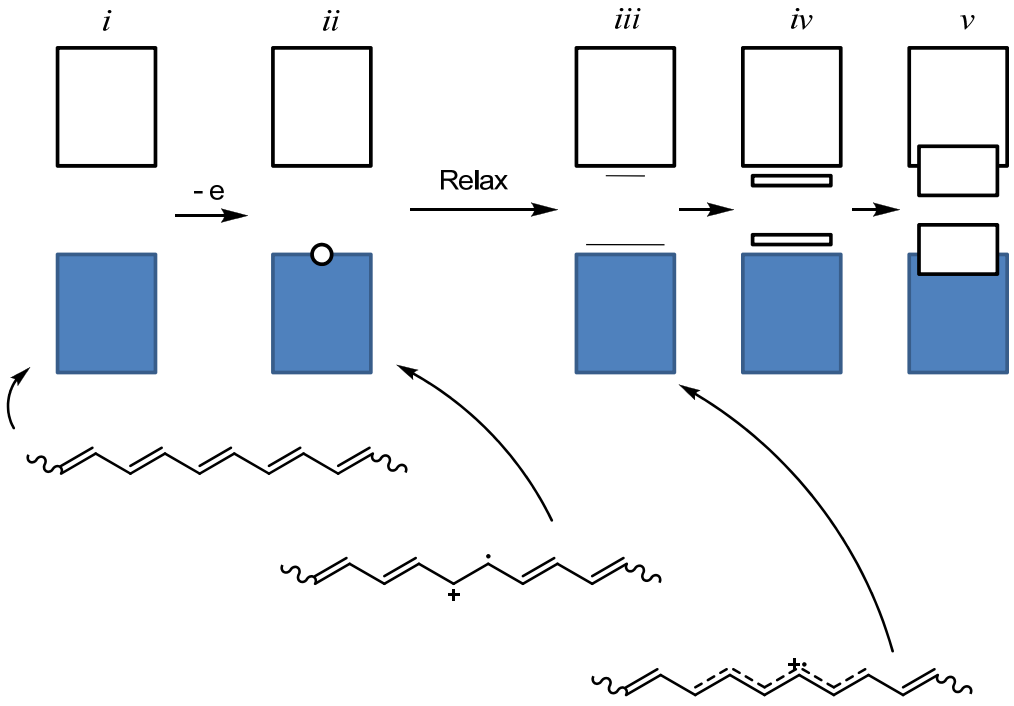

Figure 1.3. The evolution of the band structure upon p-type doping of a polyacetylene.

1.1.3. Current research on applications of conjugated polymers

A great number of research projects and research groups in academic and industrial laboratories worldwide are examining applications of conjugated polymers. Most focus is given to light emitting diodes (LED),[14-17] solar cells,[11] and chemical and biological sensors.[18,19]

The first polymer light-emitting diode, synthesized by Burroughs et al., involved a single layer of poly(p-phenylene vinylene), PPV.[20] The conductive PPV layer was prepared from dichloro-p-xylene and the device is shown in Figure 1.4. Burroughs and coworkers achieved a significant photoluminenscence quantum yield of ~8%, suggesting that the polymer can be used for the development of large-area light-emitting displays. Now polymer LEDs are widely used in television screens, computer displays, and portable system.[21]

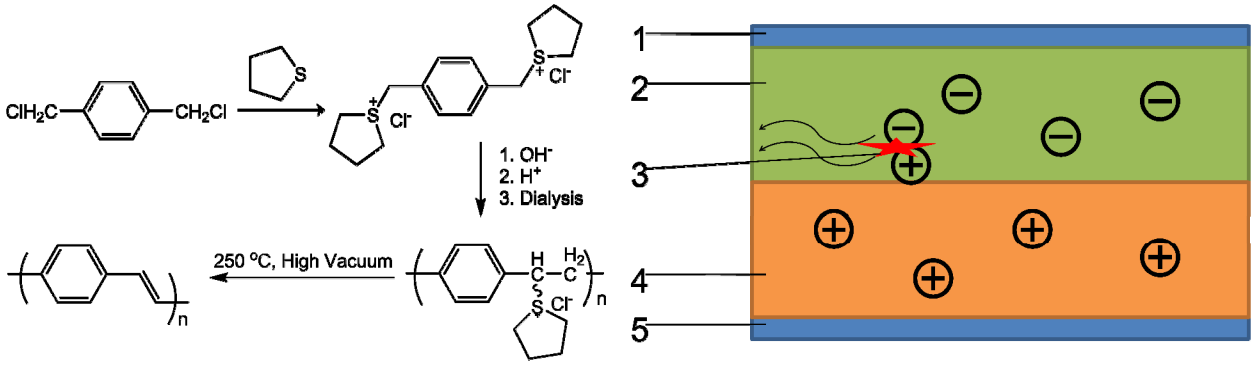

Figure 1.4. Synthesis of PPV and schematic of a PLED: 1. Cathode (−), 2. Emissive Layer, 3. Emission of radiation, 4. Conductive Layer, 5. Anode (+)[20] Reprint with permission from Wikipedia article "Organic light emitting diodes"

Solar cells are another important field for applications of conjugated polymers. Materials having a delocalized π electron system can absorb sunlight, create photogenerated charge carriers, and transport these charge carriers. Research on organic solar cells generally focuses on solution processable organic semiconducting molecules/polymers or on vacuum-deposited small molecules.[11]

Figure 1.5 shows a schematic device structure for PPV/fullerene bulk heterojunction solar cells. To convert light into electricity by such an organic solar cell, it needs following steps. Absorbing a photon first creates an exciting state, or an exciton, that is, the bound electron-hole pair. The exciton dissociates and the separated charge is transported within organic semiconductors to the respective electrodes. For efficient photovoltaic devices, strong electric fields are necessary to dissociate excitons, and the created charges need to be transported to the appropriate electrodes within their lifetime. Blending conjugated polymers with electron acceptors, such as fullerenes, is a very efficient way to break apart excitons into free charge carriers, and provide sufficient driven forces for the charge carriers. Compared to silicon-based devices, polymer solar cells still have the problem of lower efficiency, but their advantages of lightweight, having less environment impact, and being flexible and customizable on the molecular level show great promise for decreasing the cost of solar energy. [11]

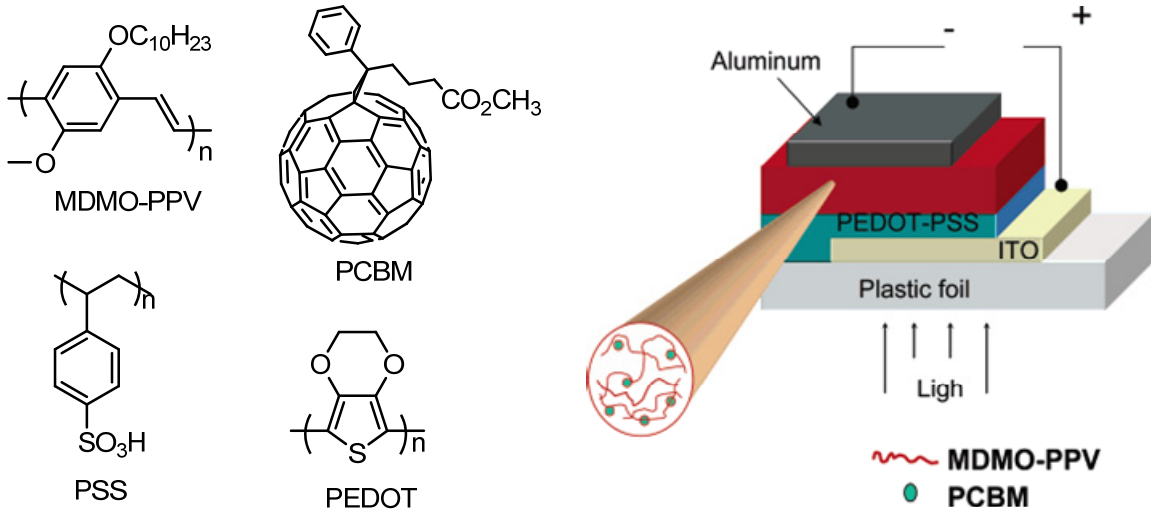

Figure 1.5. A schematic device structure for polymer/fullerene bulkheterojunction solar cells. Reproduced with permission from ref. 11, Copyright 2007 American Chemical Society.

Conjugated polymers make very good sensors because of their potential to exhibit collective properties that are sensitive to very minor perturbations. In particular, the optical properties,

electrical conductivity, and energy migration of conjugated polymers provide amplified sensitivity.[18] Based on diverse sensing mechanisms, conjugated polymer can be used as sensors to display changes in electrical conductivity in response to analyte interactions, and to detect changes in the system's chemical potential and electron absorption properties. Conjugated polymer-based sensors can also be applied to detect changes in fluorescence intensity, energy transfer, wavelength (excitation and emission), and lifetime. Figure 1.6 shows a schematic chemical sensor based on amplifying-fluorescent conjugated polymers.[18,19]

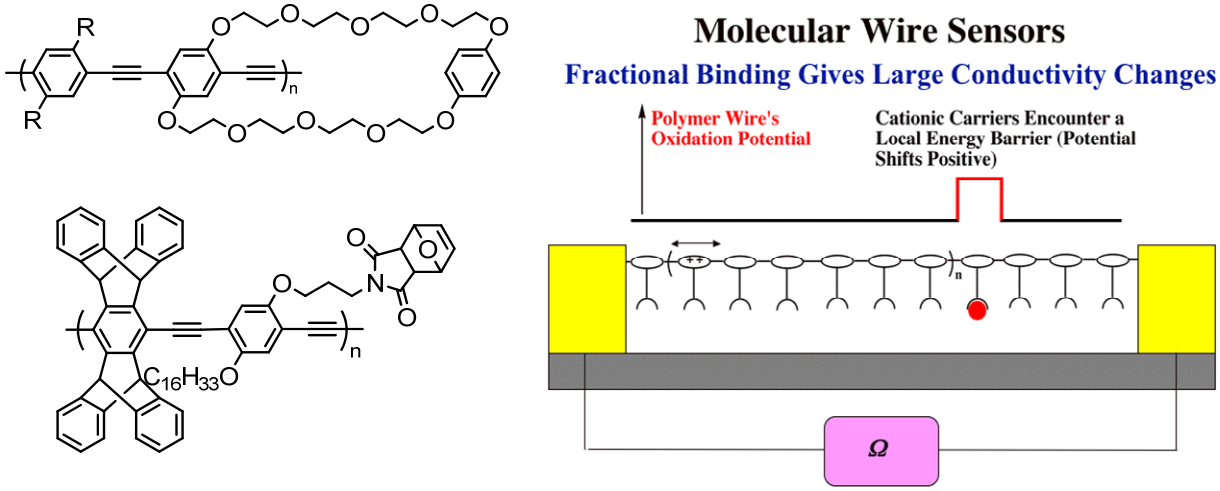

Figure 1.6. Chemoresistivity-based sensory systems based on functionalized PPEs. Reproduced with permission from Ref. 18, Copyright 2000, American Chemical Society.

1.1.4. Major preparation methods of conjugated polymers

Conjugated polymers are mainly produced by condensation polymerization. However, the biggest concern of these materials is the solubility and technological processability. Conjugated polymers are generally insoluble and brittle due to the high rigidity of backbones, and many efforts have been taken to improve their solubility and processability, such as adding flexible side chains. Many systems have now been developed with desirable combinations of

conductivity and processability. Scheme 1.1 lists typical preparation methods for several classic conjugated polymers.

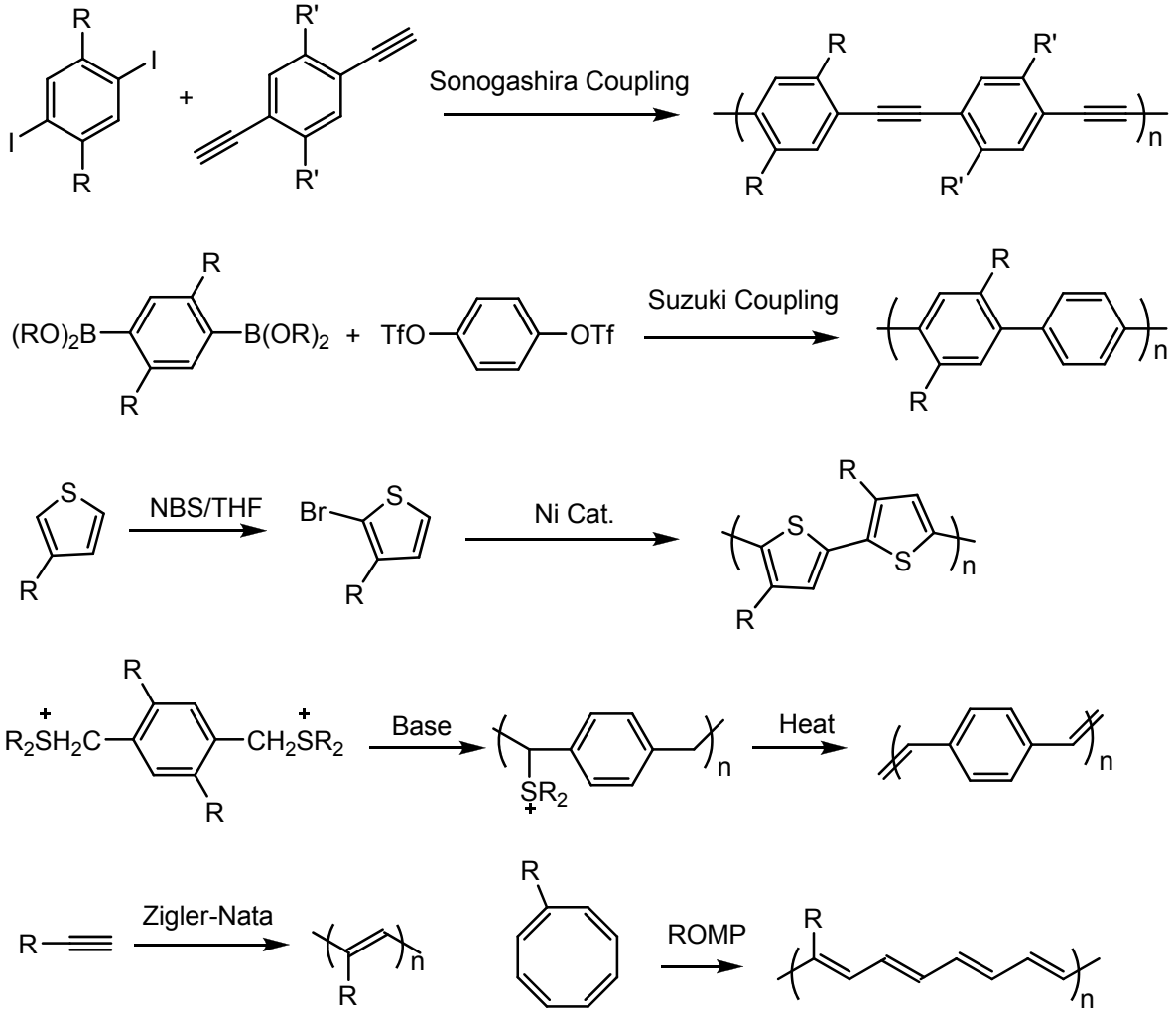

Scheme 1.1. Typical synthesis methods for classic conjugated polymers[13,20,22,23]

1.2. Polydiacetylenes

Polydiacetylenes, or PDAs, are conjugated polymers with alternating double and triple bonds along the polymeric backbone. They form a unique class of conjugated polymers which combines highly ordered conjugated backbones and flexible side chains bearing tunable functionality. The non-linear optical properties resulting from the quasi 1-dimensional π systems make PDAs excellent multiphoton absorbers.[24-26] In addition, PDAs are good candidates for

sensing materials; many PDAs undergo a visible color change in response to environmental perturbations like temperature, pH and ligand-receptor interactions.[27-30]

1.2.1. Preparation of PDAs by topochemical polymerization

Preparing highly ordered PDAs presents a substantial synthetic challenge for the common solution-based polymerization methods introduced in Scheme 1.1: the disordered diyne molecules can react by either 1,2- or 1,4-addition, leading to a polymer with an irregular, branched backbone instead of regular repeat units. However, if the diynes are aligned appropriately in the solid state, their arrangement in space will control their reactivity, leading to ordered topochemical polymerization.[31]

Baughman[31] reported the empirical parameters necessary for a regioregular head-to-tail diyne polymerization (Scheme 1.2). The translational distance between related atoms in each diyne is ideally 4.9 Å, matching the repeat distance in the target PDA. The 1,4-polymerization reaction also works most effectively when the diynes stack at a 45° angle. Finally, the contact distance should be as close as possible to the Van der Waals distance for the two reacting carbon atoms (3.5 Å). These parameters will effectively place the monomer atoms in the diynes so that the molecular motion required to approach polymerization is minimized. The diyne monomers can then undergo a topochemical polymerization to form an ordered PDA. Ordered alignment of functionalized diynes can be achieved in single crystals,[32,33] layered crystalline films,[34] vesicles and ordered inorganic host matrices.[35]

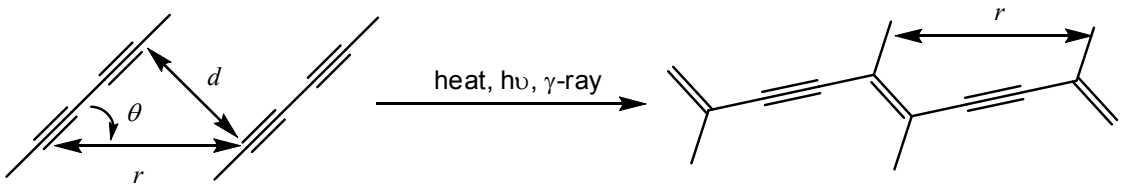

Scheme 1.2. Alignment of diynes for topochemical polymerization. Optimal values are r = 4.9 – 5.0 Å, θ = 45°, and d = 3.5 Å

1.2.2. Research progress on preparing functional PDAs

Topochemical polymerization of diacetylene derivatives in the crystalline state, as first reported by Wegner et. al using 1,2-bis(p-tolylsulphonyloxymethylene)-1-buten-3-ynylene,[32] proceeds along a unique crystal direction and is strictly controlled by the crystal packing parameters described in section 1.2.1.

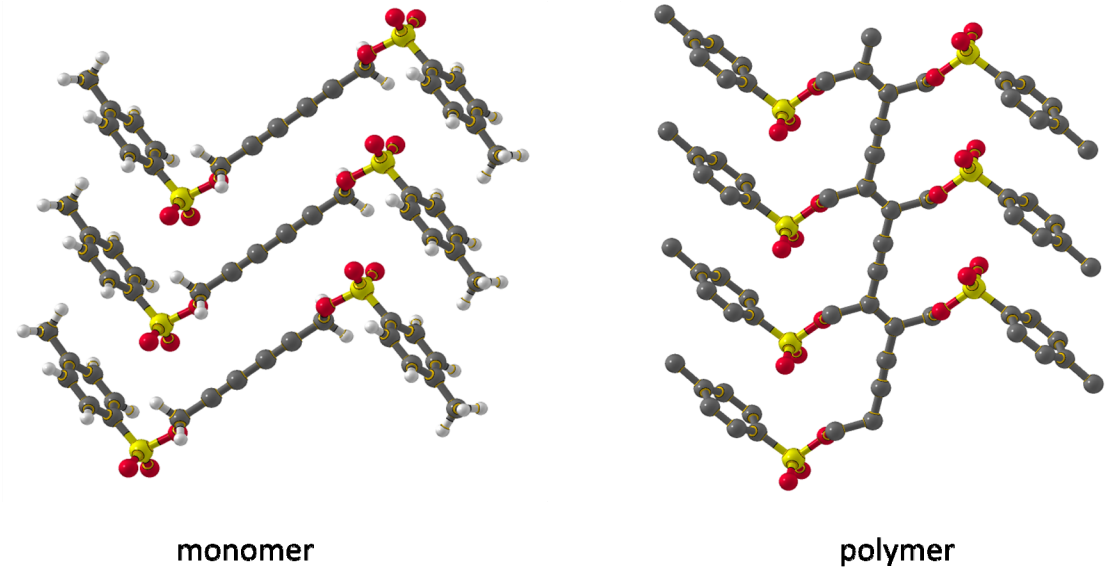

Figure 1.7. Crystal structures of 1,2-bis(p-tolylsulphonyloxymethylene)-1-buten-3-ynylene and its polymer.[32]

Frauenrath has reported an alternating diyne copolymer utilizing perfluorophenyl-phenyl interactions.[36] Within the co-crystals of 2,4-hexadiynyl dibenzoate and 2,4-hexadiynyl bis(pentafluorobenzoate), phenyl and perfluorophenyl groups are stacked face to face with little parallel displacement. Interestingly, the alternating packing of the diyne groups of the two

monomers is not parallel, with the repeat distance of 5.10 Å on one end but 4.80 Å on the other. UV irradiation of the co-crystals led to a deep red diyne copolymer characterized by single-crystal X-ray diffraction (XRD) and Raman spectroscopy.

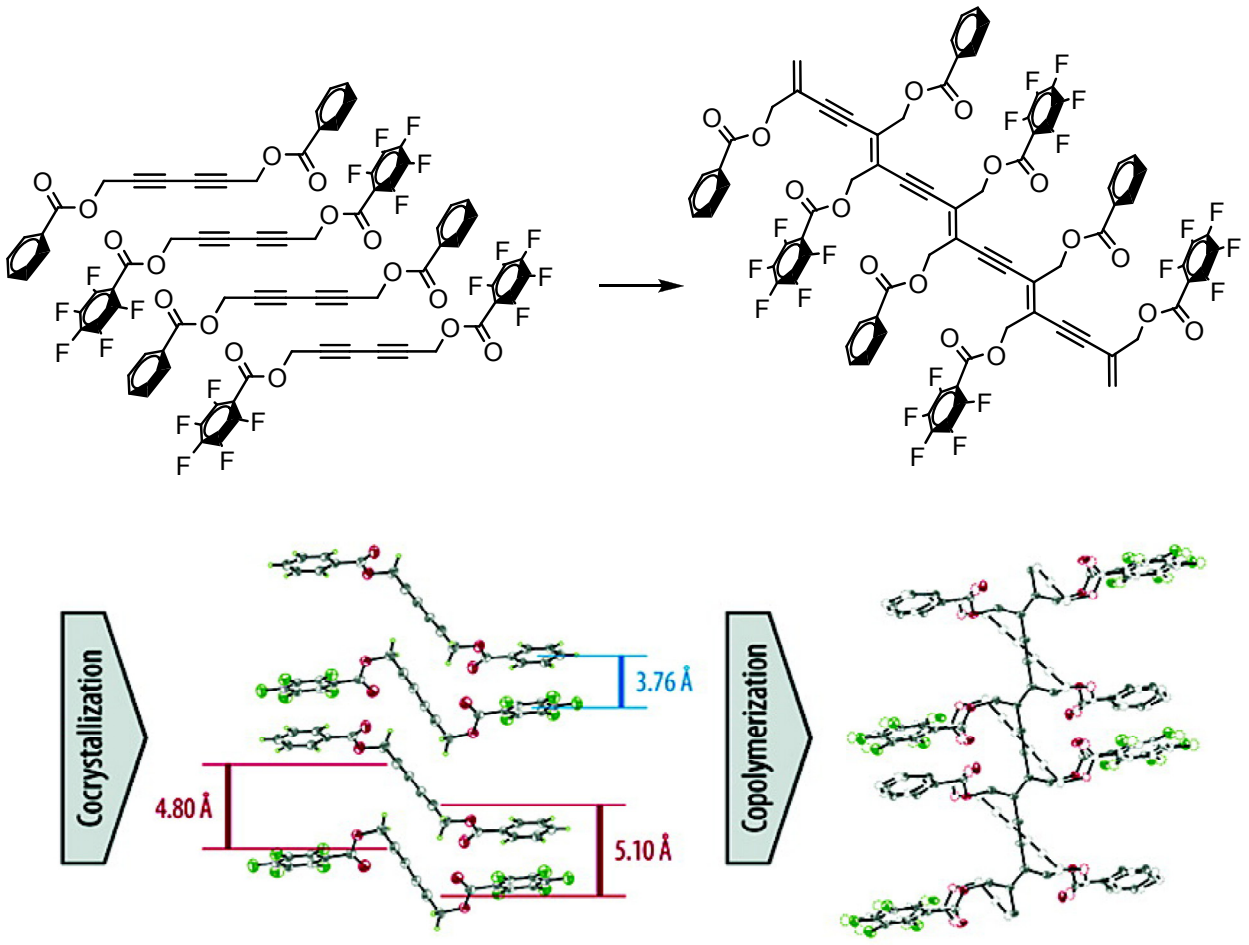

Scheme 1.3. Alternating poly(diacetylene) copolymer by topochemical polymerization of co-crystals between 2,4-hexadiynylene dibenzoate and 2,4-hexadiynylene bis(pentafluorobenzoate). Reprinted with permission from Ref 36, Copyright 2006, American Chemical Society.

Instead of single crystals, a variety of diynes can be assembled and polymerized in layered films, which have been extensively studied by spectroscopic methods.[35,37,38] Layered films still require optimal packing of the diyne units to allow ordered topochemical polymerization. In these systems, the side chains dominate the packing of diyne monomers. Appropriate substituents or headgroups are tuned to direct the ordered alignment of monomers to approach

the desired PDA products. Preparing self-assembled PDA materials in Langmuir-Blodgett films, liposomes, and multilayer coatings has been reviewed recently by Reppy.[30]

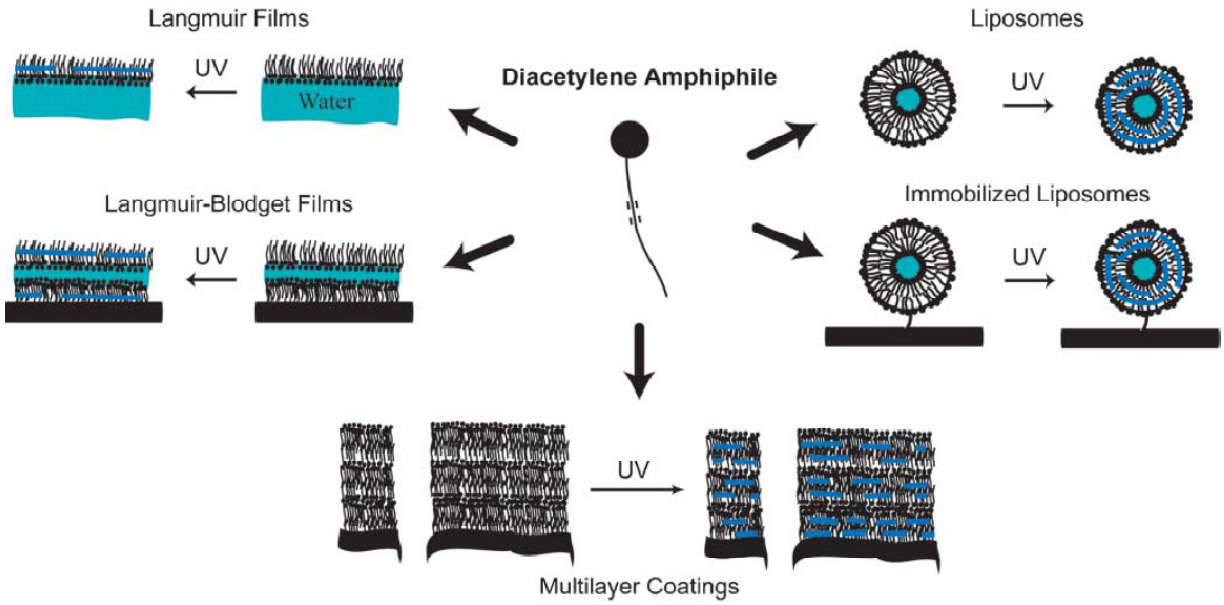

Figure 1.8. Diyne amphiphiles form a variety of self assembled structures that can be photopolymerized. Reprint with permission from ref. 30, Copyright 2007, the Royal Society of Chemistry.

In the case of PDA vesicle formation, the lipids must hydrate and also organize into the correct packing and orientation to undergo the 1,4 addition to the conjugated polymer. Charych and coworkers have extensively investigated using double-chained phospholipids to form multilayer PDA vesicle structures, as listed in Figure 1.9.[35] In particular, the surface of the PDA vesicles can be modified by bio-recognition molecules, so that the materials can be applied for biosensing based on their biochromic responses of binding analytes. This work will be introduced in Section 1.2.3.

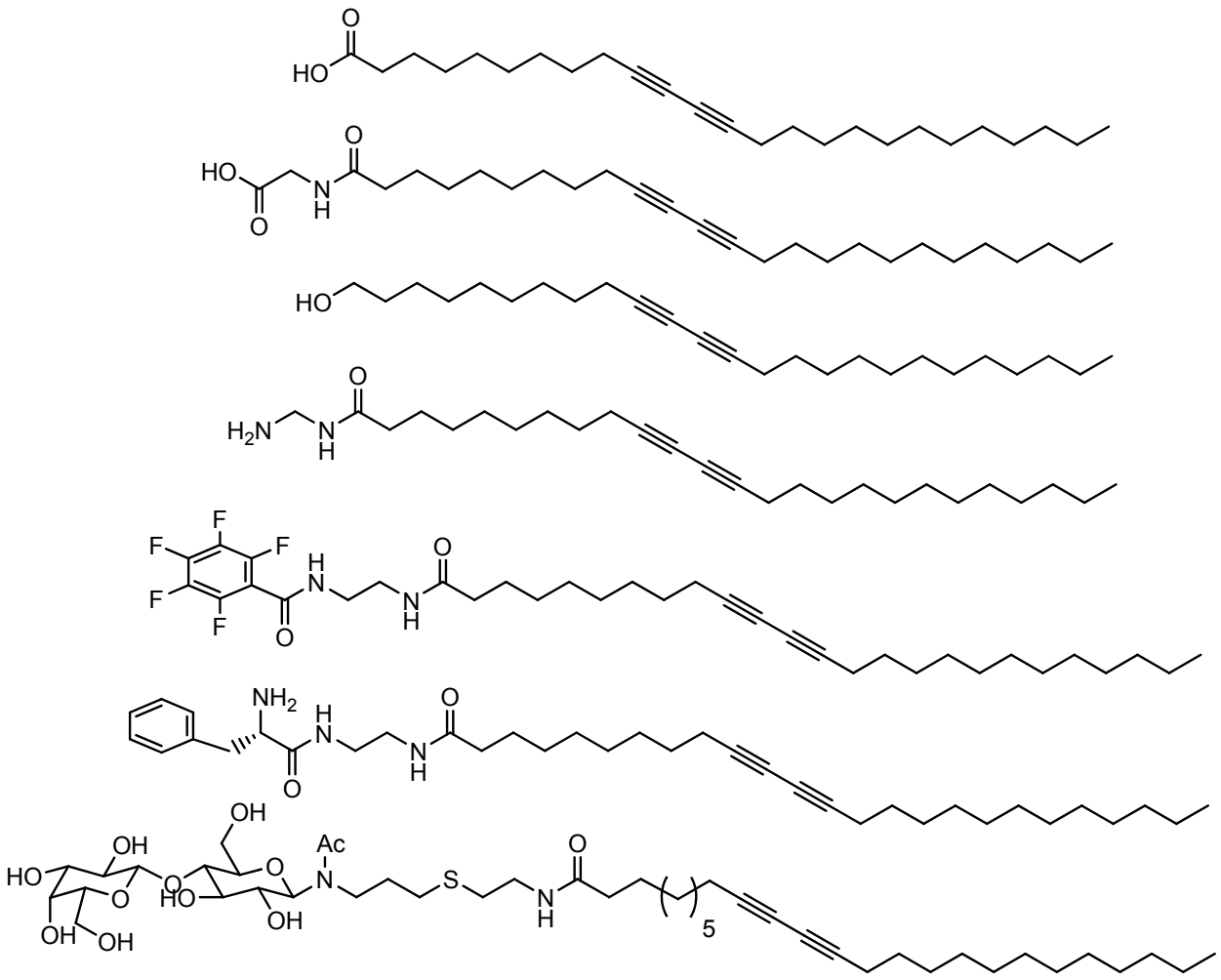

Figure 1.9. Diacetylene lipid structures. (The last two can only hydrate to form unpolymerized vesicles)[35]

1.2.3. Chromism of functional PDAs and related applications

The topochemical polymerization of ordered diyne monomers can result in exceptionally high conjugation of PDA. The extended π–conjugated chains can absorb lights at different wavelengths, leading PDA's to take on colors from blue to red to yellow. The longer the effective π-conjugation length of the PDA, the longer the wavelength of the light it absorbs. Absorption spectra of PDA materials typically contain several peaks with maxima at *ca.* 650, 550, and 500 nm. These peaks are associated with the blue (650 nm) and red forms of PDA (550 nm and 500 nm).[30] There are absorption peaks at 450 nm reported for green PDA solids[39] and

peaks at *ca.* 400 nm for yellow PDA solutions.[40,41] Absorption peaks at higher than 700 nm have also been observed for PDA films and particles; these are rare but are correlated with materials containing exceptionally high effective conjugation lengths.[34,42,43]

The wavelength and intensity of absorbance peaks for a given PDA material depend on its effective conjugation length, which can be affected by the structure of the polymer side chains, the extent of polymerization, the polymer's material form, and the environment of the polymer. Color changes for PDA materials take place in response to heat (thermochromism),[44,45] organic solvents (solvatochromism),[46,47] mechanical stress (mechanochromism),[48] and ligand-receptor interactions (affinochromism).[27,49,50] These changes usually coincide with reduction in the higher wavelength absorbances and growth of lower wavelength absorbances, which register to the eyes as shifts from blue to red, red to yellow, etc.

Considerable research effort has been devoted to elucidating the mechanisms of color change in PDA materials caused by environmental changes, although this has proven to be a difficult challenge and the mechanisms are still not fully understood. One explanation to the color change of PDA materials is the conformational changes in the polymer backbone, caused by the changes in the structure of the side chains assembly, including both the packing of the methylenes and bonding interactions at the side chain headgroups.[38,51,52] Figure 1.10 exhibits a schematic representation of conformational changes in PDA during the color transition.

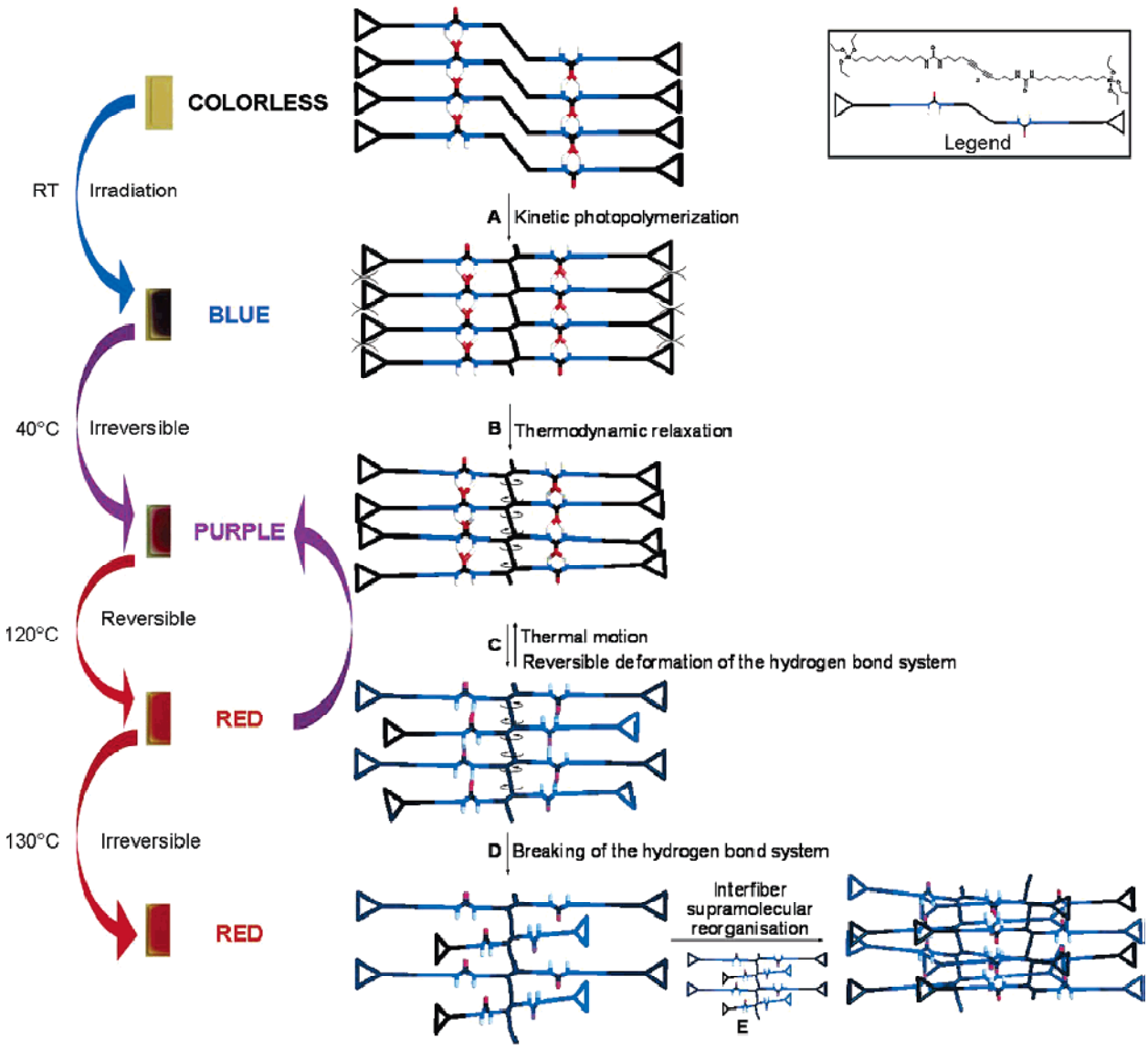

Figure 1.10. Schematic representation of the molecular organization in the supramolecular assembly of PDA in the different thermochromic phases. Reprinted with permission from Ref 34. Copyright 2006, American Chemical Society.

Another view of the mechanism of the chromism is the intermolecular aggregation.[40] In this hypothesis the color change involves the aggregation of polymer chains or segments which form a micelle-like structure consisting of many polymer chains or segments. The aggregation process forces the polymer chains together, resulting in the formation of extended rod-like polymer chains which causes the color change. This theory is supported by the fact that the particle size of PDA changes during the colorimetric change, as shown in Figure 1.11.[53]

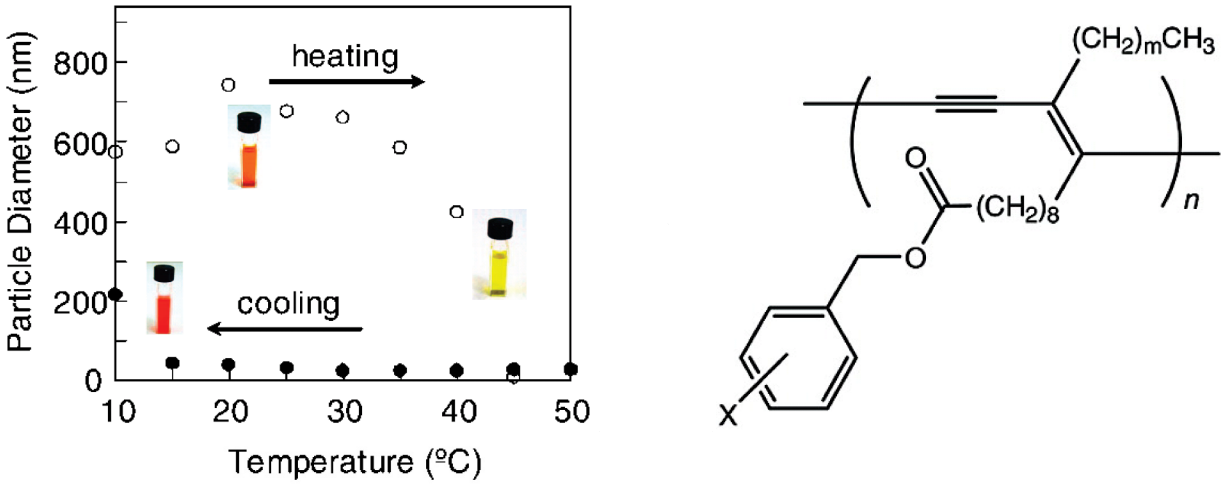

Figure 1.11. Change in particle diameter of a PDA at various temperatures in THF determined by dynamic light scattering measurement. Reproduced with permission of ref. 53, Copyright 2008, American Chemical Society.

The exceptionally high conjugation of PDAs and their environmentally sensitive optical characteristics make PDAs excellent candidates for chemical and biological sensing materials, in addition to the applications of conjugated polymers introduced in Section 1.1.3. In an interesting early experiment, Charych and co-workers prepared a PDA Langmuir-Blodgett film, functionalized with sialic acid, and showed that the film undergoes a blue-to-red change when exposed to an influenza virus, as shown in Figure 1.12.[27]

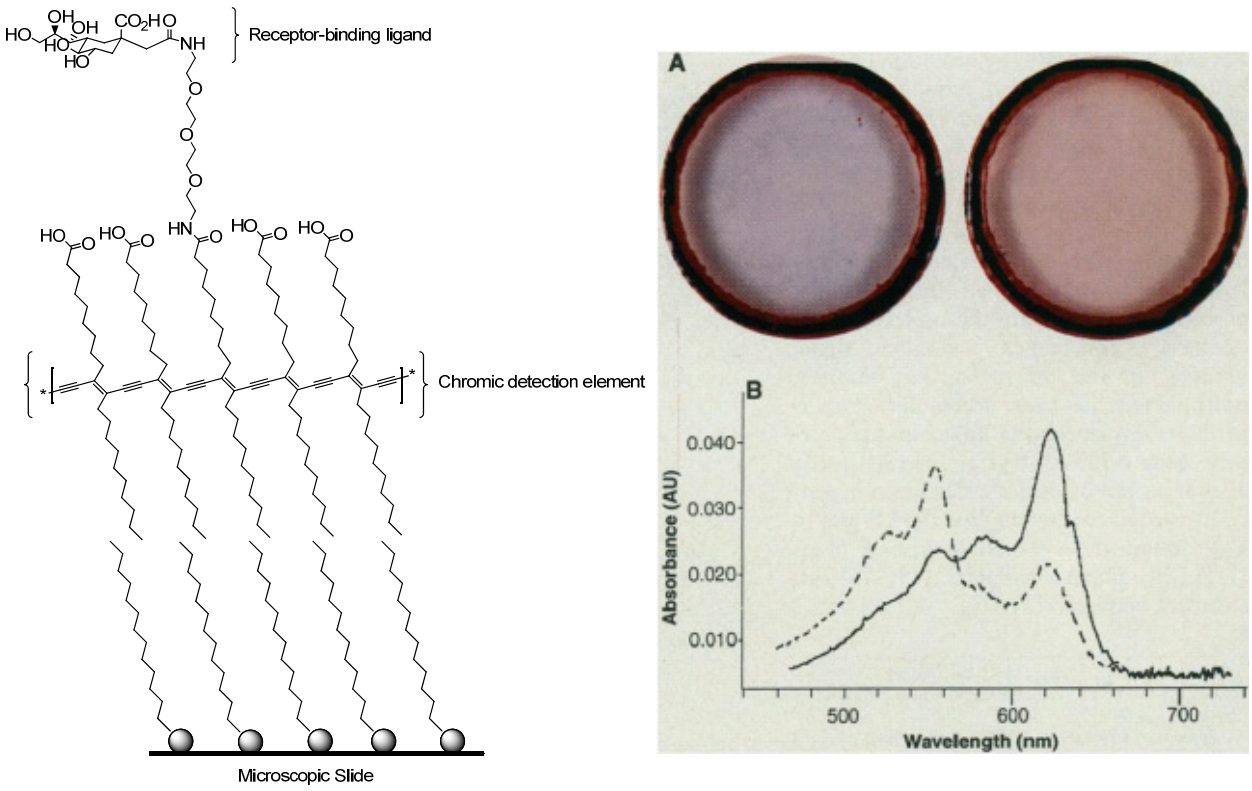

Figure 1.12. Schematic diagram of a polymerized bilayer assembly and colometric detection of influenza. The film changes from blue to red after being exposed to virus. Reproduced with permission from ref. 27, Copyright 1993, American Association for the Advancement of Science.

Since the report of Charych's influenza virus detecting systems, a variety of colorimetric PDA-based chemo/biosensors have been investigated. A schematic representation of PDA sensor systems reported to date is shown in Figure 1.13.[54] Based on the occurrence of a blue-to-red color transition, PDA vesicles can be used as colorimetric DNA sensors, if immobilized with probe DNA molecules and undergo the color change upon binding with complementary strands of DNA;[55] glucose detectors, based on ligand-induced conformational changes of hexokinase immobilized on a PDA monolayer;[56] metal ion detectors, formed by embedding an ionophore into a PDA lipsome;[57] enzyme detecting sensors, driven by a hydrophilic-to-hydrophobic transformation of an enzyme-substrate;[58] and colorimetric PDA sensor systems based on specific antibody-antigen interactions.[59]

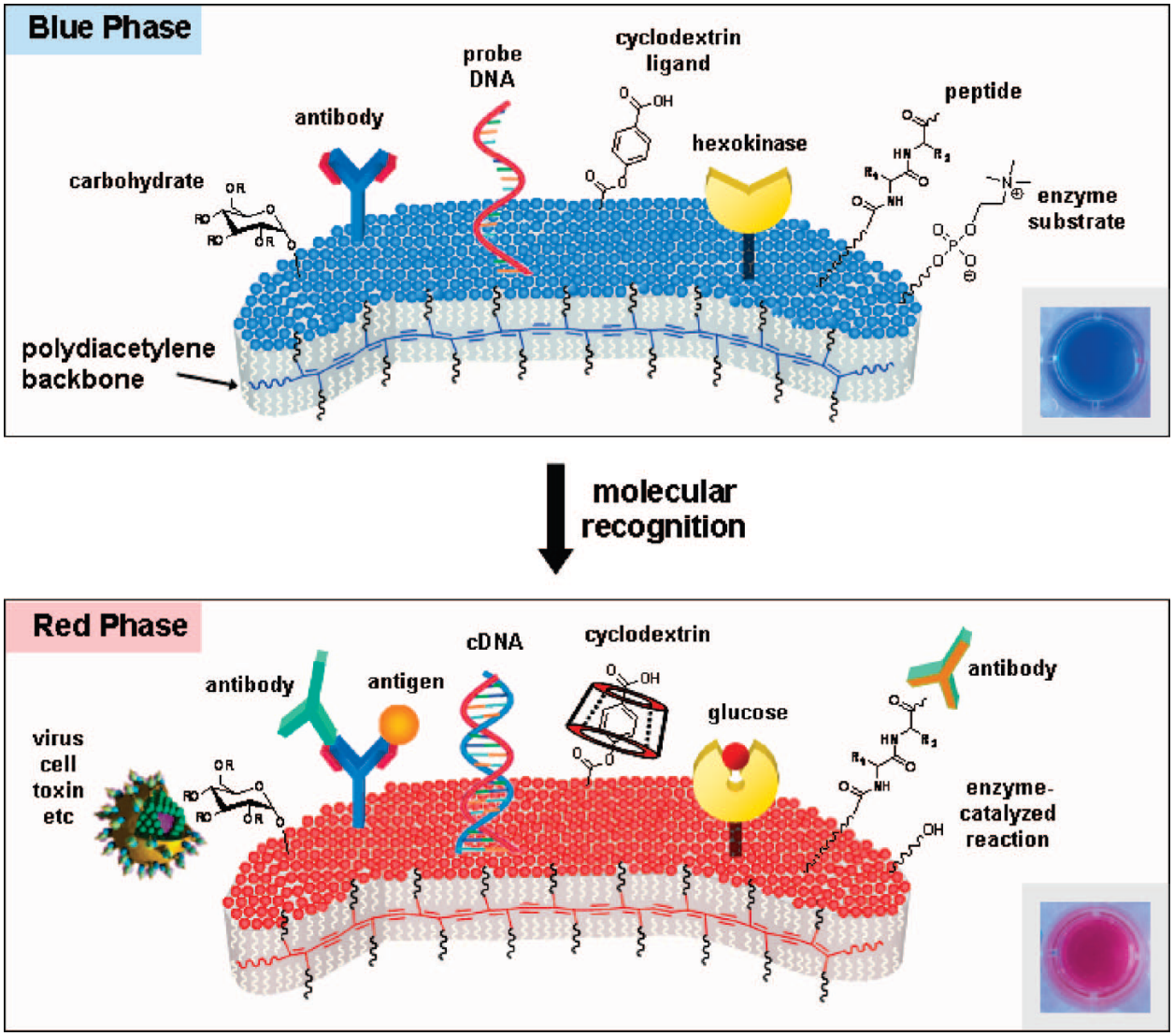

Figure 1.13. A schematic representation of surface ligands and their interactions with target molecules in colorimetric PDA sensors. Reprinted with permission of ref. 54, Copyright 2008, American Chemical Society.

1.3. Poly(diiododiacetylene)

The above introduction has shown the promising applications of PDAs, and demonstrated how chemists creatively design and prepare PDAs for these applications. However, preparing PDAs from topochemical polymerization brings experimental complexity and uncertainty. Complicated amphiphilic side chains with polar headgroups are necessary in order to build self-assembling complex with favorable packing parameters for diyne centers. Some PDAs, such as

poly(aryldiacetylene), are desirable targets predicted to have particularly strong nonlinear optical absorptions, but their preparation by topochemical polymerization is limited because the optimal packing can not be reached due to steric hindrance.[60] No reliable method for preparing poly(aryldiacetylene)s has been developed so far.

Poly(diiododiacetylene) (PIDA, **1** in Scheme 1.4) is our designed target polymer and represents a possible solution to the general problem of PDA synthesis. PIDA contains the PDA backbone but with only iodine substituents. The abundance of coupling methods available for replacing iodine by functional substituents on the backbone scaffold makes PIDA a potential precursor to a wide variety of PDAs. Several hypothetical examples are shown in Scheme 1.4 below.

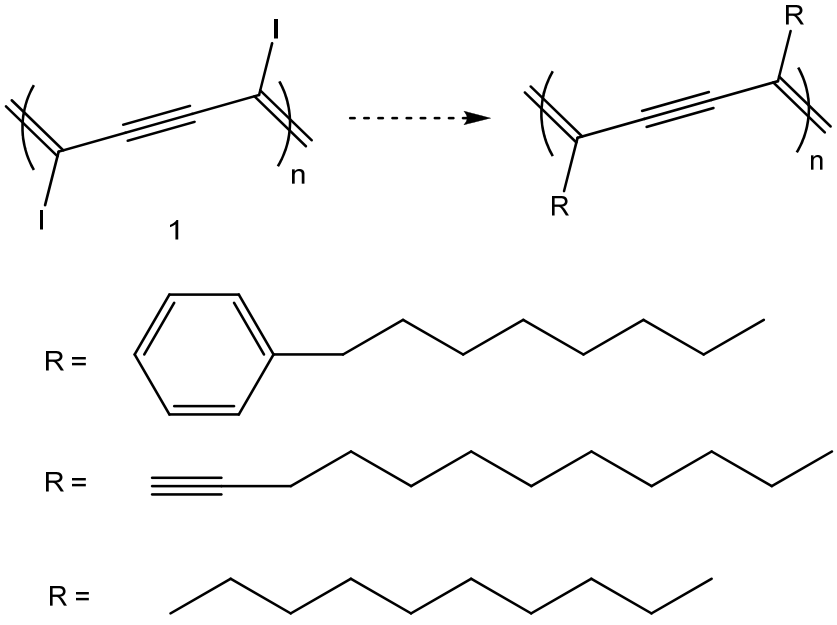

Scheme 1.4. Schematic representation of the syntheses of functionalized PDAs from PIDA.

PIDA may also act as a precursor to carbyne, the hypothesized linear sp-hybridized allotrope of carbon $(-C\equiv C-)_n$.[61] Currently no definitive synthesis of carbyne has been reported. Researchers have approached carbyne by rational synthesis of discrete polyyne rods with up to 28-carbon long, allowing for the prediction of many of its properties.[62,63] PIDA is a promising

precursor to fully ordered carbine. With its linear arrangement of carbon atoms and single iodine leaving groups, transformation of PIDA to carbine requires only the dissociation of carbon-iodine bonds by electrochemical or thermo reduction, as shown in Scheme 1.5.

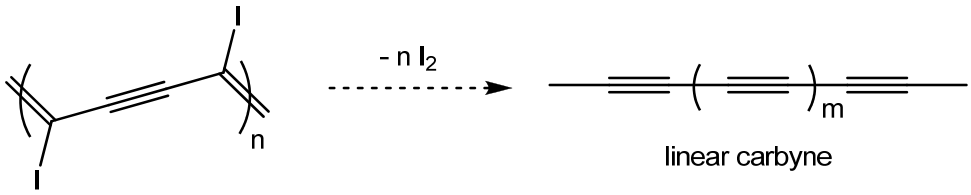

Scheme 1.5. A possible approach to linear carbyne from PIDA.

In addition, because of the simplicity of its structure, PIDA can provide insights into the color transitions observed in other PDAs. Chromatic changes in PDAs in response to environmental stimuli have served as the basis for the majority of PDA-based sensing materials, as was introduced in Section 1.2.3, but to elucidate the mechanisms of the color and emission changes in PDA materials has proven to be a great challenge. Studies have shown that the factors affecting the chromic state and the susceptibility to chromic change of PDA materials include rotational changes in the polymer backbone, changes in the structure of the side-chain assembly, and hydrogen-bonding interactions at the side-chain head-groups.[51,52] The aggregation states and the transition of the polymer backbone from extended rod-like segments to discrete coils further confuse discussion of the interplay between the conjugated polymer backbone and the ensemble material structure in determining the observed optical properties.[40,64] PIDA has no side chains, presenting an important test case in the study of PDA optical properties.

1.4. Host-guest supramolecular co-crystal strategy

To prepare stereoregular PIDA requires ordered alignment of the monomer diiodobutadiyne. As a linear rod-shape molecule, diiodobutadiyne forms needle-shaped crystals that are disordered along the direction of the molecular axis. In these crystals, the alignment of the monomers is

random, preventing order polymerization. Here, the strategy used is a host-guest co-crystal system developed by Lauher and Fowler.[65] Host molecules are designed to contain the necessary groups to create a hydrogen-boned network with a repeat distance of about 4.9 Å. Ureas and oxalamides are usually used as hosts, because they form self-complementary hydrogen bonding networks with repeat distances of 4.6 Å and 5.0 Å respectively (Figure 1.14), matching well the 4.9 Å distance requirement for diyne 1,4-polymerization.[66] The end groups in the hosts and guest diyne monomers are designed to match each other to enforce intermolecular interactions between the hosts and guests.

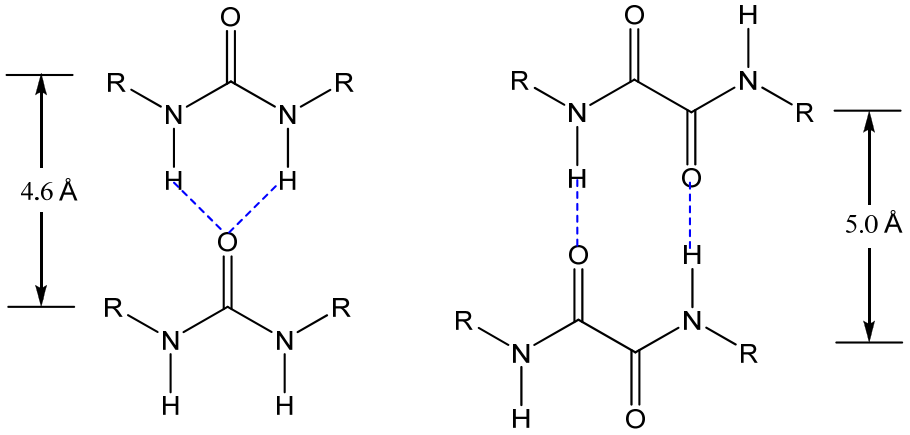

Figure 1.14. Self-assembling in ureas and oxalamides.[66]

The host-guest co-crystal system is synthetically convergent and flexible. The structure and function are divided, with the structure established by the host and imposed upon the functional guest. A library of prepared urea or oxalamide molecules can be set up to provide hosts favorable to the topochemical polymerization of desired functional diyne guests.[65] A successful host-guest co-crystal is shown in Figure 1.15,[65] the result of which presents a single crystal with polymer chains embedded in a lattice of the host molecules. The oxalamide host molecules form an α-network with a repeat distance of 4.97 Å, only slightly longer than the ideal value of 4.9 Å. The

neighboring C(1)-C(4) atoms are 3.38 Å apart, very close for nonbonded atom. Heating the single crystal brings about a clean polymerization.

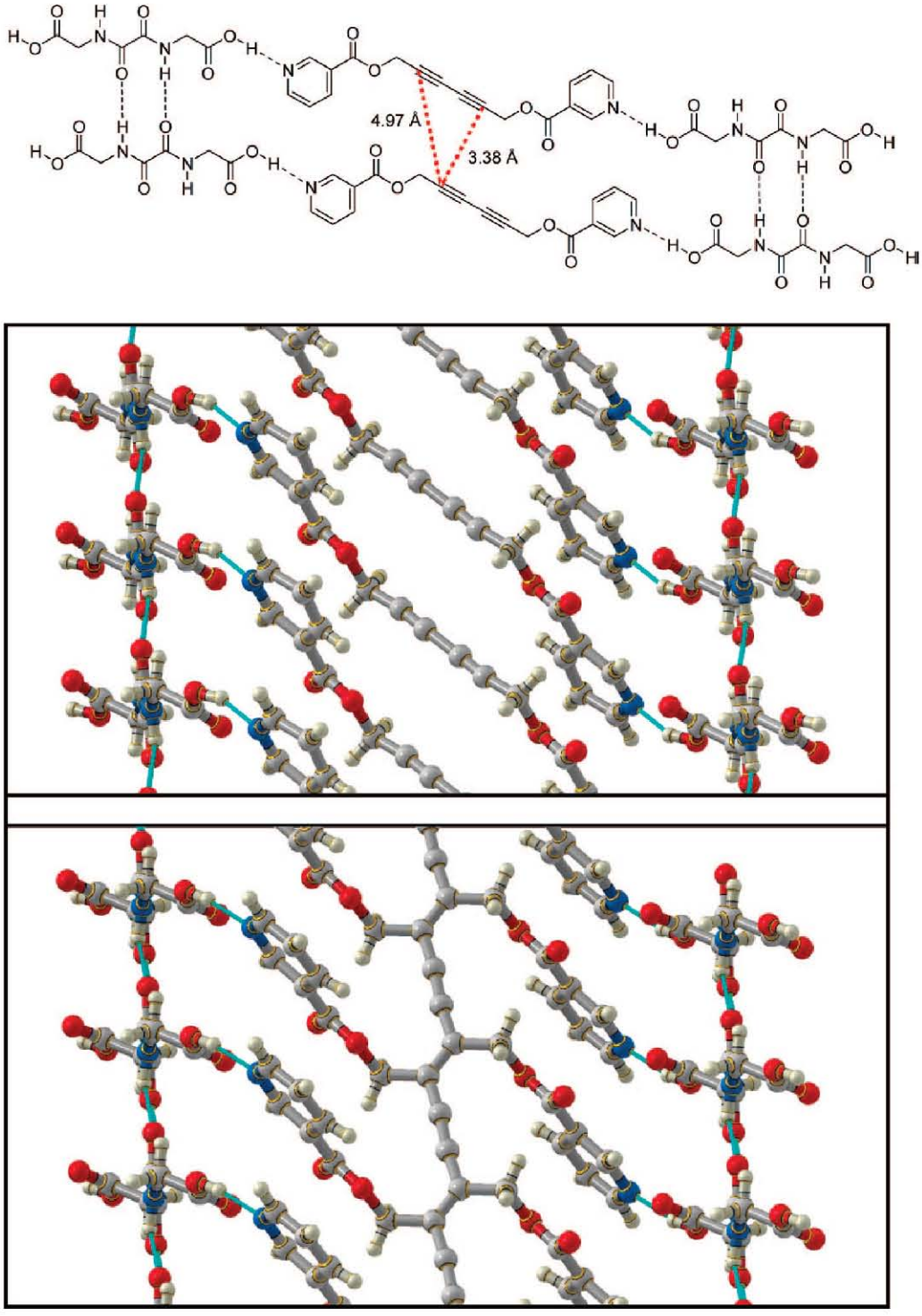

Figure 1.15. A designed single-crystal-to-single-crystal topochemical polymerization. Reprinted with permission from ref. 65, Copyright 2008, American Chemical Society.

The significance of the host-guest strategy is the ability to use hosts to organize diyne monomers into ordered asemblies, providing a reliable way to reach the designed PDA topochemically. The functionalities in the host and guest can be tuned to approach suitable packing parameters for topochemical polymerization. Little can be done to change the molecular packing of a single molecule. However, the host-guest co-crystal strategy can be used to tune the molecular packing of the guest, leading to the desired PDA.

1.5. Building host-guest co-crystals with diiodobutadiyne by halogen bonds

Host-guest co-crystal strategy provides assembled scaffoldings for guest diynes with controlled molecular spacing. In our situation, to align monomer diiodobutadiyne within the host framework, we take advantage of the strong Lewis acidity of highly polarizable iodine substituents. In iodoalkynes, this effect is magnified because *sp* hybridization increases the electronegativity of the carbon atom bonded to iodine, polarizing the C-I bond toward carbon. Diiodobutadiyne will assemble with appropriate base-terminated hosts via "halogen bonds", the Lewis acid-base interactions between electrophilic iodine and nucleophilic bases.

1.5.1. Halogen bonds

In analog to the more common hydrogen bonds, the term "halogen bonds" refers to the noncovalent interaction between a halogen atom (Lewis acid) and a neutral or anionic Lewis base.[67] The first report on the ability of halogen atoms to form well-defined adducts with electron donor species dates back to 1863 when Guthrie described the formation of the $H_3N\cdots I_2$ complex.[68] After that, halogen bonds are widely applied in supramolecular architectures with solid[69] and gas[70] adducts.

The general scheme D···X–Y of halogen bonding is shown in Figure 1.16. The halogen X is Lewis acidic, which accepts electron pairs and behaves as a halogen bonding donor. D is Lewis

base, and behaves as an electron donor and halogen bonding acceptor. Y can be carbon, nitrogen, halogen, etc. The intensity of halogen bonding relies on charge transfer, electrostatic effects, polarization, and dispersion contributions. The stronger the intensity, the shorter the D···X distance. Among all four halogen atoms, the tendency to form strong halogen bonding is F < Cl < Br < I. Dihalogen molecules, and interhalogens form strong halogen bonds. The more electron-withdrawing Y is, the stronger is the halogen bonding. As to halocarbons, their halogen bonding strength order is C*sp*-X > Csp^2-X > Csp^3-X, with there is no observed halogen bonding in unfunctionalized monohaloalkanes due to competing nucleophilic substitution. D is any Lewis base, among which anions usually are better electron donors neutral species, and nitrogen provides stronger halogen bonding than oxygen and sulfur.[67]

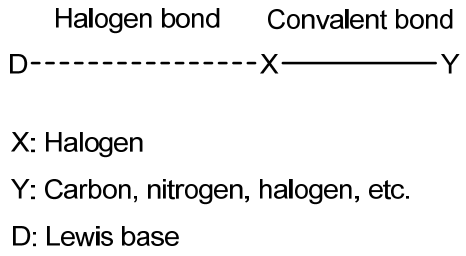

Figure 1.16. Scheme of a halogen bonding complex

Theoretical calculations exhibits that the electron density is anisotropically distributed around the halogen nucleus within a halogen bonding complex, and the effective halogen atomic radius along the X–Y bond axis is much smaller than in the direction perpendicular to this axis.[71] Based on an extensive investigation of halogen bonding examples in the Cambridge Structure Database (CSD), as shown in Figure 1.17, Resnati and co-workers proved that the D···X–Y angles are located in a specific range close to 180°, and the shorter the halogen bonds, the more linear they are.[67]

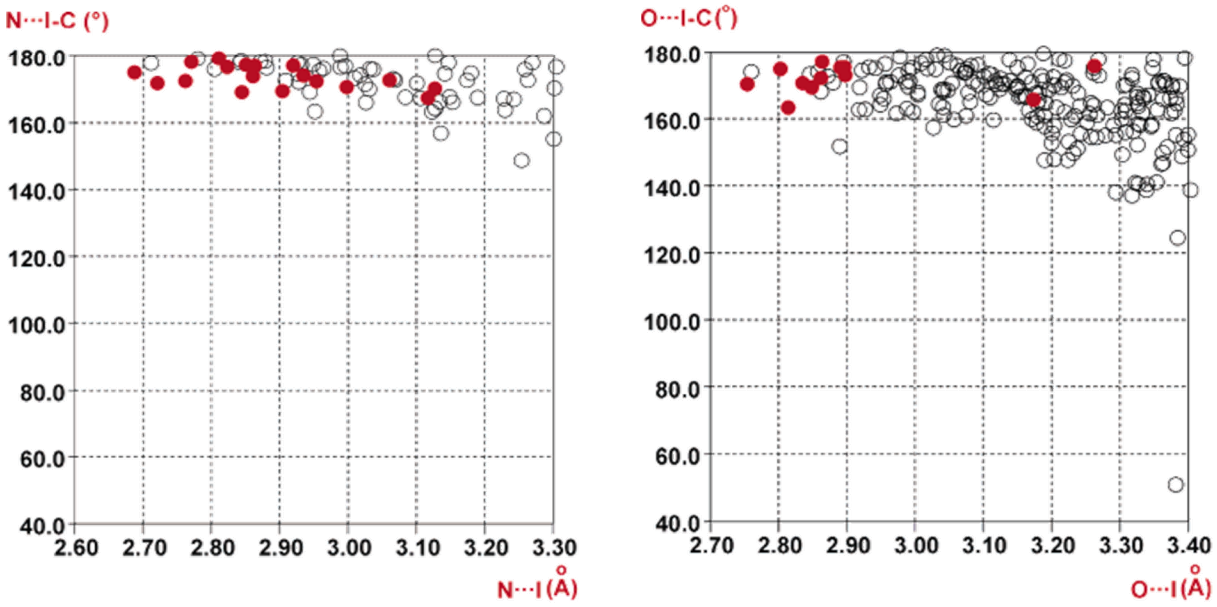

Figure 1.17 Scatterplots derived from the CSD (298,097 crystal structures; only error-free and nonpolymeric structures containing single-bonded iodine atoms and showing no disorder with R < 0.06 are considered) reporting N···I-C angle (deg) vs N···I distance (Å) (top) and O···I-C angle (deg) vs O···I distance (Å) (bottom) data for crystal structures containing intermolecular N···I and O···I contacts, respectively. Red circles correspond to crystals of iodofluorocarbons. Reprinted from ref. 67, Copyright 2005, American Chemical Society.

1.5.2. Current research on iodoalkynes

As introduced in Section 1.5.1, iodoalkynes are good Lewis acids as a result of the polarizability of iodine and the higher electronegativity of sp-hybrized carbon.[72,73] They can form very strong halogen bonds with certain Lewis bases. The Goroff group have extensively investigated the Lewis acidity of iodoalkynes, and their Lewis acid-base interactions, i.e., the basis of halogen bonding, between iodoalkynes and Lewis bases.[74-77]

Gao and Goroff reported an unusual change in the ^{13}C NMR shifts of the α-carbons of iodoalkynes in different solvents, which was first discovered when characterizing two new iodine-capped carbon rods, diiodohexatriyne and diiodooctatetrayne.[74] The chemical shifts of the α-carbons are 0.9 (in diiodohexatriyne) and 1.9 (in diiodooctatetrayne) ppm in $CDCl_3$. The shifts

change to 14.6 and 17.9 ppm separately in DMSO-d_6. This increase of NMR chemical shift is attributed to a Lewis acid-base interaction between the iodine and the oxygen in DMSO.

However, halogen bonding would predict an increase in the electron density at the α-carbon, and therefore a decrease in its chemical shift.[67] To investigate this controversy the Goroff group have closely examined the effect of Lewis bases on the NMR spectra of iodoalkynes, which offers a potential probe for measuring and comparing the noncovalent interactions between iodoalkynes and various Lewis bases. [75] Rege and Goroff calculated the structures, energies, and ^{13}C NMR chemical shifts of two iodoalkyne-DMSO complexes have been calculated, and their calculated geometries are shown in Figure 1.18. The linearity of O···I-C in each complex, and the O-I distances that are shorter than the sum of the oxygen and iodine van der Waal radii (3.55 Å),[78] suggesting a charge-transfer interaction within the complex. It was hypothesized that this interaction between iodoalkyne and a Lewis base polarizes both C-I σ bond and the alkyne C-C bond, deshileds the electron cloud around the nucleus of α-carbon, and increases the chemical shift of α-carbon as what being observed.

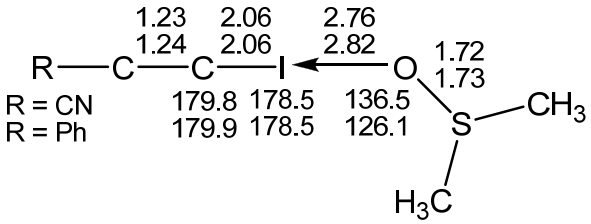

Figure 1.18. Calculated geometries (QCISD/LanL2DZ) for two Lewis acid-DMSO complexes. Bond lengths (in Å) and bond angles for nitrile derivative are shown above those for phenyl derivative.

The above hypothesis was proved to be incorrect by follow-up experimental studies of the ^{13}C NMR of iodoalkynes in Lewis-basic solvents, which revealed a strong solvent dependence of ^{13}C NMR shifts of α-carbons in two different iodoalkynes, 1-iodo-1-hexyne and diiodoethyne.[76] The similarity of the solvent effect for two iodoalkynes suggests that carbon-carbon bond polarization may not play a role in the change in chemical shift. To examine the role of bulk

solvent properties in the observed NMR shifts, studies in neat solvents of various basicity and polarity were carried out. The observed NMR shifts of the α-carbons of the two iodoalkynes in different solvents, together with the literature basicity of corresponding Lewis bases, are listed in Table 1.1. Among the several empirical modes of solvent basicity used for correlating the observed chemical shifts, Gutmann's donor numbers and Taft and Kamlet's β values disclose a linearly increase in the α-carbon shift as a function solvent basicity, indicating that acid-base interactions are responsible for the observed change in chemical shift; while Reichardt's E^{N}_{T} and Taft and Kamlet's π^* parameters exhibit poor correlations with chemical shift changes, excluding the role of solvent polarity in affecting the observed chemical shift.

Table 1.1. Neat solvent NMR data and selected solvent parameters.

Solvent	δ(1)[b]	δ(2)[c]	DN[d]	E^N_T[e]	β[f]	π^*[f]	B_{soft}[g]	δ($CHCl_3$)[h]
Hexanes	-7.95	-1.45		0.009	0.00	-0.08		
$CDCl_3$	-7.96	0.62		0.256				
$CHCl_3$	-7.10	0.61		0.259	0.00	0.58	1.0	0.20
Dichloroethane	-6.89	1.34		0.327				
CCl_4	-6.29	0.47		0.052			0.0	
Benzene	-6.10	1.27	0.1	0.111	0.10	0.59	10.0	
Ethyl acetate	-4.53	3.47	17.1	0.228	0.45	0.55		
Diethyl ether	-4.40		19.2	0.117	0.47	0.27	20.5	0.74
Acetonitrile	-3.62	5.26	14.1	0.460	0.31	0.75	17.0	0.56
THF	-3.33	4.67	20.0	0.207	0.55	0.58	25.0	0.79
Acetone	-2.72	5.80	17.0	0.355	0.48	0.71	18.0	0.92
Dimethyl sulfide	-1.56	7.31		0.065				
DMF	0.27	8.68	26.6	0.404	0.69	0.88	30.0	1.30
Triethylamine	2.78		31.7	0.043	0.71	0.14		1.22
DMSO	3.55	12.36	29.8	0.444	0.76	1.00	32.0	1.32
Quinoline	3.75	13.67		0.269			50.0	
Pyridine	3.85	13.03	33.1	0.302	0.64	0.87	57.5	1.56
HMPA	5.09	11.65	38.8	0.315				2.06
Diethylamine	7.10			0.145				
N-methylenimidazole	7.17	16.40						

[a] Chloroform used as purchased, including 1% ethanol as stabilizing agent. [b] ^{13}C chemical shift of the α-carbon of 1-iodo-1-hexyne, relative to externail cyclohexane-d_{12} lock. [c] ^{13}C chemical shift of the α-carbon of diiodoethyne, relative to external acetone-d_6 lock. [d] Gutmann's donor number.[79] [e] Reichardt's E^N_T values.[80] [f] Taft and Kamlet's β and π^* parameters.[81,82] [g] Laurence's B_{soft}.[72] [h] ^1H chemical shift of chloroform.[83]

Moss and Goroff have undertaken a qualitative examination of the molecular orbitals of diiodoethyne and its complexes with one and two ammonia molecules, as shown in Figure 1.19.[77] The major change in the molecular orbitals of the complex compared to original iodoalkyne is the introduction of the nitrogen lone pair(s), which donates electron density into the C-I antibonding orbital and increases the paramagnetic deshielding at the α-carbon.[84]

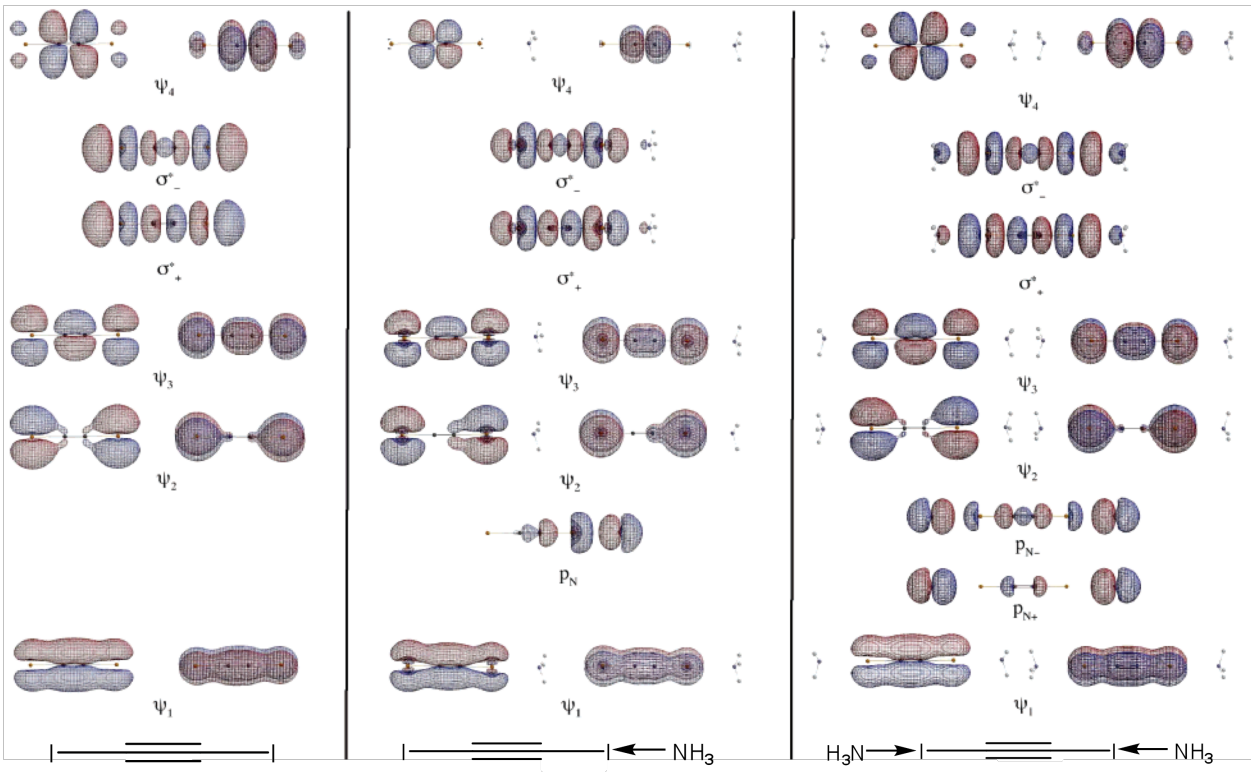

Figure 1.19. Frontier molecular orbitals of diiodoethyne and its mono- and bisammonia complexes. Reproduced with permission from Ref. 77, Copyright 2005, American Chemical Society.

1.5.3. Building desired co-crystals by halogen bonds

Halogen bonds have been recognized as a reliable organizational motif in the solid state,[67] in addition to traditional noncovalent controls in crystal engineering such as hydrogen bonding and π-π stacking.[85] Experimental and computational work in Goroff group[74-77] and by other researchers[67,69,72], as introduced above, has demonstrated that iodoalkynes are good Lewis acids and halogen bonding donors due to the polarizability of iodine and the higher eletronegativity of sp-hybridized carbon. Using the crystal engineering methods developed by Lauher and Fowler, the Lewis acidity of the monomer diiodobutadiyne can be applied to prepare the polymer PIDA. Based on halogen bonding, we can build co-crystals between the monomer and oxalamide or urea hosts with appropriate Lewis basic end-groups, such as nitrile and pyridine, to approach the desired PIDA via topochemical polymerization within co-crystals. Scheme 1.6 shows a designed

host-guest co-crystal system. The preparation of various host-guest co-crystals to approach successful topochemical polymerization within these co-crystals will be comprehensively described in the following chapters.

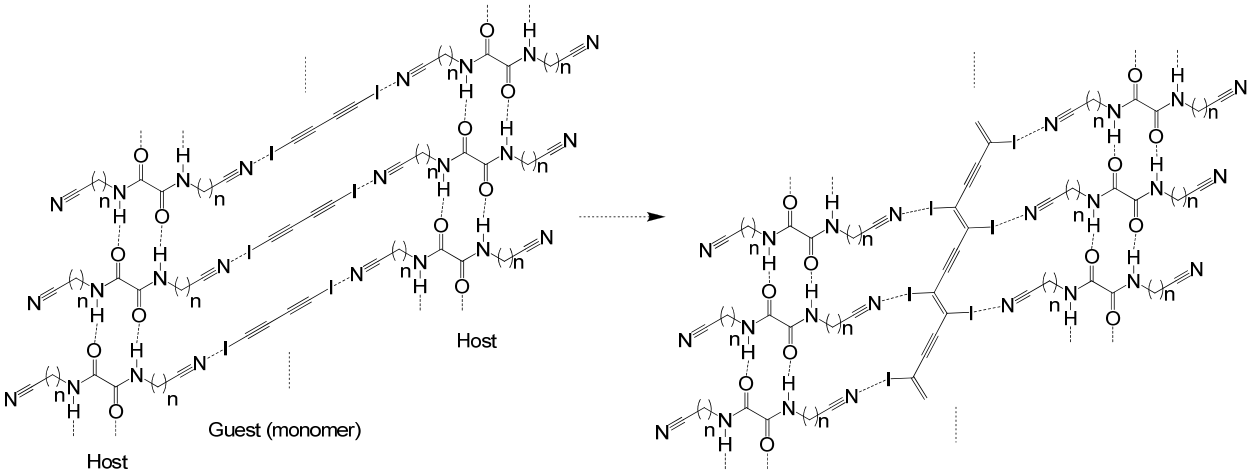

Scheme 1.6. Approaching target PIDA with the co-crystals built by nitrile-oxalamide hosts and guest monomers.

Recently, we reported the first preparation of PIDA in co-crystals between monomer and an oxalamide host with terminal nitrile group.[86] The produced polymer, resulted from a spontaneous topochemical polymerization within co-crystals between bis(nitrile) oxalamide host and monomer, has a copper-colored shiny appearance and clear resolved crystal structure (Figure 1.20). However, the weakness of N-I halogen bonds, and the flexibility of the side chain of the host, make it challenging to obtain large quantities of the PIDA co-crystals. By developing a new methodology for preparing co-crystals by the same host, PIDA crystals with well defined structures can be produced reliably and in large quantities.[87] Based on that, a more comprehensive characterization than was previously possible, as well as the investigation of the material's unique chemical and physical properties, will be presented respectively.

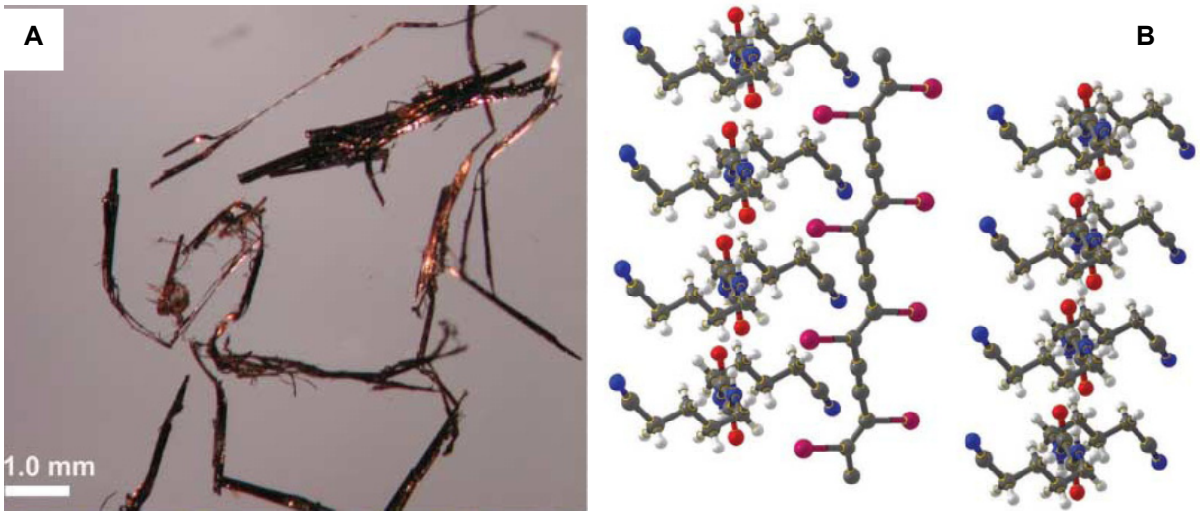

Figure 1.20. PIDA co-crystals, microscopic images (A) and crystal structure determined by X-ray diffraction (B). Reprint with permission from Ref. 86, Copyright 2006, American Association for the Advancement of Science.

Chapter 2. Building Host-Guest Co-crystals to Approach PIDA

To approach the targeted PIDA by the host-guest co-crystal strategy, we planned to use monomer diiodobutadiyne (**1**) as the guest, and pyridyl or nitrile-functionalized ureas or oxalamides (**2-10**) as the hosts to form the co-crystals (Figure 2.1). Based on Lewis acid-base (halogen bonding) interaction, together with the hydrogen bonding network provided by host molecules, monomer **1** is expected to align for the desired polymerization reaction. This chapter describes the co-crystals between **1** and host **2** – **6**. Within these co-crystals, the aligned monomers cannot undergo a spontaneous topochemical polymerization, but external energy or pressure can induce the crystals to yield the desired polymer in some situations. Chapter 3 discusses the co-crystals with host **7** – **10**.

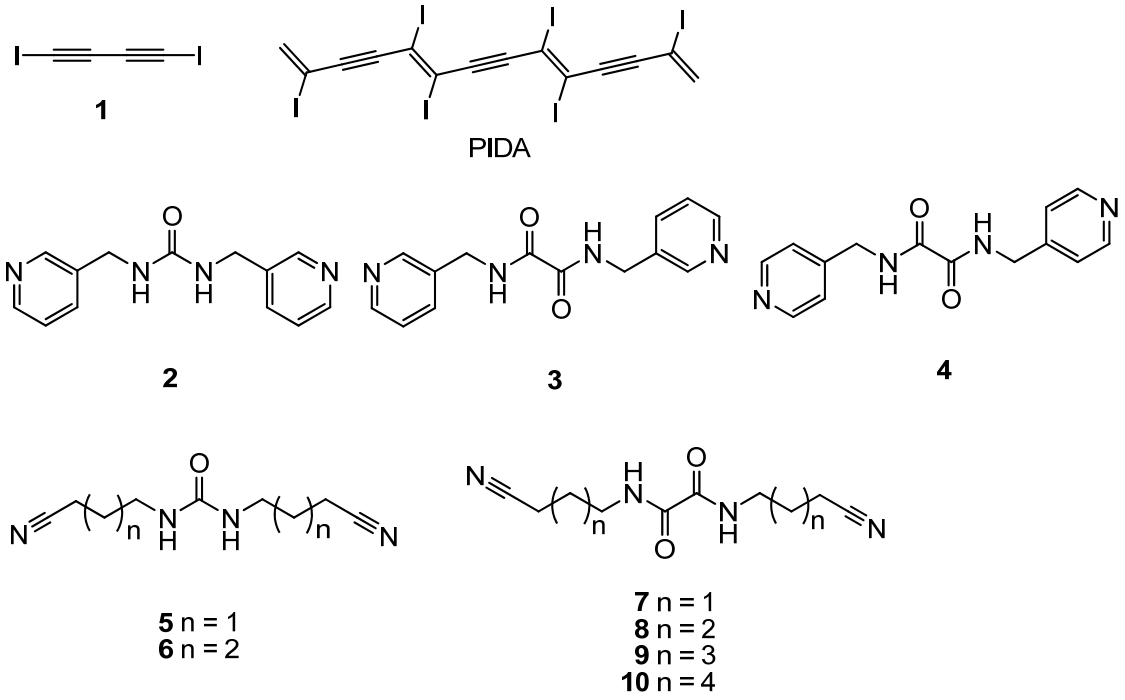

Figure 2.1. Structures of monomer **1**, PIDA, and host molecules **2**-**10**.

2.1. Synthesis of monomer 1 and hosts 2 – 6

Monomer **1** has been known for over a century since Baeyer first reported its synthesis in 1885.[88] Recent improvements in techniques for halogenating alkynes involve preparing them directly from trimethylsilyl-protected precursors,[89] which makes it very convenient to prepare monomer **1** and other iodo-capped carbon rods[74] from trimethylsilylalkynes in one step. Prepared by the method shown in Scheme 2.1, diiodobutadiyne **1** appears as light yellow powder or needle like crystals, and decomposes quickly at room temperature.

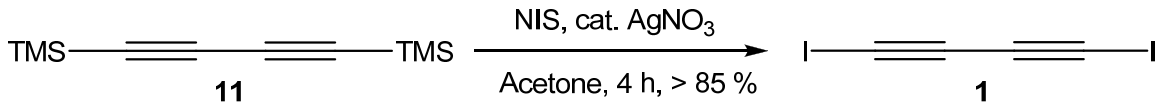

Scheme 2.1. Synthesis of monomer **1**.

The synthesis of hosts is well developed by our group and our collaborators Joseph W. Lauher and Frank W. Fowler.[65] Hosts **2** and **3** were first designed and prepared as ligand hosts for the controlled spacing of silver salts in a crystal.[90] They can be prepared from pyridylamine **12**, which reacts with triphosgene to give **2**, and reacts with diethyl oxylate to produce **3**. In a slightly modified method, diethyl carbonate was used instead of highly toxic triphosgene in the preparation of **2**.[91]

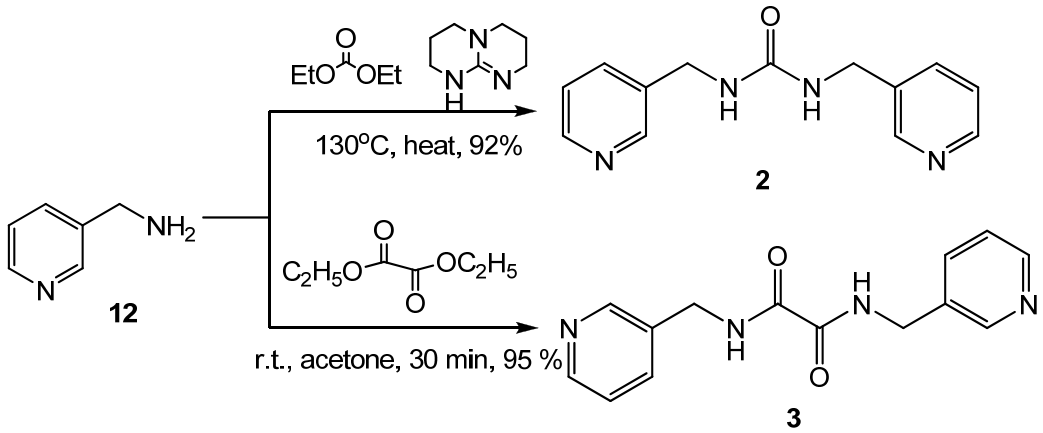

Scheme 2.2. Synthesis of host **2** and **3**.

The bis(alkylnitrile) urea hosts **5** and **6** were prepared from bromoalkylnitriles, via azide and amine intermediates, as shown in Scheme 2.3. An advantage of this method is that it produces a symmetric urea host with desired chain length by simply changing the starting bromoalkylnitrile to have the corresponding chain length. When 3-bromoproponitrile **13** reacted with sodium azide, it gave poor yield of 3-azidoproponitrile **18**. The strong electron-withdrawing *β*-nitrile group makes the *α*-proton very acidic, which favors elimination over the desired substitution. The reactions between sodium azide and the other starting materials with longer alkyl chains (**14** – **17**) gave much higher yields. $CoCl_2$-catalyzed reduction of azides **19** – **22** by sodium borohydride[92] gives the corresponding amine products **23** – **26**. We prepared compound **23** in a yield of 47% and **24** in 63% by this method, less than literature yields for similar reactions,[92] but enough to continue on to the formation of the final hosts. Aminonitriles **23** and **24** reacted with triphosgene in an ice bath overnight under the protection of argon to give the ureas **5** and **6**. Aminonitriles **23**-**26** can also be used to prepare oxalamide hosts **7**-**10** correspondingly, which we will discuss in the next chapter.

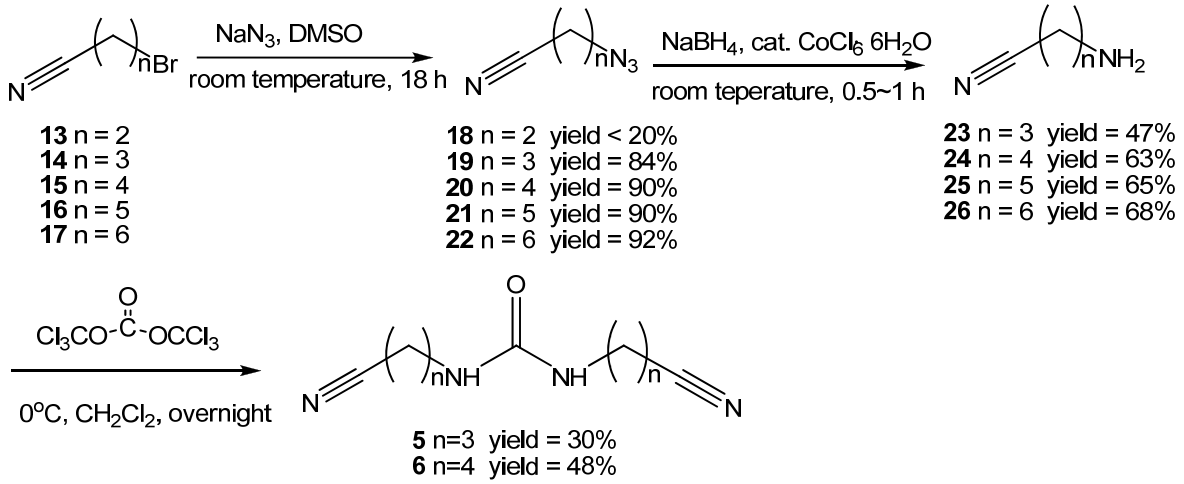

Scheme 2.3. Synthesis of hosts **5** and **6**

Hosts **5** and **6** are white or colorless crystals after workup. Their crystal structures, determined by X-ray diffraction (XRD), illustrated the ordered packing of the molecules through

hydrogen bondings (Figure 2.2). They provide a self-complementary scaffold in the solid state, despite the flexible side chains.

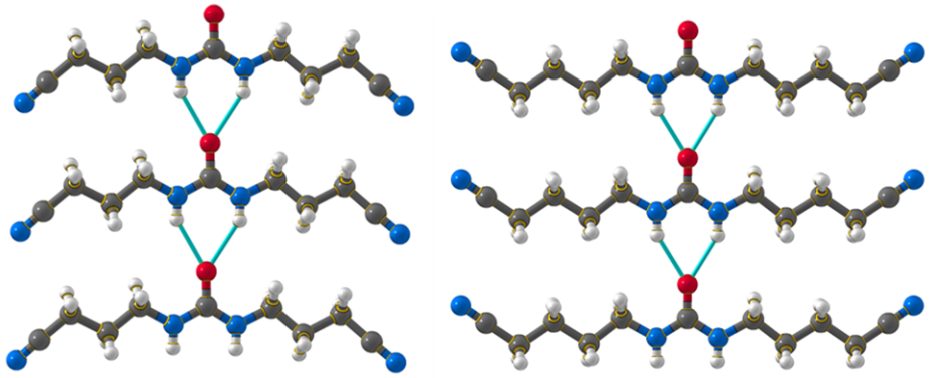

Figure 2.2. Crystal structures and packings of host **5** (left) and **6** (right). Unit cell parameters of **5** (Orthorhombic, space group $Pbc2_1$) are a = 4.6500(19) Å, b = 12.098(5) Å, c = 18.191(8) Å; α = 90°, β = 90°, γ = 90°,V=1023.3(7) $Å^3$; Unit cell parameters of **6** (Orthorhombic, $Pbc2_1$) are a = 13.678(8) Å, b = 39.47(2) Å, c = 4.602(3) Å; α = 90°, β = 90°, γ = 90°,V= 2485(2) $Å^3$

2.2. Building co-crystals between 1 and hosts 2 – 4

Lauher and Fowler discovered that compounds **2** – **4** are excellent co-crystallizing hosts to promote the ordered assembly of hydrogen-bond donors.[66] Curtis and Webb applied them in forming co-crystals with monomer **1**.[93] Each of these hosts contains two pyridine rings that form halogen bonds with **1**, and the co-crystals have a stoichiometry of 1:1 as expected.[93] Figure 2.3 shows the crystal structures for each co-crystal. In co-crystal **2•1**, additional vacancies between neighboring host molecules are also filled with methanol molecules.

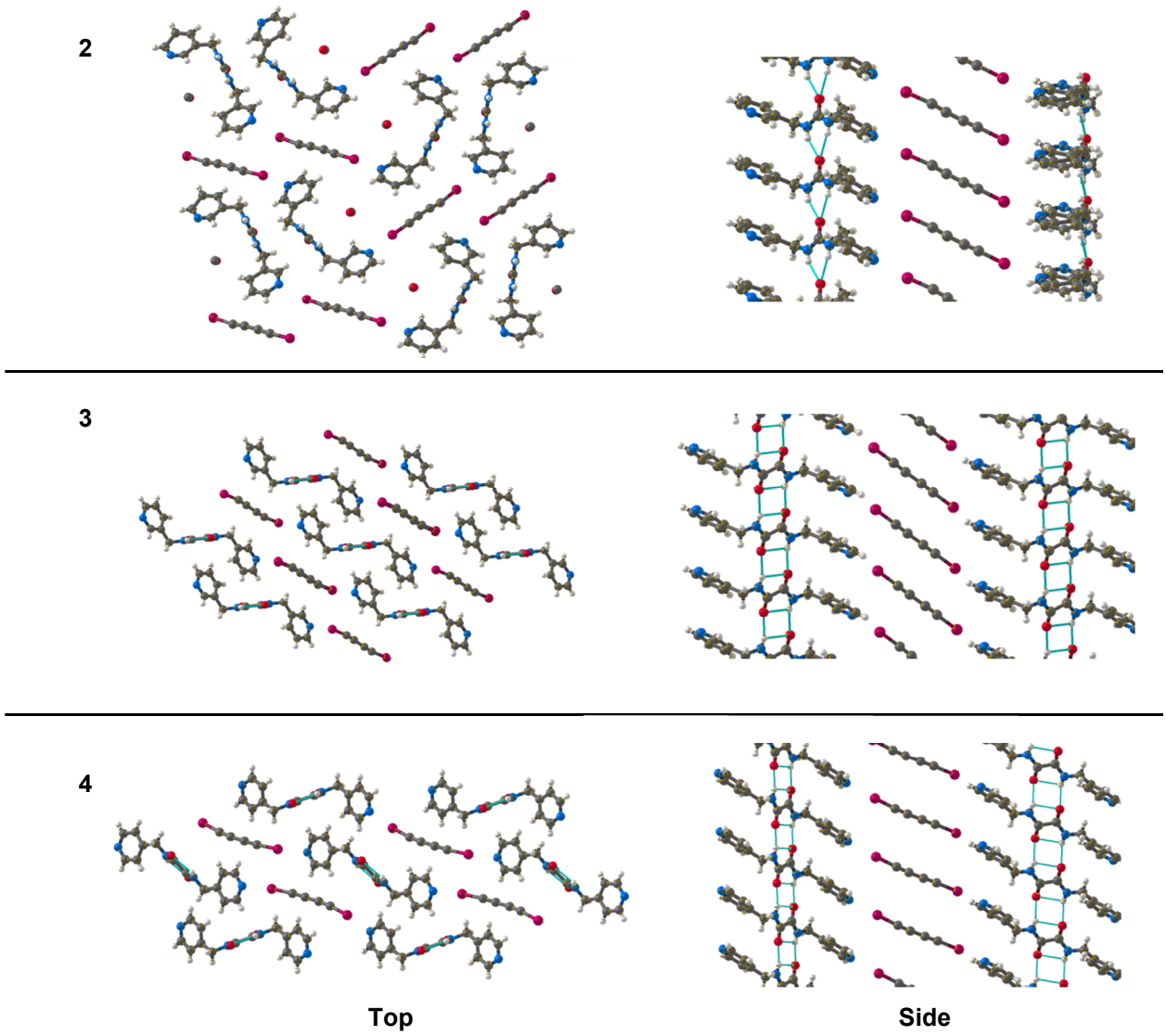

Figure 2.3. Crystal structures of co-crystals **2•1**, **3•1**, and **4•1.**

However, it is difficult for these co-crystals to polymerize under conventional conditions like heat or UV irradiation. Table 2.1 lists the geometry parameters of aligned monomers within these co-crystals, which do not fit Baughman's requirement[31] and disfavor the topochemical polymerization.

Table 2.1. Structure parameters of co-crystals formed by pyridyl hosts and monomer (data is taken from ref. 20). Parameters *r*, *d*, and θ of aligned diynes are illustrated in Scheme 1.2.

Co-crystals	*r* (Å)	*d* (Å)	θ (°)
2·1	4.53	4.36	63
3·1	5.11	3.90	65
4·1	5.02	4.89	61

Lauher and Fowler discovered that a two-dimensional β-network with alternating parallel urea and oxalamide subnetworks has an average repeat distance of 4.87 Å, as shown in Figure 2.4.[66] Based on that we proposed to build such a three-component supramolecular network, including bispyridal urea **2**, C_4I_2, and bispyridyl oxalamide **3**, hoping it would land in a sandwich type co-crystal **2·1·3** with proper alignment for the polymerization of **1** (Figure 2.5). This work is done together with REU student Daniel Miranda.

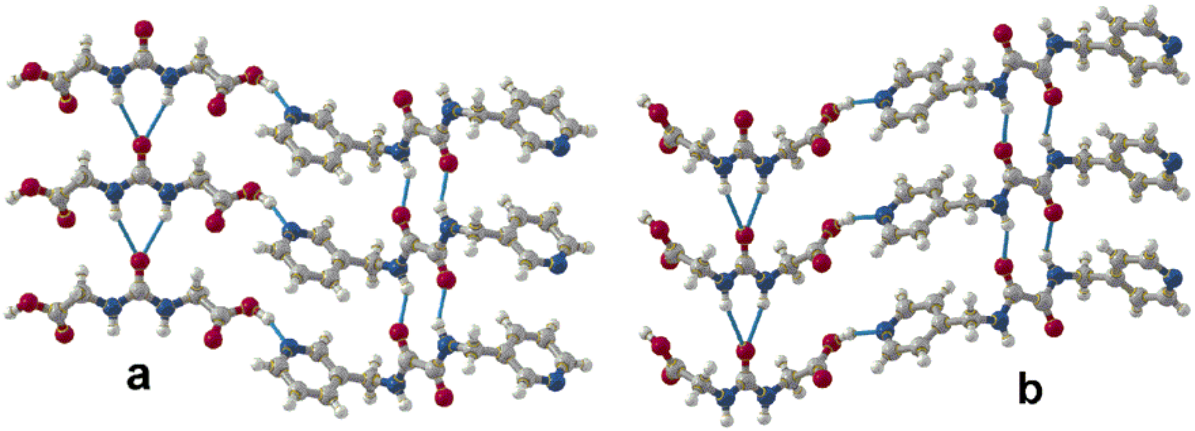

Figure 2.4. Crystal structures of co-crystals **glycinal-urea·3** (A) and **glycinal-urea·4** (B). The repeat distance for **a** is 4.87 Å and for **b** is 4.88 Å. Reprinted with permission from Ref 8, Copyright 2001, American Chemical Society.

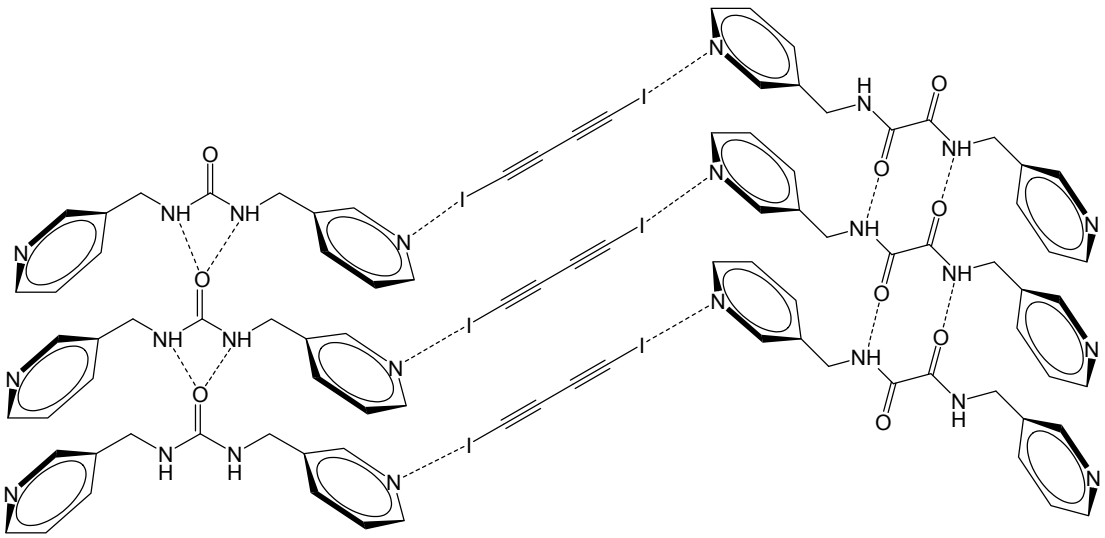

Figure 2.5. Hypothetical 3-component supramolecular network among **1, 2, 3**.

To create this sandwich type co-crystal, mixtures of hosts **2** and **3** and guest **1** were dissolved in methanol with stoichiometries of 1:1:1, 1:2:1, 1:4:1, respectively. Slow evaporation of these solutions in low temperature resulted only in white co-crystal **2•1** and yellow co-crystal **3•1**. No 3-component **2•1•3** co-crystals were created by this method.

Interestingly, the **2•1** co-crystals obtained by this route have a different packing than what was previously reported.[93] As shown in Figure 2.5, monomer **1** is aligned by halogen-bonding with **2** in a stoichiometry of 2:1. In this way, the co-crystal provides three types of packed guests. However, the packing parameters of all 3 types of guest are not appropriate for their polymerization.

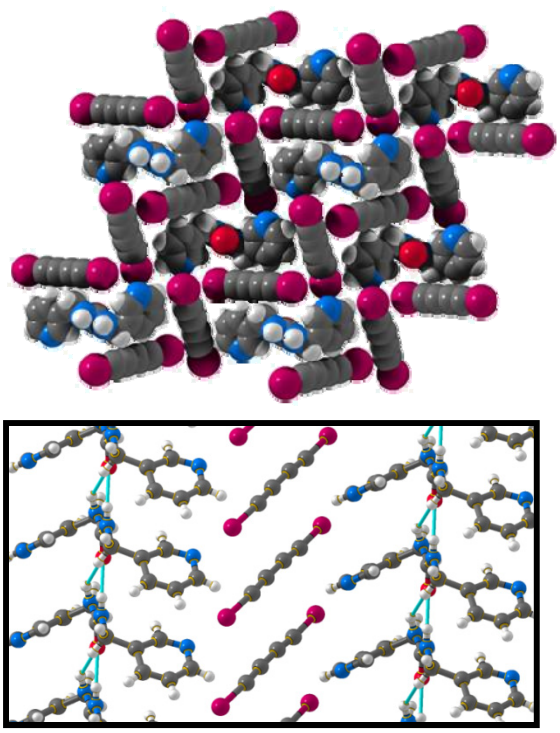

Packing	r (Å)	d (Å)	θ (°)
A	4.53	4.36	63
B	5.11	3.90	65
C	5.02	4.89	61

Figure 2.6. Crystal structure of co-crystal **2•1**. Unit cell parameters: Space group P-1; Unit cell dimensions a = 4.469(2) Å, b = 16.399(7) Å, c = 18.116(8) Å; α = 74.407(8)°, β = 84.618(7)°, γ = 82.207(7)°, Volume = 1264.8(10) Å^3. The inserted table lists packing parameters of different aligned guests.

2.3. Inducing topochemical polymerization of 1 within co-crystal 3•1

2.3.1. Pressure induced polymerization

Co-crystals **3•1** and **4•1** have repeat distances more appropriate for ordered topochemical polymerization (5.11 Å for **3•1** and 5.02 Å for **4•1**). In co-crystal **3•1**, the tilt angle θ (51°) is also near the ideal value, so that the intermolecular C1-C4 distance d is relatively small (3.90 Å). In co-crystal **4•1**, the θ is larger (65°) that C1 of one monomer is closer to C2 of the neighboring diyne than to C4 (4.65 vs 4.88 Å), but previous experience has demonstrated that r is more important than d in determining the success of diyne polymerization.[33] Despite the promising alignment of monomer **1** in these co-crystals, previous attempts to induce ordered polymerization in these materials by heat, UV irradiation, or γ rays have been unsuccessful.

Recent research work in our group by Christopher Wilhelm et, al. discovered that co-crystals **3•1** and **4•1** can be polymerized under mechanic high pressure.[94] Exposing these co-crystals to high external pressure (0.3-10 GPa) in a diamond-anvil cell (Left, Figure 2.7) induces an irreversible 1,4- polymerization of **1**. Although the samples are no longer crystalline (Right, Figure 2.7) after being pressed, the produced PIDA within these co-crystals, as characterized by Raman (Figure 2.8) and ^{13}C MAS NMR (Figure 2.9), indicates that high pressure is an efficient method in inducing the topochemical polymerization.

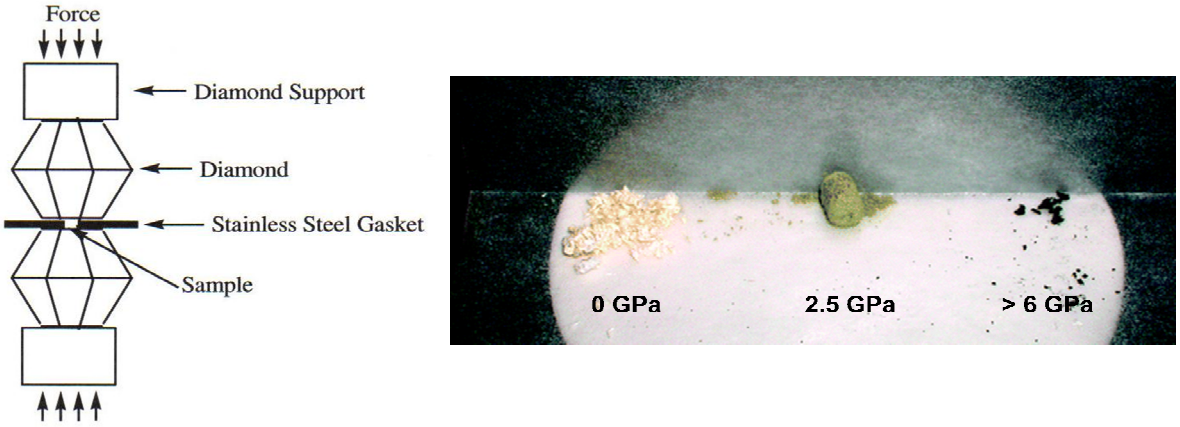

Figure 2.7. Left: A schema of the diamond-anvil cell; Right: Powdered samples of the **3•1**, before and after pressing to different pressures. Reproduced with permission of Ref. 94, Copyright 2008, American Chemical Society.

Raman spectra of the initial co-crystals (Figure 2.8 A,C) contain identifiable peaks corresponding to diyne **1** and the oxalamide host **3** or **4**. The Raman spectrum of partially pressed **3•1** co-crystals shows three new peaks visible at 962, 1394, and 2055 cm^{-1}, while that of partially pressed **4•1** co-crystals contains the same three high-intensity peaks (962, 1394, and 2055 cm^{-1}), as shown in Figure 2.8 D.

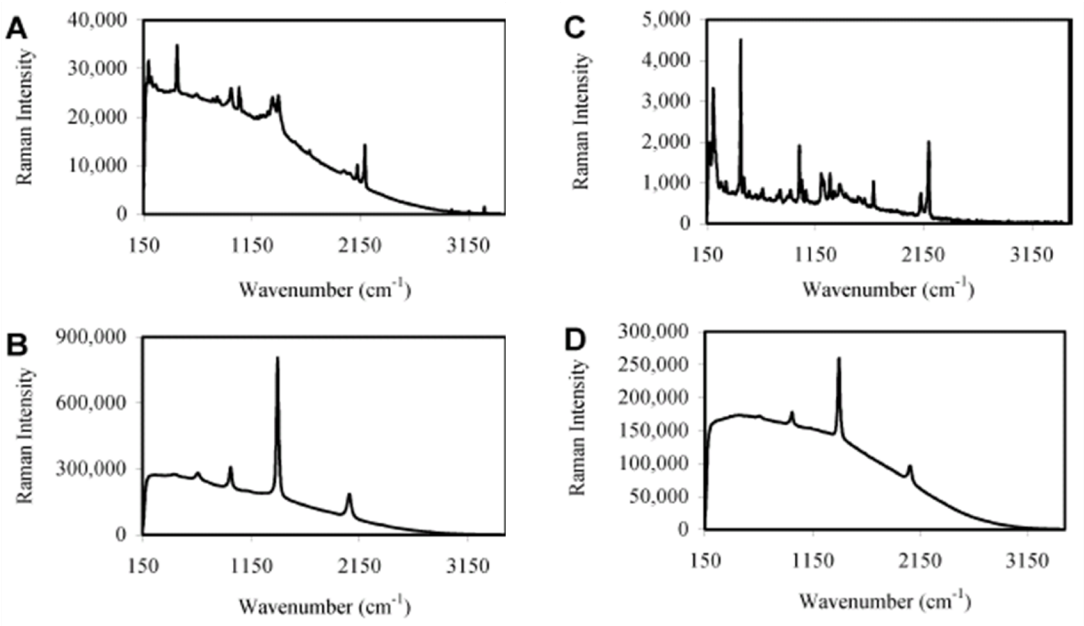

Figure 2.8. Raman spectra of the co-crystals: (A) **3•1** before pressing; (B) **3•1** after pressingto 2.8 GPa; (C) **4•1** before pressing; (d) **4•1** after pressing to 3 GPa. Reproduced with permission of Ref. 94, Copyright 2008, American Chemical Society.

Solid-state ^{13}C MAS NMR studies further prove the formation of PIDA with the pressed co-crystals. The two new resonances at 110 ppm and 89 ppm (Figure 2.9 B, red arrows) are consistent with the carbons in PIDA.[87] The co-crystal with host **3** contains >90% polymer after pressing. In contrast, the co-crystal with host **4** reaches only ~55% of polymerization.

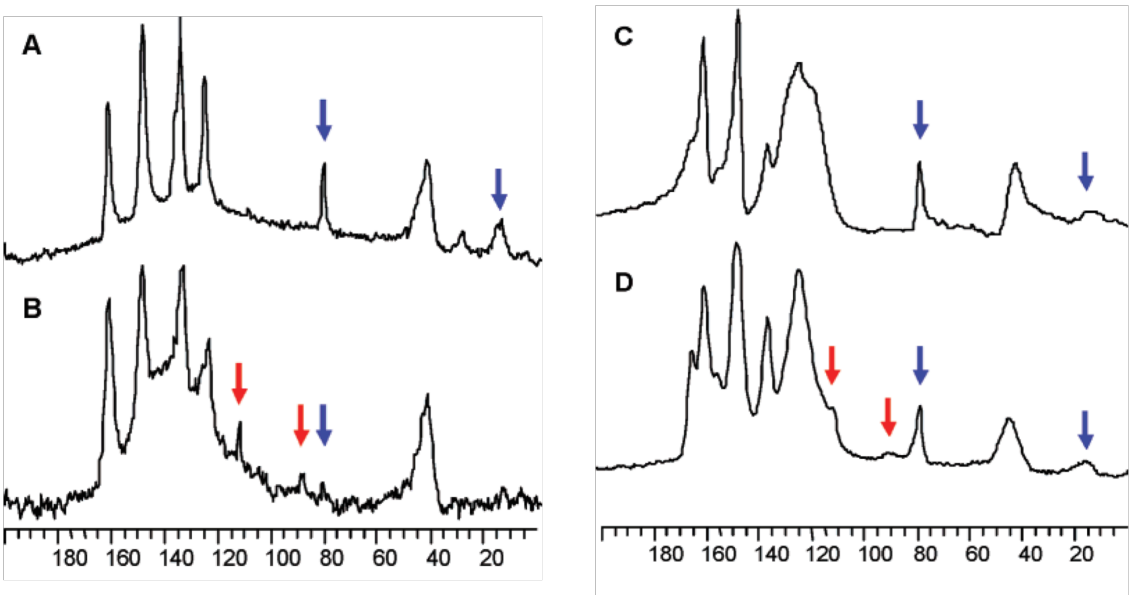

Figure 2.9. 13C MAS NMR spectra of the co-crystals: (A) **3•1** before pressing; (B) **3•1** after pressing to >6 GPa; (C) **4•1** before pressing; (D) **4•1** after pressing to >6 GPa. Blue arrows indicate peaks corresponding to **1**; red arrows indicate peaks corresponding to PIDA. Reproduced with permission of Ref. 94, Copyright 2008, American Chemical Society.

2.3.2. Thermo effect on polymerization

Although heat can not induce the comprehensive topochemical polymerization within co-crystal **3•1**, it does assist the partial 1,4- reaction of ordered monomer **1**. Co-crystal **3•1** prepared at low temperature (-20 °C) is light yellow (Figure 2.10 A). Upon warming to room temperature, the co-crystals undergo a color change in a short time, as show in Figure 2.10 B. The yellow-to-blue/green color change indicates internal transitions with a corresponding increase in conjugation, i.e., the polymerization of monomers. After a longer time, the blue color of the co-crystals becomes deeper, until they finally turn dark several days later. These changes were followed visually (Figure 2.10) as well as crystallography.

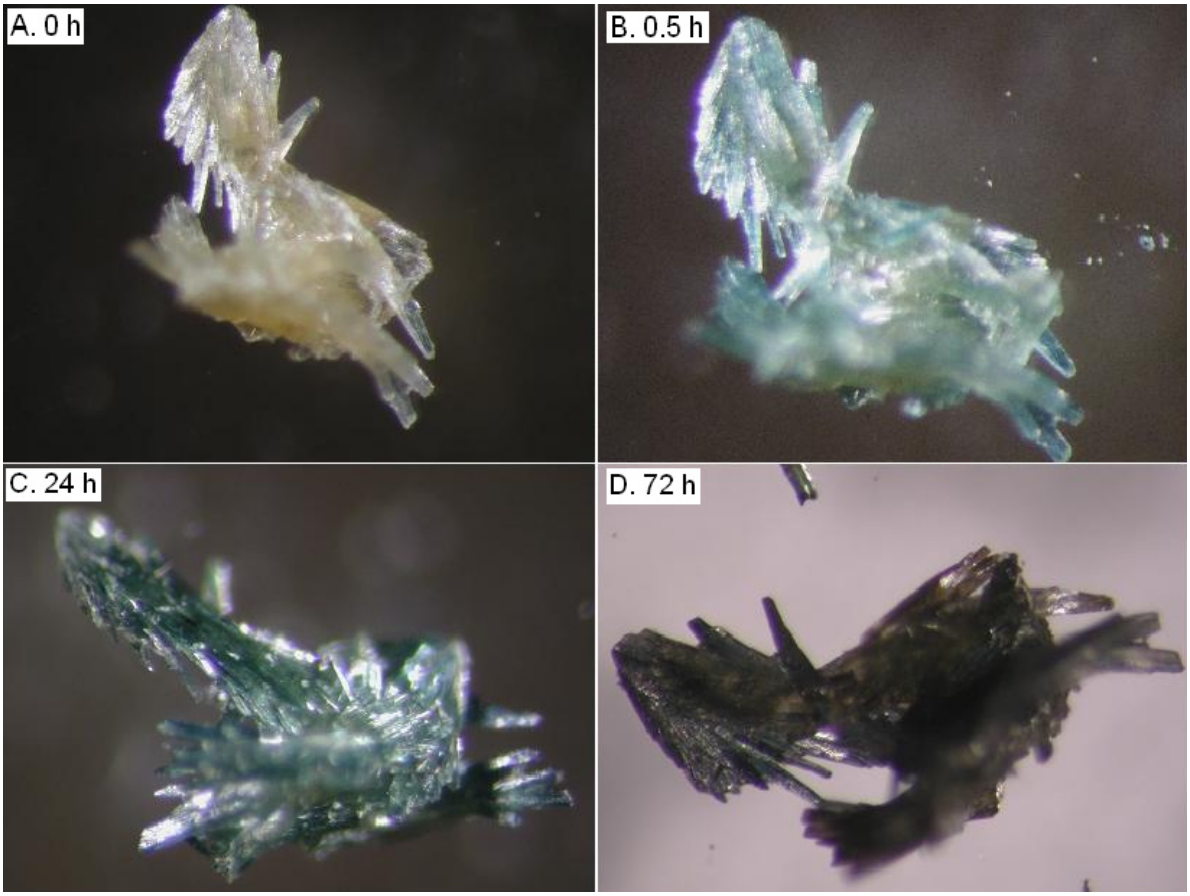

Figure 2.10. Microscopic images of co-crystals **3•1**, taken after increasing time at room temperature.

A single crystal from this batch was monitored by X-ray diffraction during the week. Table 2.2 lists the unit cell change of the mounted single crystal. Each unit cell parameter decreases with increasing time, indicating an overall shrinking of the crystals. The volume decrease of the crystal represents the change toward polymerization, which has a smaller unit cell compared to monomer crystals.

Table 2.2. Unit cell change of the single crystal **3•1** upon heating. A – D are the crystal structures taken after increasing time at room temperature, as shown in Figure 2.10**;** E: starting from sample D, heating at 40 ^{o}C for 1 week; F: starting from sample E, heating at 75 % for another 2 days.

Crystal	Temp.	Time	a (Å)	b (Å)	c (Å)	α (^{o})	β (^{o})	γ (^{o})	V (Å^{3})	R1 %
Reference[93]	r. t.	N/A	5.109	8.604	11.779	96.15	99.49	103.28	491.34	5.53
A, B	r. t.	0 h	5.107	8.641	11.747	96.25	99.61	103.84	490.29	7.33
C	r. t.	24 h	5.079	8.591	11.692	96.22	99.55	103.72	482.92	7.47
D	r. t.	72 h	5.040	8.523	11.592	96.16	99.54	103.58	471.74	5.94
E	40 ^{o}C	1 week	4.999	8.442	11.600	96.28	98.67	102.97	466.44	8.09
F	75 ^{o}C	2 d	4.947	8.264	11.770	96.33	97.23	100.95	464.21	11.71

The structure parameters of aligned monomers also changed consequently (Table 2.3). The most obvious change is that the repeat distance of the guest molecules decreases from 5.11 Å to 5.04 Å, closer to the ideal repeat distance of 4.9 Å for polymerization. But other parameters such as C1-C4 distance and guest declination angle do not change too much. The bond length of C-C triple bond increases but that of C-C single bond decreases, showing the positive change from monomer to polymer.

Table 2.3 The change of structure parameters of aligned guests in co-crystal **3•1**. *r* is the repeat distance of **1**; *d* is the C1-C4 distance; θ is the declination angle of **1**; A – F are the same as those in Table 2.2.

Crystal	*r* (Å)	*d* (Å)	θ (°)	C≡C (Å)	C−C (Å)
Reference[93]	5.11	3.99	49.8	1.148	1.371
A, B	5.11	3.86	48.8	1.187	1.423
C	5.08	3.87	49.1	1.122	1.322
D	5.04	3.85	49.4	1.209	1.412
E	5.00	3.88	49.3	1.168	1.786
F	4.95	4.30[a]	48.1	1.289	1.494

a: The distance was measured based on the disordered structure.

Encouraged by these results, we decided to continue studying the microscopic changes in co-crystal **3•1**. Remaining at room temperature, no further changes were observed in the crystal structure. However, heating the crystals quickly had already been shown to lead to disordered mataerials.[93] We decided to expose the co-crystals to mild heating over a longer time. This so called "slow-heating mode" helps to maintain crystallinity of the crystal as long as possible.[33] After heating the sample at 40 °C for one week, the crystal structure showed disorder characteristic of partial polymerization (Figure 2.11, E in Table 2.2). Heating the sample at 75 °C for another two days caused a more significant change in its crystal structure (Figure 2.11, F in Table 2.3). However, further heating this sample destroyed the crystallinity of the material. Continued characterization of slow-heated co-crystals **3•1** by powder diffraction, Raman, and solid-state ^{13}C NMR have been performed by Christopher Wilhelm, and are reported

elsewhere.[95]

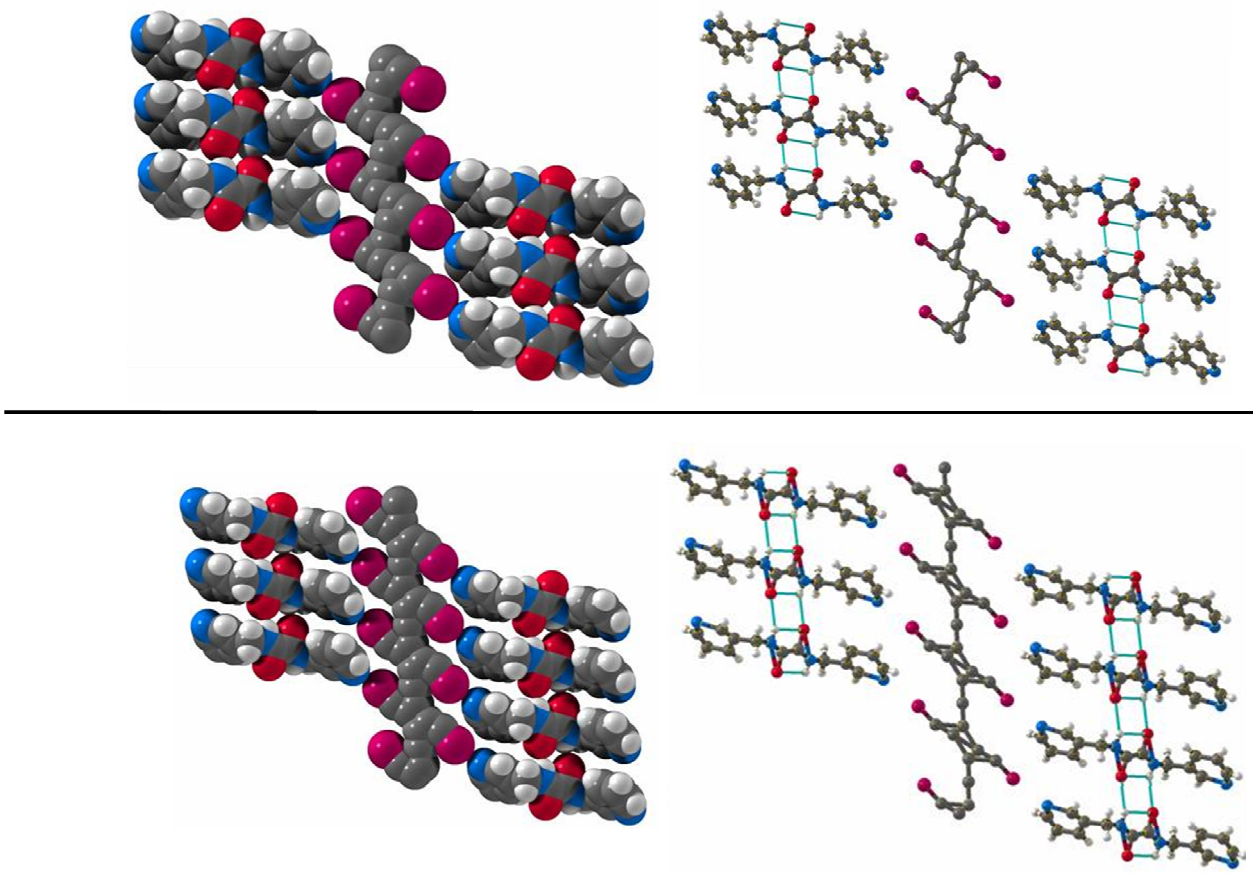

Figure 2.11 Structure of co-crystal **3•1** during slow heating. E: the single crystal kept at 40 ^{o}C for 1 week; F: the crystal then kept at 75 ^{o}C for another 2 days

2.4. Building co-crystals between 1 and hosts 5 – 6

Like pyridine, the nitrile is also a Lewis basic functional group, although a weaker electron-pair donor. The synthesis of bis(alkylnitrile) urea host **5** and **6** is shown in **Scheme 2.2**. To form co-crystals of guest monomer **1** with host **5** or **6**, saturated solutions of compound **1** and each host have been prepared with a stoichiometry of 1:1, using methanol or chloroform as solvent. These solutions were kept at low temperature (-20 ^{o}C) to grow co-crystals. Only the co-crystals grown by slow evaporation from chloroform solutions provide XRD quality crystals. However, these crystals decompose when they are exposed to room temperature and light. By XRD we can

obtain the crystal structure of co-crystal **5•1** before it decomposes (Figure 2.12), but co-crystal **6•1** decomposes very quickly, and no information could be obtained from XRD.

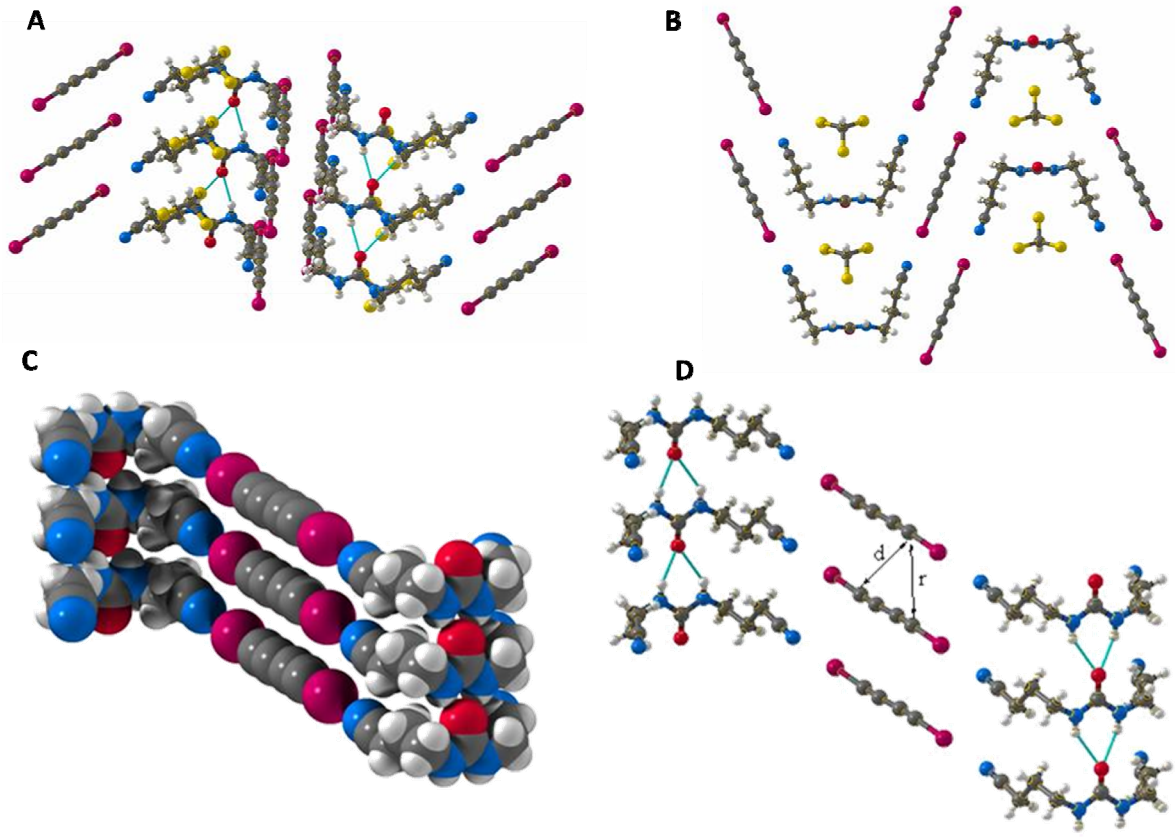

Figure 2.12. Crystal structure of co-crystal **5•1**. (A): Side view; (B): Top view; (C) Alignment of **1** by host **5**; (D) packing parameters shown in balls and sticks view, with *r* of 4.60 Å, *d* of 4.64 Å, and θ of 67.2°. Unit cell parameters: Space group $P2_1/m$; Unit cell dimensions a = 4.595(3) Å, b = 26.388(13) Å, c = 8.885(5) Å; α = 90 °, β = 94.633(11) °, γ = 90 °, Volume = 1073.7(10) Å^3

The crystal structure of co-crystal **5•1** illustrates the presence of solvent chloroform within the crystals. When the temperature increases to room temperature, chloroform molecules escape from the crystal lattice, leading to the decomposition of the crystal. To further explore these changes within the co-crystals **5•1** and **6•1**, they were submitted to Raman spectroscopy.

Raman spectra of these two co-crystals show interesting changes during decomposition, although the packing parameters for guests are not ideal for polymerization. Figure 2.11 includes Raman spectra of urea host **5**, and co-crystal **5•1** before and after decomposition. The un-

decomposed co-crystal spectrum contains the peaks corresponding to the urea host and C_4I_2 guest. The spectrum also contains a strong fluorescence background, which proves the formation of co-crystal and interaction between host and guest. When the co-crystal decomposes, the Raman spectrum becomes completely different, with all functional-group peaks disappearing and a strong florescence absorption emerging. This spectrum will be discussed with those of other co-crystals in Chapter 4.

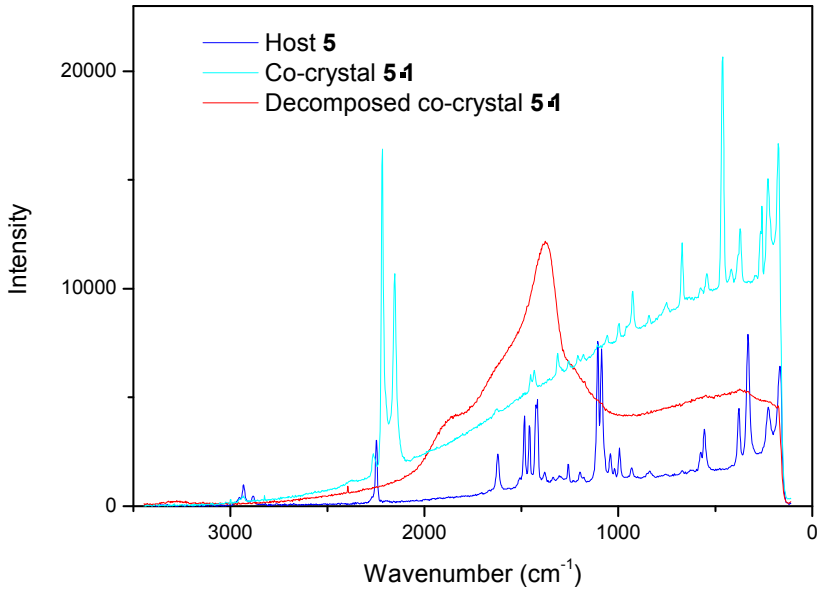

Figure 2.13. Raman spectra of host **5**, co-crystal **5•1** and decomposed co-crystal **5•1.**

Comparing the Raman spectra of urea host **6** and the co-crystal **6·1**, the Raman intensities for the co-crystals, both initially and after decomposition, are much higher than the urea host alone. This observation suggests that the major functional group peaks, other than the nitrile of host, are covered by fluorescence signal in the co-crystal spectra. Only C≡N, C≡C, and C-I stretches are visible in the Raman spectrum of the initial co-crystal **6•1.** After the co-crystal decomposes, an intense peak corresponding to a C=C double bond stretch (1552 cm^{-1}) appears in the Raman spectrum. This peak is consistent with the Raman spectrum of PIDA shown in Section **2.3.1**.

After the decomposed co-crystal has been kept at room temperature for 3 or 4 weeks, the Raman spectrum shows a broad hump with very high intensity.

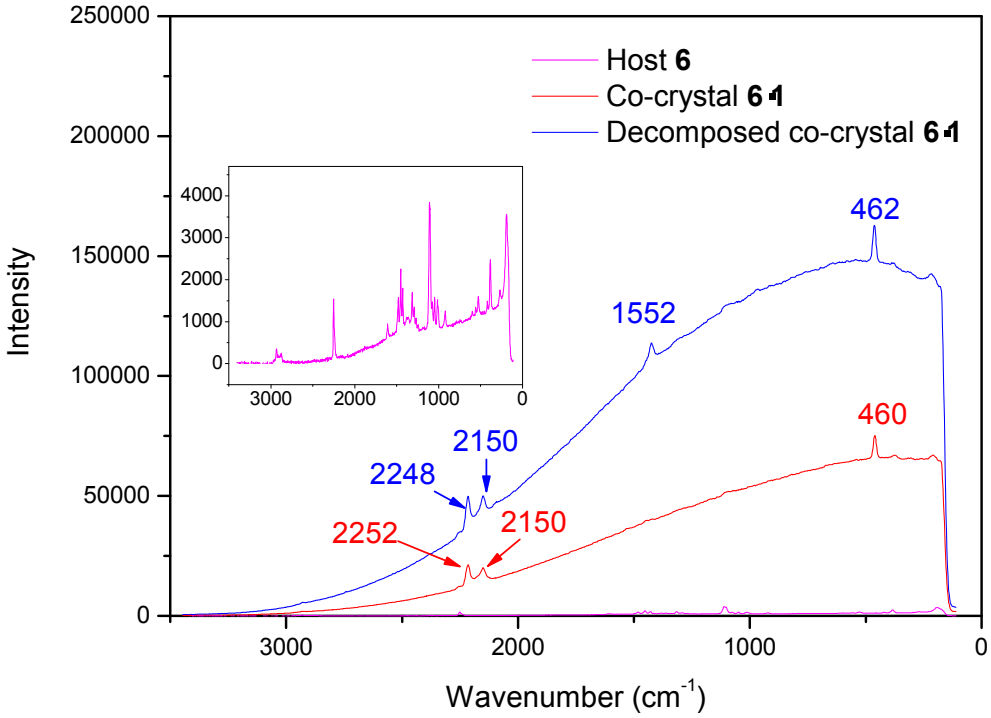

Figure 2.14. Raman spectra of host **6**, co-crystal **6•1** and decomposed co-crystal **6•1**.

The attempt to induce the topochemical polymerization within co-crystals of **1** and host **2** – **6** has successfully demonstrated that the host-guest co-crystal strategy is an efficient method to approach PIDA. Further studies indicate that co-crystals made of host **8** and **10** produce fully polymerized PIDA spontaneously at room temperature. Chapter 3 discusses co-crystals of **1** and host **7** – **10**, and the preparation of PIDA by single-crystal-to-single-crystal topochemical polymerization.

2.5. Experimental details

2.5.1. Synthesis of organic compounds

Diiodobutadiyne (1):[74] 1,4-Bis(trimethylsilyl)butadiyne (194.6 mg, 1 mmol) was dissolved in 30 mL acetone. To this solution were then added 130.5 mg (0.76 mmol) $AgNO_3$ and 550.6 mg (2.37 mmol) N-iodosuccinimide (NIS). Aluminum foil was used to wrap the reaction vessel. The reaction mixture was stirred at room temperature for 4 h. During the reaction, TLC test should be taken to confirm the reaction being completed. Then the mixture was extracted with hexanes/water. The combined organic layers were dried with $MgSO_4$ and concentrated in vacuo to afford a light yellow product. The product weighed 215.3 mg (yield 80%): ^{13}C NMR (400 MHz, $CDCl_3$) δ 79.97, -2,70.

***N,N'*-Bis(3-pyridylmethyl)urea (2)**:[90] A mixture of 3-(aminomethyl)pyridine **12** 1.30 mL (10 mmol), diethyl carbonate 0.60 ml (5 mmol) and 1,5,7-triazabicyclo[4.4.0]dec-5-ene (TBD) 50 mg (0.36 mmol) was heated with an oil bath at 130 ^oC for 12 h, under magnetic stirring. The flask was equipped with an air condenser and left open throughout the course of the reaction. After cooling to 80 °C, hot water (20 mL) was added and vigorous stirring was continued for an additional 30 min. The solid product was then filtered off and purified by recrystallisation from methanol. The product of white crystals weighed 426.6 mg (yield 37%): ^1H NMR (300 MHz, DMSO) δ 8.47 (s, 2H), 8.41 (d, J = 5.4 Hz, 2H), 7.78 (d, J = 7.5 Hz, 2H), 7.39 (m 2H), 4.59 (N-H), 4.36 (d, J = 5.9 Hz, 4H). m. p. 129.0~131.0 ^oC (literature 129 – 130 ^oC).

***N,N'*-Bis-pyridin-3-ylmethyl-oxalamide (3)**:[90] 3-(aminomethyl)pyridine **12** (0.033 mol, 3.44 mL) was dissolved in 30 ml acetone and stirred. Diethyl oxalate (0.015 mol, 2.04 mL) was then added into pyridine solution at room temperature. After 20 m of reaction, the solid that precipitated was collected and purified by recrystallization from CH_3OH to give colorless crystals 3.466 g (yield: 85 %): mp 189.5-192.5 °C (literature 188 – 189 ^oC), ^1H NMR (300 MHz,

DMSO-d_6): δ 4.33 (d, *J* = 6.3 Hz, 2H), 7.33 (dd, *J* = 4.5 Hz, 3.0 Hz, 2H), 7.65 (dt, *J* = 7.8 Hz, 2H), 8.46 (dd, *J* = 1.8 Hz, 2H), 8.48 (d, *J* = 2.1 Hz, 2H), 9.42 (t, *J* = 6.3 Hz, 2H).[90]

3-azidopropanenitrile (13):[96] Sodium azide (600 mg, 9.25 mmol) was added to a solution of 3-bromoproponitrile (0.510 mL, 6.17 mmol) in DMSO (15 mL). After 20 h of stirring at room temperature, 20 ml of water was added, and the solution was extracted by diethyl ether (50 ml x 3). The organic phase was washed by H_2O (50 mL x 2) and then dried ($MgSO_4$) and concentrated under reduced pressure to give pure 3-azidopropioonitrile as colorless oil 143.1 mg (yield 12.1 %). $C_3H_4N_4$ ^{1}H NMR (300 MHz, $CDCl_3$) δ 3.58 (t, *J* = 6.0 Hz, 2H), 2.59 (t, *J* = 6.3 Hz, 2H), IR (KBr): 2252, 2119 cm^{-1}.

4-azidobutyronitrile (19):[86] Sodium azide (845.1 mg, 13 mmol) was added to a solution of 4-bromobutyronitrile **14** (0.640 ml, 6.5 mmol) in DMSO (15 mL). After 20 h of stirring at room temperature, 30 ml of water was added, and the solution was extracted by diethyl ether (50 mL x 3). The organic phase was washed by H_2O (50 mL x 2) and then dried ($MgSO_4$) and concentrated under reduced pressure to give pure 4-azidobutyronitrile 600.7 mg (yield 84 %) as colorless oil. ^{1}H NMR (300 MHz, $CDCl_3$) δ 3.47 (t, *J* = 6.3 Hz, 2H), 2.45 (t, *J* = 6.9 Hz, 2H), 1.89 (q, *J* = 6.3 Hz, 2H), consistence with literature data.

4-aminobutyronitrile (23):[86] To a mixture of **19** (220.0 mg, 2.0 mmol) and $CoCl_2 \cdot 6H_2O$ (0.048 g, 0.2 mmol), at room temperature was added dropwise under stirring a solution of $NaBH_4$ (0.152g, 4.0 mmol) in H_2O (4 mL). The formation of a black precipitate indicated the formation of a cobalt boride species. The mixture was stirred at room temperature for 15 min and then adjusted to PH 14 by adding 2M NaOH solution. The mixture was extracted by ethyl acetate (20 mL x 5). The organic phase was dried ($MgSO_4$) and concentrated under reduced pressure to

give 78.9 mg **23** as yellow oil (yield 47%). ^{1}H NMR δ 2.84 (t, *J* = 6.9 Hz, 2H), 2.44 (t, *J* = 7.2 Hz, 2H), 1.77 (q, *J* = 6.9 Hz, 2H), 1.15 (bs 2H).

N, N-(bispropylnitrile) urea (5): A mixture of 4-aminobutyronitrile **23** 174.4 mg (2.08 mmol) and triethyl amine 0.251 ml (1.80 mmol) was dissolved in 5 ml anhydrous CH_2Cl_2 under argon protection at 0 ^{o}C. The A solution of triphosgene 59.3 mg, 0.2 mmol) in anhydrous Ch_2Cl_2 (1 ml) was then added dropwise under stirring. After 12 h reaction, a light yellow solution was obtained and TLC plate (CH_2Cl_2:Methanol = 10:1) showed 2 spots, the one of which R_f is 0.5 and the other R_f is 0.3. The solution was purified by column chromatography (CH_2Cl_2:Methanol = 10:1) to give pure **5** 50.5 mg (yield 43.4%) as colorless crystals. (R_f = 0.5). m.p. 87~87.5 ^{o}C. ^{1}H NMR (300 MHz, DMSO-d_6) δ 5.98 (t, *J* = 5.4 Hz, 2N-H), 3.03 (q, *J* = 6.0 Hz, 4H), 2.44 (t, *J* = 7.2 Hz, 4H), 1.64 (m, 4H). ^{13}C NMR (400 MHz, DMSO-d_6) δ158.00, 120.46, 38.17, 25.91, 13.81. IR (KBr disc) (cm^{-1}): 3325.23, 2245.69, 1623.83, 1580.88. ESI/MS m/z M+1: 194.90.

5-azidopentanenitrile (20):[86] Sodium azide (600 mg, 9.25 mmol) was added to a solution of 5-bromovaleronitrile **15** (0.72 ml, 6.5 mmol) in DMSO (15 mL). After 20 h of stirring at room temperature, 30 mL of water was added, and the solution was extracted by diethyl ether (50 mL x 3). The organic phase was washed by H_2O (50 mL x 2) and then dried ($MgSO_4$) and concentrated under reduced pressure to give pure **20** 688.0 mg (yield 89.9 %) as colorless oil. ^{1}H NMR (300 MHz, $CDCl_3$) δ 3.35 (t, *J* = 6.0 Hz, 2H), 2.39 (m 2H), 1.76 (m 2H), consistent with literature data.

5-aminopentanenitrile (24):[86] To a mixture of **20** (435.5 mg, 3.51 mmol) and $CoCl_2{\cdot}6H_2O$ (0.095 g, 0.4 mmol), at room temperature was added dropwise under stirring a solution of $NaBH_4$ (0.332g, 8.78 mmol) in H_2O (9 mL). The formation of a black precipitate indicated the formation of a cobalt boride species. The mixture was stirred at room temperature for 60 min and

then adjusted to PH 14 by adding 2M NaOH solution. The mixture was extracted by ethyl acetate (20 mL x 5). The organic phase was dried ($MgSO_4$) and concentrated under reduced pressure to give 216.9 mg amine (yield 63.0%). ^{1}H NMR (300 MHz, $CDCl_3$): δ 2.70 (bt, 2H), 2.33 (t, J = 6.9 Hz 2H), 1.64 (m, 4H).

***N, N'*-(bisbutylnitrile) urea (6):** A mixture of 5-aminopetanenitrile **24** 94.7 mg (0.97 mmol) and triethyl amine 0.201 mL (1.46 mmol) was dissolved in 5 mL anhydrous CH_2Cl_2 under argon protection at 0 ^{o}C. A solution of triphosgene 47.8 mg, 0.16 mmol) in anhydrous CH_2Cl_2 (1 ml) was then added dropwise under stirring. After 12 h reaction, a light yellow solution was obtained and TLC plate (CH_2Cl_2:Methanol = 8:1) showed 2 spots, the one of which R_f is 0.7 and the other R_f is 0.5. The solution was purified by column chromatography (CH_2Cl_2:Methanol = 8:1) to give pure urea product 51.4 mg (yield 47.7%). (R_f = 0.5). m.p. 85.5 - 87.5 ^{o}C. ^{1}H NMR (400 MHz, $CDCl_3$) δ 4.52 (bt, 2NH), 3.22 (q, J = 4.5 Hz, 4H), 2.40 (t, J = 5.1 Hz, 4H), 1.68 (m, 8H). ^{13}C NMR (400 MHz, DMSO-d_6) δ158.37, 119.85, 39.49, 29.69, 22.89, 17.12. IR (KBr disc, cm^{-1}): 3325.23, 3332.27, 2949.62, 2879.24, 2248.82, 1609.21, 1576.06. ESI/MS m/z M+1: 222.96.

2.5.2. Growing co-crystals

Co-crystals made between host **2**~**6** and guest **1** were prepared at low temperature (-20 °C). The saturated solutions of individual host in methanol or chloroform were prepared by adding the solvent into 0.02 mmol of each host until all of the solid right dissolved. Monomer 1 (6 mg, 0.02 mmol) was added into each of the saturated solution respectively. The mixed solutions were then stored in -20 °C freezer with no disturbance. One week later the crystals would come out from the solutions.

2.5.3. Instrumental methods

Microscopy. Optical microscope images were taken under polarized light with a Nikon SMZ800 optical microscope (Nikon Instruments, Incorporated, Melville, New York).

Single crystal X-ray diffraction (XRD). Crystals were selected and mounted on glass fibers using epoxy adhesive. Each crystal was centered, and the X-ray intensity data were measured on a Bruker AXS diffractometer by using graphite-monochromated Mo radiation. The data were collected using SMART 32 software; the data were processed using SMART 32, SAINTPLUS 5.0, and SHELXTL 6.2.

Chapter 3. Single-crystal-to-single-crystal topochemical polymerization

The nitrile-iodine halogen bond is significantly weaker than the pyridine-iodine interactions, but bis(nitrile) oxalamide hosts **7** – **10** (Figure 3.1) co-crystallize monomer **1** efficiently. Sun and Goroff discovered that in co-crystals with host **8**, monomer **1** polymerizes spontaneously to form PIDA in a single-crystal-to-single-crystal transformation, as shown in Figure 3.1.[86]

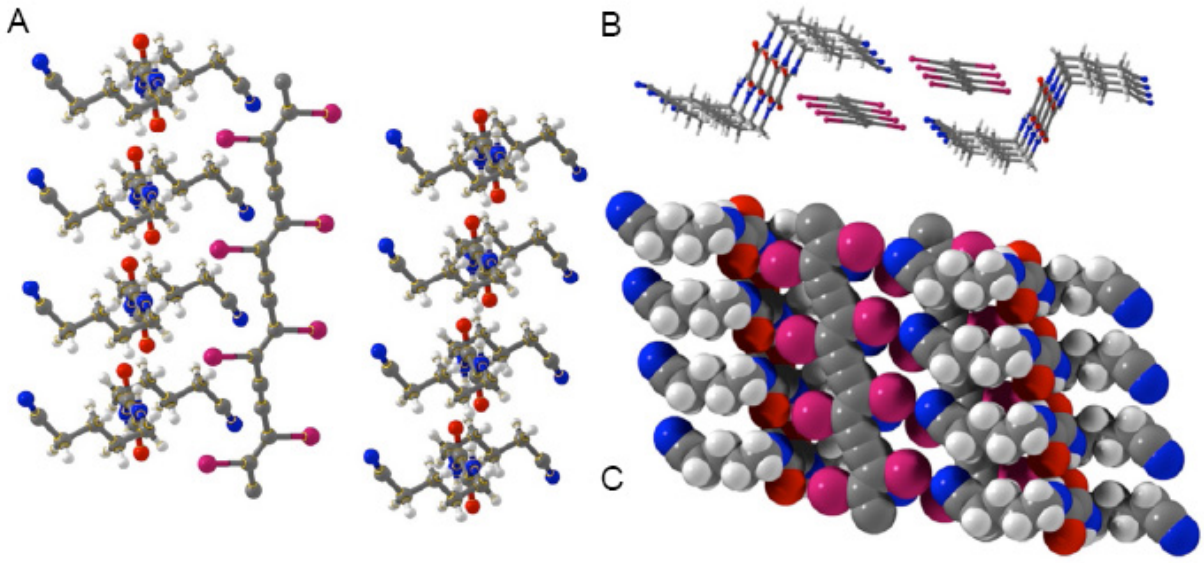

Figure 3.1. Crystal structure of PIDA co-crystals as reported. (A): A single polymer chain and associated host molecules; (B): Top view in balls and sticks mode; (C): Side view in space filling mode. Reprinted from Ref. 86, Copyright 2006, the American Association for the Advancement of Science.

In the crystal structure, the polymer strands are all parallel to the oxalamide hydrogen-bonding network, with a repeat distance of 4.94 Å, close to the expected value of 4.9 Å. The nitrile nitrogen atoms in the host are each halogen-bonded to iodine atoms, as predicted. However, the other half of the iodine atoms of **1** in the crystal has close contacts to oxalamide oxygen atoms rather than nitrile nitrogens, leading to a stoichiometry of 1:2 instead of the predicted 1:1 ratio. The oxygen atoms of host **8** are simultaneously acting as hydrogen-bond acceptors, suggesting that they also contribute to the crystal packing structure.

However, preparing large quantities of PIDA proved to be challenging due to the poor solubility of the host and the relatively weak halogen bonds between the host and guest, which restricts further characterization and application of the material. Based on a new methodology for preparing co-crystals of **1** with host **8**, and similar studies with hosts **9** and **10**, PIDA crystals with well-defined structures can be produced reliably and in large quantities. This development makes it realistic to carry out studies of the unique optical, electronic, and chemical properties of the material, and to explore other applications of PIDA. Most of these results have been reported in Ref. 87.

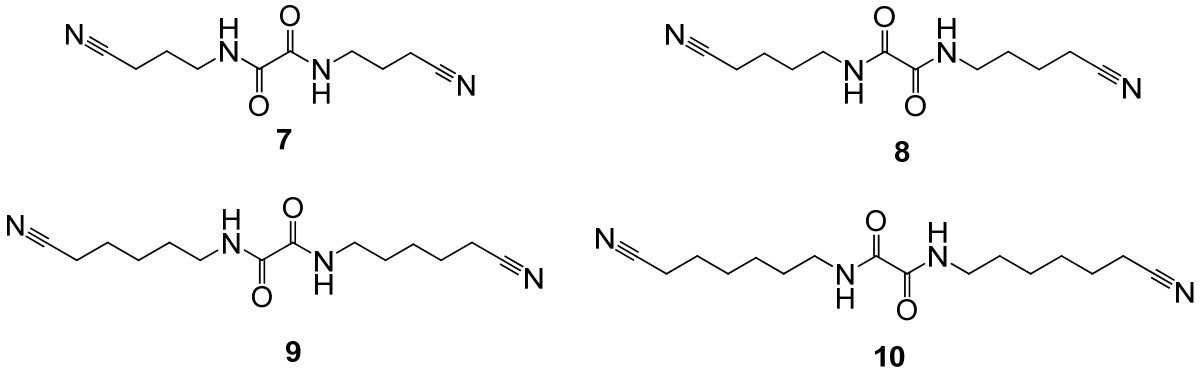

Figure 3.2. Bis(nitrile) oxalamide hosts **7** – **10**.

3.1. Synthesis of hosts 7 – 10 and building co-crystals between 1 and hosts 7 – 8

Bis(nitrile) oxalamide hosts **7** – **10** can be synthesized from aminonitriles **23** – **26**, the synthesis of which have been introduced in Section 2.1. The coupling between aminonitriles and diethyl oxylate produce the corresponding oxalamides with satisfactory yields.

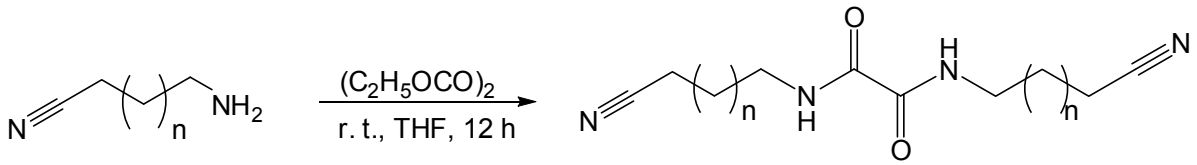

Scheme 3.1. Synthesis of bis(nitrile) oxalamides **7** – **10**.

It has been reported that host **7** can be used to form co-crystal **7•1**.[86] Similar to the co-crystals introduced in Chapter 2, the nitrile nitrogens are halogen bonded to the iodines of **1**, as shown in Figure 3.3. The repeat distance *r* in this co-crystal is 5.25 Å, longer than the target 4.9 Å needed for polymerization. The C1-C4 distance *d* is 4.0 Å, and the tile angle θ of aligned **1** is 51°. Attempts to induce polymerization in these co-crystals by Sun have thus far been unsuccessful.[86]

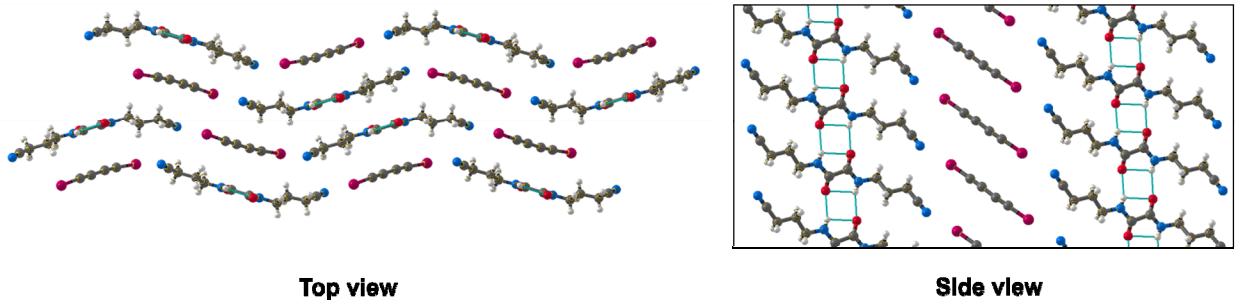

Figure 3.3. Crystal structure of co-crystal **7•1**.[86]

Co-crystal **8·PIDA** can be prepared by slow evaporation of methanol solutions containing **8** and **1**.[86] However, the preparation of this co-crystal used to be difficult due to the limited solubility of the host, and the relatively weaker interaction between nitriles and iodines. Here we have developed a new crystal growth method which can greatly increase the yield of polymer products. The methanol solution of host **8** and monomer **1** in a stoichiometry of 1:2 is purified first by centrifuge. Following slow evaporation of the solution in a shallow crystallization dish, which is covered with needle-punched aluminum foil, produces blue needle-shaped crystals in a

yield of up to 40%. Among the needle products, copper-colored crystals with lengths of up to 2 cm quality can be isolated for XRD study. The resulting crystal structure, shown in Figure 3.4, confirms them to be **8·PIDA**, consistent with previously published result.[86]

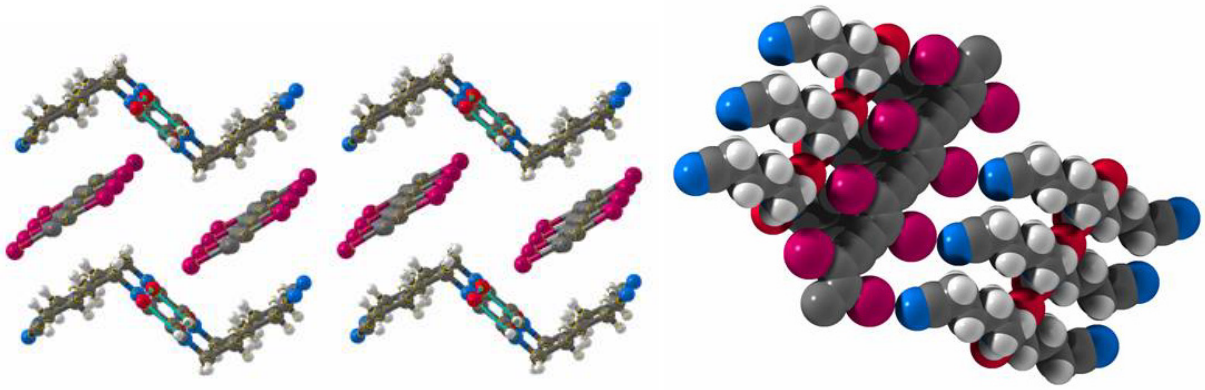

Figure 3.4. Crystal structure of co-crystal **8•PIDA**. Unit cell parameters: Space group P-1; Unit cell dimensions a = 4.9395(17) Å, b = 8.699(3) Å, c = 15.821(6) Å; α = 94.874(8) °, β = 97.664(6) °, γ = 98.583(7) °, Volume = 662.3(4) Å^3

3.2.Blue and copper-colored materials

The newly developed method enables us to produce the desired PIDA reliably in much larger yield. However, as has been described, the majority of the produced crystals are blue (Figure 3.5 A) rather than metallic colored (Figure 3.5 C). The amount of the copper-colored samples obtained each time is much less than that of the blue samples, the structure of which we could not determine directly from XRD. Further characterization and application of these blue samples requires determination of their structure first. Interestingly, the blue samples turn copper-colored after being placed at room temperature for one week (Figure 3.5 B), indicating that the blue samples may have a similar structure to their copper-colored counterparts. Since the blue samples were formed under the same conditions as copper-colored ones, we proposed that the difference between them is either the alignment of the polymer fibers or the degree of polymerization.

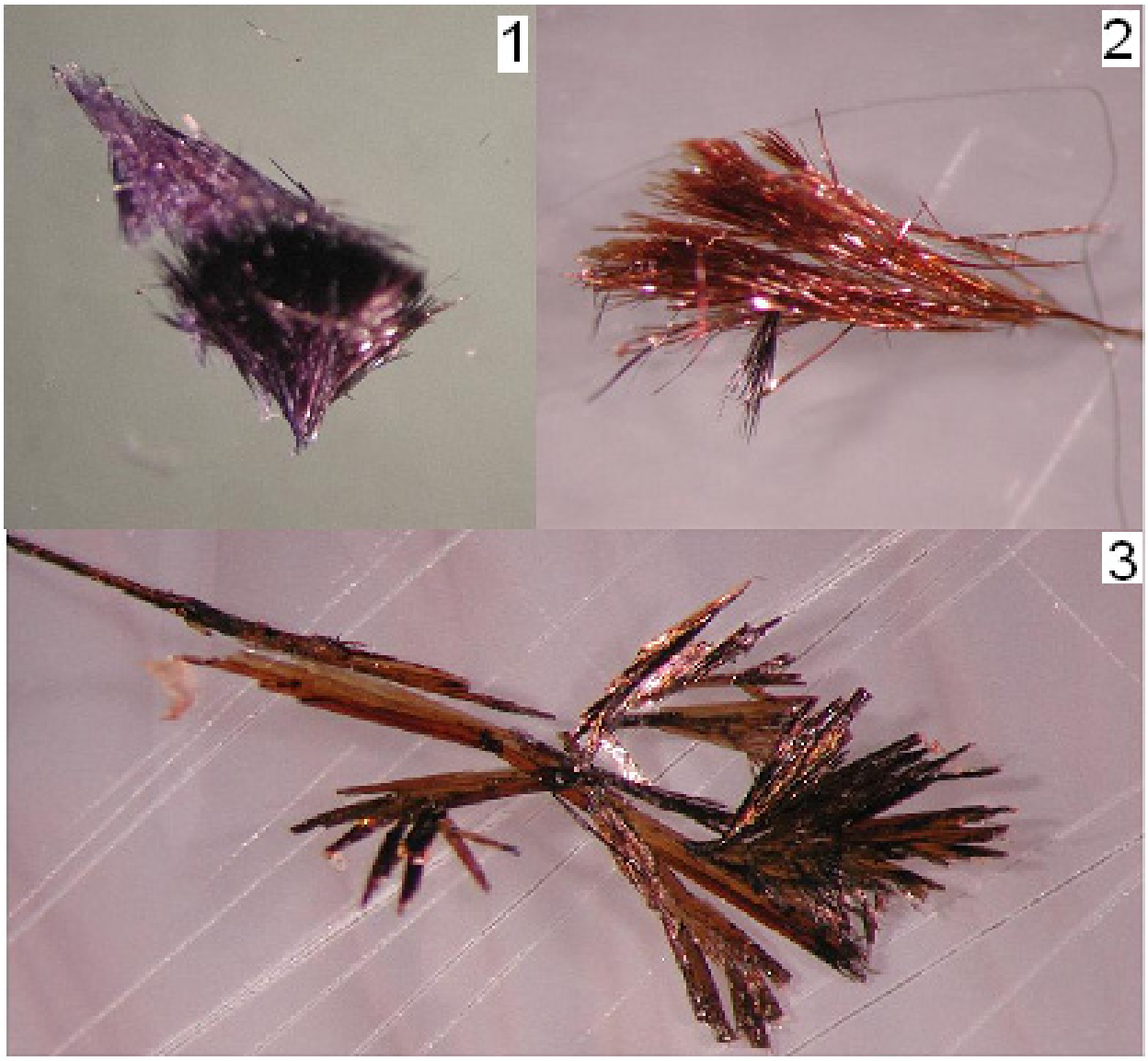

Figure 3.5. Microscopic images of PIDA co-crystals. 1: blue co-crystals; 2: blue co-crystals allowed to sit at room temperature for 1 week; 3: Original copper-colored co-crystals

To test these hypotheses, we took the SEM images of all these materials. Figure 3.6 shows the microscopic and SEM images of blue material and copper-colored material separately. The average width of the blue crystals is about 10 μm while that of the copper-colored crystals is 5 or 6 times larger. This might explain how the copper-colored samples can provide XRD-quality single crystals to clarify the structure but the blue samples cannot.

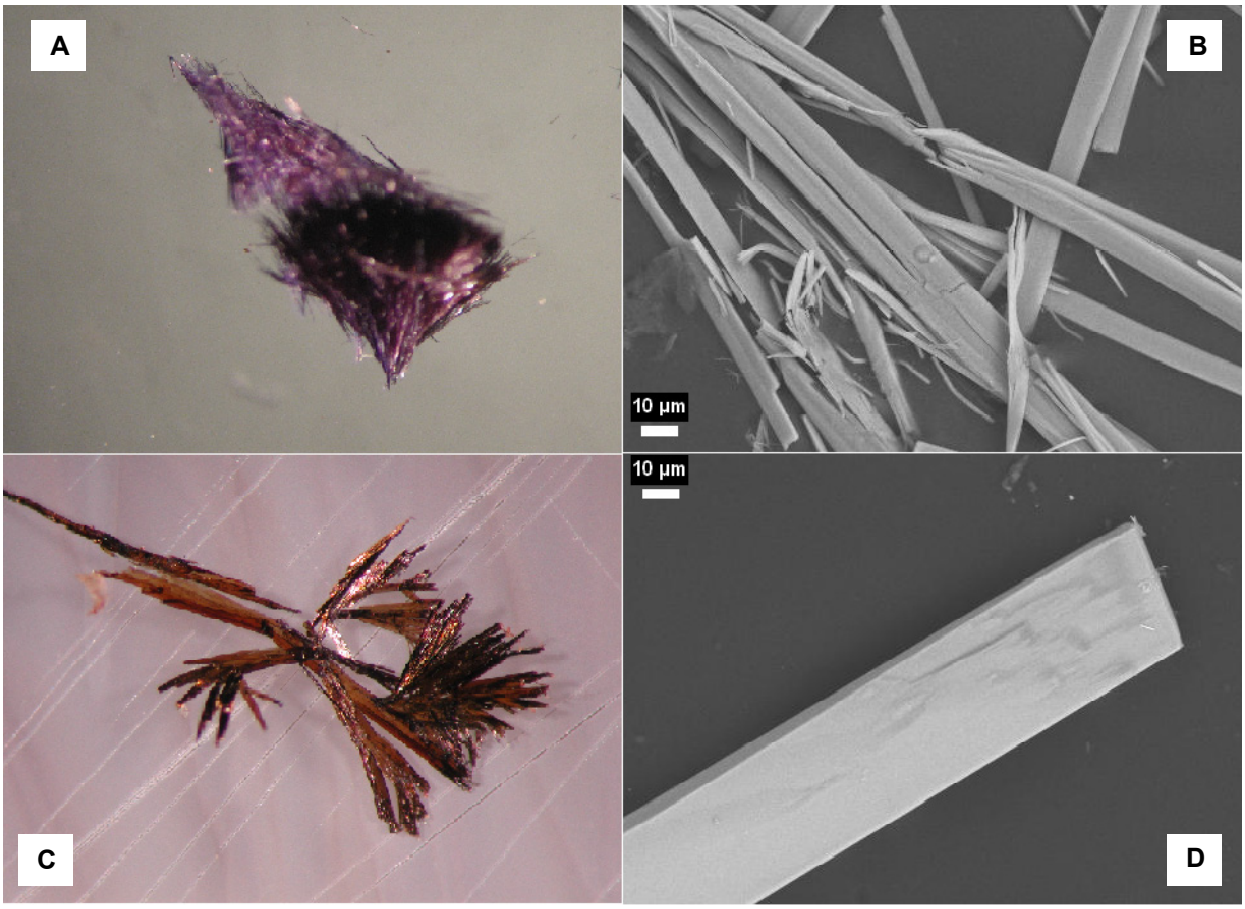

Figure 3.6. Microscopic and SEM images of blue and copper-colored samples. A: optical microscopic image of the blue samples; B: SEM image of the blue samples; C: optical microscopic image of the copper-colored samles; D: SEM image of the copper-colored sample.

Dispersing the copper-colored fibers in methanol by sonication prepares samples for transmission electron microscopy (TEM), which were performed in collaboration with Oak Ridge National Laboratory. TEM images of these materials reveal that these fibers are composed of very thin polymer strands (Figure 3.7). Electron diffraction of the material indicates the ordered alignment of these parallel strands, suggesting that the difference sizes between the blue sample and the copper-colored sample might attribute to the amount of these parallel stands they contain.

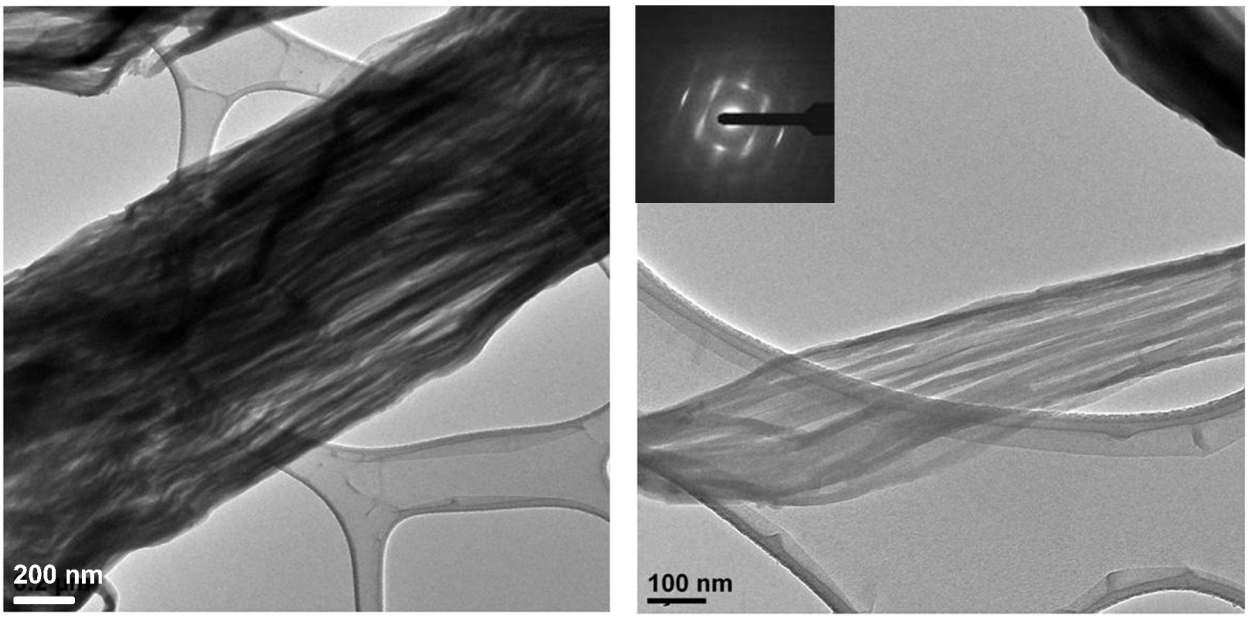

Figure 3.7. TEM images of copper-colored samples in a further scale after separating by sonication. Inset is the electron diffraction on the strands. Images were taken by Dr. Karren L. More, Oak Ridge National Laboratory.

SEM and TEM images can only provide us information on the morphology of the materials, while Raman spectroscopy provides internal structural information. The Raman spectrum of the copper-colored crystals also provides strong evidence for the formation of PIDA (Figure 3.8). The strong Raman intensity indicates the high polarization of excitation caused by conjugation, and the peaks at 971, 1415, and 2072 cm^{-1} represent the stretch of the C-C, C=C, and C≡C in the backbone, respectively.

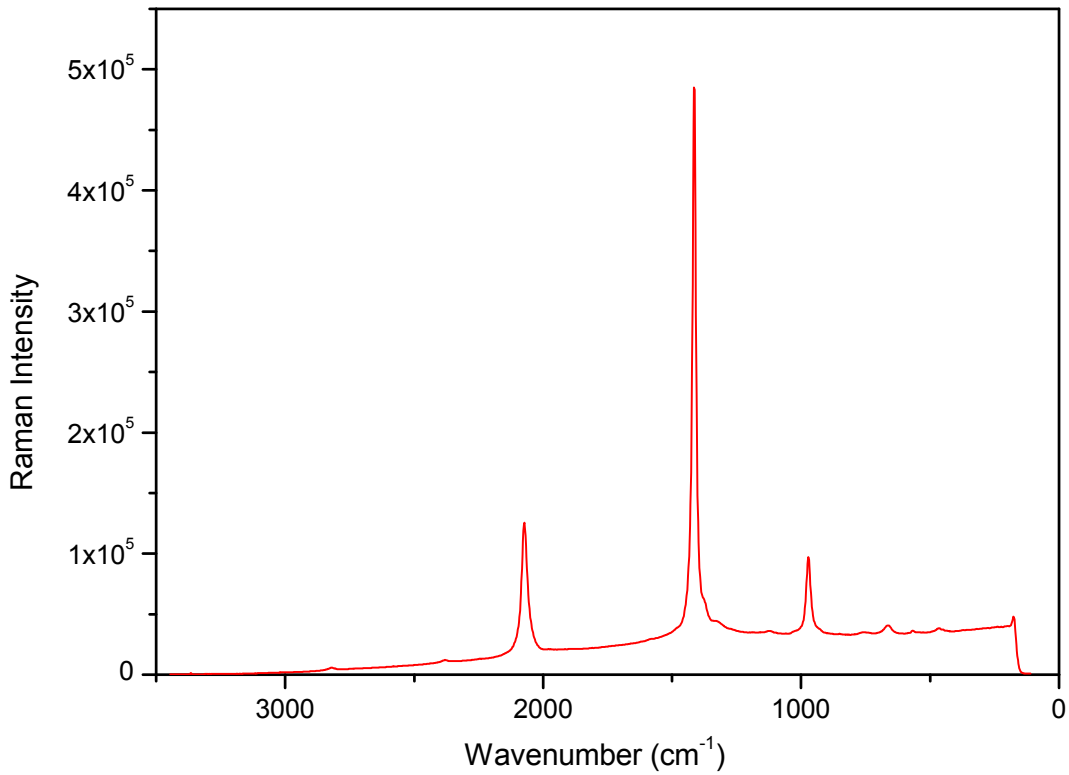

Figure 3.8. Raman spectrum of co-crystal **8•PIDA**.

The Raman spectra of the blue crystals (Figure 3.9) are similar to that of the **8•PIDA** (Figure 3.8) co-crystal, showing clearly the presence of polymer. The main difference between the Raman spectra of the blue and copper-colored samples is their intensity. The Raman scattering intensity of the copper-colored crystals is much larger than that of the blue ones. The frequencies of the blue crystals are consistent with those in Figure 3.8, but there is a frequency shift towards lower energy in the Raman spectra of some blue crystals. The reason for this shift is thus far unknown, but the general consistency between the Raman spectra of the two samples provides strong evidence that the blue samples contain polymers as well.

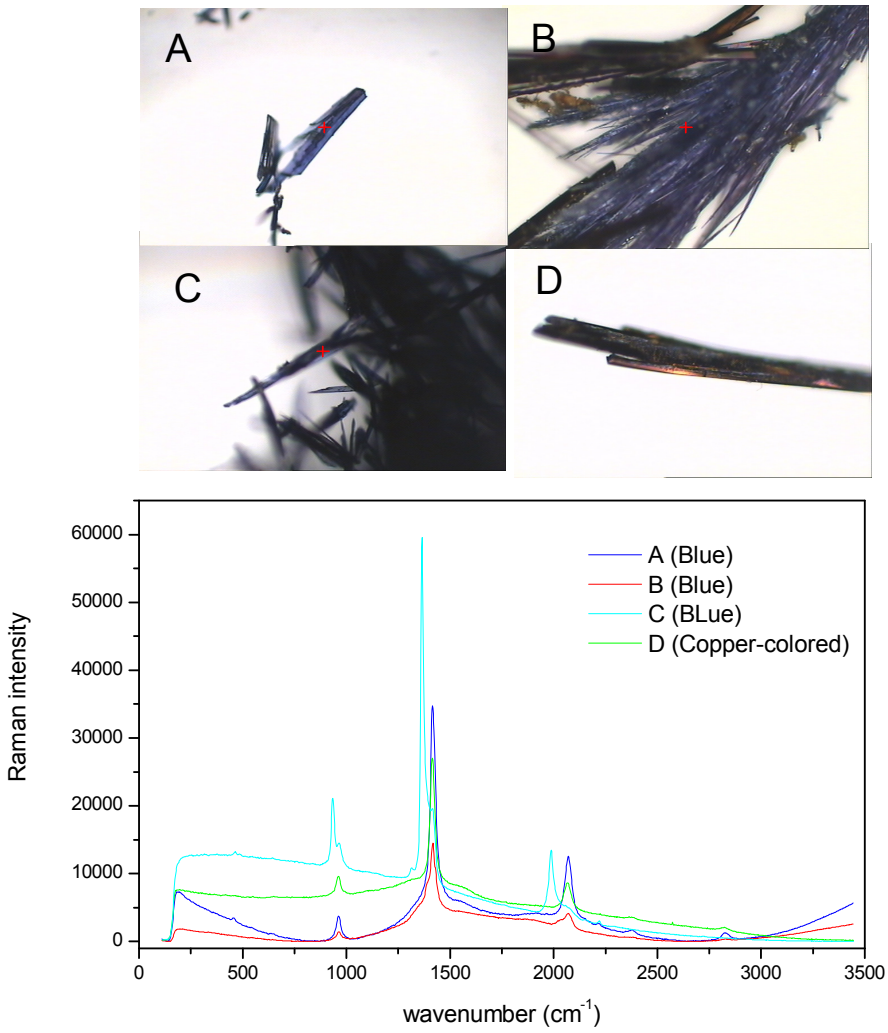

Figure 3.9. Raman spectra of the blue and the copper-color materials. The images on top show the solid samples under test. A, B, C: Blue crystals; D. Copper-colored crystals, the actual intensity of which is 10x larger.

3.3.Single-crystal-to-single-crystal topochemical polymerization

To identify the structure of the blue material produced with host **8**, crystals were grown at 4 °C, thereby reducing the solvent evaporation rate. The blue crystals acquired under these conditions have similar appearance to those grown at room temperature, but they are larger, allowing for structural determination by X-ray diffraction. After staying at room temperature for

one week, these big blue crystals turn darker and darker, until appear metallic appearance finally, as shown in Figure 3.10.

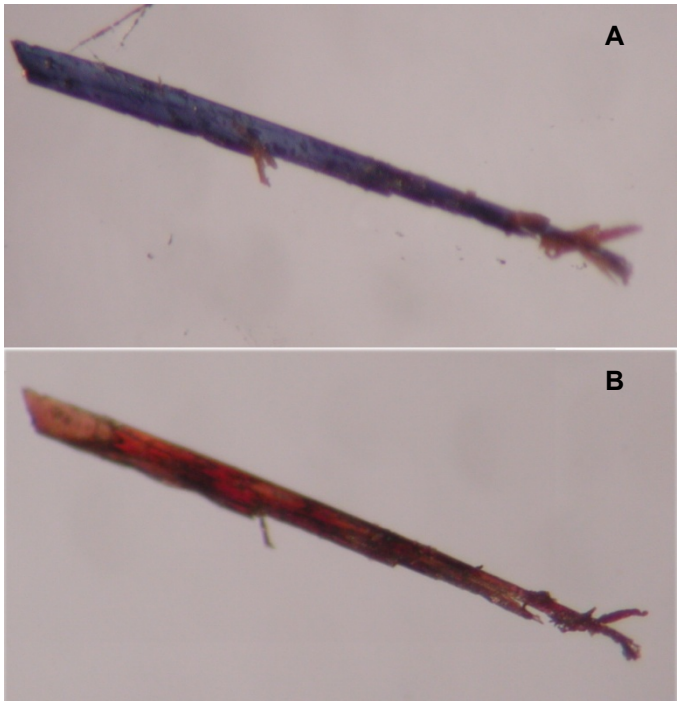

Figure 3.10. Color change of a blue single crystal recorded by microscope. A: The original blue single crystal; B: the crystal after turning copper-colored and shiny during a stay at room temperature for one week.

The X-ray diffraction studies demonstrate that these initial co-crystals contain primarily the monomer (Figure 3.11), in 2:1 co-crystal with the host. In the **8·1** co-crystals, half the iodine atoms of **1** are halogen-bonded to the nitrile nitrogen atoms, and half are in close contact with the oxalamide oxygens. Compared to the polymer co-crystals, the halogen bonds of the monomer in these co-crystals have a more linear geometry, with an N-I-C angle of 177^{o} and an O-I-C angle of 164^{o}

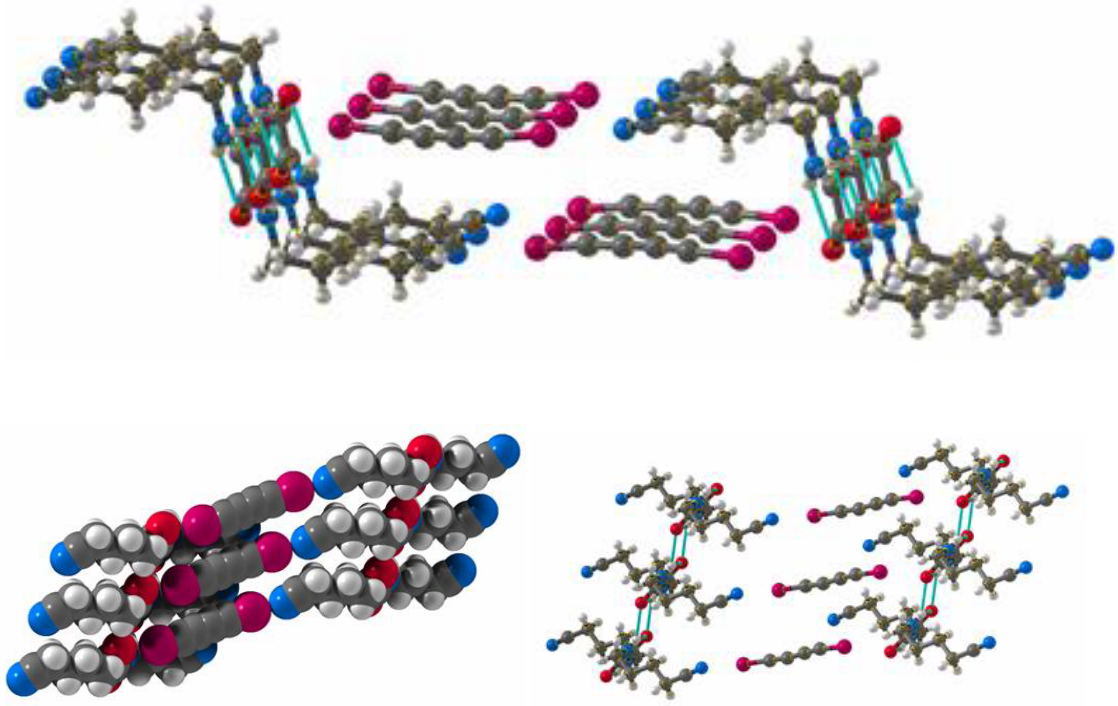

Figure 3.11. Crystal structure of co-crystal **8•1**. Unit cell parameters: Space group P2(1)/m; Unit cell dimensions a = 4.980(4) Å, b = 8.509(6) Å, c = 16.242(12) Å; α = 92.121(11)°, β = 96.382(14) °, γ = 97.568(12) °, Volume = 677.0(8) Å^3

This single crystal of co-crystal **8•1** will polymerize spontaneously at room temperature. After 3 days, the crystal structure changed to a co-crystal structure between host **8** and a mixture of monomer and polymer (Figure 3.12). The alignment between hosts and guests remains unchanged, with iodine atoms halogen bond nitrogen and oxygen respectively, and the ratio of monomer to polymer is about 45:55.

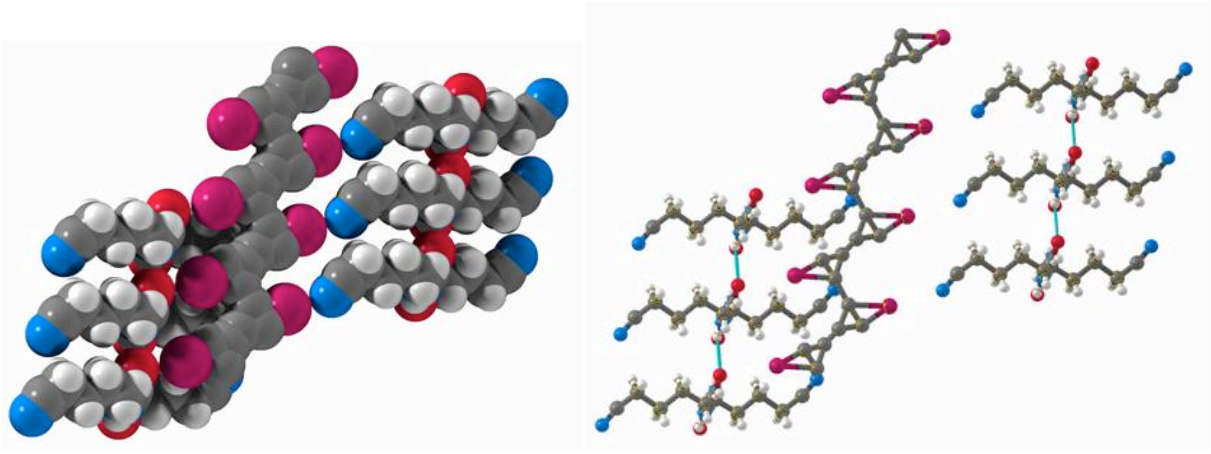

Figure 3.12. Crystal structure of partially polymerized co-crystal **8·1**. Unit cell parameters: Space group P-1; Unit cell dimensions a = 4.936(3) Å, b = 8.565(6) Å, c = 15.998(11) Å; α = 92.591(18) °, β = 96.745(15) °, γ = 97.862(18) °, Volume = 664.1(7) Å^3

Four days later, X-ray diffraction studies demonstrated that the crystal structure changed to a fully polymerized PIDA, consistent with previous result shown in Figure 3.4. Thus we have observed the complete transformation of this solid-state polymerization within single crystals. These observations match our expectation that the arrangement of host and guest in the co-crystal is determined by interactions of the monomer, before polymerization begins. This single-crystal-to-single-crystal topochemical polymerization is shown in Figure 3.13.

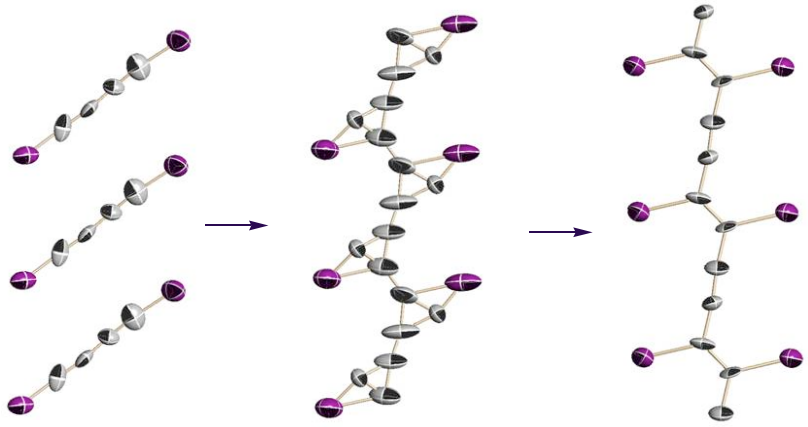

Figure 3.13. Transition of aligned C_4I_2 in co-crystals from monomer to polymer via monomer-polymer mixture (with around 45% monomer and 55% polymer), shown by ORTEP drawing.

Note that the blue color of the initial co-crystal indicates the presence of some polymer. Weiser has demonstrated that PDAs forming in a monomer crystal can be observed by UV/Vis absorption at mole fractions less than 10^{-5}.[97] Initially, the polymerization concentration is too low to be detected by X-ray diffraction, but is still observable by eye, as shown in Figure 3.14 A. During a week at room temperature, these crystals undergo a transition in appearance from opaque blue to copper-colored and highly reflective, with a concurrent transformation in the crystal structure to the previously observed PIDA co-crystal. As the mole fraction of polymer nears 100%, the crystals take on a characteristic metal-like appearance (Figure 3.14 B).

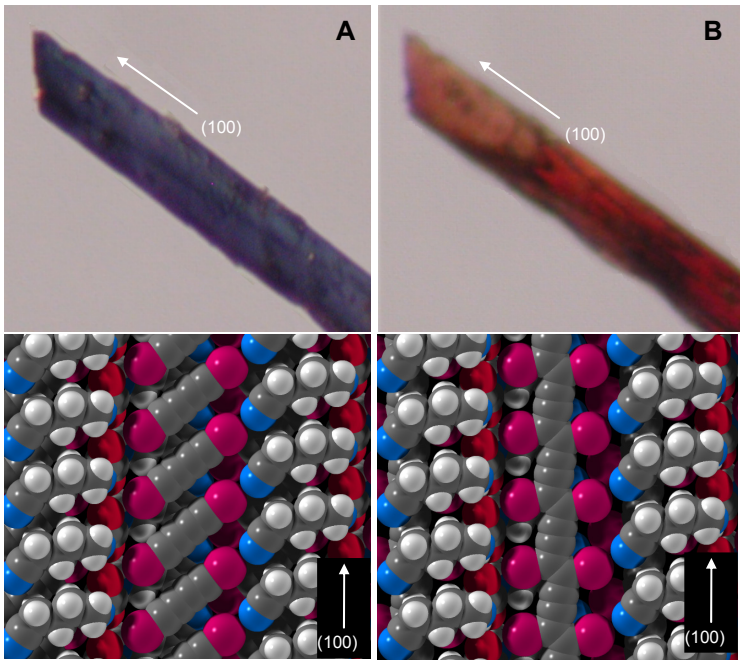

Figure 3.14. Crystal structures of a single crystal when it was blue (A) and metallic (B) appearance.

By studying the polymerization procedure and comparing the crystal structures of monomer co-crystal and polymer co-crystal (Figure 3.15), we can obtain important information which may be helpful in studying other potential polymerizable co-crystals. During the topochemical polymerization, the N-I-C angle changes from 177° to 165°, and the O-I-C angle changes from

164° to 131°. These observations match our expectation that the arrangement of host and guest in the co-crystal is determined by interactions of the monomer, before polymerization begins.

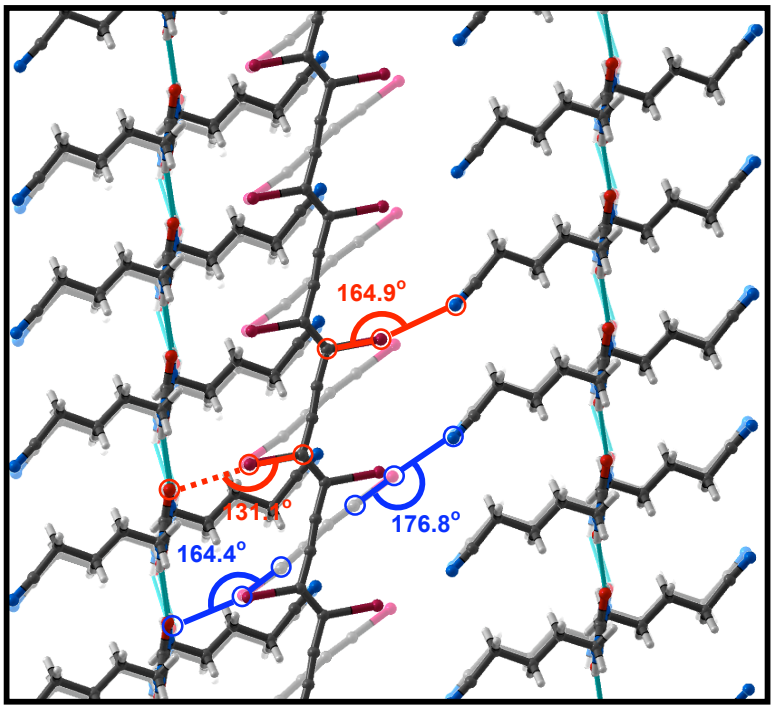

Figure 3.15. The pale background drawing shows the structure of co-crystal **8•1**. The bold foreground drawing shows the structure of co-crystal **8•PIDA**.

From Figure 3.15 we can see that when monomer changed to polymer, both host and guest molecules underwent apparent movement inside the single crystal, which leads to a slight change in the unit cell of the co-crystal (Table 3.1, Table 3.2) during this procedure. This unit cell change is similar to that of co-crystal **3•1** we studied above, both co-crystals having experienced shrinkage during polymerization.

Table 3.1. Unit cell change of co-crystal **8•1** during polymerization.

Crystal	a (Å)	b (Å)	c (Å)	α (°)	B (°)	γ (°)	V (Å^3)	R1 %
8•1	4.980(4)	8.509(6)	16.242(12)	92.121(11)	96.382(14)	97.568(12)	677.0(8)	6.36
Intermediate	4.9460(12)	8.654(2)	15.951(4)	93.940(6)	97.199(6)	98.220(6)	667.8(3)	9.19
8•PIDA	4.9395(17)	8.699(3)	15.821(6)	94.874(8)	97.664(6)	98.583(7)	662.3(4)	6.00

Table 3.2. Related structure parameter change of co-crystal **8•1**.

Crystal	I-I (Å)	I-N (Å)	I-O (Å)	C-I-N (°)	I-N-C (°)	O-I-C (°)	C-O-H (°)
8•1	4.98	2.93	3.09	176.8	159.4	164.4	143.0
Intermediate	4.95	3.24	3.18	160.3	158.9	162.1	152.4
8•PIDA	4.94	3.09	3.54	164.9	157.3	131.1	154.2

The structure parameters of co-crystal **8•1** are more favorable for the polymerization than the other co-crystals, so that C_4I_2 monomers can polymerize spontaneously at room temperature (Table 3.3). Because the structure parameters of aligned monomers within the other co-crystals are less favorable, completing the polymerization requires external energy or force, such as high pressure and temperature. These external factors can affect the crystal structure, cause other chemical changes, or destroy the crystals.

Table 3.3 The change of structure parameters of aligned guests in co-crystal **3•1** and **8•1**. *r* is the repeat distance; d is the C1-C4 distance; θ is the declination angle of the guest molecules; A~F represent co-crystal **3•1**, taken from Table 2.3.

Crystal	*r* (Å)	*d* (Å)	*θ* (°)	C≡C (Å)	C-C (Å)
A, B	5.11	3.86	48.8	1.187	1.371
C	5.08	3.87	49.1	1.122	1.423
D	5.04	3.85	49.4	1.209	1.322
E	5.00	3.88	49.3	1.168	1.412
F	4.95	4.30	48.1	1.289	1.786
8•1	4.98	3.88	50.1	1.266	1.303

3.4. Building co-crystals between 1 and hosts 9 – 10

We have successfully prepared PIDA by host-guest co-crystal strategy. Host **8** can efficiently form co-crystals with monomer **1** and produce the desired PIDA in satisfactory yield. Host **7**, whose side chain is one carbon shorter than host **4**, can also form co-crystals with monomer **1**, but failed to provide appropriate alignment from the polymerization. Thus it becomes very interesting to investigate the efficiency of other nitrile hosts with different side-chain lengths, such as hosts **9** and **10**. At the same time, the comprehensive characterization of PIDA and the investigation of the application of PIDA require the material in large quantity. Exploring new hosts may provide more efficient routes to the material.

The slow evaporation of solvent from a solution of diyne **1** and host **9** or **10** produces similar blue crystals but in greater yields, attributed to the longer side chains and the resulting better solubility of the hosts. No highly reflective material is isolated initially from either system. The pale blue co-crystals made with host **9** (Figure 3.16) turned dark grey after staying at room temperature for 1 week. A clearly resolved crystal structure could not be obtained by X-ray diffraction due to the low quality of the crystals, but we can determine the unit cell from the incomplete diffraction data. The results indicate that the crystal contains **1** and **9** in a 1:1 ration.

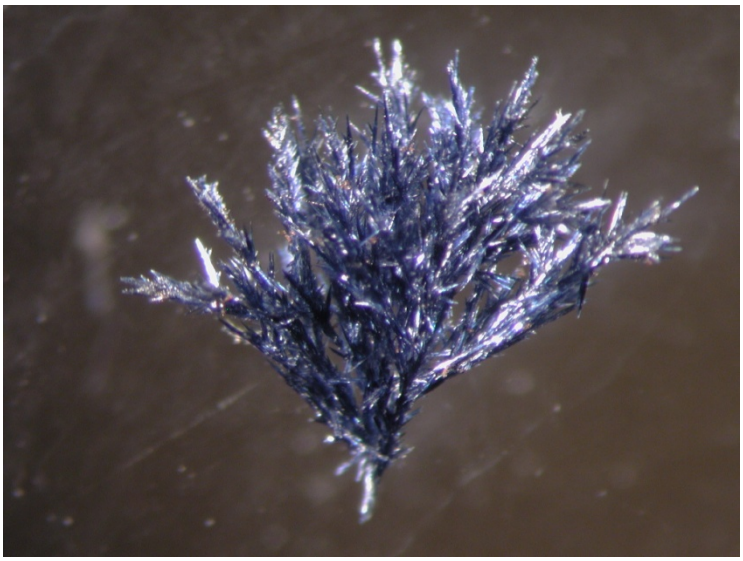

Figure 3.16. Blue crystals formed by host **9** and **1**. Unit cell parameters: a = 5.074 Å, b = 7.523 Å, c = 13.839 Å, α = 79.09 °, β = 83.45 °, γ = 73.62 °, V = 496.67 Å^3.

FTIR spectra of the crystals further identified their compositions. Figure 3.17 is a comparison of the IR spectra of host **9** alone and the crystals. Besides all the functional peaks from host **9**, the IR spectrum of the crystals contains a weak peak at 2075 cm^{-1}, matching that of triple bond stretching in monomer **1**. Both FTIR and X-ray diffraction results suggest that the blue crystals are co-crystals of host **5** and **1**. These **5·1** co-crystals turn dark over time rather than taking on a metallic appearance, and they are no longer crystalline after the color change. Further characterization methods used to explore the inherent structural information will be described in later chapters.

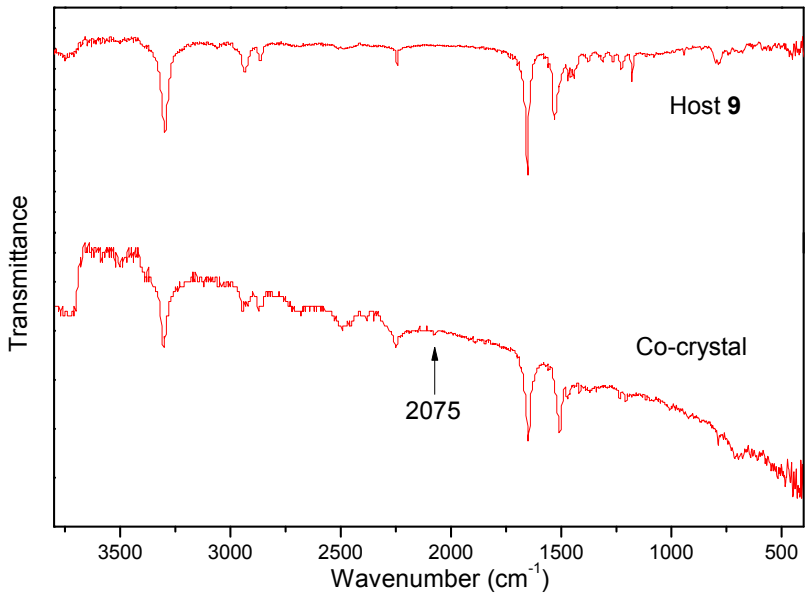

Figure 3.17. FTIR spectra of host **9** and blue co-crystal between **9** and **1**.

Host **10** has a much better solubility than the previously described hosts, attributed to the elongated side chains. Slow evaporation of a solution of **10** and **1** in methanol produces blue crystals with a yield of over 50%. After staying at room temperature for one week, the blue crystals gained a metallic appearance with a gold color (Figure 3.18), experiencing a similar color transition as co-crystal **8·PIDA**.

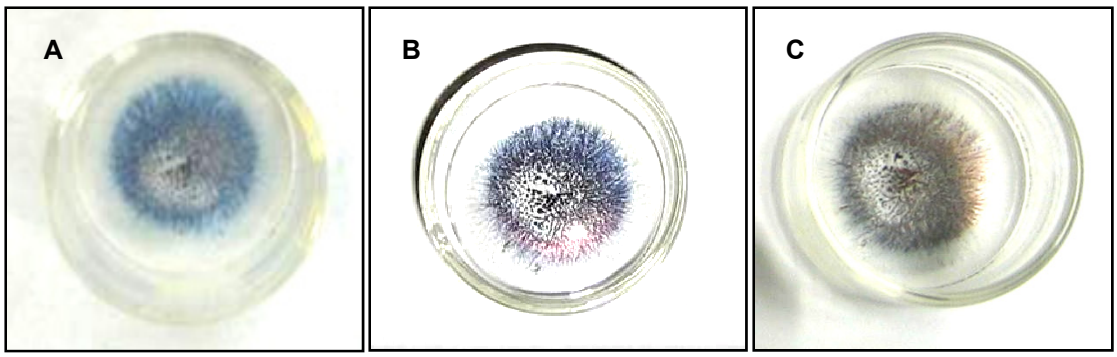

Figure 3.18. Color changes of the **10·1** co-crystals at room temperature. A: Original crystals grow from a solution of host **10** and **1**; Middle: The crystals after 2 days at room temperature; C: The crystals after 1 week at room temperature.

When initially formed, the co-crystals form a quasi-homogeneous layer at the bottom of the crystallization dish. After finishing the color transition, the crystals appear metallic gold under reflected light (Figure 3.19 A, C) but deep blue under transmittion light (Figure 3.19 B). However, it is difficult to determine the crystal structure completely by XRD, due to the relatively poorer crystal quality. From the best single crystal obtained (Figure 3.19 D), the unit cell was determined. The polymer can be distinguished in this crystal, but the host appears to be disordered.

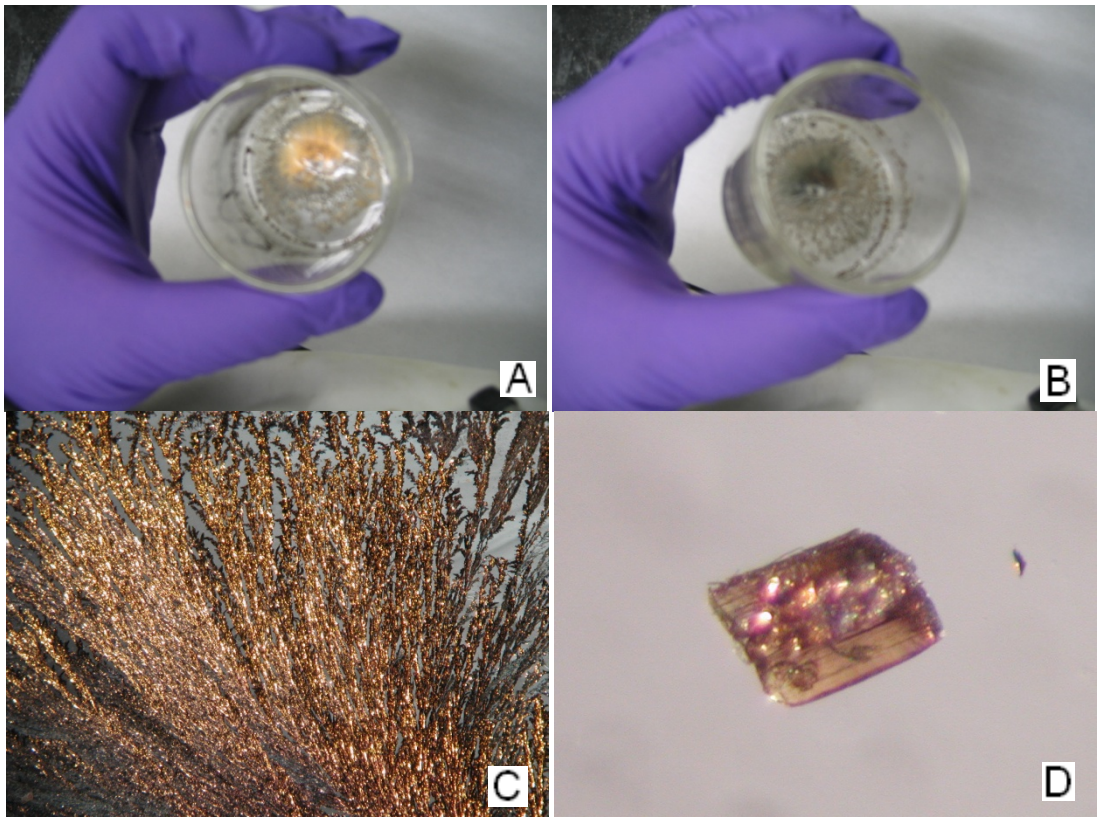

Figure 3.19. Optical images of co-crystals formed with host **10**, after undergoing the color transition. **A**: The appearance under reflected light; **B**: the appearance under transmitted light; **C**: co-crystals viewed from microscope under polarized light; **D**: quasi single crystal used for XRD.

During the initial stage of single crystal X-ray diffraction procession, the co-crystals were too small to acquire enough diffraction reflections. With the improvement of crystallization method, the crystal's quality is increased. Although it is still difficult to solve the molecular structure, the information about its unit cell can be obtained. The volume of unit cell shown in Figure 3.20 is only 382 $Å^3$, just half of what it should be. It contains half of the host molecule and one unit of PIDA, with the R1 as low as 15%. The host molecules are disordered and cannot be explained from the view of chemistry. Other value of unit cell parameters have been tested, with doubled volume either by doubling b or c value, the similar shape of co-crystal will still be obtained, but the error R1 is much higher (25%). Within the co-crystals, the iodine atoms are resolvable, and they are consistent with the proposed all-planar polymer structure.

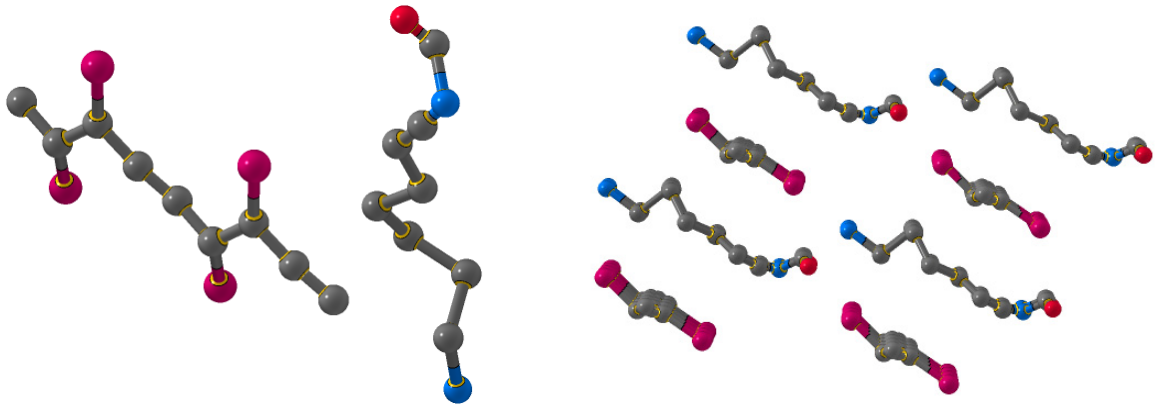

Figure 3.20. Molecular structure obtained from crystal showed in Figure 3.19 D. Unit cell parameters: Space group P1; a = 4.922 Å; b = 7.734 Å; c = 10.733 Å; α = 69.49°; β = 87.52°; γ = 89.89°; Volume = 382.29 $Å^3$.

Although the mosaicity of co-crystals **9·1** and **10·1** prevents complete analysis of their structures by X-ray diffraction, the diffraction data do provide well defined unit cells of both co-crystals. From their unit cells, we are able to determine the ratio of host to guest each. Based on an assumption that host/guest ratio is 1:1, the measured non-hydrogen atomic volume of co-crystal **9·1** is 19.1 $Å^3$, and the calculated density is 1.94 (Mg/m^3). Both values match well with previous fully determined co-crystals. In contrast, the unit cell parameters of co-crystal **10·PIDA** suggest a 1:2 ratio of host and guest within the co-crystal; the non-hydrogen volume (22.0 $Å^3$) and calculated density (2.02 Mg/m^3) for a 1:2 stoichiometry both are consistent with those observed in co-crystal **8·PIDA** (Table 3.4).

Table 3.4. Comparison of unit cell parameters of all co-crystals. (Non-H atomic volume and calculated density of co-crystals are based on the host guest ratios for each co-crystal.)

	7·1	**8·PIDA**	**9·1**		**10·PIDA**	
a (Å)	5.2545(18)	4.9395(17)	5.074(7)		4.885(3)	
a (Å)	14.956(5)	8.699(3)	7.523(11)		10.630(7)	
a (Å)	23.581(8)	15.821(6)	13.84(2)		15.348(11)	
α (^{o})	90	94.874(8)	79.10(3)		69.953(15)	
β (^{o})	91.338(5)	97.664(6)	83.46(2)		88.292(12)	
γ (^{o})	90	98.583(7)	73.63(2)		87.491(14)	
Volume (Å^3)	1852.6(11)	662.3(4)	496.7(12)		748.0(9)	
Formula units Z	4	1	1		1	
Host/Guest Ratio	1:1	1:2	**1:1**	1:2	1:1	**1:2**
Non-H atomic Volume (Å^3)	21.0	22.1	**19.1**	15.5	26.7	**22.0**
Calculated density (Mg/m^3)	1.879	2.141	**1.940**	2.949	1.350	**2.020**

The SEM images of PIDA made from host **10** have also been measured to describe the morphology of the materials, as shown in Figure 3.21. Another benefit of SEM is to provide a measure of electron transport through the material. However, due to the limitations of the experimental conditions, SEM images could not be obtained unless the materials were coated with Au. Compared with the needle shape of co-crystal **8·PIDA**, the co-crystal **10·PIDA** appears more like thin flakes, but also composed of numerous parallel tightly-aligned fibrils. The crystal surface includes some smooth regions, but it is difficult to find a fully smooth crystal, and the thin morphology makes the crystal difficult to keep flat in a long range. These caused the difficulty in collecting a perfect single crystal for XRD. TEM images (Figure 4.3) show the separated strands and fibrils of this kind of materials. The material has been sonicated in ethanol for 1 h before taking the TEM. These strands are still packed and hard to separate, but the situation is much better than those made from host **8**. The smallest diameter of these fibrils is about 10 nm and also shows the potent to apply as nanowires.

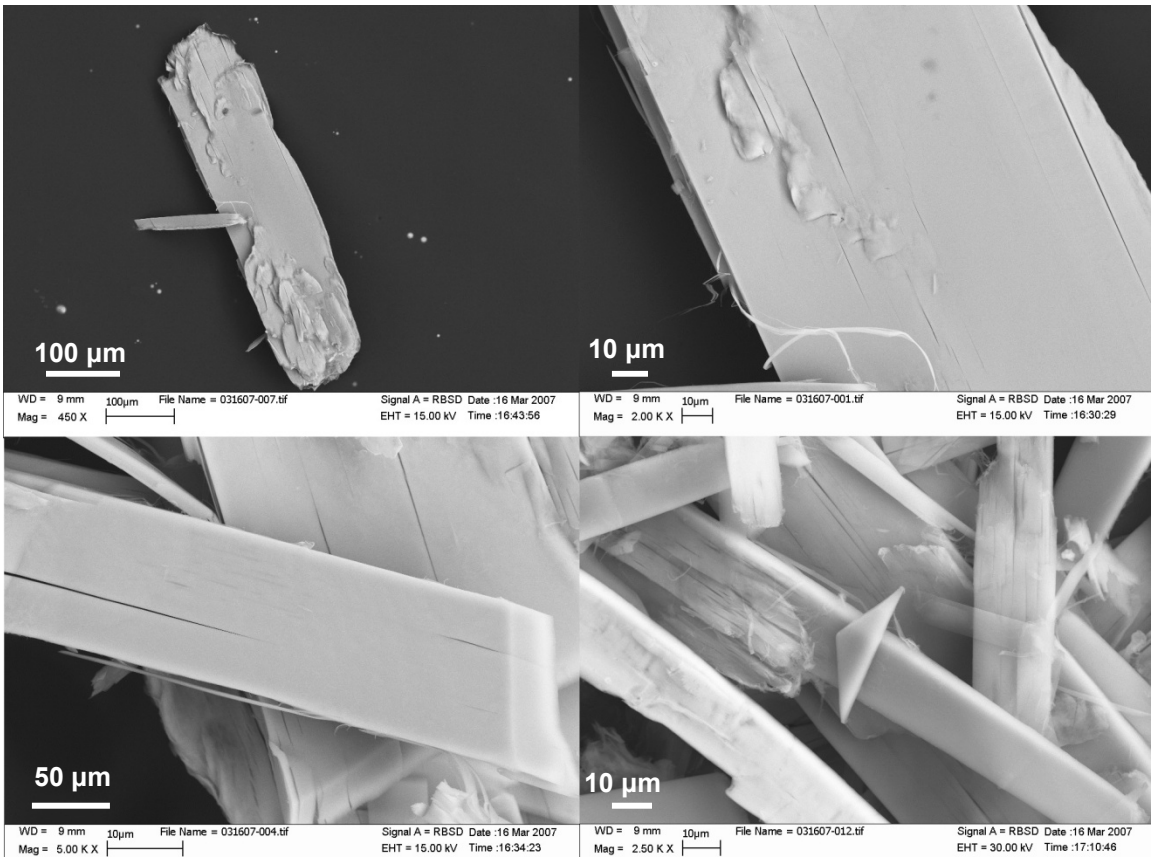

Figure 3.21. SEM images of PIDA co-crystals made from host **10**.

3.5.Odd-even effect on the topochemical polymerization

The appearance of the crystals formed between hosts **7** – **10** and monomer **1**, and the results of the X-ray diffraction demonstrate an odd-even effect based on the length of the alkyl chains in the host molecules. As have been reported, host **7** forms co-crystals with monomer **1** in a ratio of 1:1, and the repeat distance of packed monomers in these co-crystals is 5.25 Å.[86] These brown co-crystals turn dark and decompose at room temperature with no polymerization observed. The co-crystals **9·1** have the same host-guest stoichiometry of 1:1. They have a blue color when they are formed, indicating that polymer chains have been formed at low concentration. However, these **9·1** co-crystals turn dark at room temperature gradually in stead of gaining the metallic appearance, characteristic of a high degree of polymerization.

In contrast, in the case of hosts **8** and **10**, each of the hosts contains an even number of methylene groups in their alkyl side-chains. The co-crystals **8·1** and **10·1** have a host/guest stoichiometry of 1:2, and these co-crystals undergo spontaneous topochemical polymerization with a corresponding color transition from blue to metallic color.

The above results provide a new example of the odd-even effect which have been reported previously in the polymerization and chromism of PDA materials.[98,99,100] The alkyl chain length of each host determines the packing of the host and the guest in the co-crystals and the success of the desired polymerization. When the host has an odd number of methylene groups in each alkyl chain, each iodine atom in the guest forms a halogen bond with a terminal nitrogen of the guest, as designed. Topochemical polymerization cannot complete within these co-crystals. When the number of methylene groups in each host side chain is even, the stoichiometry shifts to 2:1, and one iodine atom in each guest is in close contact with a host carbonyl oxygen. These co-crystals produce PIDA spontaneously at room temperature. The fact that the carbonyls are also simultaneously acting as hydrogen-bonded acceptors suggests that the interaction between iodine and oxalamide oxygen is not likely to provide significant stabilization. On the contrary, the difference in observed stoichiometry and polymerizablility must come from different spatial requirements for the odd vs. even hosts.

Further characterizations of these co-crystals by ^{13}C MAS NMR, Raman spectroscopy, and UV-Vis absorption spectroscopy support the picture obtained from X-ray diffraction, and the odd-even effects consequently. These data will be introduced in Chapter 4 comprehensively.

Table 3.5. Odd-even effect of host side chain lengths on topochemical polymerization of guests **1**.

Host [a]	Color [b]	Host guest stoichiometry	Repeat distance	Spontaneous Polymerization
7	Brown to dark	1:1	5.25	No
8	Blue to copper-colored	1:2	4.94	Yes
9	Blue to dark	1:1	5.07	No
10	Blue to gold	1:2	4.89	Yes

a. Host compound numbers, corresponding to the number of CH_2 groups in the host side chains; b. Color transitions of co-crystals staying at room temperature for 1 week

3.6. Experimental details

3.6.1. Synthesis of organic compounds

5-Azidopentanenitrile (20):[86] Sodium azide (600.0 mg, 9.25 mmol) was added to a solution of 5-bromovaleronitrile **15** (0.72 mL, 6.5 mmol) in DMSO (15 mL). After 20 h of stirring at room temperature, 30 mL of water was added, followed by extraction with diethyl ether (50 mL x 3). The organic phase was washed with H_2O (50 mL x 2) and then dried ($MgSO_4$) and concentrated under reduced pressure to give pure 4-azidobutyronitrile (**21**) as colorless oil (688.0 mg yield 89.9 %). ^{1}H NMR (300 MHz, $CDCl_3$) δ 3.35 (t, J = 6.0 Hz, 2H), 2.39 (m 2H), 1.76 (m 4H).

5-Aminopentanenitrile (24):[86] To a mixture of **20** (435.5 mg, 3.51 mmol) and $CoCl_2 \cdot 6H_2O$ (95 mg, 0.4 mmol), at room temperature was added dropwise under stirring a solution of $NaBH_4$ (332 mg, 8.78 mmol) in H_2O (10 mL). The formation of a black precipitate indicated the formation of a cobalt boride species. The mixture was stirred at room temperature for 60 min and then adjusted to pH 14 by addtion 2M NaOH (*aq*). After extraction with ethyl acetate (20 mL x 5), the organic phase was dried ($MgSO_4$) and concentrated under reduced pressure to give amine

11a as yellow oil. (216.9 mg, 63.0%). ^{1}H NMR (300 MHz, $CDCl_3$): δ 2.70 (bt, 2H), 2.33 (t, *J* = 6.9 Hz 2H), 1.64 (m, 4H), 1.37 (br, 2H).

***N,N'*-(Bispentanenitrile) oxalamide (8):**[86] To a solution of 5-aminopentanenitrile **24** (294.0 mg, 3.00 mmol) in 10 mL of THF was added diethyl oxalate (191 μL, 1.40 mmol). After stirring for 12 h at room temperature, TLC in dichloromethane/methanol 8:1 showed a spot at R_f 0.5. The solvent was removed at reduced pressure and the crude products were purified by recrystallization in methanol to give N, N´-bispentanenitrile oxalamide **8** as white crystals (182.1 mg, yield 52%). M.p. 125.0-125.5 ^{o}C. ^{1}H NMR (300 MHz, $CDCl_3$) δ 7.48 (s, 2H), 3.40 (q, 4H), 2.40 (t, 4H), 1.73 (m, 8H).

6-Azidohexanenitrile (21):[87] Sodium azide (553 mg, 8.52 mmol) was added to a solution of 6-bromohexanenitrile **16** (1 g, 5.68 mmol) in DMSO (15 mL). After 20 h of stirring at room temperature, 30 mL of water was added, followed by extraction with diethyl ether (50 mL x 3). The organic phase was washed with H_2O (50 mL x 2) and then dried ($MgSO_4$) and concentrated under reduced pressure to give pure 6-azidobutyronitrile (**21**) as a colorless liquid (734 mg, 95.0 %). ^{1}H NMR (300 MHz, $CDCl_3$) δ 3.30 (t, *J* = 4.8 Hz, 2H), 2.36 (t, *J* = 5.4 Hz, 2H), 1.76 (m 6H). ^{13}C NMR (400 MHz, $CDCl_3$) δ119.6, 51.3, 28.4, 26.1, 25.2, 17.3.

6-Aminohexanenitrile (25):[87] To a mixture of **21** (477.4 mg, 3.51 mmol) and $CoCl_2{\cdot}6H_2O$ (95 mg, 0.4 mmol), at room temperature was added dropwise under stirring a solution of $NaBH_4$ (332 mg, 8.78 mmol) in H_2O (10 mL). The formation of a black precipitate indicated the formation of a cobalt boride species. The mixture was stirred at room temperature for 60 min and then adjusted to pH 14 by adding 2M NaOH (*aq*). After extraction with ethyl acetate (20 mL x 5), the organic phase was dried ($MgSO_4$) and concentrated under reduced pressure to give 259.4 mg amine **25** as a yellow oil (259.4 mg, 66.0%). ^{1}H NMR (300 MHz, $CDCl_3$): δ 2.70 (t, 2H, *J* =

6.9 Hz), 2.35 (t, 2H, *J* = 6.8 Hz), 1.67 (m, 2H), 1.49 (m, 4H). ^{13}C NMR (400 MHz, $CDCl_3$) δ 119.6, 41.4, 32.2, 25.9, 25.2, 17.9.

***N,N'*-(Bishexanenitrile) oxalamide (9):** To a solution of 6-aminohexanenitrile **25** (336.5 mg, 3.00 mmol) in 10 mL of THF was added diethyl oxalate (191 μL, 1.40 mmol). After stirring for 12 h at room temperature, TLC in dichloromethane/methanol 8:1 showed a spot at R_f 0.4. The solvent was removed under reduced pressure and the crude products were purified by recrystallization from methanol to give N, N´-bishexanenitrile oxalamide **9** as white crystals (229.5 mg, 55.2%). M.p. 136-137 ^{o}C. ^{1}H NMR (400 MHz, $CDCl_3$) δ 7.48 (s, 2H), 3.33 (q, 4H, *J* = 6.8 Hz), 2.40 (t, 4H, *J* = 7.2 Hz), 1.73-1.45 (m, 12H.) ^{13}C NMR (400 MHz, $CDCl_3$) δ 160.1, 119.6, 39.4, 28.8, 26.1, 25.2, 17.3. ESI-MS $C_{14}H_{22}N_4O_2$ M=278, (M+1)/z 279.02. IR (KBr disc) 3296, 2937, 2245, 1653 cm^{-1}.

7-Azidoheptanenitrile (22):[87] Sodium azide (543 mg, 8.35 mmol) was added to a solution of 7-bromoheptanenitrile **17** (1.000 g, 5.26 mmol) in DMSO (15 mL). After 20 h of stirring at room temperature, 30 mL of water was added, followed by extraction with diethyl ether (50 mL x 3). The organic phase was washed by H_2O (50 mL x 2) and then dried ($MgSO_4$) and concentrated under reduced pressure to give pure 7-azidoheptanenitrile (**22**) as colorless liquid (751 mg, 94.0 %). ^{1}H NMR (300 MHz, $CDCl_3$) δ 3.28 (t, 2H, *J* = 6.6 Hz), 2.35 (t, 2H, *J* = 6.9 Hz), 1.57 (m, 8H). ^{13}C NMR (400 MHz, $CDCl_3$) δ 119.8, 51.5, 28.8, 28.4, 26.2, 25.4, 17.3, FTIR (KBr disc) 2096, 2245 cm^{-1}.

7-Aminoheptanenitrile (26):[87] To a mixture of **22** (533 mg, 3.51 mmol) and $CoCl_2{\cdot}6H_2O$ (95 mg, 0.40 mmol), at room temperature was added dropwise under stirring a solution of $NaBH_4$ (332 mg, 8.78 mmol) in H_2O (10 mL). The formation of a black precipitate indicated the formation of a cobalt boride species. The mixture was stirred at room temperature for 60 min and

then adjusted to pH 14 by adding 2M NaOH (*aq*). The mixture was extracted by ethyl acetate (20 mL x 5). The organic phase was dried ($MgSO_4$) and concentrated under reduced pressure to give amine **26** as yellow oil (288.1 mg, 65.1%). ^{1}H NMR (300 MHz, $CDCl_3$): δ 2.70 (bt, 2H), 2.33 (t, 2H, J = 6.9 Hz), 1.64 (m, 4H). ^{13}C NMR (400 MHz, $CDCl_3$) δ 119.9, 42.2, 33.6, 28.7, 26.2, 25.5, 17.2.

***N,N'*-(Bisheptanenitrile) oxalamide (10):** To a solution of 7-aminoheptanenitrile **26** (378.0 mg, 3.00 mmol) in 10 mL of THF was added diethyl oxalate (191 μL, 1.40 mmol). After stirring for 12 h at room temperature, TLC in dichloromethane/methanol 8:1 showed a spot at R_f 0.4. The solvent was removed at reduced pressure and the crude products was purified by recrystallization in methanol to give N, N´-bisheptanenitrile oxalamide **10** as white crystals (252 mg, 54.9 %). M.p. 98-99.5 ^{o}C. ^{1}H NMR (400 MHz, $CDCl_3$) δ 7.45 (s, 2H), 3.31 (q, 4H, J = 6.8 Hz), 2.33 (t, 4H, J = 7.2 Hz), 1.71-1.37 (m, 16H). ^{13}C NMR (400 MHz, $CDCl_3$) δ 160.1, 119.8, 39.7, 29.2, 28.5, 26.2, 25.5, 17.3. ESI-MS $C_{14}H_{22}N_4O_2$ M=306, (M+1)/z 307.3. IR (KBr disc) 3293, 2924, 2242, 1652 cm^{-1}.

3.6.2. Crystal growing method

Co-crystals between hosts **7** – **10** and monomer **1** were prepared by slow evaporation. To a 0.02 mM methanol solution of host, guest **1** was added with a host/guest stoichiometry of 1:1 (hosts **7** and **9**) or 1:2 (host **8** and **10**). The mixed solution was centrifuged to remove any undissolved particles. The supernatant layer was transferred into a 50 ml crystallization dish. The dish was then covered tightly by an aluminum foil, with 10 – 15 needle holes on it. Leaving the dish at room temperature with no disturbance would produce the desired crystals when all the solvent evaporated. Slow evaporation of the solution of host **7** and **1** produces brown crystals, while in the cases of other hosts, blue crystals can be obtained by the slow evaporation method.

3.6.3. Instrumental methods

Scanning electron microscopy (SEM): SEM images were taken with a field emission scanning electron microscope (SEM, Leo 1550) operated at accelerating voltages of 15 kV and equipped with Energy Dispersive X-ray Analysis (EDAX) capabilities. Specifically, each sample was deposited onto a Si wafer, which was then attached to the surface of a brass stub using a copper tape. Samples were then conductively coated with gold by sputtering for 10-20 s to minimize charging effects under SEM imaging conditions.

Electron microscopy: High resolution transmission electron microscopic images, electron diffraction, and energy dispersive X-ray spectrum (EDS) were obtained using a Hitachi HF-3300 operated at 300 kV, with the help of Dr. Karren L. More at Oak Ridge National Laboratory. Images were acquired with digital camera and CCD (Gatan. Inc.O, and processed using DigitalMicrograph and DIFPACK software (Gatan, Inc.). Co-crystals were dispersed in H_2O, and isolated PIDA fibers were dispersed in methanol before loaded to TEM grids.

Chapter 4. Comprehensive Characterization of PIDA Co-crystals

The development of new conditions for the formation of PIDA via single-crystal-to-single-crystal topochemical polymerization enables us to perform a more comprehensive characterization of PIDA than was previously possible. In addition to single-crystal X-ray diffraction, PIDA co-crystals have been fully characterized by electron microscopy, ^{13}C MAS NMR, Raman, and UV-Vis absorption spectroscopy. The comprehensive characterization of PIDA co-crystals will help to carry out studies on the unique optical, electronic, and chemical properties of the material and to investigate its potential applications. Many of these results were previously published in Ref. 87.

4.1. ^{13}C MAS NMR

The insolubility of the PIDA co-crystals makes it difficult to characterize them by solution-phase NMR. However, magic-angle spinning NMR (MAS-NMR) techniques allow for NMR characterization of the solid samples. As introduced in Section 2.3.1, MAS-NMR has been employed to characterize the pressed **3·1** and **4·1** co-crystals.[94] The technique has also been applied to study co-crystals formed with the nitrile hosts, particularly the co-crystals formed with hosts **9** and **10** that cannot be identified completely by X-ray diffraction. All the MAS NMR experiments described below were conducted by Christopher Wilhelm.

The ^{13}C MAS-NMR spectrum of co-crystal **8·1**, characterized previously by X-ray diffraction, contains peaks at 161.2, 122.6, 39.2, 29.2, 24.6, 16.7 ppm (corresponding to the host) and 80.0 ppm (monomer β-carbon), while the α-carbon of the monomer, a broad peak in the range of 10-20 ppm,[94] is hidden by the host methylene carbon peaks, as shown in Figure 4.1A. The spectrum of polymer co-crystal **8·PIDA** exhibits two new peaks at 110.6 and 80.1 ppm, attributed to the β (sp) and α (sp^2) carbons of PIDA, respectively (Figure 4.1B). The polymer α-

carbon has very similar chemical shift to the monomer β-carbon, but it is much broader because of the interaction of the α-carbon with the quadrupolar iodine atom.

Using the ^{13}C NMR spectra of co-crystals **8·1** and **8·PIDA** as reference, we can determine the composition of the co-crystals formed with hosts **9** and **10**. The NMR spectrum of the dark blue, week-old co-crystals with host **9**, shown in Figure 4.1C, does not include clear resonances corresponding to either monomer or polymer carbons. Instead, there is a very broad peak or collection of peaks in the range of 70 to 100 ppm. After heating these co-crystals in a vacuum oven at 30 ^{o}C for 1 month, the NMR spectrum shows a new resonance at 110 ppm and a broader signal centered at 81 ppm (Figure 4.1D). The co-crystals with host **5** evidently polymerize very slowly at room temperature, turning dark gradually. Heating the samples increases the rate of polymerization, but the crystals do not regain crystallinity. Figure 4.1E shows the NMR spectrum of the gold co-crystals formed with host **10**, with one peak at 109.6 ppm and another double peak signal centered at 85.0 ppm. The reason for this splitting in the peak attributed to the α-carbon, but this double peak integrates at a ratio of ~1:1 with the peak at 110 ppm, corresponding to the β-carbon, indicating the formation of fully polymerized PIDA within the co-crystals.

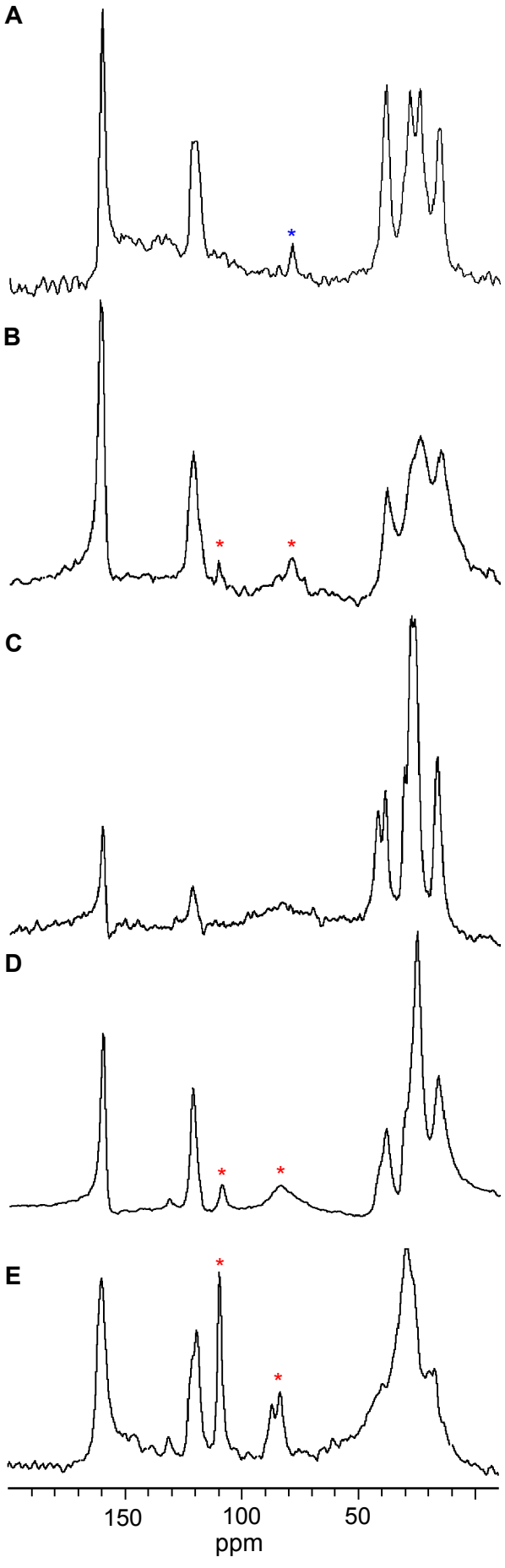

Figure 4.1. Solid-state ^{13}C NMR spectra of co-crystals. A: Co-crystal **8·1**; B: Co-crystal **8·PIDA**; C: Black co-crystals prepared with host **9**; D: Co-crystals in C after heating under vacuum at 30 °C for 1 month; E: Gold cocrystals with host **10**. (* monomer **1**; * PIDA).

4.2. Raman Spectroscopy

Raman spectroscopy is a sensitive tool for identifying the alternating ene-yne structure of poly(diacetylenes). Figure 4.2 shows the progressive change in the Raman spectrum of co-crystals with host **8** over the course of the topochemical polymerization of **1**. The Raman spectrum of the initial blue **8·1** co-crystals has a relatively low scattering intensity, shown as the blue spectrum in Figure 4.2. The band at 1413 cm^{-1}, corresponding to a carbon-carbon double bond stretching mode, indicates the presence of some polymer, consistent with the crystals' blue color. After staying at room temperature for 3 days, when the crystals have turned deeper blue and have an approximately 50 % degree of polymerization, as determined by X-ray diffraction, the Raman scattering intensity has increased greatly, and three major bands appears at 962 cm^{-1}, 1415 cm^{-1}, and 2067 cm^{-1}, corresponding to the carbon-carbon single, double, and triple bond stretches, respectively (ν(C–C), ν(C=C), ν(C≡C). When the crystals have been fully polymerized, with a coppery appearance, the Raman intensity (red spectrum, Figure 4.2) increased to about 100 times of that of the initial spectrum. Here, ν(C–C) is found at 971 cm^{-1}, ν(C=C) is at 1415 cm^{-1}, and ν(C≡C) is at 2071 cm^{-1}.

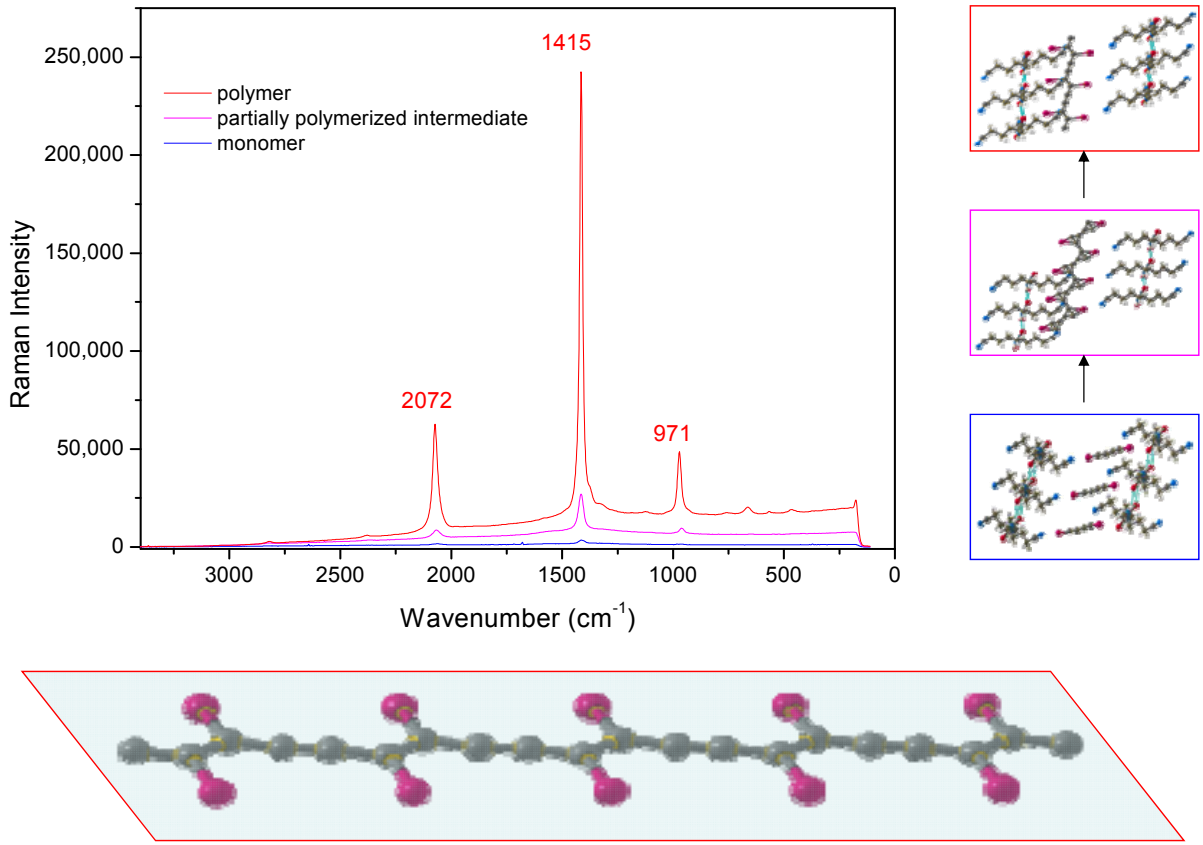

Figure 4.2. Raman spectra of monomer (blue), partially polymerized (purple), polymer (red) co-crystals made by host **8**. The right boxes contain the co-crystal structures in corresponding stages.

These observations are consistent with the increased concentration of polymer within these co-crystals. The polymer itself exhibits a very strong Raman spectrum because of the large polarizability of the poly(diacetylene) backbone. Initially, the co-crystals contain only small amounts of polymer. As the reaction proceeds, the spectrum for the polymer increases in intensity. However, the energies of the Raman scattering peaks do not change significantly, indicating that the observed signal even at the start comes from the low concentration of polymer in the sample. The scattering from the polymer dwarfs any signal from the less polarizable monomer or short intermediate oligomers.

As MAS NMR experiments, the Raman spectrum of PIDA in co-crystals formed with host **8** can be used as a reference to study the co-crystals formed with other hosts. There are no

significant bands consistent with that of a polydiacetylene in the spectrum of co-crystal **7·1** (Figure 4.3 A) indicating that topochemical polymerization is not efficient within this co-crystal. The Raman spectrum (Figure 4.3 B) of the blue co-crystal **9·1** is similar to that of co-crystal **8·1**, showing several peaks at 958, 1324, 1405, and 2055 cm^{-1}. The peaks at the frequency of 958, 1405, and 2055 cm^{-1} correspond to C-C, C=C, and C≡C stretch respectively, consistent with the known polymer. There is an additional peak at 1324 cm^{-1} other than traditional C=C stretching, which may be attributed to the C=C stretching in oligomers with different conjugation length. The low scattering intensity of C=C stretch in the Raman spectrum indicates that the monomers in this blue crystal experienced a low-degree polymerization and the resulting polymer chains are dilute in the monomer matrix. The Raman spectrum of co-crystal **9·1** remains almost unchanged after the co-crystals turn dark, suggesting that the polymer chains remain at low concentration.

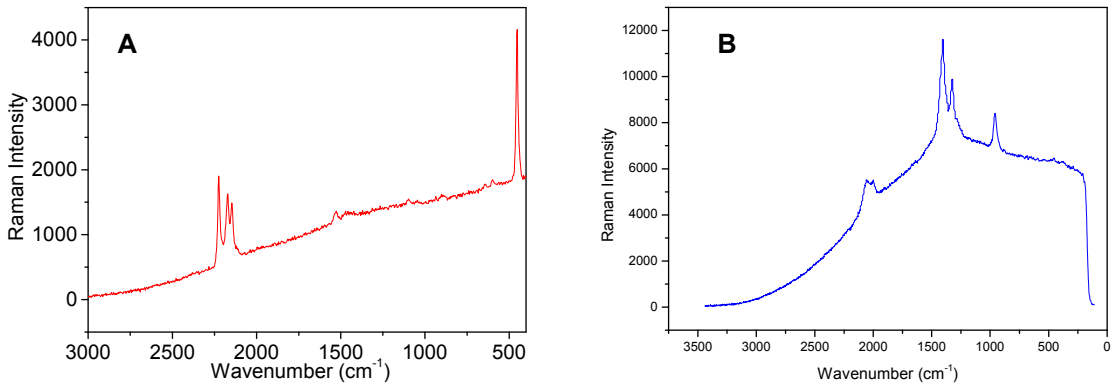

Figure 4.3. Raman spectra of co-crystals **7·1** (A) and **9·1** (B).

The Raman spectrum of co-crystal **10·PIDA**, as shown in Figure 4.7, contains three peaks at 917, 1407, and 2074 cm^{-1}, matching PIDA co-crystals made with host **8**. The Raman spectrum, together with the results from ^{13}C MAS NMR, provide important evidence for the complete polymerization of monomer **1** to PIDA within the co-crystals with host **10**. These data are

especially important, given that the structure of the gold-colored co-crystals can only be solved partially by single-crystal X-ray diffraction.

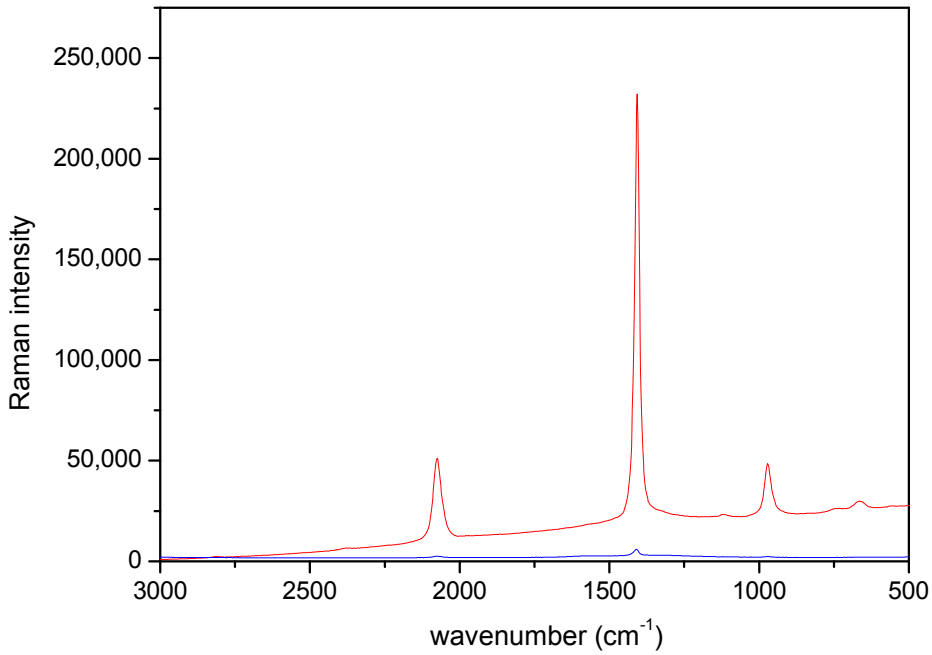

Figure 4.4. Raman spectra of co-crystals formed with host **10**. Blue: blue co-crystals primarily containing monomer; Red: blue co-crystals turned gold, containing fully polymerized PIDA.

4.3. UV-Vis Absorption Spectroscopy

An important method to characterize the formation of the poly(diacetylene) backbone is UV/Vis absorption spectroscopy. The flaky morphology of the **10·PIDA** co-crystal (Figures 3.19 and 3.21) provides a very good substrate to measure the electronic absorption spectrum of the polymer. The crystals are thin enough to allow light to pass through, and in these co-crystals, the individual polymer chain is completed planar and isolated from one another.

As shown in Figure 4.5, the absorption spectrum of the starting blue crystals exhibits a double-peak absorption with maxima at 594 nm (minor) and 653 nm (major), which is consistent with the blue **8·1** co-crystals (594 nm and 650 nm)[86], typical of an ordered PDA.[47] Similar to

Raman spectroscopy, the absorption spectrum indicates that polymerization has been initialized in the blue crystals, given that it detects the strongest absorption of the material, which could result from a very low concentration of the polymer within a monomer matrix. After the crystals turn gold, with a metallic appearance, the double-peak absorption shifts to 621 nm (minor) and 680 nm (major), indicating an increase in conjugation.

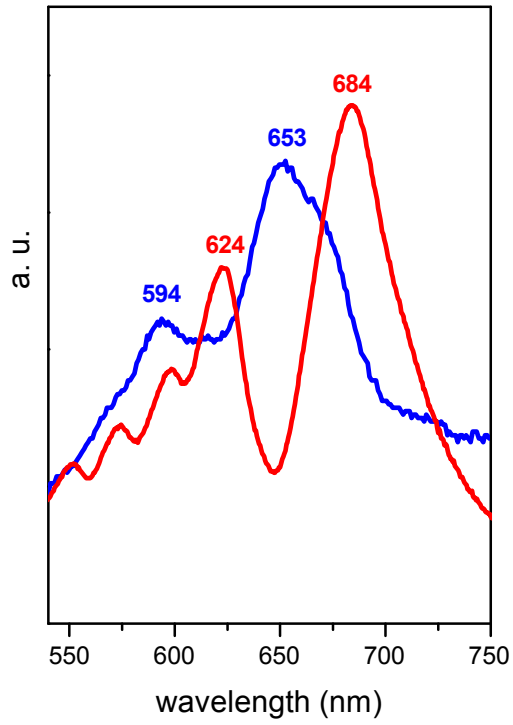

Figure 4.5. UV-visible absorption spectra of co-crystals made from host **10**: change from blue crystals (blue) to metallic gold (red).

In addition, the absorption spectrum of the gold-colored shiny crystals shows a series of satellite peaks after the second maximum peak.[97] To test that these peaks are not caused by reflections from the crystal, the sample was tested at different tilt angles, and similar absorption spectra were obtained (Figure 4.6).

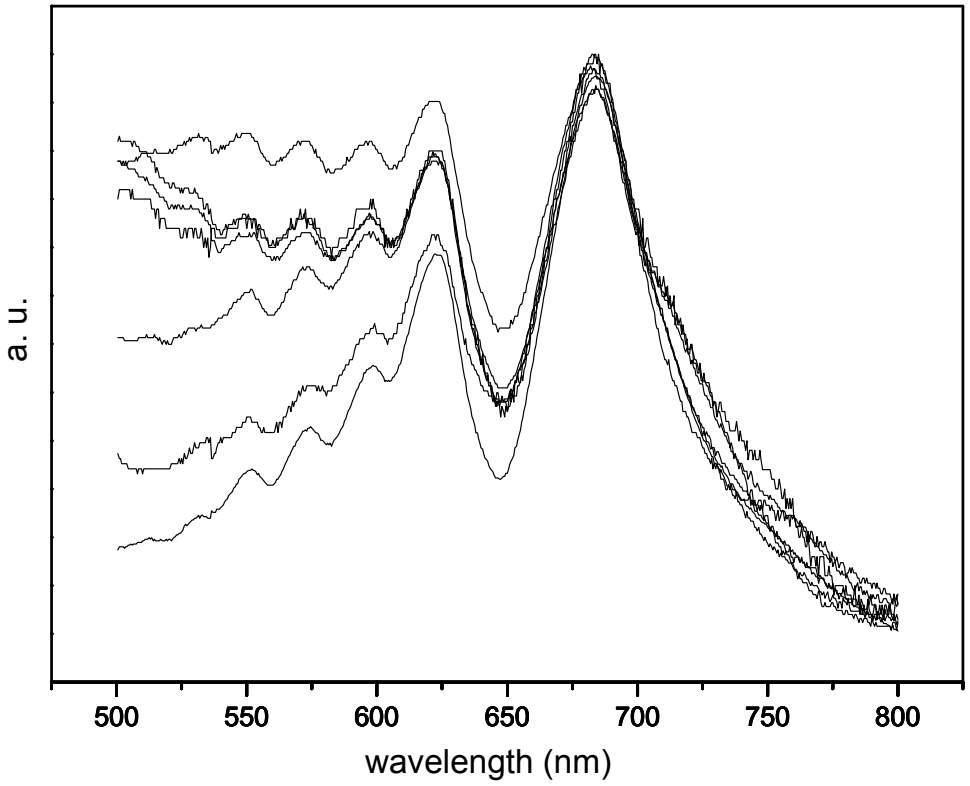

Figure 4.6. UV-visible absorption spectra of co-crystals **10·PIDA** at different positions and tilt angles.

Figure 4.7 shows the absorption spectrum of gold **10·PIDA** crystals plotted as a function of wavenumber (cm^{-1}). On this frequency scale, the major absorption peak at 684 nm corresponds to an energy of 14,617 cm^{-1} (1.8 eV), consistent with the π-π* transition of the polymer backbone. This transition is followed by a detailed vibrational progression, resulting from exciton coupling to the double-bond (D ≈ 1400 cm^{-1}, as determined by Raman) and triple-bond

($T \approx 2100\ cm^{-1}$) stretching modes, and an extended high energy tail, attributed to free motion of excitons along the chain.[101]

Similar vibronic progressions have been observed in the reflectance spectra of substituted PDAs and the derived absorption spectra from these measurements.[97] Weiser, Schott and coworkers have also observed some vibrational overtones in the absorption spectra of poly(diacetylene) chains diluted in a monomer matrix.[102] However, to our knowledge, this is the first directly acquired absorption spectrum of a fully polymerized poly(diacetylene) to show this detailed vibronic resolution. The low energy of the major absorption in the UV/Vis spectrum of the cocrystals and the highly resolved vibronic satellites are consistent with PIDA's highly planar structure. The clean, detailed spectrum indicates that each of the polymer chains has the same geometry and environment, without significant interchain interactions. Previously, such a well resolved PDA spectrum could only be approached by theoretical models.[103] According to theoretical studies by Weiser and co-workers,[97,101,104] vibronic progressions in optical spectra of PDA crystals derive from the high polarizability of the singlet excitons, which are also responsible for the large nonlinear susceptibility $\chi^{(3)}$ observed in PDAs.

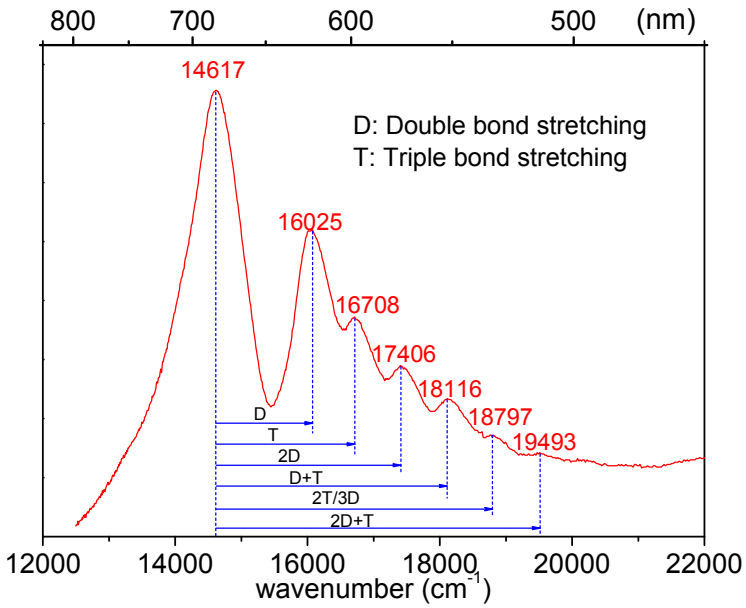

Figure 4.7. UV/Vis absorption spectrum of **10·PIDA** co-crystals, plotted as a function of wavenumber.

4.4. Polymerization in Aqueous Suspensions

To investigate the polymerization process, we examined the spectroscopic changes in water suspensions of the **10·1** co-crystals (Figure 4.8). Co-crystals of monomer **1** and host **10** can be dispersed into water to form quasi-homogeneous microcrystalline suspensions. The blue curve in Figure 4.8A shows the absorption spectrum of the suspension formed when blue crystals made with host **10**, determined by Raman spectroscopy (Figure 4.4) to contain primarily monomer, were dispersed in water. The major absorption peak at 650 nm and the vibrational satellite at 594 nm suggest the presence of oligomers or polymer chains, dilute in a monomer crystal matrix at a mole fraction that cannot be detected by X-ray diffraction or NMR. The blue suspension turns darker in color after 3 days at room temperature (Figure 4.8B) and the two major absorption peaks shift to 679 and 621 nm. These changes indicate an increase in the effective conjugation length of the polymer, as the reaction progresses within the microcrystalline particles. After 3 more days, the absorption spectrum of the suspension shows a maximum absorption peak at 689

nm and a clearly resolved vibronic progression (Figure 4.8C). The excellent match between the absorption spectra of the water suspension and solid crystals indicates complete topochemical polymerization within the suspended particles.

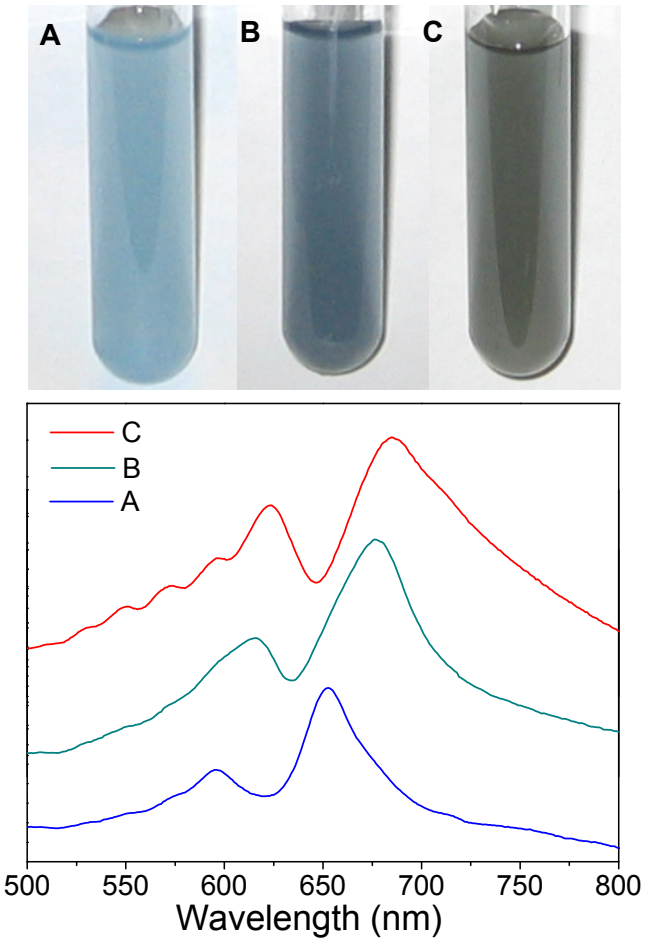

Figure 4.8. Absorption spectroscopic change of a water suspension of co-crystals made with host **10**. A: Blue **10·1** co-crystals dispersed in water; B: Water suspension A turns dark blue after 3 days at room temperature; C: Suspension A appears dark gray after 6 days at room temperature.

Formation of these water suspensions, before polymerization, can also be used to control the size distribution of the resulting polymer cocrystals.[105,106,107] TEM images of the micron-sized monomer co-crystals demonstrate that the particle size decreases as the sonication time

increases. Figure 4.9 indicates the size distribution of the particles, based on a statistical comparison of over 100 particles for each. When blue **10·1** co-crystals are initially dispersed in water by sonication, individual particles exceed the TEM dimensions. After 30 min of sonication, the co-crystals are broken into particles with average diameters of 5 μ. Further sonication results in smaller size and a finer dispersion of the particles. For example, after 120 min of sonication, most particles have diameters of approximately 2 μ, dispersed more evenly throughout the suspension.

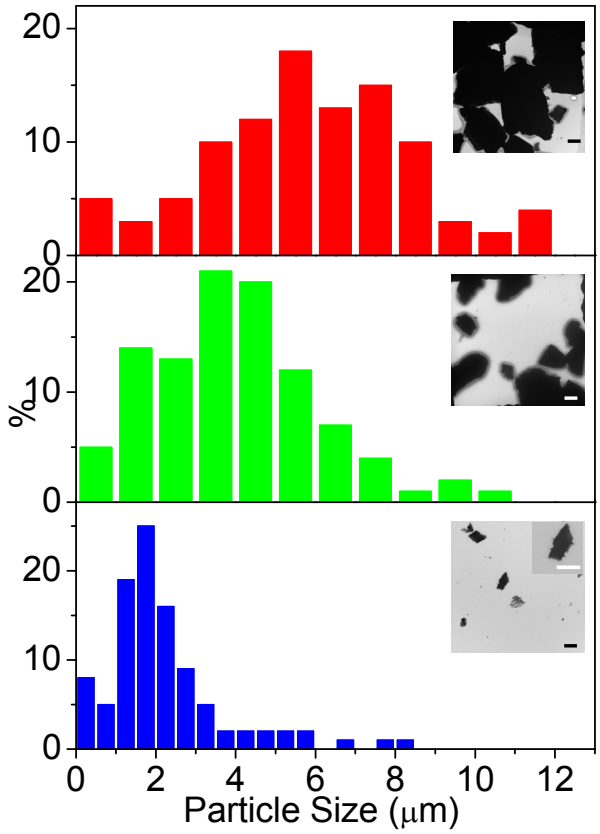

Figure 4.9. Size distributions of microcrystalline particles obtained by dispersing **10·1** co-crystals in water via sonication over varying times. Red: 30 min; Green: 60 min; Blue: 120 min. Insets are typical SEM images of the particles after the corresponding treatment (Scale bars are 2 μ).

In general cases, the topochemical polymerization of a poly(diacetylene) in an optimal crystalline lattice has been shown to proceed quantitatively, spanning the length of each microcrystal.[108,109] In the single crystal shown in Figure 4.10, poly(diacetylene) is formed in a single-crystal-to-single-crystal transformation, with polymer chains reaching both ends of the single crystal. The monomer crystals can be separated into smaller particles with different sizes, due to the relatively weaker noncovalent interaction between monomers. A good method to break the monomer crystals is ultra-sonicating the crystals as a suspension in a non-solvent medium such as water. The particle size can be controlled by changing the power and time of sonication, as shown in Figure 4.9. Because the crystal size is expected to be directly related to the resulting polymer length, this sonication provides a route to control the molecular weight distribution of the polymer in general.

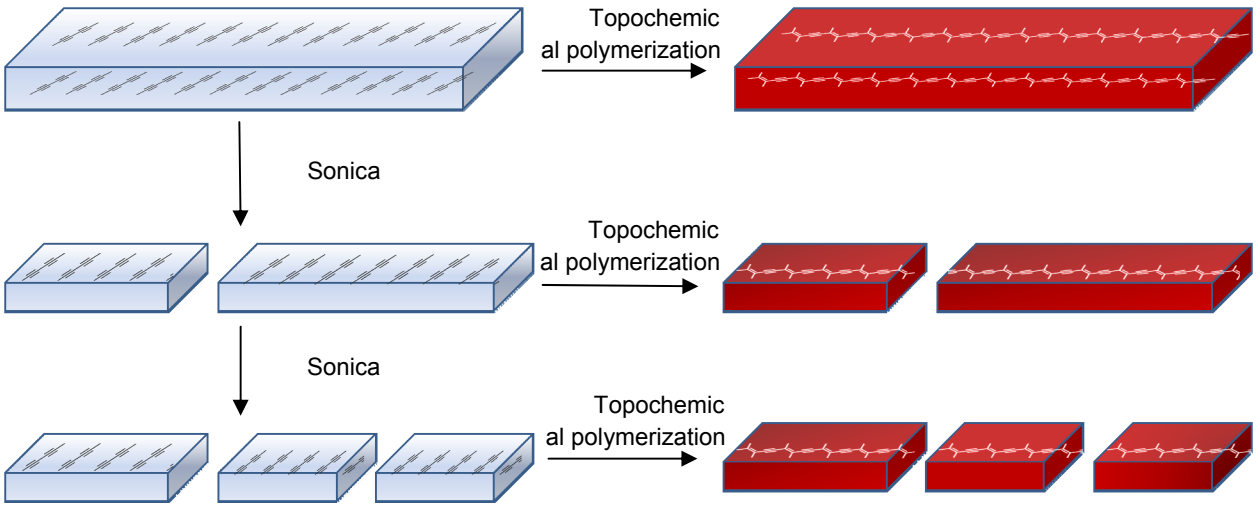

Figure 4.10. A schematic representation of controlling the molecular weight of poly(diacetylene) by controlling its particle size.

4.5. Conclusion

In addition to single-crystal X-ray diffraction, we have completed characterized the PIDA co-crystals and their polymerization procedure by ^{13}C MAS NMR, Raman, and electron absorption spectroscopy. We have also investigated using the size of microcrystalline co-crystals to control the molecular weight of the desired polymers. In addition, PIDA can be isolated from its co-crystal matrix for further study. In Chapter 5, we will describe this work in detail.

4.6. Experimental details

Solid-state ^{13}C Magic-Angle-Spinning NMR (MAS-NMR): All MAS-NMR spectra were measured by Christopher Wilhelm taken at room temperature using a Varian Infinity Plus 360 NMR spectrometer, with a 4 mm double resonance probe and zirconia rotor. The probe was tuned to 90.5 MHz for ^{13}C and 360.0 MHz for ^{1}H. The ^{13}C MAS-NMR spectra were collected using a CP RAMP pulse program with a contact time of 2 ms and a pulse delay of 2 s. The number of steps in the CP RAMP ranged from 8-12 and the amplitude step size ranged from 0.001 to 0.01, with a typical ^{1}H decoupling amplitude of 83 kHz. These parameters lead to an X channel amplitude range of 0.3100-0.4000. Over 1000 scans were acquired. All isotropic peaks were first identified by obtaining spectra with magic-angle spinning frequencies of both 6 and 8 kHz, in addition to the spectra presented here, which were measured at a frequency of 15 kHz.

Raman. Raman spectroscopy was performed using a Thermo Nicolet Almega dispersive Raman spectrometer coupled with an infinity corrected, confocal design microscope. The spectrometer uses a 785-nm class I laser, and the data were collected in the reflection mode of the microscope at a slit width of 25 μm. The data were analyzed using the Omnic software suite (Nicolet, USA).

Electron absorption spectroscopy: The electronic absorption spectra of solid samples were collected using a Shimadzu UV-2550 Spectrophotometer, scanning from 900 nm to 200 nm with a resolution of 0.5 nm. Crystallization dishes containing layers of crystals were put directly in the spectrophotometer with the beam penetrating to the center of the crystal layer. The spectra of suspensions were collected using a Cary-100 UV/Visible Scan Spectrophotometer, scanning from 900 nm to 200 nm with a resolution of 1 nm.

Chapter 5. Isolation of PIDA

The gold **10·PIDA** co-crystals can be dispersed in water (Figure 5.1A) or organic solvents such as methanol, THF or chloroform. The host oxalamide **10** is insoluble in water, but much more soluble in organic solvents. After extensive sonication and rinsing, these solvents give a clear blue suspension (Figure 5.1 B). The blue suspensions start out transparent, but begin to show visible fibers after minutes or hours without sonication (Figure 5.1 C). These fibers are PIDA aggregates, and this chapter discusses studies of these aggregates.

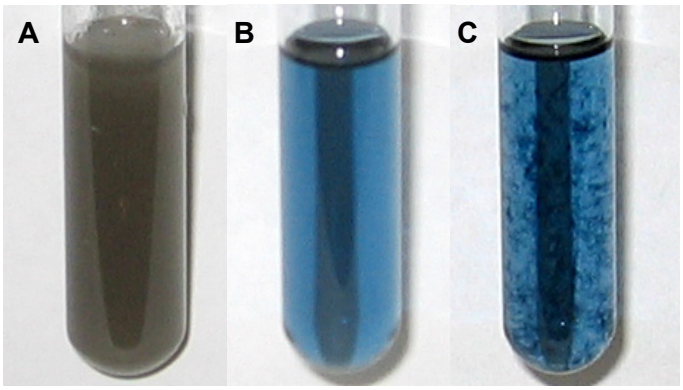

Figure 5.1. Suspensions and aggregates of PIDA. A: Gold **10·PIDA** co-crystals dispersed in water; B: Suspension of PIDA in THF; C: Suspension B, after 2 h at room temperature, with visible aggregation.

5.1. UV/vis absorption change of PIDA suspensions

The color change in PIDA suspensions, and the subsequent aggregation of the polymer, can be followed by UV-Vis absorption spectroscopy. Figure 5.2 shows the absorption spectra of several different suspensions, each prepared using gold co-crystals of fully polymerized PIDA and host **10**. The red spectrum was measured using an aqueous suspension, such as that pictured in Figure 5.1A. This spectrum is indistinguishable from the previously measured spectrum of gold **10·PIDA** co-crystals in the solid state (Figure 4.7). If the gold **10·PIDA** co-crystals are dispersed in an organic solvent such as methanol, THF, or chloroform, the spectrum quickly takes on a different appearance. As shown in the brown curve in Figure 5.2, the initial spectrum

upon forming the suspension in THF (or the other organic solvents) includes a new broad shoulder at about 750 nm, and a simultaneous broadening of the shorter-wavelength vibronic satellites. Subjecting the suspension to centrifuge, decanting the supernatant layer, and redispersing in fresh solvent by sonication further wash away the host. After multiple cycles of the operation, the UV/Vis spectrum stabilizes as the blue curve in Figure 5.2, losing all vibrational definition, and the long-wavelength absorption becoming more prominent. When the UV/Vis absorption spectrum stops changing, the suspension is fully depleted of host **10** by this extensive rinsing procedure. This PIDA suspension has been characterized by Raman, FTIR, MAS NMR and will be described in details in Section 5.2.

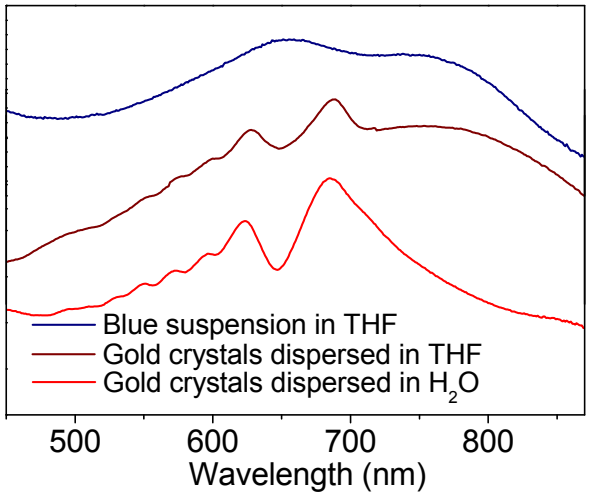

Figure 5.2. UV/Vis absorption spectra of suspensions of gold color **10·PIDA** co-crystals. Red: Aqueous suspension of **10·PIDA** co-crystals, as pictured in Figure 5.1A; Brown: **10·PIDA** co-crystals immediately after dispersing in THF; Blue: PIDA suspension in THF, after the extensive rinsing procedure until the spectrum stabilized.

To test the stability of these suspensions, we examined the UV/Vis absorption behavior upon dilution of the suspensions. Figure 5.3 shows the UV/Vis spectrum of the initial host-depleted suspension, as well as the spectra after successive dilution. The linear relationship between the absorption at multiple wavelengths (570, 665, and 738 nm, respectively) and relative

concentration indicates that the suspensions obey Beer's Law (inset, Figure 5.3), suggesting that the aggregates are not in dynamic equilibrium under these conditions. However, high-speed centrifugation (10,000 rpm, 1h) leads to removal of the absorbing particles, confirming that the blue sample is a suspension, rather than a true solution.

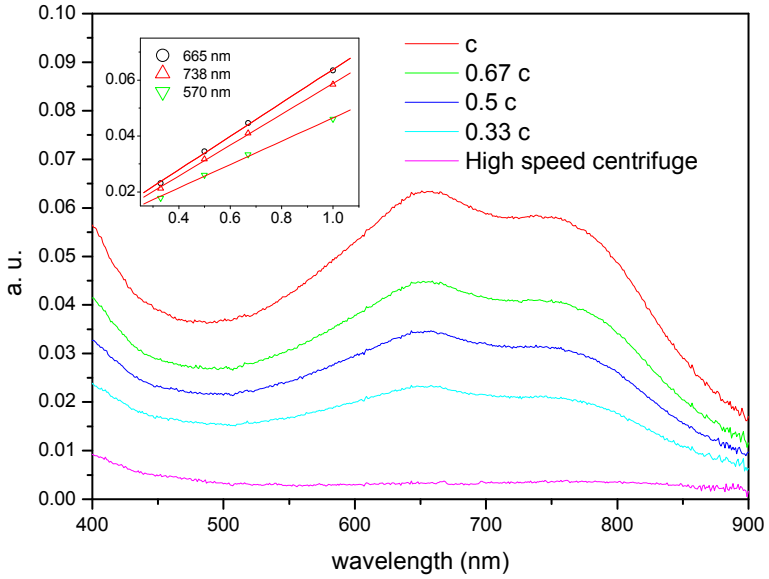

Figure 5.3. Absorption spectra of PIDA/THF system after high-speed centrifuge.

The appearance of the absorbance at longer wavelength can be attributed to a new lower-energy exciton generated either by increase of conjugation length or inter-chain aggregation. We do not have complete X-ray diffraction data on the **10·PIDA** co-crystals, but we can determine unambiguously that the polymer backbone is fully planar from the solved iodine atoms positions. In addition, other spectroscopic studies (Raman and MAS-NMR, described in Section 5.2) indicate that the polymer in these crystals is indistinguishable from the material in the **8·PIDA** co-crystals. Thus, it seems most likely that the UV/Vis spectrum of the gold **10·PIDA** co-crystals, with its λ_{max} at approximately 690 nm, represents the polymer in a completely planar

conformation. We believe inter-chain interactions are the most reasonable explanation of the observed low-energy absorption.

5.2. Characterizing obtained PIDA fibers

After obtaining host-depleted PIDA suspensions, as described in Section 5.1, the polymer in the suspension can be further characterized by transmission electron microscopy (TEM). TEM images of drop-casted samples revealed that the morphology of PIDA changes from flaked co-crystals to filaments, the diameter of which can be as low as 50 nm, as shown in Figure 5.4.

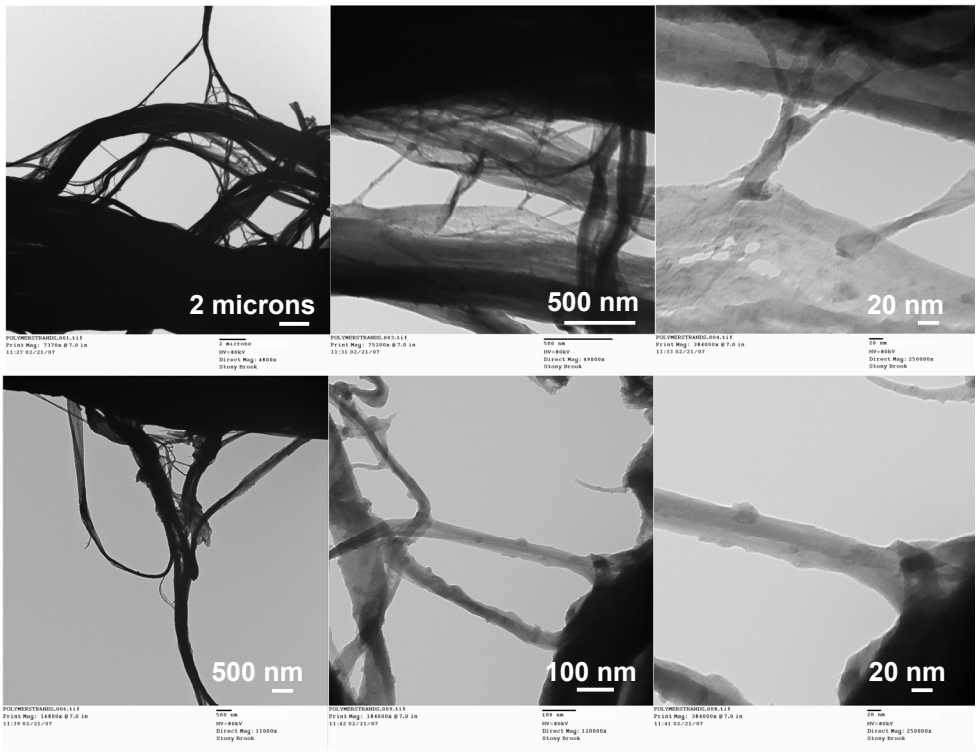

Figure 5.4. TEM images of isolated PIDA fibers.

Attempts to characterize these PIDA fibers by high resolution (HR) TEM, with the help of Dr. Karren L. More at Oak Ridge National Laboratory, failed to determine their nano-structures. Figure 5.5 exhibits the HR TEM image of PIDA fibers and electron diffraction on selected area.

There is no long-range order exists in the TEM image and electron diffraction results indicate that these fibers are amorphous on a nano-scale.

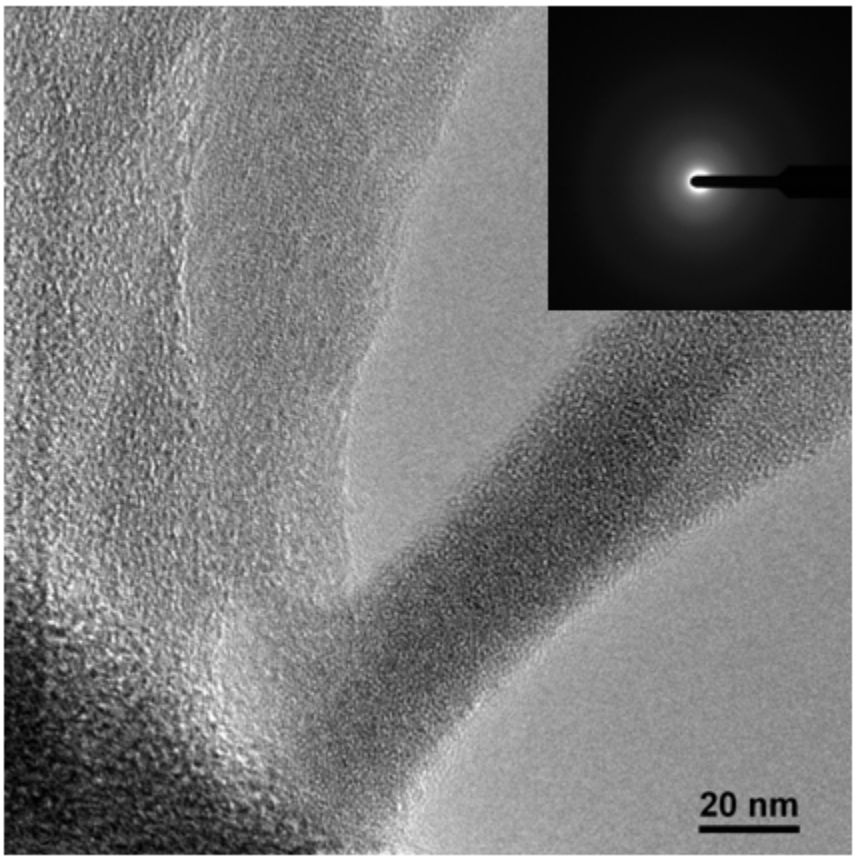

Figure 5.5. High-resolution TEM image of PIDA fibers and electron diffraction of selected area. Inset is the electron diffraction of the fibers.

When the PIDA fibers are dispersed in organic solvents, the suspensions appear blue. By high speed centrifuge, the PIDA fibers condense at the bottom of the centrifuge tube, leaving supernatant as a clear layer on top. The supernatant appears light pink if using chloroform as solvent, and shows yellow if using methanol, caused by a small amount of dissociated iodine from PIDA. The solid mass of PIDA fibers condensed at the bottom of the centrifuge tube are soft rather than previous crystalline, but still remain metallic shiny and highly reflective under polarized light, as shown in Figure 5.6. Dispersing these solid mass back in organic solvents, such as methanol or chloroform, by sonication regenerates blue suspensions containing PIDA

fibers. *The isolated PIDA become explosive after removing all the solvents, and one should be very cautious when handling them.*

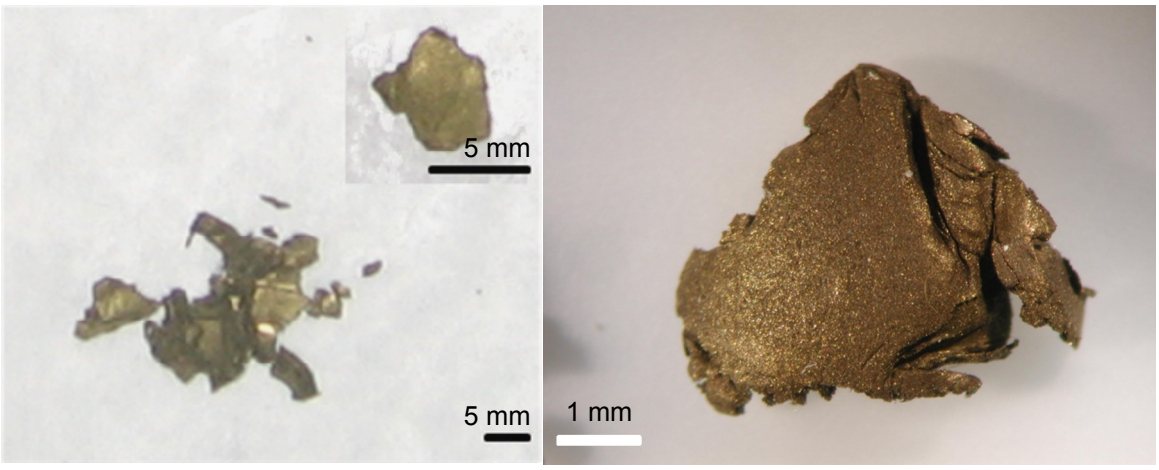

Figure 5.6. Optical microscopic image of isolated PIDA collected after centrifuge.

While the morphologies of PIDA co-crystals and PIDA fibers are different, their Raman spectra are very similar. Figure 5.7 exhibits the Raman spectra of PIDA fibers solid (shown in Figure 5.6), PIDA co-crystals and PIDA suspensions in THF. The comparison of these Raman spectra indicates that PIDA backbone survives during processing. The relatively lower Raman scattering intensity of isolated PIDA may be attributed to its amorphous morphology. In addition, it also decomposes under the laser power.

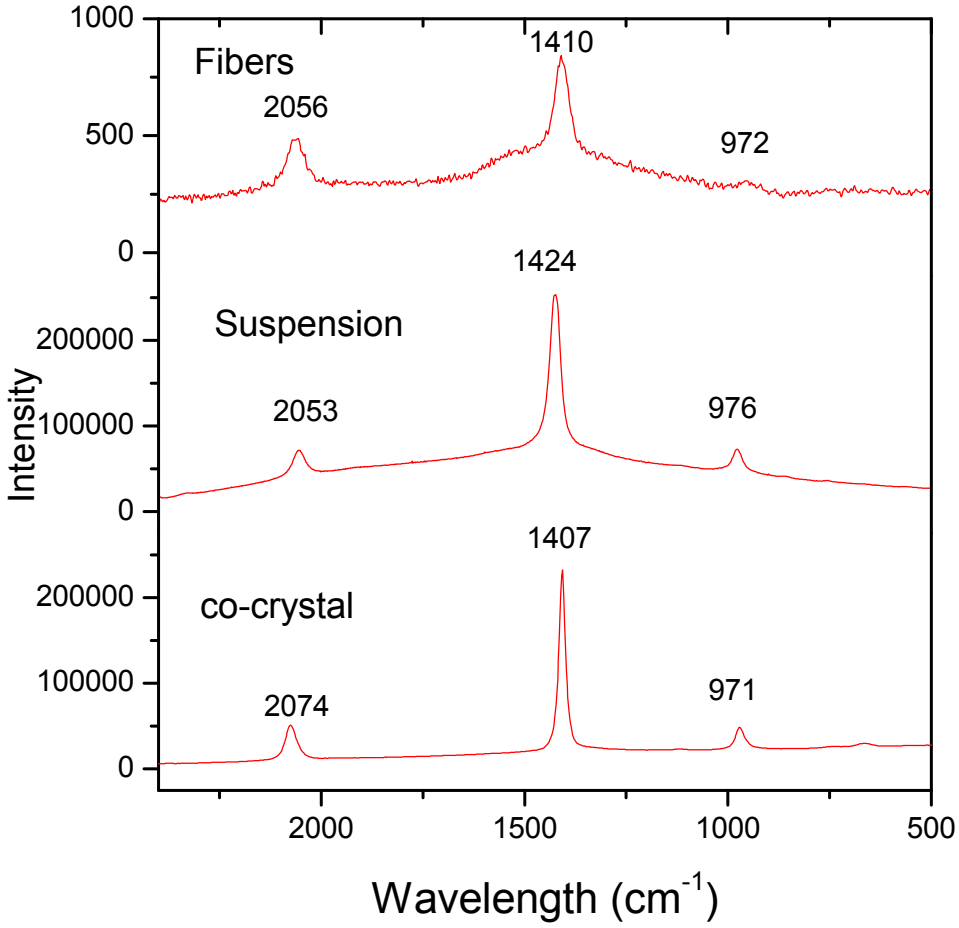

Figure 5.7. Raman spectra of PIDA fibers, PIDA suspensions in THF, and co-crystal **10·PIDA**.

To test whether the host compound has been fully removed from these sold PIDA samples, we turned to FTIR spectroscopy. PIDA is a very weak IR absorber, because of its symmetric, non-polar structure. In contrast, the host, which cannot be seen by Raman, is much more visible by IR spectroscopy. Figure 5.8 shows the FTIR spectra of co-crystal **10·PIDA** and of the solid PIDA samples shown in Figure 5.6. After the extensive rinsing procedure described in Section 5.1, all the peaks of the co-crystal attributed to host disappear. In particular the peaks at 1641 and 2239 cm^{-1}, which corresponds the C=O and C≡N stretches respectively, are no longer visible

after the isolation process, indicating that all the host molecules have been washed out by sonication and PIDA is isolated from the co-crystal matrix in the aggregate fibers.

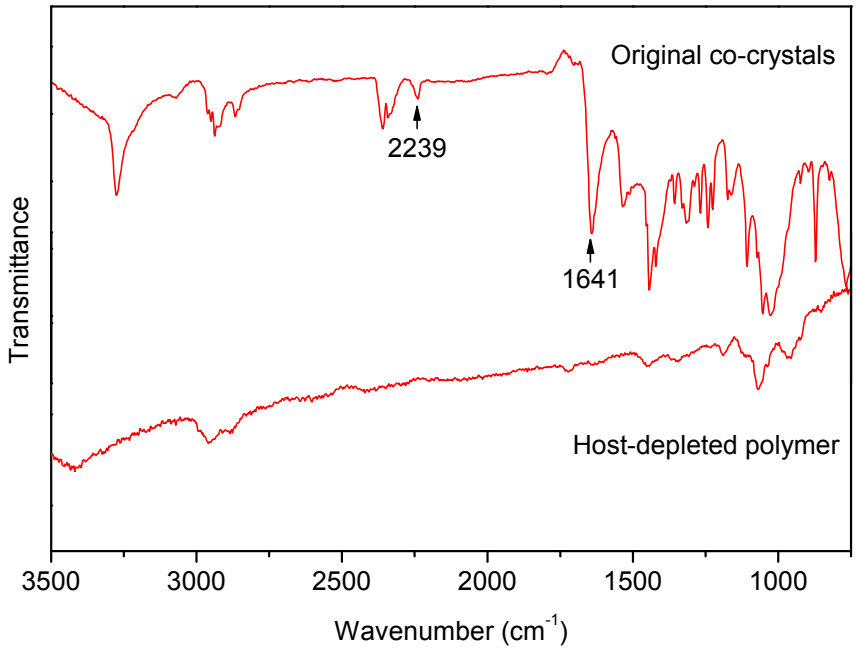

Figure 5.8. IR spectra of co-crystals **10·PIDA** and of the isolated polymer after extensively rinsing polymer co-crystals in organic solvents. The peaks at 2239 (C≡N) and 1641 (C=O) cm^{-1} are no longer visible in the lower spectrum.

Colleague Christopher Wilhelm has encountered many difficulties in attempts to obtain a ^{13}C MAS NMR of the isolated PIDA fibers. With no hydrogen atoms to help decrease the relaxation time, isolated PIDA gives very weak NMR signals. In addition, several attempts to load the sample into a rotor for MAS NMR experiments led to *explosion*. With great care, Wilhelm succeeded in obtaining the ^{13}C MAS NMR spectrum, which shows only the α-carbon and β-carbon of PIDA (Figure 5.9). There is no host carbon peaks in the spectrum, indicating that we have successfully prepared a fibrous material that contains only PIDA inside.

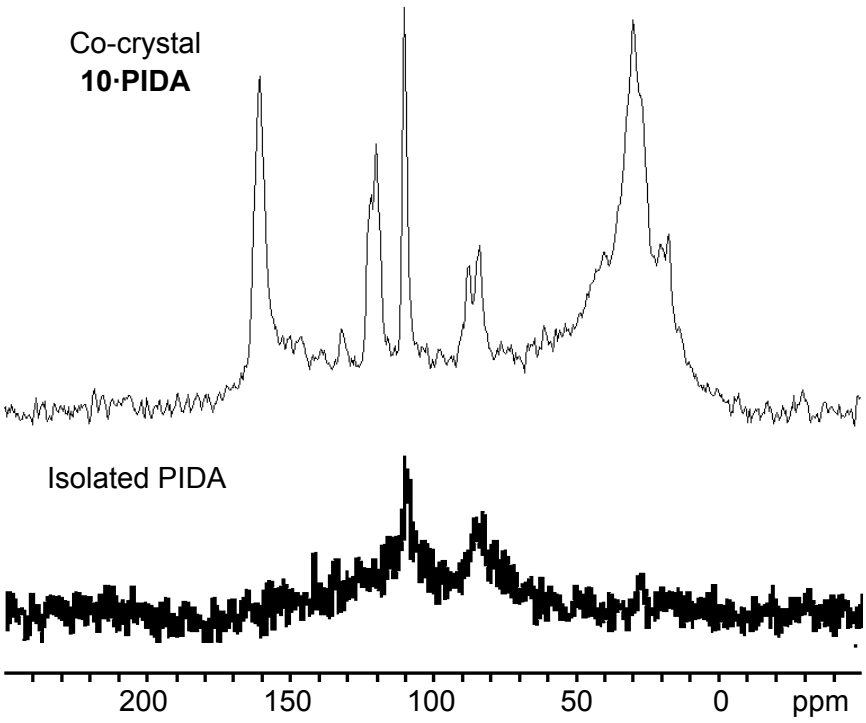

Figure 5.9. 13C MAS NMR spectra of co-crystal **10·PIDA** and isolated PIDA.

5.3. Identifying the alignments of PIDA within the nanofibers

High resolution TEM and electron diffraction, as shown in Figure 5.5, suggest that there is no ordered alignment of the polymer chains within PIDA fibers. However, these results may be affected by the fact that organic polymers are soft, and high-energy electron beams can destroy their nanostructure. To continue examining the alignment of PIDA within the nanofibers, we have used polarized Raman, in collaboration with Dr. David B. Geohegan at Oak Ridge National Laboratory, and powder X-ray diffraction, with the help of Dr. Peter Khalifah at Stony Brook.

Figure 5.10 shows the polarized Raman spectrum of the PIDA fibers. Compared with the regular Raman spectrum, it shows two new peaks, at 2388 cm^{-1} and 2817 cm^{-1}, in addition to previously well defined single-bond (S), double-bond (D), and triple-bond (T) stretching. The

energy of the peak at 2388 cm^{-1} is equal to the sum of the single-bond and double-bond peaks. The energy of the peak at 2817 cm^{-1} can be assigned as 2D.

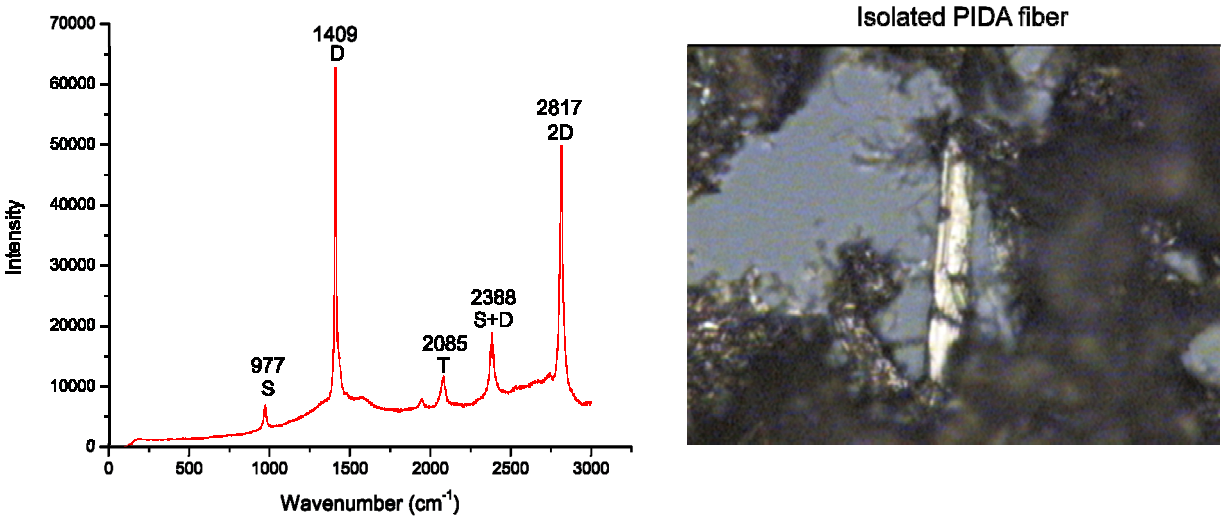

Figure 5.10. Polarized Raman spectrum of the isolated PIDA fiber shown at right.

Raman polarization studies have been used to study the orientation of PIDA fibers, as shown in Figure 5.11. In Figure 5.11 A, the fiber was aligned perpendicular to the polarization direction of the laser beam. The scattering intensity of the fiber is relatively lower. When the fiber was aligned parallel to the Raman polarization, shown in Figure 5.11 B, the scattering intensity increased tremendously. The ratio of the intensities of each peak (e.g., I_S / I_D) changed significantly after changing the direction of fibers, indicating that the fiber is highly anisotropic and the polymers within the fiber are oriented uniaxially.[110-112]

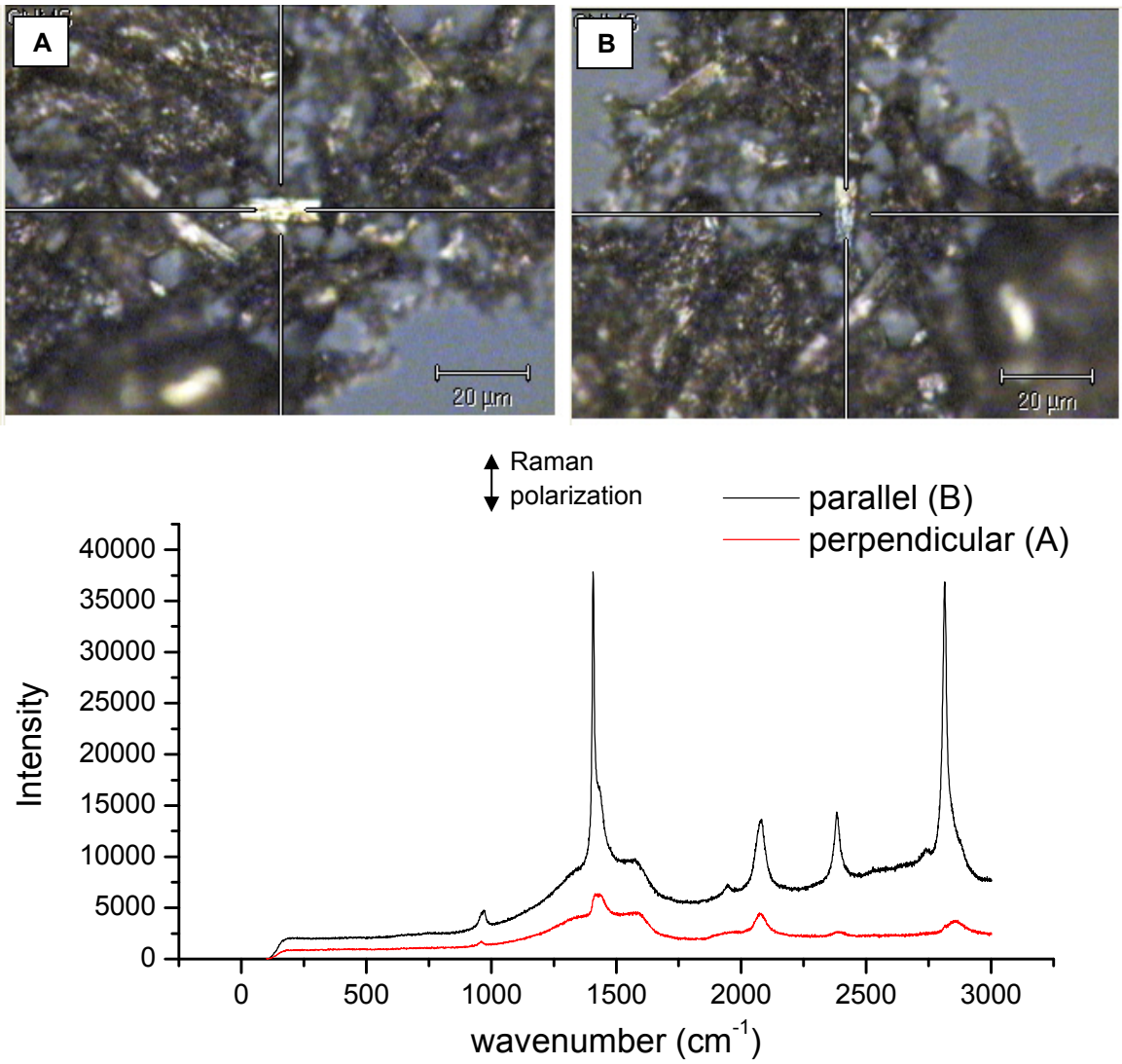

Figure 5.11. Polarized Raman measurements of a PIDA fiber in geometries perpendicular (A) and parallel (B) to Raman polarization.

Raman mapping can further characterize the orientation and morphology of the PIDA fibers. As shown in Figure 5.12A, the selected area on a PIDA fiber was divided into 334 pixels, on each of which a polarized Raman spectrum was collected. Using a chosen scale on the Raman spectrum, as shown in Figure 5.19D, the Raman scattering intensities of every pixeled spectrum was represented by different colors, forming a Raman mapping of selected area in Figure 5.19A.

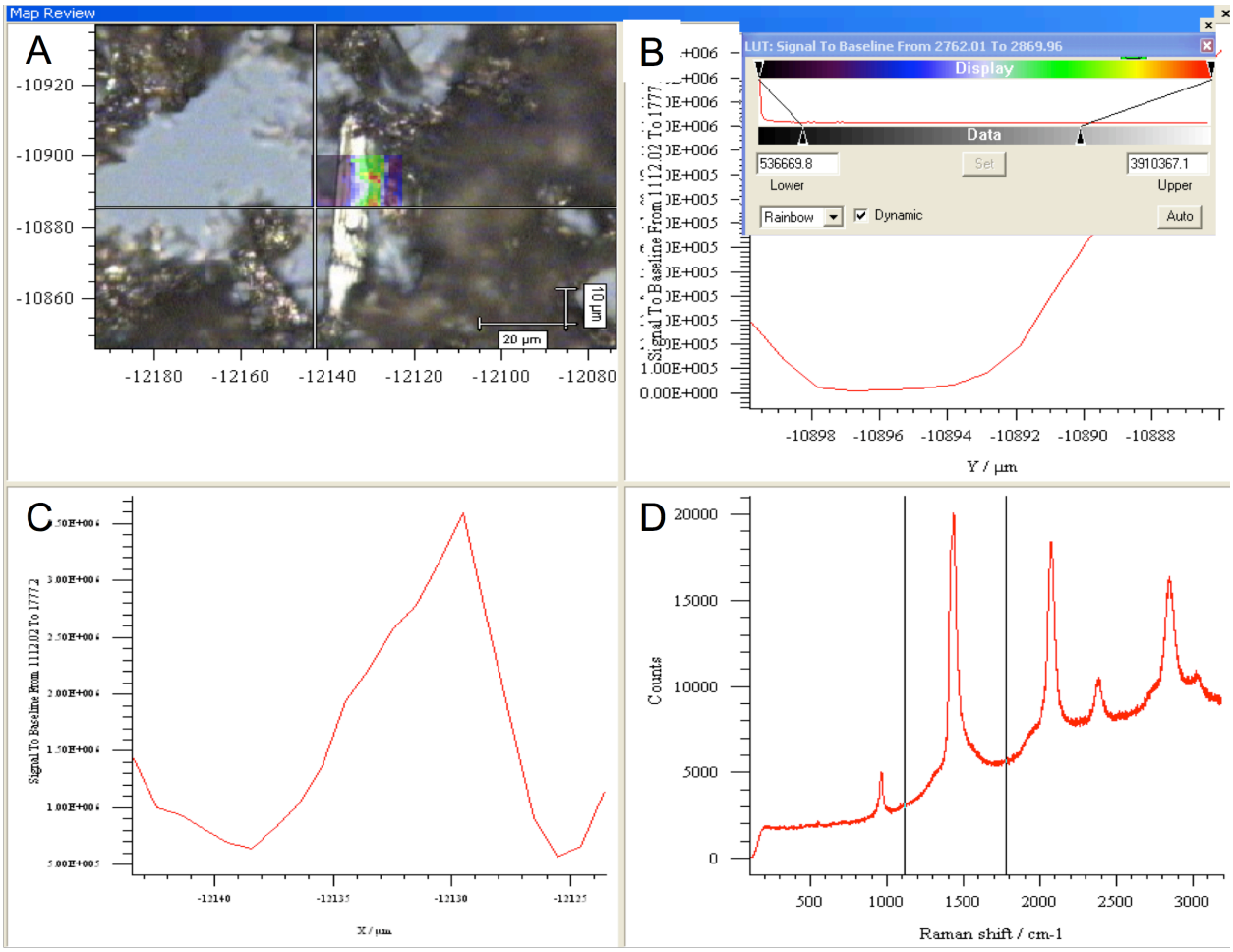

Figure 5.12. Raman mapping of selected area on a PIDA fiber, referenced by D band at 1407 cm^{-1}. A: Raman scattering intensity at each point represented by the color of that pixel; B: the scale of the scattering intensity represented by different colors; C: Raman scattering intensity along the x-axis of the area; D: The referenced frequency range (D band at 1407 cm^{-1}).

Figure 5.12 illustrates the Raman mapping of selected area on a PIDA fiber, using the D band at 1407 cm^{-1} as reference. Figure 5.13 illustrates the Raman mapping of the same area, reference by the S band at 977 cm^{-1}. Both mapping clearly indicate the homogeneity of the PIDA fiber containing highly oriented polymer chains.

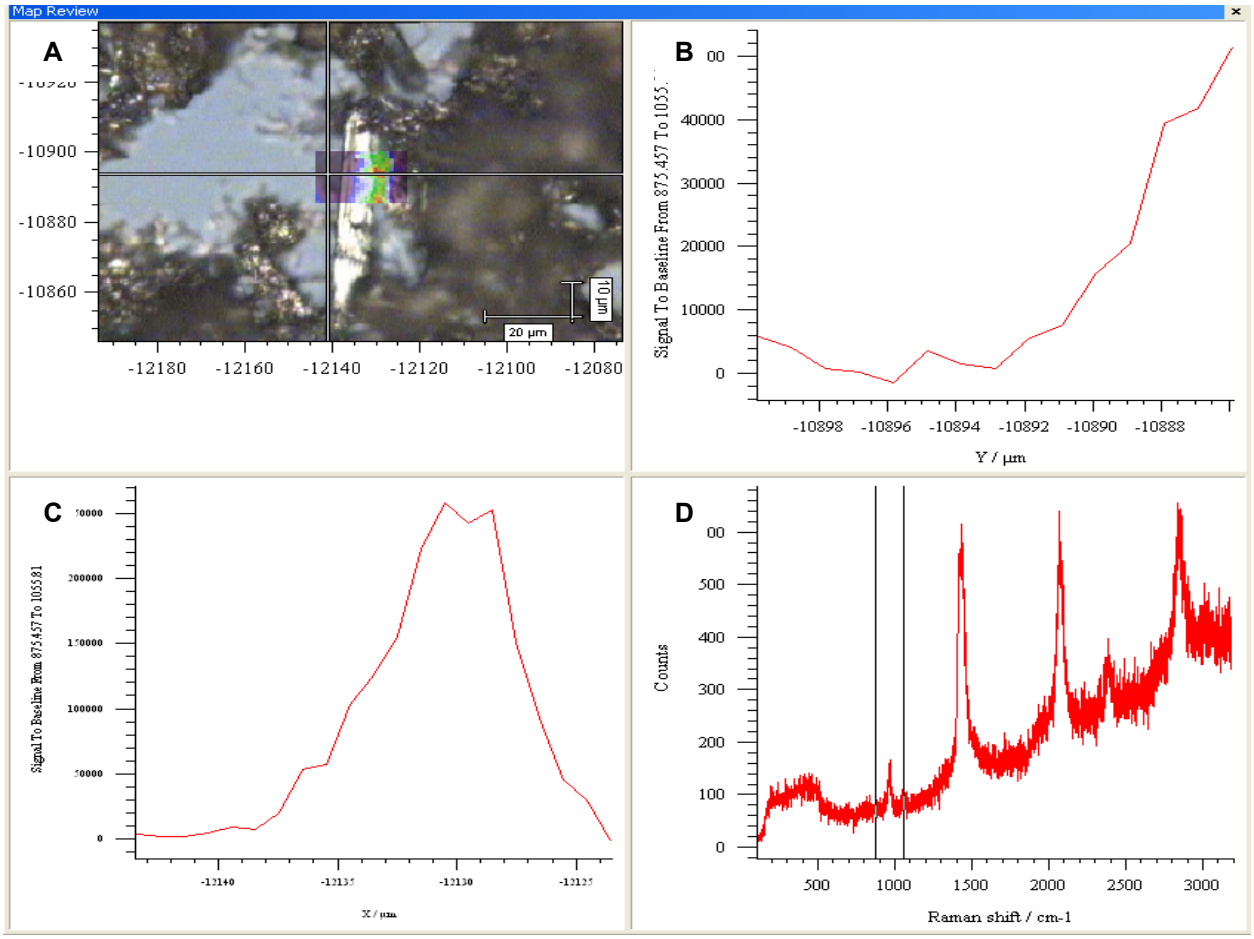

Figure 5.13. Raman mapping of selected area on a PIDA fiber, referenced by S band at 977 cm^{-1}. A: Raman scattering intensity at each point represented by the color of that pixel; B: Raman scattering intensity distribution along the y-axis; C: Raman scattering intensity distribution along the x-axis; D: The referenced frequency range (S band at 977 cm^{-1}).

The above polarized Raman measurements indicate that PIDA fibers are uniaxial filaments. We would like to understand how the parallel polymer chains are packed within these fibers. Compared with its monomer diiodobutadiyne and other polyynes, PIDA fibers are relatively more stable at room temperature unless being pressured. The only difference between PIDA and polyyne is that PIDA can be considered as an addition product of iodine to every other triple bond of polyyne. The big Van Der Waal's radius of iodine atoms should play an important role in keeping carbon backbones away from interactions. We can explore the packing style of

adjacent polymer chains by powder X-ray diffraction, the result of which is shown in Figure 5.14.

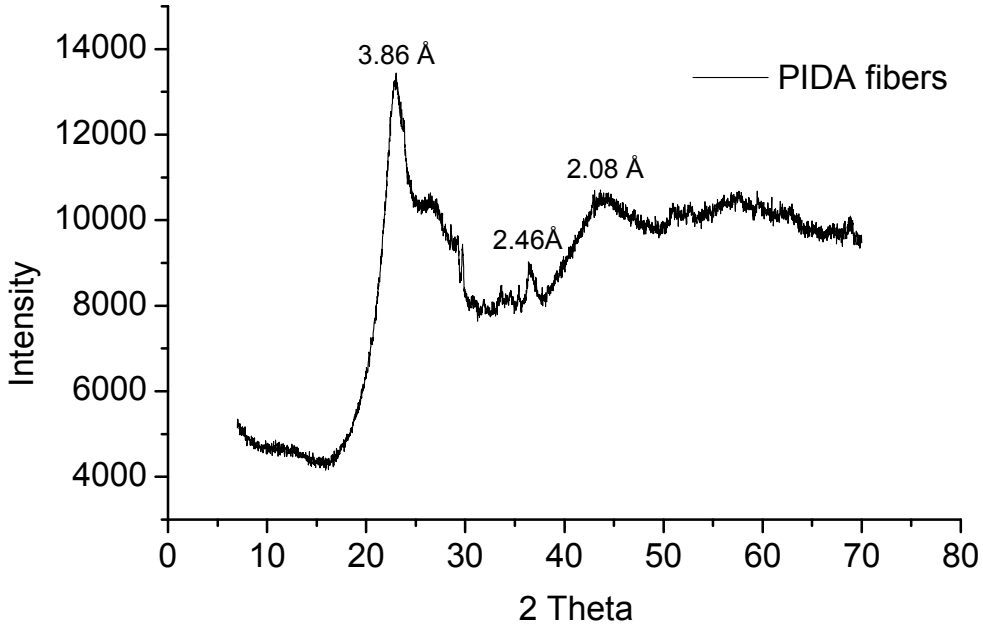

Figure 5.14. Powder X-ray diffraction of isolated PIDA fibers.

Powder X-ray diffraction of isolated PIDA fibers shows a major peak corresponding to a d-spacing of 3.86 Å. Since iodine has a much larger atomic number than carbon, the spectrum mainly results from the diffraction of iodine atoms in the polymer. The powder X-ray diffraction result suggests that there is some periodicity within the isolated PIDA fibers. The PIDA chains within the aggregates are disordered on a macroscopic scale. However, the PIDA aggregates may contain large numbers of microcrystalline or nanocrystalline grains composed of parallel stacked polymers. In a crystalline grain, these parallel stacked polymers enable the material to diffract. In addition, they may be responsible for the electronic excitons that are observed in the visible absorption spectrum of the PIDA suspensions. Figure 5.15 lists several hypothetical stacking modes within the PIDA fibers based on the diffraction results.

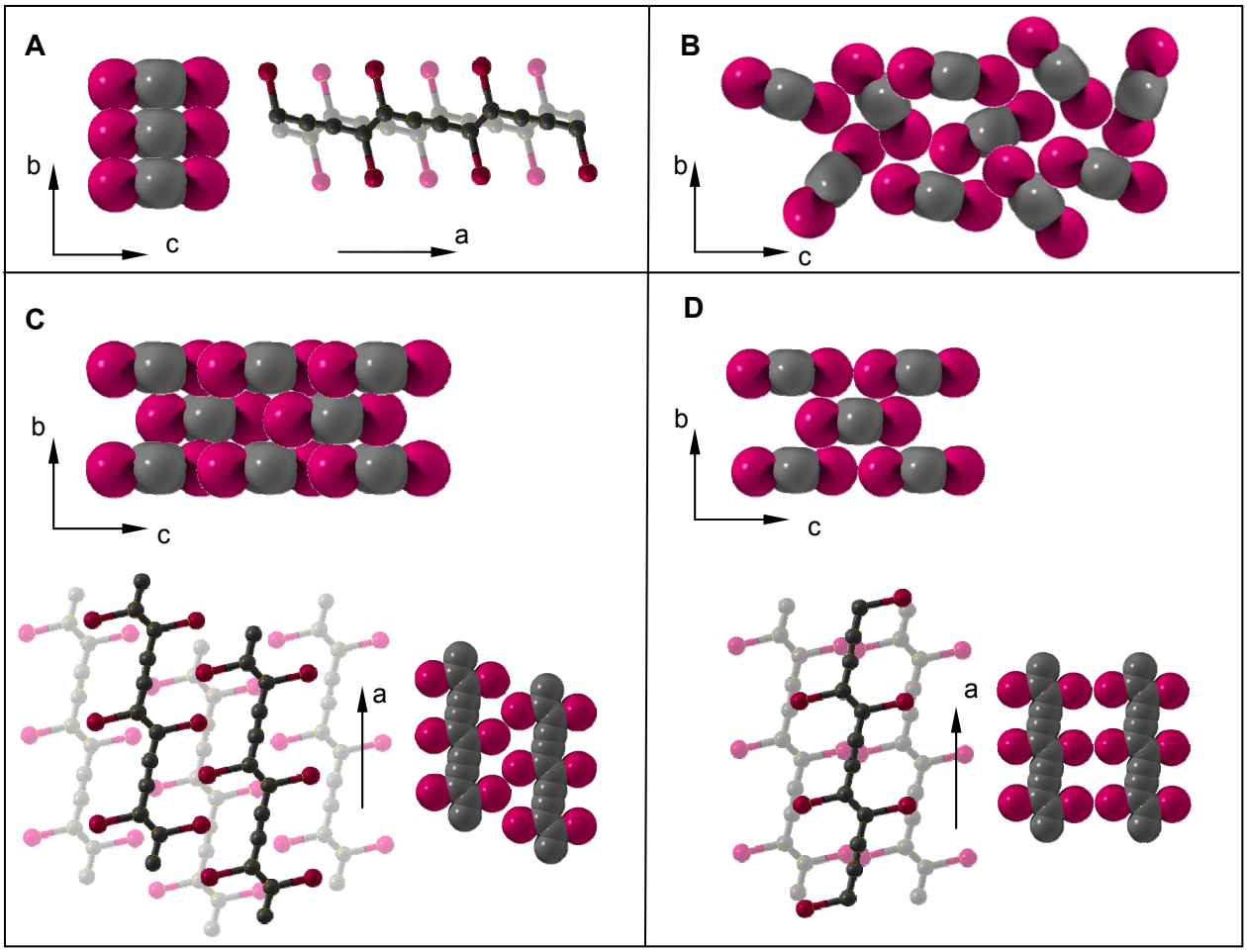

Figure 5.15. Hypothetical stacking modes within PIDA aggregates. (a axis is the PIDA chain direction; b, c axes depict the cross section of parallel stacked polymer chains)

Among the hypothetical modes listed in Figure 5.15, structure A is a face-to-face stacking mode, i.e., polymer chains pack according to π-π interactions between backbones. In mode A, the iodine substituents are staggered so that the polymer backbones contact each other and electrons can transfer through overlapped π orbitals. The d-spacing should be around 3.5 Å. Mode A is consistent with other conjugated polymers like poly(thiophene)[113] and poly(phenylene-ethylene).[114] However, the backbones of these polymers are aromatic and stable when taking this stacking. PIDA is composed of alternating double-triple bonds, which should be very reactive when two adjacent backbones are as close as 3.5 Å. In mode B, adjacent chains

contact each other randomly, dominated by the interaction between iodine and backbone. The periodicity comes mainly from the Van der Waal's radius of iodine ~ 4.0 Å.[115]

Structures C and D are face-centered stacks, i.e., polymer chains packed graphite-like through the interaction between electron deficient iodine atoms and the electron rich backbone. Their d-spacings should be between 3.5 Å and 4.0 Å, consistent with the peaks in the powder XRD spectrum. However, the π orbitals of individual polymer strand are too far away from one another and cannot account for the observed visible absorption shoulder. The interaction of the iodine atoms with the π-conjugated backbone is not fully understand, but may also play a role in formation of an exciton.

In addition, using a 532 nm laser, the Raman spectrum of isolated PIDA shows a completely different spectrum consistent with sp^2-hybrized carbon, as shown in Figure 5.16. Returning to irradiation at 785 nm, the Raman scattering signal does not revert to the previous observed signal for PIDA, but suggests the irreversible transformation of PIDA to graphitic carbon.

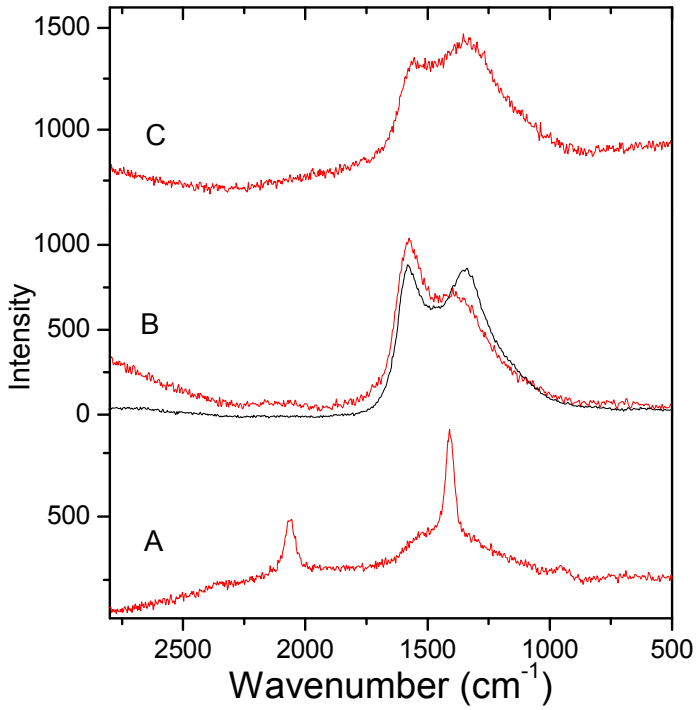

Figure 5.16. Raman spectra of isolated PIDA solids under different laser wavelengths. A: 785 nm; B: laser changed to 532 nm, and in comparison with the Raman of graphite (black line); C: laser returns to 785 nm. The detected area keeps unchanged during the whole experiment.

In comparison, the same experiment on **10·PIDA** co-crystals shows that the Raman spectrum reverts to the original but with a lower scattering intensity after the laser beam switch, shown in Figure 5.17, indicating that the PIDA structure survives with the protection of the host molecules. This observation further suggests that inter-chain reaction of PIDA strands occur upon irradiation at 532 nm to produce a cross-linked carbon-rich substance, a reaction which may be exothermic enough to drive formation o the lowest energy product, graphitic carbon.

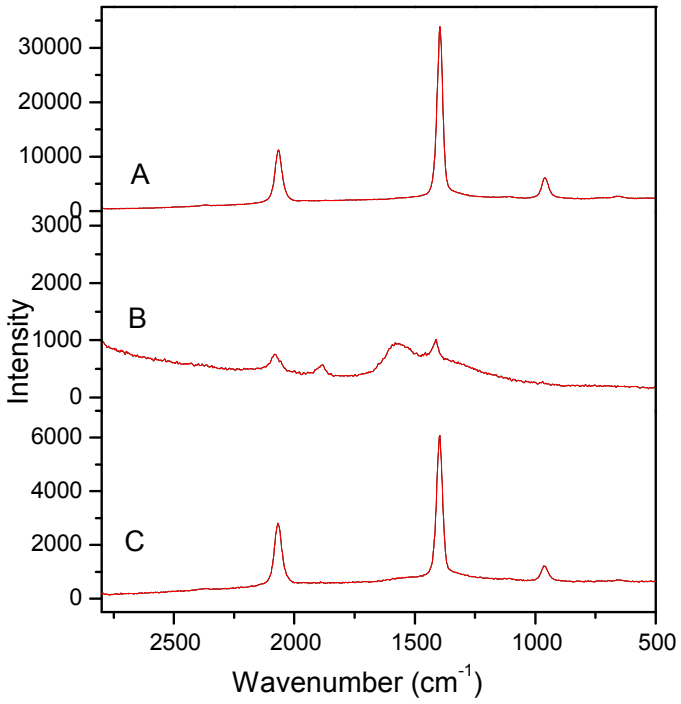

Figure 5.17. Raman spectra of **10·PIDA** co-crystals under different laser wavelengths. A: 785 nm; B: laser changed to 532 nm, and in comparison with the Raman of graphite (black line); C: laser returns to 785 nm. The detected area keeps unchanged during the whole experiment.

5.4.Thermal experiments on isolated PIDA

A very important property of poly(diacetylene)s is the ability to change color (mainly blue-red transitions) due to external stimulations, such as temperature. There are different views about the mechanism of the chromism, but a common explanation is the side-chain effect. The ordered side chains of the polydiacetylene help to keep the backbones in a planar conformation, with a maximal conjugation length, so that the polydiacetylene appears blue.[52] When the side chains become disordered as a result of external stimulations, like temperature, pH, the planar conformation of the backbone is destroyed, which leads to a shorter conjugation length and makes the PDA appear red. When the destruction to the order of side chain is slight and the side chains become ordered again, the chromism of the PDA is reversible; otherwise, if the side chain

can no longer reorder, this PDA chromism is irreversible. PIDA is an important test case for examining the source of this color change, because PIDA has no steric interactions from side chains.

To investigate the conformational change in PIDA upon changing thermal conditions, the absorption spectra of PIDA solution in THF at different temperatures from 25 ^{o}C to 50 ^{o}C were measured, as shown in Figure 5.18. The absorption spectrum almost remains unchanged, indicating that there is no conformational change in this range of temperature range.

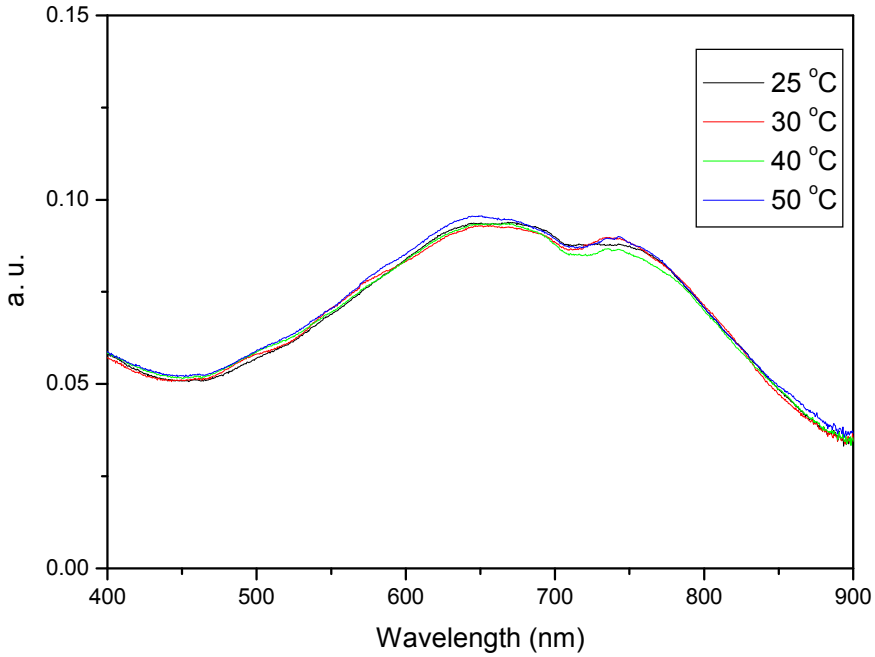

Figure 5.18. The absorption spectra of PIDA/HFIP in different temperature.

The temperature range that can be examined for PIDA suspensions is limited by the boiling point of the solvent. To further investigate the conformational change in PIDA at higher temperatures, a film of PIDA was prepared by drop-casting a dilute suspension of PIDA in methanol onto a glass slide. The maximum absorption peaks of the film are consistent with those of the suspension (Figure 5.19 A). The film was placed in a vacuum oven under Argon and

heated gradually. The film did not change color until it was heated up to 100 °C. However, when the temperature increased to 120 °C, the film experienced an irreversible color change to dark brown and no absorption peaks in the visible range were observed (Figure 5.19 B), indicating that the conjugated π-system was destroyed during heating.

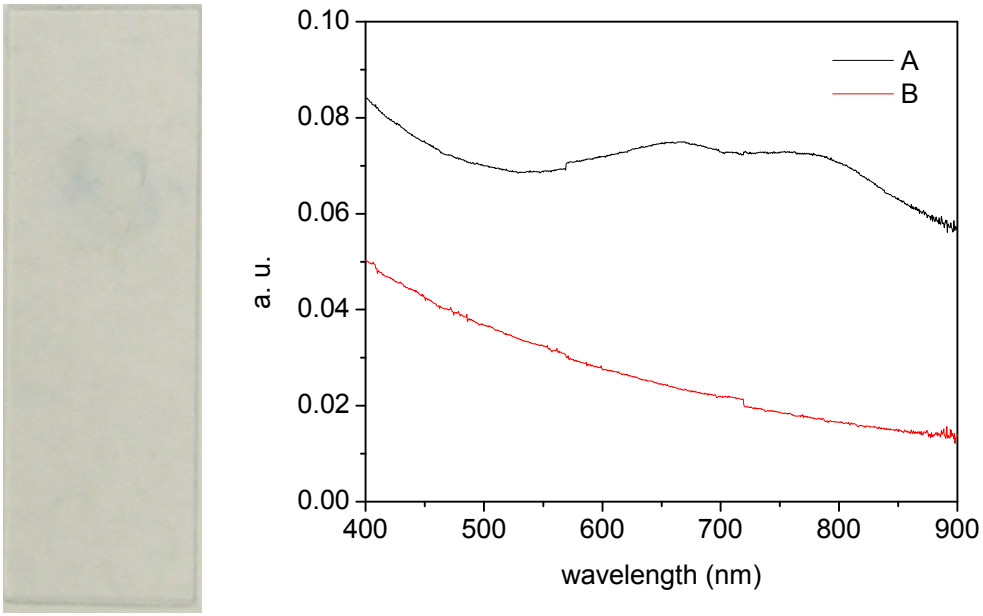

Figure 5.19. The absorption spectroscopic change of a PIDA film before (A) and after (B) heating up to 120 °C.

These experiments indicated that PIDA fibers decompose upon heating. To characterize the thermal stability and phase changes of PIDA, we have examined the polymer by thermogravimetric Analysis (TGA) and differential scanning calorimetry (DSC) of PIDA, as shown in Figure 5.20 and Figure 5.21.

TGA determines changes in sample weight in relation to changes in temperature. $T_{3\%}$ is defined as the temperature at which the weight loss is observed to be 3%, and is sometimes considered as the onset temperature for degradation of a polymer for comparative purpose.[116] As shown in Figure 5.18, $T_{3\%}$ of PIDA is 114.8 °C in air and 148.3 °C, both relative low among

polydiacetylenes.[116] Since the host was removed before measuring the TGA, this thermal behavior is attributed to PIDA. As a comparison, the TGA curve for the host **10** was also measured. Interestingly, the degradation of PIDA occurs in two stages. In the first stage (150-400 ^{o}C), the degradation occurs gradually, leaving a residue of about 20 % of the initial mass. This initial mass loss may represent thermal dissociation of iodine from the polymer as I_2, since PIDA contains approximately 80% iodine by mass with an empirical formula C_2I.

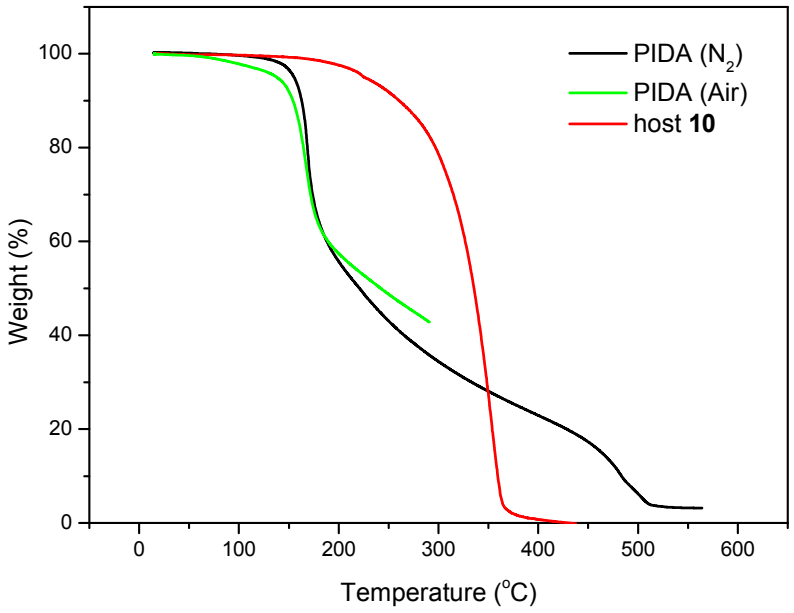

Figure 5.20. TGA of isolated PIDA under nitrogen and air.

DSC can be used to measure conformational transitions by recording the heat flux versus time or temperature. The DSC curves of PIDA in air and nitrogen are shown in Figure 5.21. There is no heat flux peak in the temperature range from room temperature to the degradation, indicating that no conformational change in the solid state of PIDA is detected by DSC before its degradation.

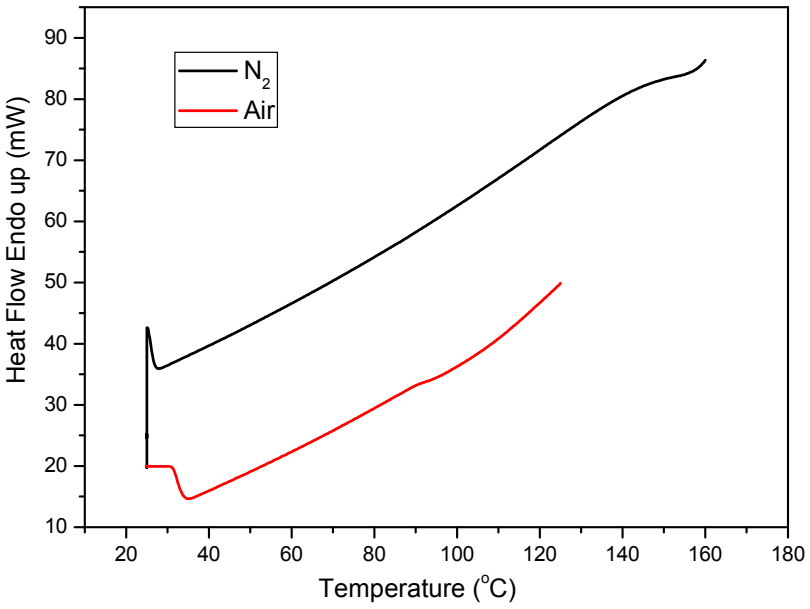

Figure 5.21. DSC of PIDA in the atmosphere of nitrogen and air.

Rather than conformational changes in PIDA backbone, the thermal treatment of isolated PIDA fibers induces dissociation of iodine from PIDA. The TGA results for isolated PIDA suggest that iodine starts to escape from the polymer when the temperature is above 100 ^{o}C. Above 500 ^{o}C, all of the iodine in PIDA is released, based bon the observed weight loss in the TGA. This result indicates that thermal treatment of PIDA could be a new method to prepare carbon or graphitic material.

In collaboration with Dr. David B. Geohegan at ORNL, PIDA fibers were annealed at 900 ^{o}C under argon atmosphere for 1 h. The resulting material remains shiny and fibrous in appearance, as characterized by the optical microscope image shown in Figure 5.22. High-resolution TEM images, taken by Dr. More at ORNL, reveal that the annealed material starts to form some short-range order, and energy dispersive spectroscopy (EDS) indicates that all iodine atoms have been released by the pyrolysis, as shown in Figure 5.23.

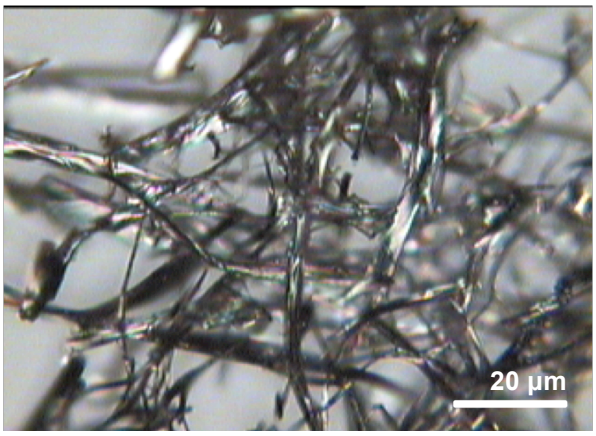

Figure 5.22. Optical microscopic image of annealed PIDA fibers.

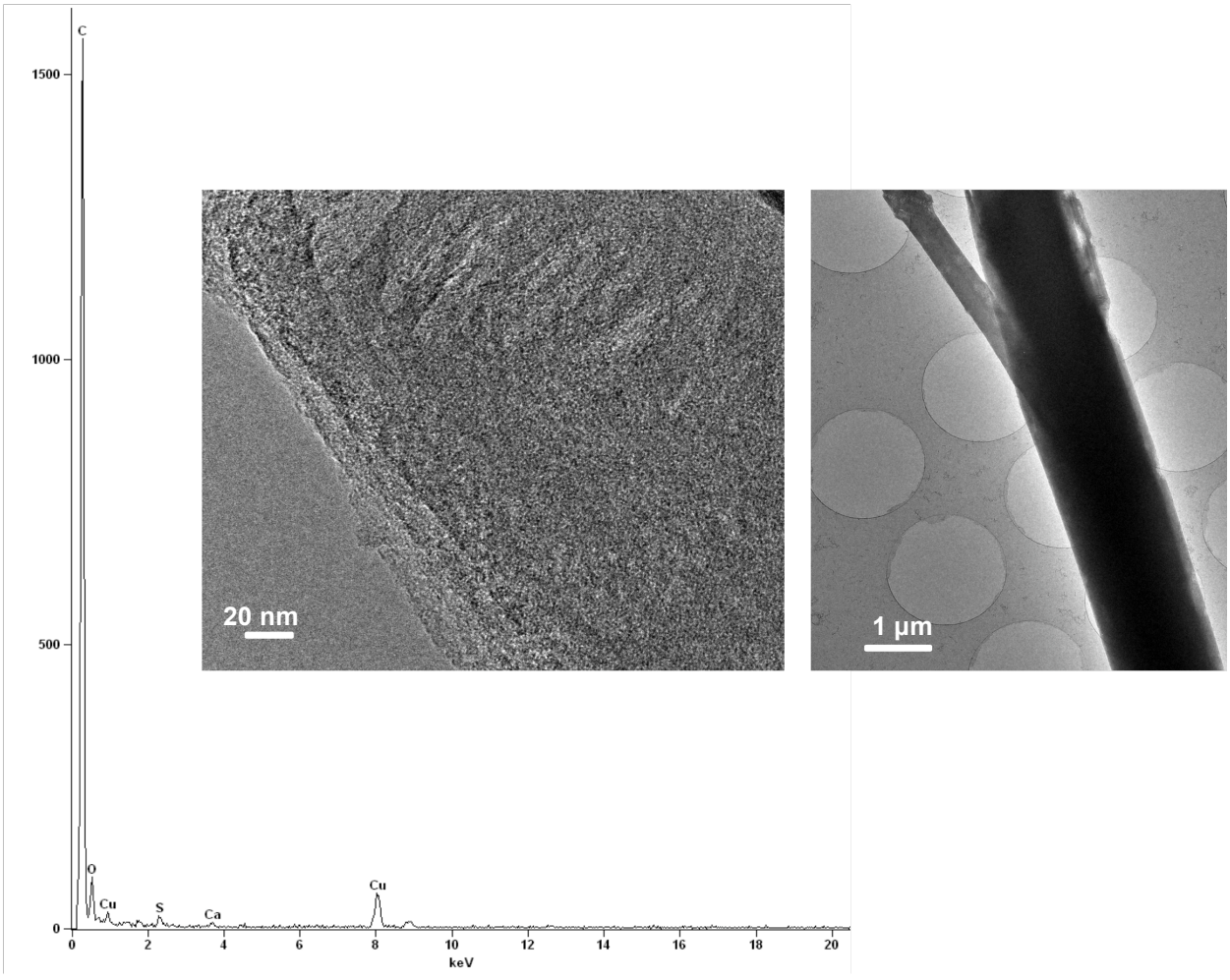

Figure 5.23. High-resolution TEM images of annealed PIDA fibers. The left plot is the EDS spectrum of selected area.

Polarized Raman measurements of the annealed PIDA fibers indicate that the material has been completely converted to all sp^2–hybridized carbon material. The peak at 1583 cm^{-1} is consistent with the graphitic carbon G band, and the broader peak centered around 1380 cm^{-1} corresponds to disordered sp^2–hybridized carbon. The polarized Raman spectra of an annealed PIDA fiber, taken with the fiber parallel and perpendicular to the Raman polarization, respectively, are almost identical, indicating that the new material becomes isotropic upon annealing, as shown in Figure 5.24.

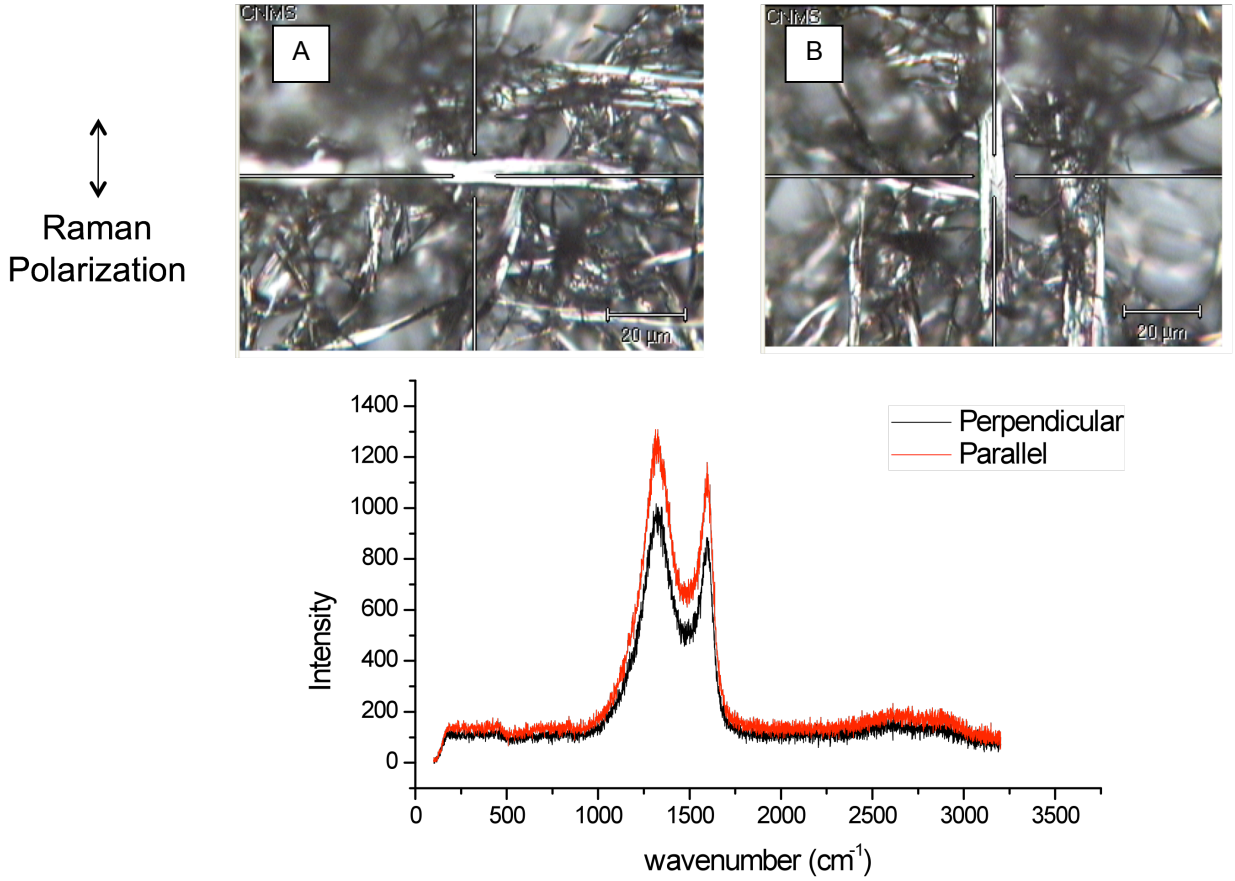

Figure 5.24. Polarized Raman measurements of an annealed PIDA fiber in geometries perpendicular (A) and parallel (B) to Raman polarization.

5.5. ESR and conduction measurements

The electron spin resonance (ESR) spectra of both PIDA co-crystals and isolated PIDA fibers, conduced with the help of Prof. Seth R. Marder and Dr. Susan A. Odom at Georgia Tech, have an asymmetric line shape, as shown in Figure 5.25. Such anisotropy in the ESR measurement, called a Dysonian line shape,[117] is typical of metal and semi-metals.[118] Conjugated organic polymers such as *trans*-polyacetylene,[119] polythiophene,[120,121] and poly(*para*-phenylene)[122] also demonstrate Dysonian EST spectra.

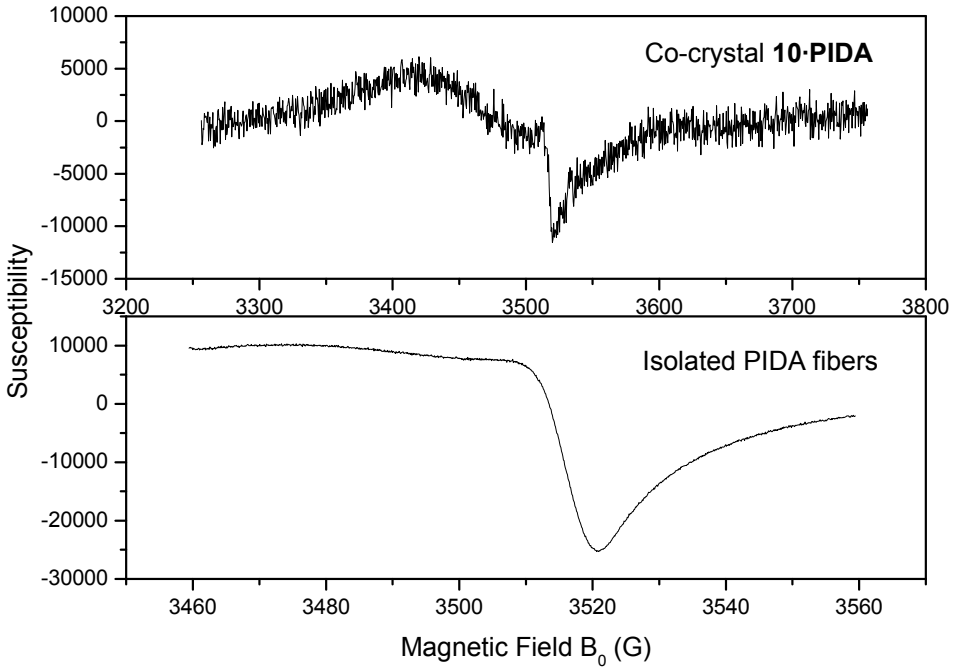

Figure 5.25. ESR spectra of co-crystal **10·PIDA** and isolated PIDA fibers.

We performed preliminary conductivity measurements on PIDA materials in collaboration with Prof. Colin Nuckolls and Dr. Xuefeng Guo at Columbia University. The resistance of a 20-μm-long PIDA fiber was measured to be about 12.5 MΩ on average, according to the DC current-voltage curve (Figure 5.26). However, determining the conductivity of this material

remains difficult, because it is difficult to estimate the cross-sectional area of the sample. AFM images of similar fibers allow for a preliminary evaluation of the conductance of the material. Using these estimates, conductivity of pristine PIDA aggregated fibers is on an order of 0.1 $S \cdot cm^{-1}$. This value is relatively high compared with those of other conjugated polymers, which range from 10^{-5} to 10^{-12} $S \cdot cm^{-1}$.[123]

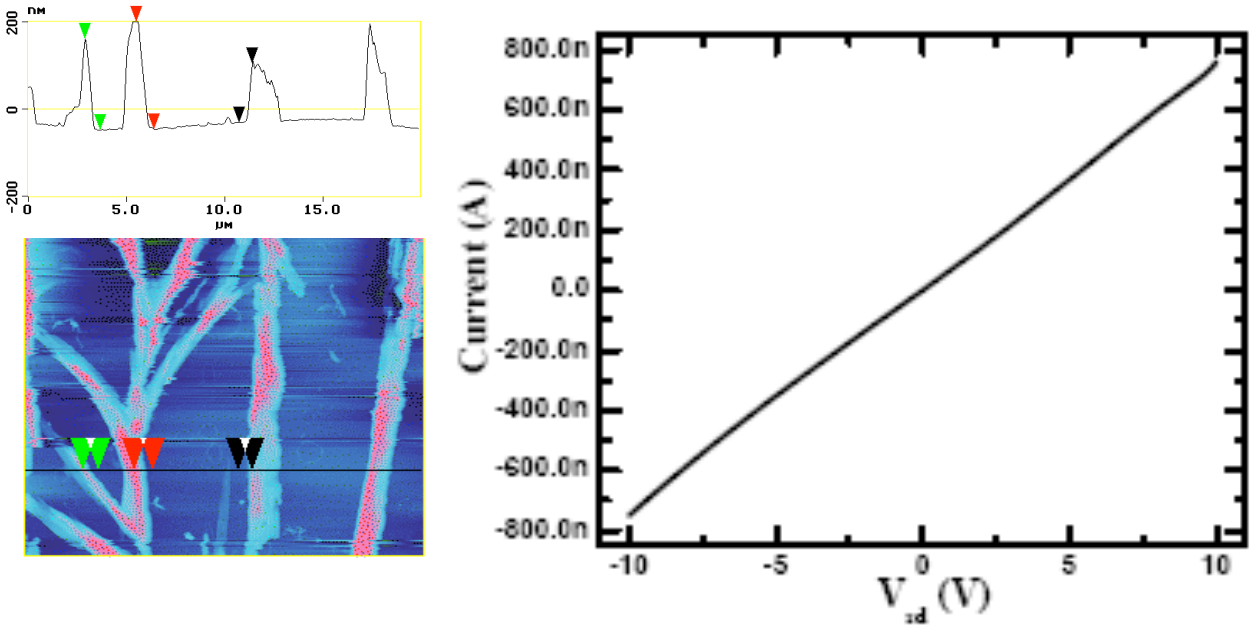

Figure 5.26. Left: AFM image of PIDA aggregate fibers. (taken by Dr. Jonas Jarvholm in Seth Marder's group, GA Tech); Right: Conductivity measurement of PIDA aggregates (measured by Dr. Xuefeng Guo, in Colin Nuckolls' group, Columbia University).

The exceptionally high conductivity of PIDA is consistent with the result from the ESR experiments. In the ESR spectrum of isolated PIDA, the Dysonian line shape suggests the high conductivity of the material. The other source for the conductivity comes from very small amount of dissociated iodine atoms, which may act as doping agent to generate mobile electrons within the polymer backbones.

5.6. Conclusion

After successfully obtaining PIDA by topochemical polymerization of diiodobutadiyne within co-crystals, PIDA can be isolated from the host-guest co-crystals by extensive rinsing and sonication in organic solvents. Isolated PIDA fibers have been completely characterized by UV/Vis absorption spectroscopy, Raman, FTIR, ^{13}C MAS NMR, electron microscopy, and ESR. Annealing isolated PIDA fibers at 900 ^{o}C can completely carbonize the material, and change PIDA fibers from anisotropic to isotropic. Treating PIDA fibers with Lewis bases can also induce dissociation of the C-I bonds, as will be comprehensively discussed in Chapter 6.

5.7. Experimental details

Solid-state ^{13}C Magic-Angle-Spinning NMR (MAS-NMR): Different from PIDA co-crystals, ^{13}C 1-Pulse MAS-NMR spectra of isolated PIDA fibers were taken at room temperature using either a Bruker Advance 700 NMR spectrometer or a Bruker Advance 600 NMR spectrometer, with the 2.5 mm double resonance probe, with the 2.5 mm zirconia rotor spinning at 31 kHz. The probe was tuned to 176.1 MHz or 150.9 MHz, respectively. The ^{13}C MAS-NMR spectra were collected using a ^{13}C 1-Pulse pulse program with decoupling, and a pulse delay of 10s. Over 1000 scans were acquired.

Polarized Raman: Polarized Raman spectroscopy was performed using a modified Renishaw 1000 spectrometer with the help of Dr. Ilia Ivanov at Oak Ridge National Laboratory. The spectrometer uses a 633-nm excitation wavelength, X-Y-Z translation stage, and additional X-Y-Rotation stage to measure the alignment of PIDA fibers. When the polarization direction of a laser beam coincides with the long axis of a polymer chain, the scattered intensity is maximized.

Electron microscopy: Transmission electron microscopy (TEM) was performed at the University Microscopy Imaging Center at the State University of New York (Stony Brook, NY). Suspensions were subjected to sonication for 1 h before placement on a carbon-coated 300-mesh copper grid and negative staining with 2% uranyl acetate. High resolution transmission electron microscopy method has been introduced in Chapter 3.

Thermogravimetric analysis (TGA) and differential scanning calorimetry (DSC): TGA and DSC were conducted with the help of Mr. Yimin Mao. TGA measurements were performed using a TGA-7 analyzer (TA instruments) in a temperature range of 25 – 600 ^{o}C at a heating rate of 20 ^{o}C/min. The measurements were carried out in both nitrogen and air environments. DSC measurements were performed using a Mettler Toledo DSC 821 instrument in a temperature range of 25 – 160 ^{o}C. The chosen heating rate was 10 ^{o}C/min.

Pyrolysis: The pyrolysis experiment was carried out under an argon stream in an electric oven, with the help of Dr. Kai Xiao at Oak Ridge National Laboratory. The PIDA fibers were added dropwise from a methanol suspension onto a quatz slide. The quatz slide was inserted into the oven and heated at 900 ^{o}C for 1 h.

Electron spin resonance: Room-temperature X-band ESR spectra were acquired using a Bruker EMX spectrometer with a frequency of 9.8 MHz. With the help of Dr. Susan A. Odom of Georgia Institution of Technology, solid co-crystals and isolated PIDA were loaded into the ESR tube directly for the measurement.

Conductivity measurements: The conductivity measurements for isolated PIDA fibers were performed using an Agilent 4155C semiconductor parameter analyzer connected to a Karl Suss (PM5) manual probe station, with the help of Dr. Xuefeng Guo at Columbia University. Isolated PIDA fibers were spin-coated onto clean silicon wafers. A shadow mask (100 μm x 100 μm

squares separated by 20 μm) was mounted on the wafer and a layer of 200 nm gold was deposited onto the fibers by thermal evaporation at pressures of $< 1x10^{-6}$ Torr. After removing the mask, PIDA fibers were located between adjacent gold electrodes with 20 μm gaps.

Chapter 6. Spectroscopic Studies of the Interactions between PIDA and Lewis Bases

6.1. Introduction

In looking for conditions to dissolve PIDA, we turned to Lewis-basic solvents and co-solvents, which have been expected to increase the solubility of PIDA by halogen-bonding interactions with the iodine atoms of the polymer. In addition, converting PIDA to other functional poly(diacetylene)s through palladium-catalyzed couplings requires using amine as an auxiliary reagent in many cases. Surprisingly, the appearance of the PIDA suspension changes significantly upon adding Lewis bases, such as pyrrolidine and pyridine.

When Lewis bases are added to the blue PIDA suspension, the color of the suspension changes to dark brown, and the absorption peaks associated with PIDA disappear correspondingly. The color change may be attributed to the Lewis acid-base interactions between the base and iodine substituents. The hypothetical formation of a halogen bonding complex between PIDA and the base is expected to interrupt the inter-chain π-π stacking within PIDA aggregates, perhaps generating isolated free rotating polymer chains. The conformation of the polymer backbone changes due to free rotation or formation of a random coil by isolated PIDA chains. The resulting decrease in the effective conjugation length may lead to the loss of absorption of PIDA.

Given these observations, PIDA might help to explain the side-chain effect in the chromism of PDAs. However, the experiments described below demonstrate the formation of free iodine atoms from the dissociation of C-I bonds during the reaction of PIDA with Lewis bases. The resulting solid material gives a Raman scattering spectrum consistent with graphitic carbon, suggesting this reaction may provide a new method to approach carbon-rich or all-carbon materials under mild conditions. In this chapter, we will comprehensively describe the

spectroscopic methods we have used to study the interactions between Lewis bases and PIDA, and to characterize the resulting base-treated materials.

6.2. UV/Vis/NIR and fluorescence spectroscopy studies

6.2.1. UV/Vis absorption spectroscopic change of adding Lewis bases to PIDA suspensions

Adding Lewis bases to the blue PIDA suspension leads to the disappearance of the blue color, as shown in Figure 6.1. When adding pyrrolidine, the color changes instantly, while pyridine takes a much longer time (at least 24 h) to change the color of the suspension. Adding other Lewis bases, including piperidine, 2-mercaptoethanol, diisopropyl amine, and DMSO, also results in a similar color change. Stronger bases cause the change more quickly. On the contrary, adding Lewis acids, such as HCl and trifluoroacetic acid (TFA), to the blue PIDA suspension does not change the color. In addition, PIDA is stable in neutral organic solvents, such as methanol, chloroform, and tetrahedrofuran (THF).

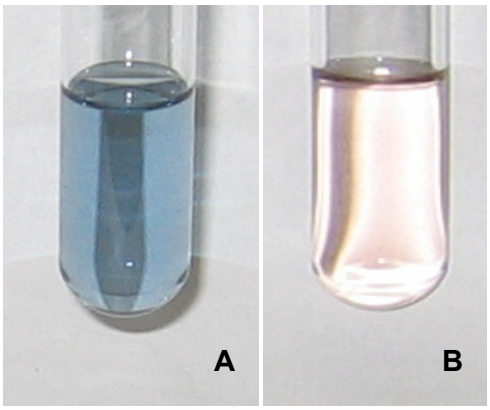

Figure 6.1. A: A blue PIDA suspension in methanol; B: Solution A after 0.05 mL pyrrolidine was added.

The absorption peaks of the blue PIDA suspension, a broad peak centered at 660 nm with a shoulder at around 750 nm, diminish during the interaction with Lewis bases, as shown in Figure 6.2. The resulting suspension appears transparent if the starting concentration of PIDA is low. After staying at room temperature for several minutes or hours (depending on the original

concentration of PIDA), the base-treated samples start to form a visible brown precipitate. After the precipitate is removed by centrifugation, the supernatant has even lower visible absorption.

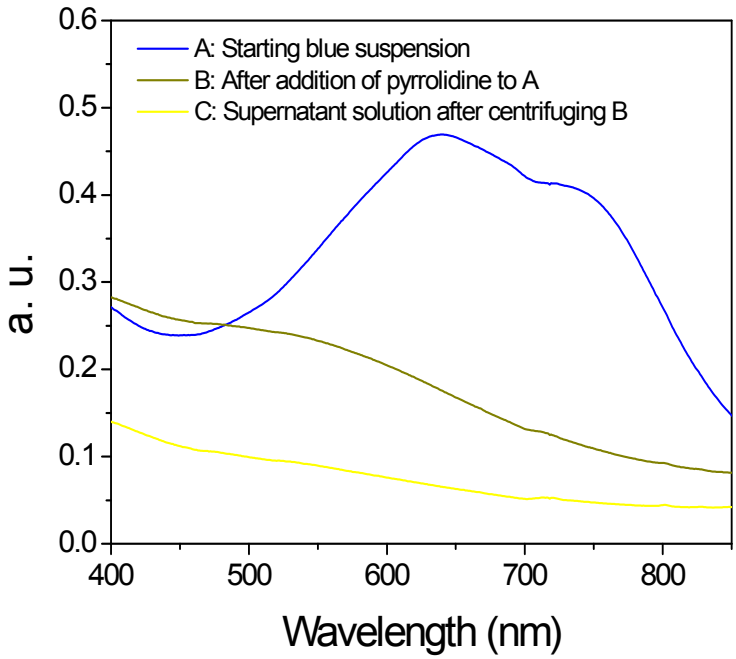

Figure 6.2. Absorption spectra of blue suspensions before (blue curve) and after (brown curve) adding pyrrolidine. Yellow curve indicates the absorption of the supernatant solution layer.

Triethyl amine affects the color of the PIDA suspension over several hours, more slowly than pyrrolidine, but faster than pyridine, and at a timescale convenient for recording the change in the absorption spectrum on a timescale. As shown in Figure 6.3, the absorption shoulder at 750 nm starts to decrease immediately after the base is added. The major absorption peak remains longer, but λ_{max} shifts to shorter wavelength. The spectrum changes more slowly over time, until neither the major peak or its shoulder can be distinguished, and the absorption spectrum remains stable with no peak above 450 nm, as shown by the yellow line in Figure 6.3.

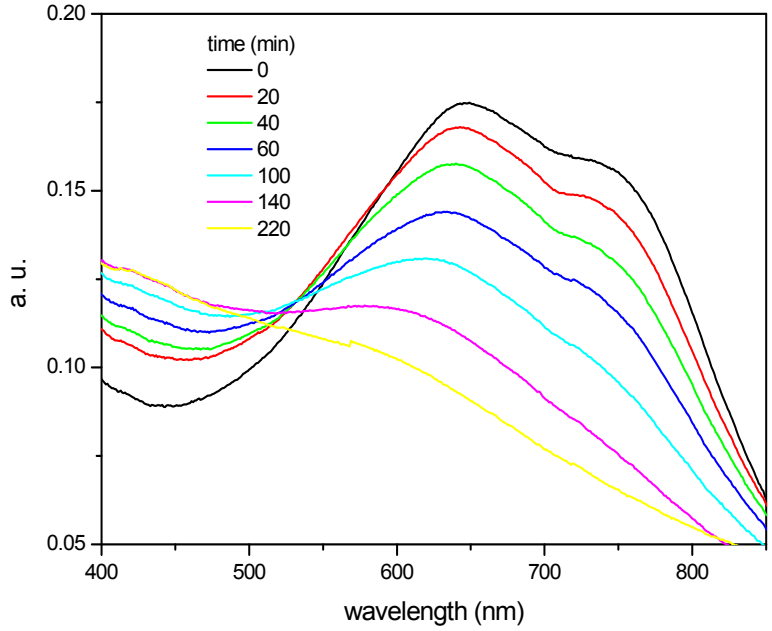

Figure 6.3. The absorption spectroscopic change of a blue PIDA suspension in methanol after adding 0.1 mL triethyl amine.

Interestingly, adding a Lewis acid, such as TFA, to a base-treated PIDA suspension causes another color transition in the system, from brown to bright yellow, as shown in Figure 6.4 C. THIS recovery of visible absorption accordingly comes at a lower wavelength absorbance at ~500 nm, with λ_{max} in Figure 6.5.

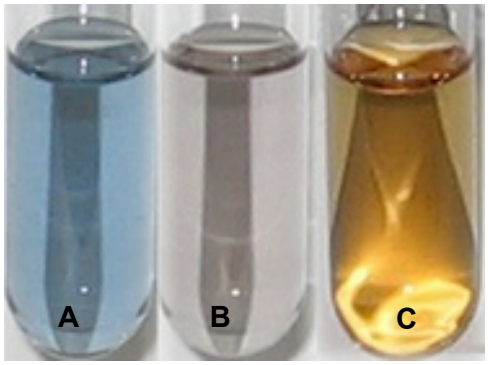

Figure 6.4. A: An isolated PIDA suspension in methanol; B: Adding 0.05 mL pyrrolidine to A; C: Adding 0.05 mL TFA to B.

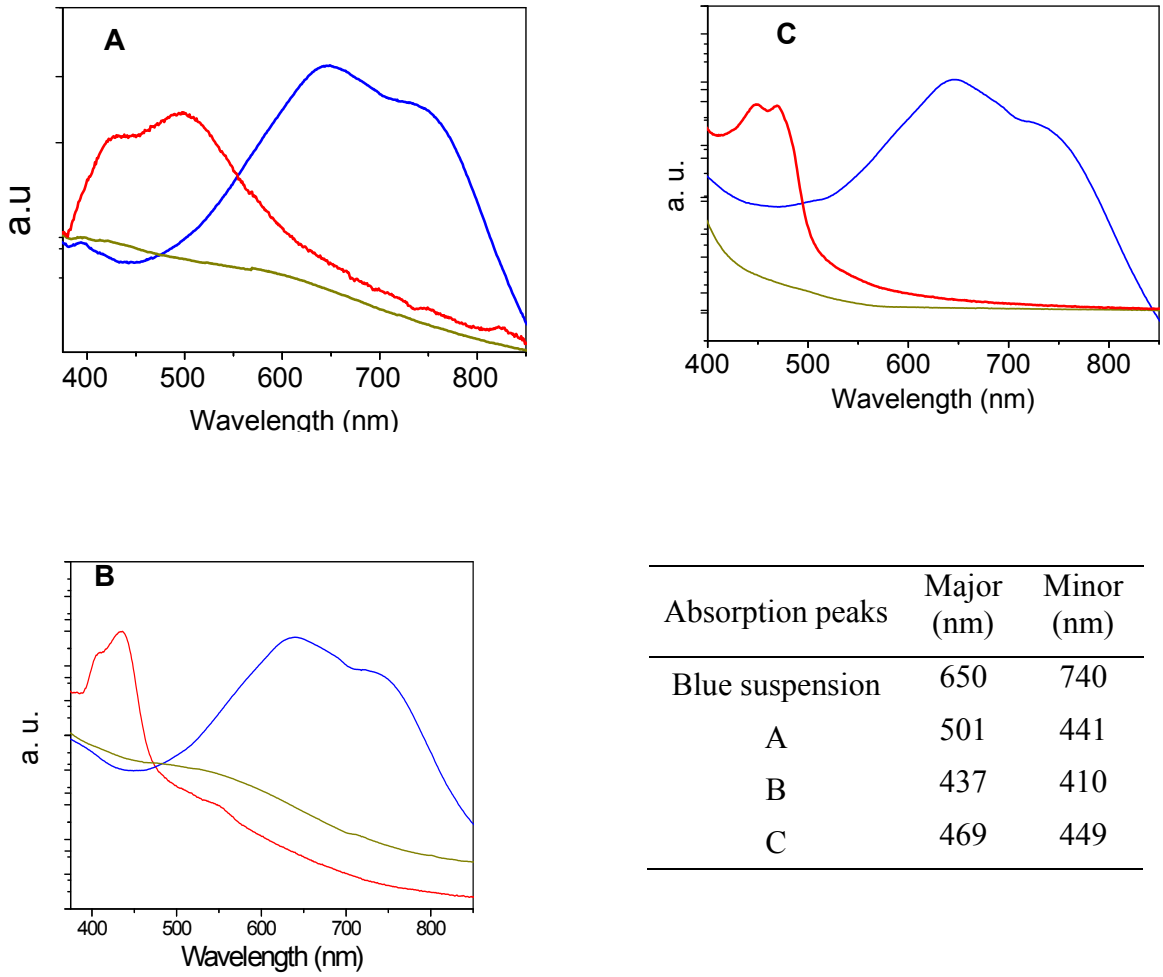

Absorption peaks	Major (nm)	Minor (nm)
Blue suspension	650	740
A	501	441
B	437	410
C	469	449

Figure 6.5. Absorption changes from adding TFA to PIDA suspensions in THF that have been treated first with Lewis bases A: triethyl amine; B: pyrrolidine; C: pyridine. Among all the spectra, blue curves represent the absorptions of the original blue suspensions; brown curves are absorptions after addition of bases to the original suspensions; red curves are absorptions after addition of TFA to the base-treated suspensions. The inserted table lists the absorption peaks of red curves of different systems.

The mechanism of these color changes upon addition of Lewis bases, and then acid, remains unidentified. As described above, this behavior may be attributed to a non-covalent Lewis acid-base interaction between PIDA and the added base, interrupting both the aggregation and the planarity of PIDA in the suspension. Addition of TFA to the yellow suspension may lead to the recovery of conjugation but at a lower wavelength absorbance at ~500 nm, resulting from re-

aggregation of PIDA strands with reduced planarity. However, adding HCl instead of TFA to base-treated PIDA also recovers the absorption, with a peak at lower wavelength of 440 nm. The absorption gained after adding HCl continues to increase and exceeds the scale of the spectrometer after overnight.

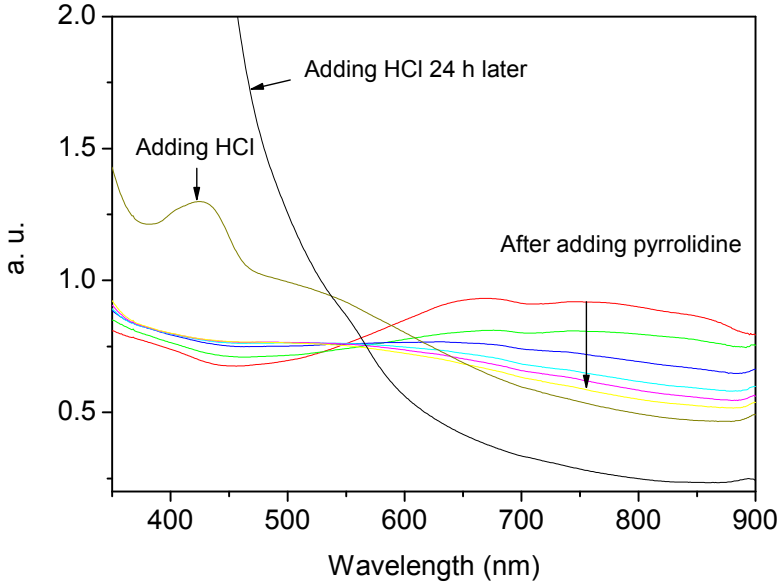

Figure 6.6. UV/Vis absorption spectra recording the interaction among PIDA, pyrrolidine and HCl.

6.2.2. UV/Vis absorption and fluorescence studies of PIDA suspensions in pyridine

Unlike pyrrolidine, the mild interaction between PIDA and pyridine enables PIDA to form a blue suspension in pyridine upon sonication. Once dispersed, it takes longer for PIDA to form visible aggregates in pyridine than in other organic solvents. This observation indicates that pyridine interacts with the iodine substituents at in an intermediate level between pyrrolidine and other neutral or acidic solvents. Figure 6.7 exhibits the absorption change of a PIDA suspension in pyridine upon staying at room temperature for 4 days. The initial blue suspension of PIDA in pyridine has a similar absorption spectrum to the other blue suspensions we have introduced in

Section 6.2.1. However, the absorbance in the visible range decreases gradually after the suspension stays at room temperature for a longer time. At the same time, a new peak centered at 366 nm emerges and continues increasing as long as the absorption above 600 nm decreases.

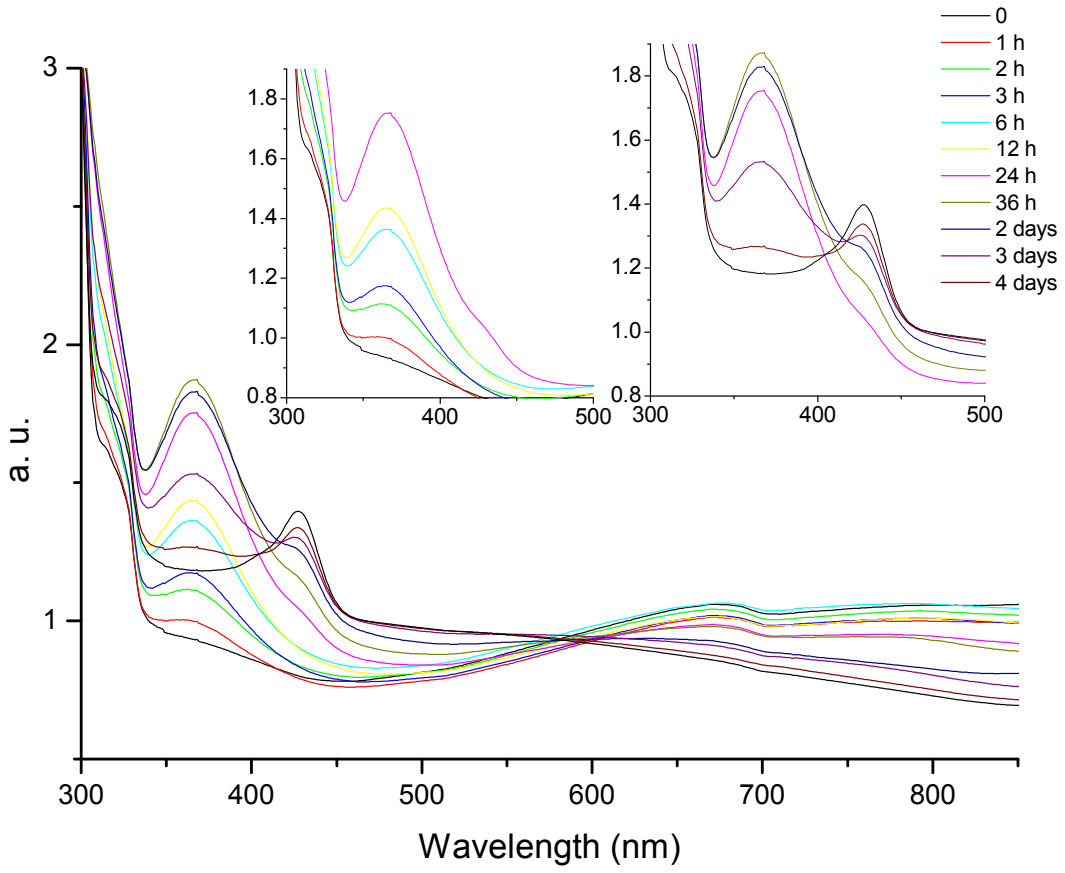

Figure 6.7. UV/Vis absorption spectroscopic change of a pyridine suspension of PIDA.

After 24 h of mixing PIDA and pyridine, a shoulder at about 430 nm appears in the spectrum, next to the peak at 366 nm. From this point, the absorbance at 366 nm starts to decrease while the absorbance at 430 nm starts to increase and develops to a separate peak centered at 428 nm. It appears that the system contains two species in dynamic equilibrium. The absorption change

upon diluting the system was recorded to test the concentration dependence of equilibrium, as shown in Figure 6.8.

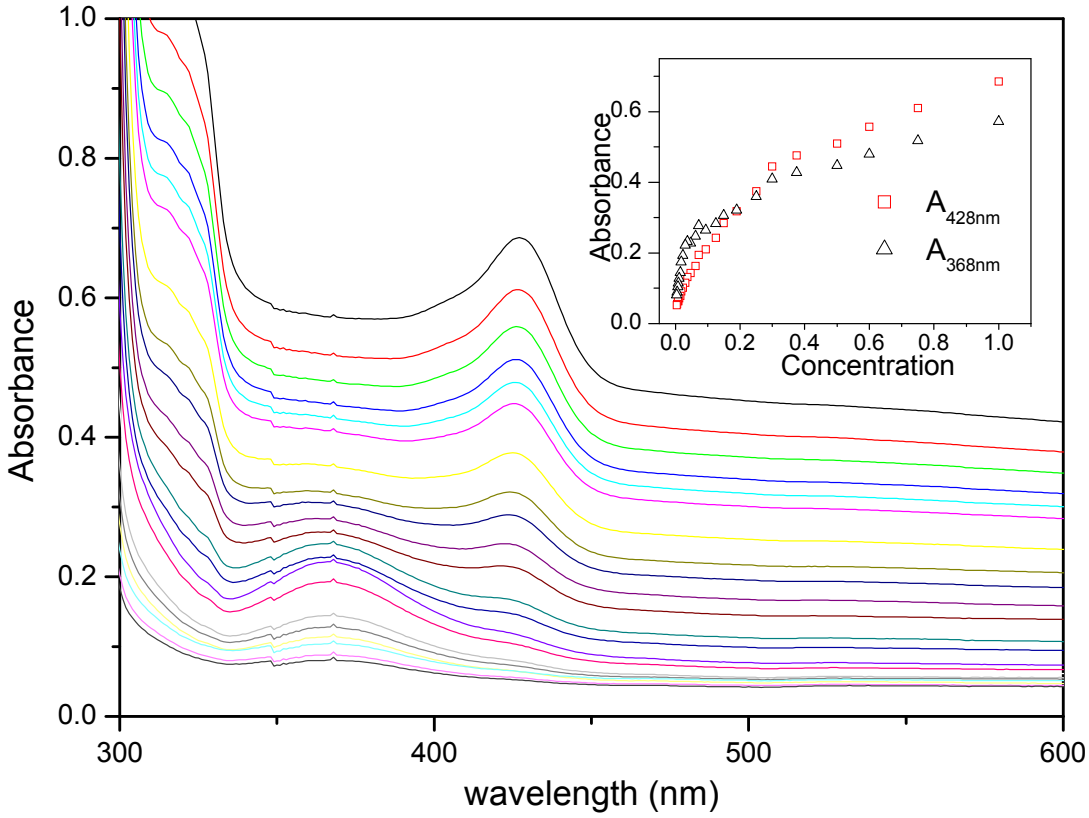

Figure 6.8. Absorption spectra of a PIDA suspension in pyridine at different concentrations, inset showing the relationship between concentration of suspension and absorbance at 428 nm and 368 nm.

The suspension was subjected to centrifugation to indentify the origin of these absorbance peaks. The supernatant layer after centrifugation gives a yellow solution, the absorption spectrum of which is shown in Figure 6.9 A. The absorption maximum is very high and exceeds the detection limit. After dilution, this solution shows a maximum absorption at 368 nm (Figure 6.9 B), consistent with the absorption peak of the suspension. The absorption spectrum is similar to that of iodine in pyridine (Figure 6.9 C). Adding $Na_2S_2O_3$ aqueous solution can quench the

absorption of both solutions in Figure 6.9 A and 6.9 C, indicating that iodine was formed in the clear pyridine solution obtained from PIDA suspensions.

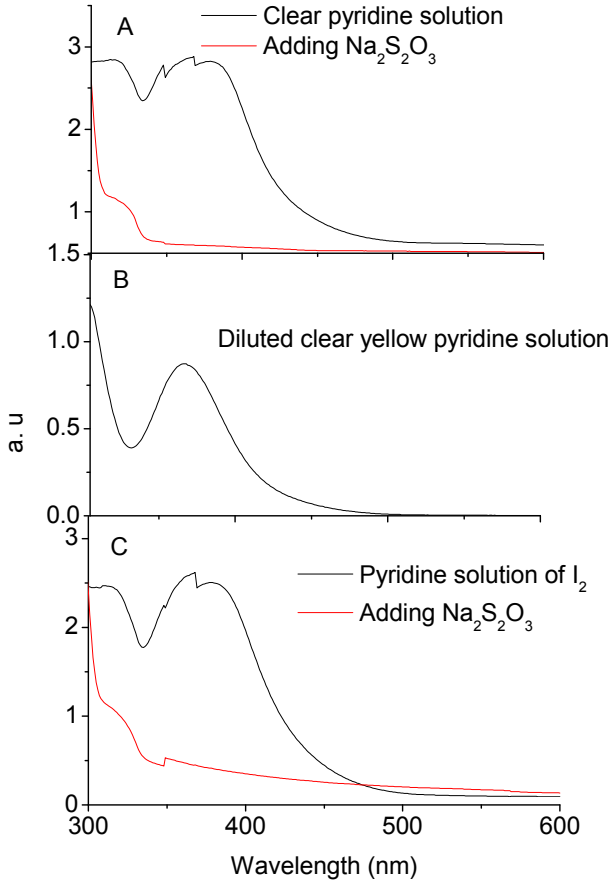

Figure 6.9. A: Absorption spectra of the supernatant solution obtained after subjecting a PIDA-pyridine suspension to centrifuge, before and after addition of $Na_2S_2O_3$; B: Dilution of the yellow solution in A until the absorption peak at 368 nm is clear; C: Absorption spectra of a pyridine solution of iodine with concentration of 0.065 mol/L, before and after addition of $Na_2S_2O_3$.

By comparing the absorbance of diluted yellow pyridine solution at 368 nm with that of a calibrated I_2-pyridine solution, the ratio of iodine in pyridine to total iodine content of the initial PIDA sample can be calculated, as listed in Figure 6.10. The amount of dissolved I_2 is less than 1% of the total iodine from PIDA at the time the visible absorption disappears, but I_2 continues to form after the PIDA suspension becomes completely black. This observation suggests that PIDA loses iodine as a result of the interaction with pyridine, but loses color first.

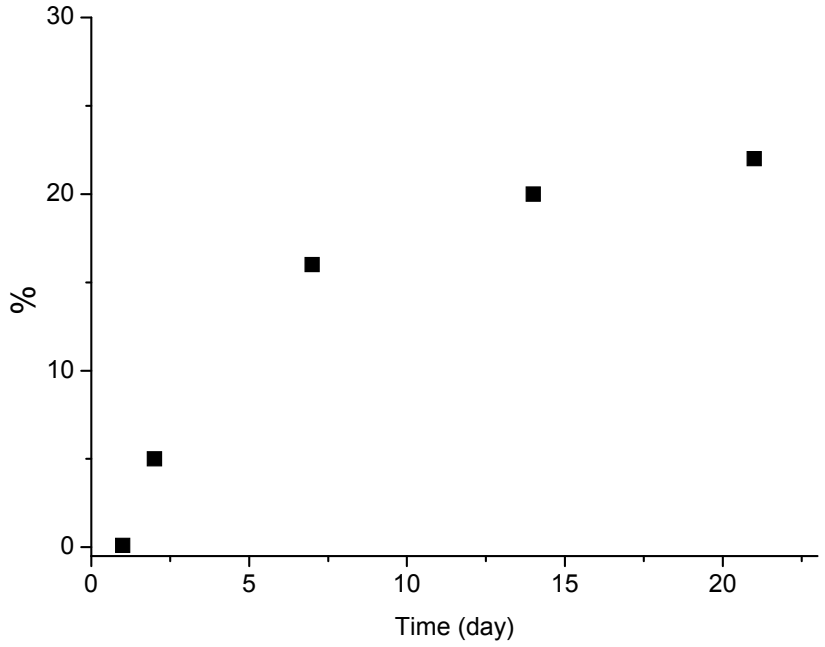

Figure 6.10. Calculated percentage of iodine dissociated from PIDA.

The yellow-brown solution produced in methanol by the interaction between pyrrolidine and PIDA has no absorption at ~360 nm, and does not change color with added aqueous $Na_2S_2O_3$, indicating that no molecular iodine is present. On the contrary, these solution forms yellow precipitate with added $AgNO_3$, suggesting that anionic iodide is formed during the reaction between pyrrolidine and PIDA. The different by-products indicate a difference in the reaction mechanisms, although both bases cause a loss of visible absorption for PIDA. Other characterization methods will be used to clarify these reactions.

The PIDA-related materials exhibit interesting fluorescent properties, as shown in Figure 6.11. The fluorescence spectrum of aqueous suspension of **10·PIDA** co-crystal shows a peak at 437 nm (Figure 6.11 A). In contrast, the blue PIDA suspension in methanol is no longer fluorescent (Figure 6.11 B), due to the formation of PIDA aggregates. The fluorescence intensities of conjugated polymers generally quench upon aggregation.[54] However, the pyridine

suspension of PIDA shows strong fluorescence, different from that of a pyridine solution of I_2, as shown in Figure 6.12 C. This observation suggests that in addition to releasing iodine from PIDA, the interaction between PIDA and Lewis bases may also interrupt the aggregation state of PIDA and generate isolated polymer chains.

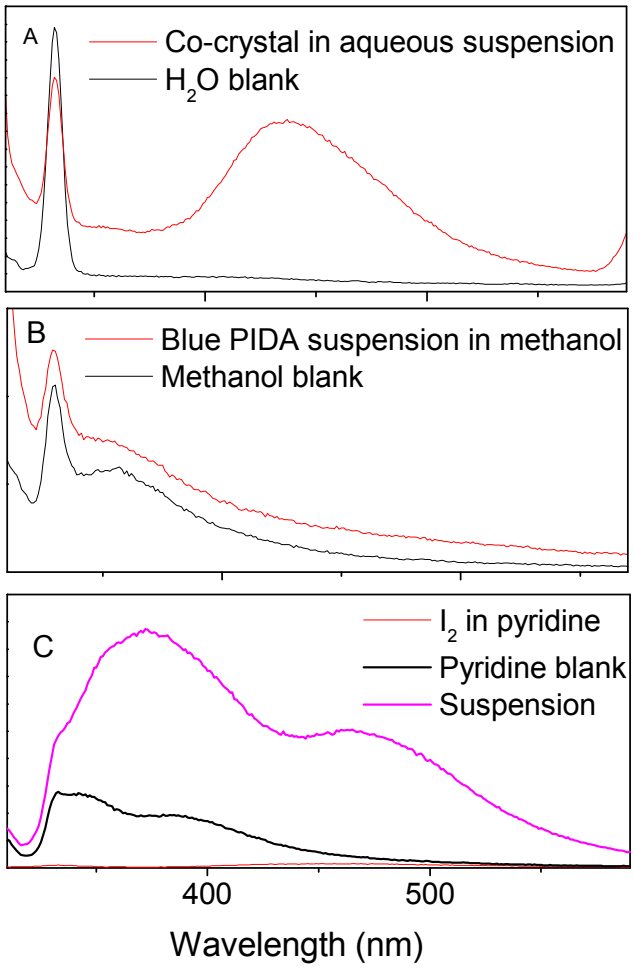

Figure 6.11. Fluorescent spectra of (A) of an aqueous suspension of co-crystal 10·PIDA, compared with blank H_2O; (B) A blue suspension of isolated PIDA in methanol, compared with blank methanol; (C) A PIDA-pyridine suspension after staying at room temperature for 2 days, in comparison with blank pyridine and pyridine solution of iodine.

6.2.3. UV/Vis/NIR spectroscopic studies

The UV/Visible/NearIR (UV/Vis/NIR) absorption spectra of PIDA have been taken at Georgia Tech in collaboration with Seth Marder and co-workers. **10·PIDA** co-crystals were dispersed in D_2O by sonication before the absorption experiments. The results are consistent in the visible light region with previous absorption spectroscopy measurements. There are no absorption peaks in the near IR area, up to 2000 nm (Figure 6.12 A). The PIDA co-crystals in D_2O suspensions were then subjected to extensive rinsing and sonication in organic solvents to remove the host. Again, the observed UV/Vis/NIR absorption spectrum of the resulting suspensions matches our previous observations in the UV and visible region but no other new absorption peaks appeared in the near IR range, as shown in Figure 6.12.

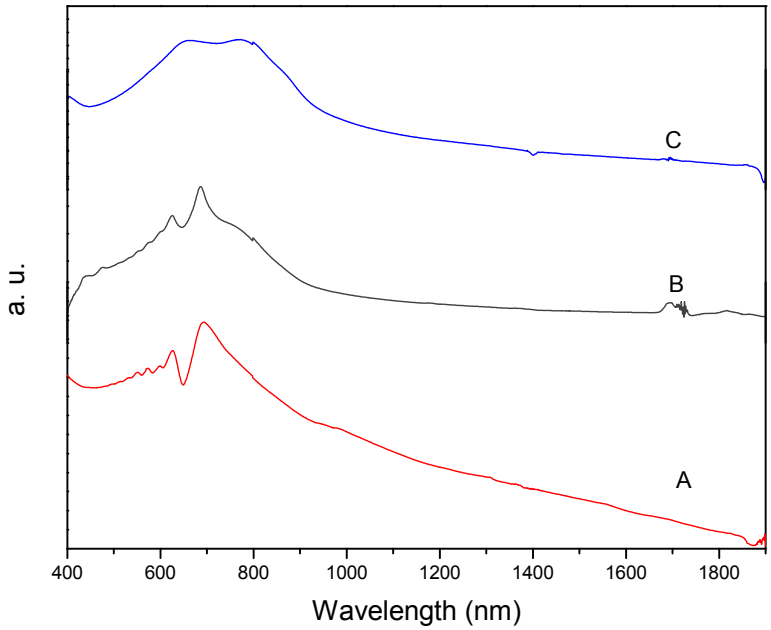

Figure 6.12. UV/Vis/NIR spectra after rinsing **10·PIDA** co-crystals in organic solvents. A: Aqueous suspensions of **10·PIDA** co-crystals; B: Dispersing **10·PIDA** co-crystals in methanol by sonication; C: Blue PIDA suspensions in methanol with no host.

Similarly, there are no new peaks in the near IR range attributed to the base-treated PIDA materials. Upon adding Lewis base, the blue PIDA suspension in THF loses absorption in the

visible range. The UV/Vis/NIR spectrum of a pyrrolidine-treated PIDA suspension, shown in Figure 6.13, includes several strong peaks between 1450 and 2000 nm, but these absorptions are attributed to the solvent itself or pyrrolidine.

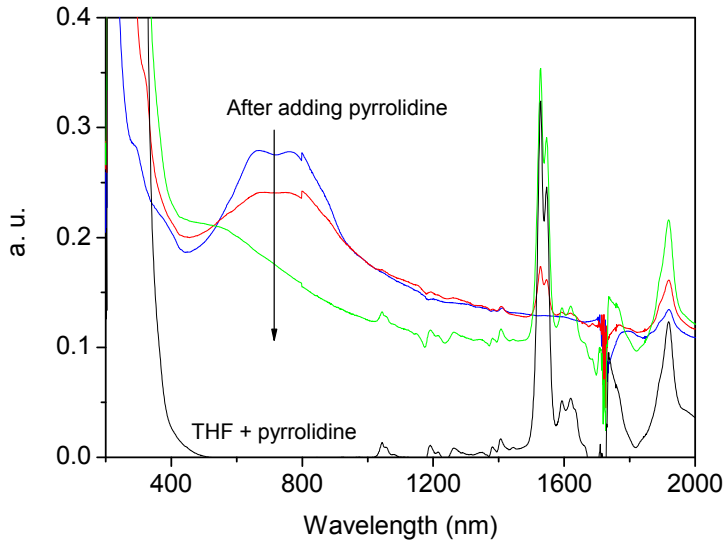

Figure 6.13. UV/Vis/NIR absorption spectra of adding pyrrolidine to PIDA THF suspensions.

To eliminate the solvent affect, the UV/Vis/NIR spectra of the solid PIDA materials were taken, with the help of Dr. Ilia Ivanov of Dr. David. B. Geohegan's group at Oak Ridge National Laboratory. Figure 6.14 illustrates the UV/Vis/NIR absorption spectra of isolated PIDA fibers and base-treated PIDA materials. All the samples show an absorption peak at around 2800 nm (3600 cm^{-1}). Both pyrrolidine-treated and pyridine-treated PIDA materials exhibit apparent absorption tails in the near IR region, indicating that the band gap of PIDA decreases upon the treatment with Lewis bases. This observation suggests that base-treated PIDA materials might have a better conductivity or electron transportation than pristine PIDA.

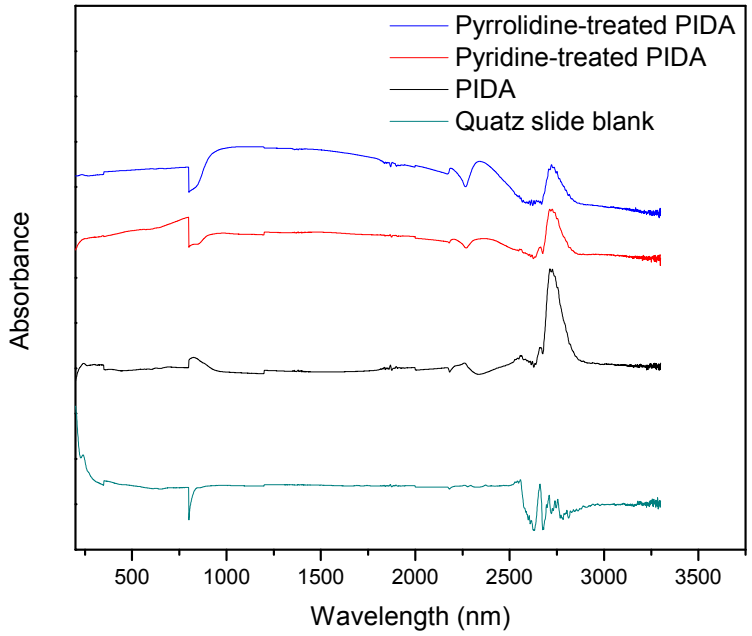

Figure 6.14 UV/Vis/NIR transmittance spectra of PIDA related materials.

6.3. ESR studies

ESR experiments reveal the formation of radicals during the interaction between PIDA and Lewis bases. Figure 6.15 showed the change in the ESR spectrum of PIDA after treatment with pyrrolidine. Upon adding pyrrolidine directly to solid isolated PIDA, the ESR spectrum changes from an anisotropic Dysonian line shape to a broad symmetric line shape without hyperfine splittings. This change indicates that the reaction generates new paramagnetic species. The g-factor changes from 2.00640 to 2.00417 immediately when pyrrolidine is added to the PIDA sample. After that, it increases to 2.00700 after 50 minutes of the reaction. The g-factor is again at 2.00497 after another 20 minutes.

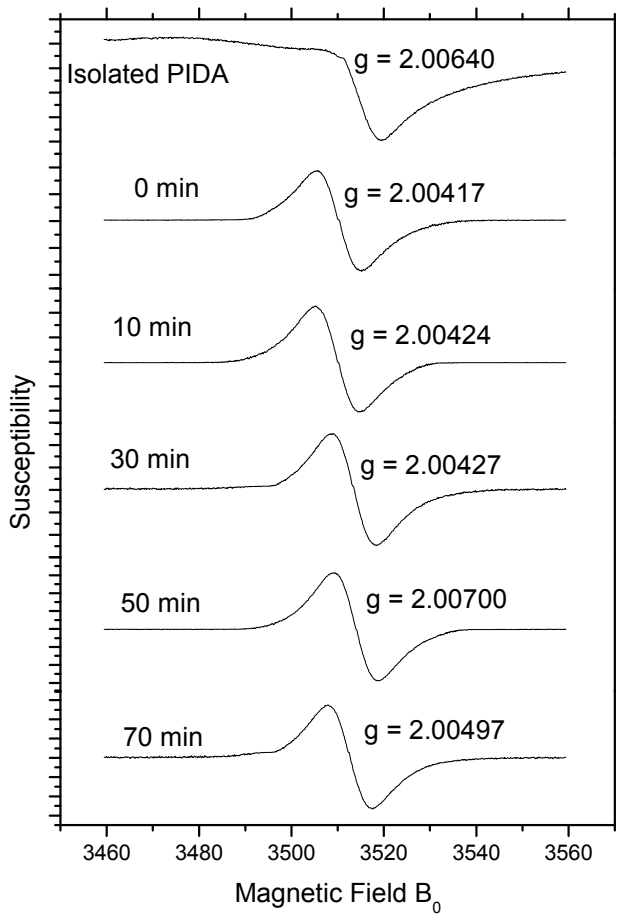

Figure 6.15. Change in ESR spectrum of isolated PIDA upon adding pyrrolidine.

Possible sources for the new radical signals include nitrogen radicalcations or iodine atoms, and conjugated radicals delocalized on the polymer chain. The delocalized radials would give a Dysonian line shape, as what has been observed on isolated PIDA. The lack of hyperfine coupling indicates that the radicals are not located on nitrogen, which would be expected to give a triplet signal. In addition, the g-factors of around 2 are not from iodine radial, leaving it still unclear about the source of the new radical signals. The values of integration at each of these spectra are plotted in Figure 6.16.

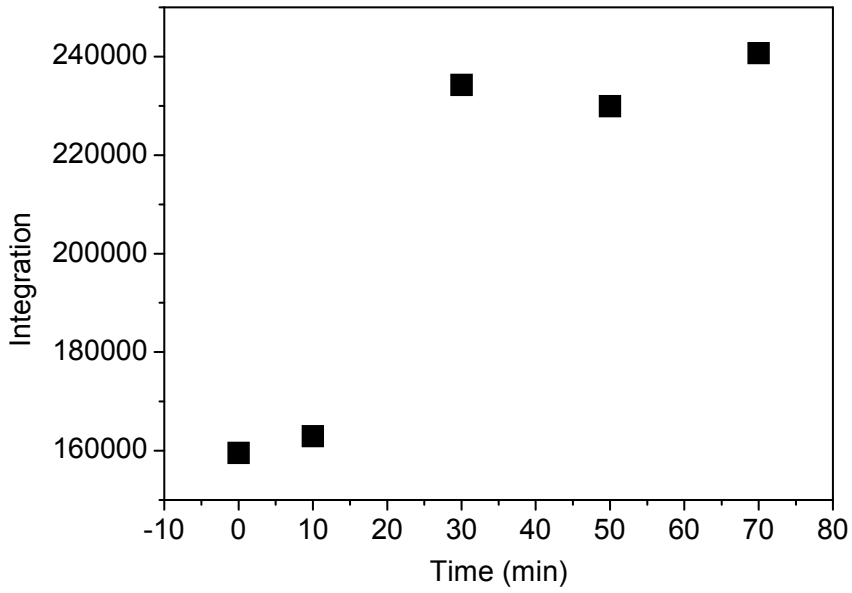

Figure 6.16. Integrations of ESR spectra shown in Figure 6.15.

Adding pyrrolidine to a PIDA suspension in THF also results in the formation of radicals, shown by the symmetric ESR spectra in Figure 6.17. The ESR spectrum of the PIDA suspension is asymmetric with a g-factor of 2.02590, different from the solid PIDA g-factor of around 2.00. However, adding pyrrolidine to the suspension changes the g-factor to 2.00486 immediately (Figure 6.17 0 min). The ESR spectrum becomes symmetric and the amount of generated radial increases significantly as the reaction remains longer at room temperature.

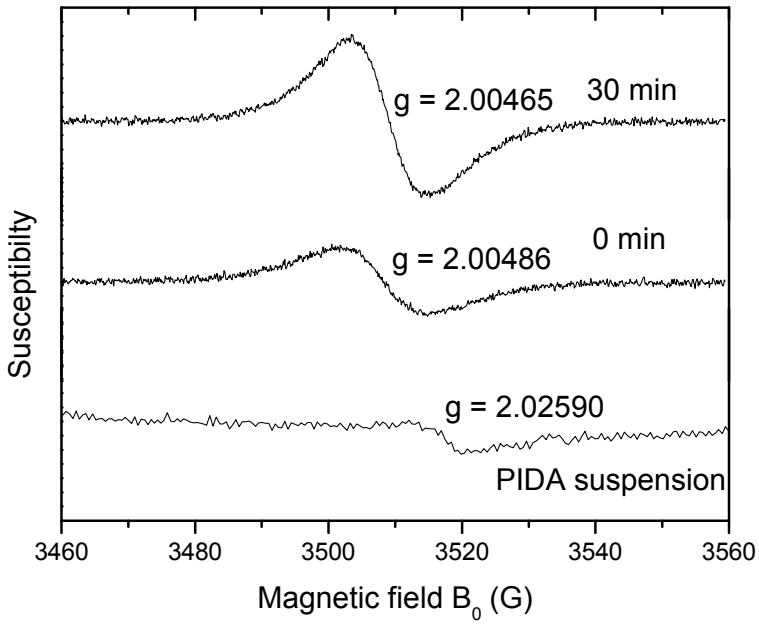

Figure 6.17. ESR spectroscopic change of adding pyrrolidine to PIDA suspension in THF.

6.4. Stoichiometric reactions between PIDA and Lewis bases

To further investigate the reaction between PIDA and Lewis bases, stoichiometric experiements were carried out where the PIDA suspension in an iodine-nitrogen stoichiometry of 1:1. Using CD_3OD as media, the ^1H NMR shift change can be used to monitor the progress of the reaction. As shown in Figure 6.18, the ^1H NMR peaks corresponding to the methylene (CH_2) protons in pyrrolidine shifts to higher frequency as pyrrolidine reacts with PIDA. After the reaction proceeds for 6 days, a new singlet peak appears at a chemical shift of 7.90 ppm.

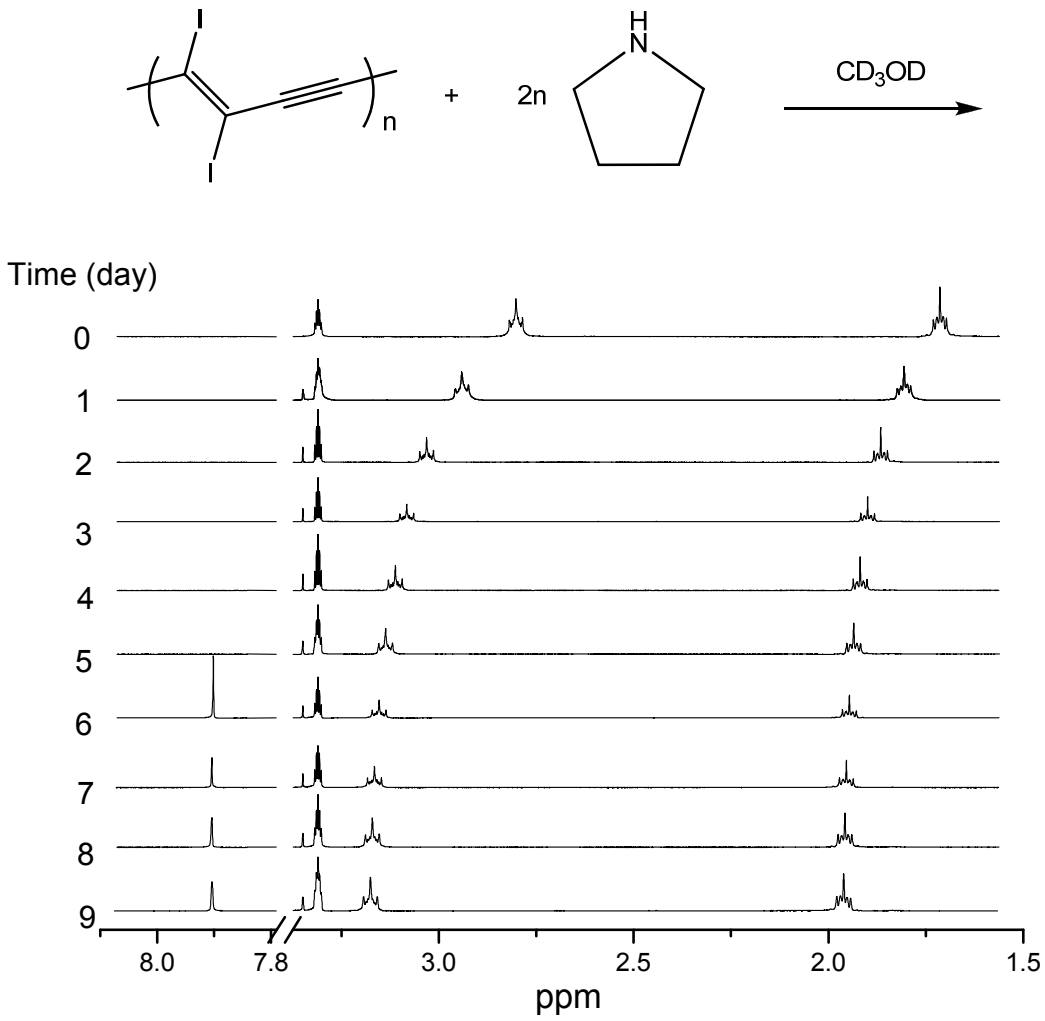

Figure 6.18. ^{1}H NMR shift change of the reaction between PIDA and pyrrolidine in the media of CD_3OD.

The plot of change in ^{1}H NMR chemical shift is shown in Figure 6.19 A. The ^{1}H NMR frequencies of both α- and β- hydrogen of pyrrolidine increase immediately upon addition to PIDA. The rate of change in chemical shifts decreases gradually. At the same time, the integrations of both α- and β- hydrogen decrease upon the reaction between PIDA and pyrrolidine, referenced by the methyl in CD_3OD, as shown in Figure 6.19 B. This suggests that

the amount of NMR-observable hydrogen decreases, possibly because pyrrolidine attaches onto the insoluble PIDA as a result of the reaction.

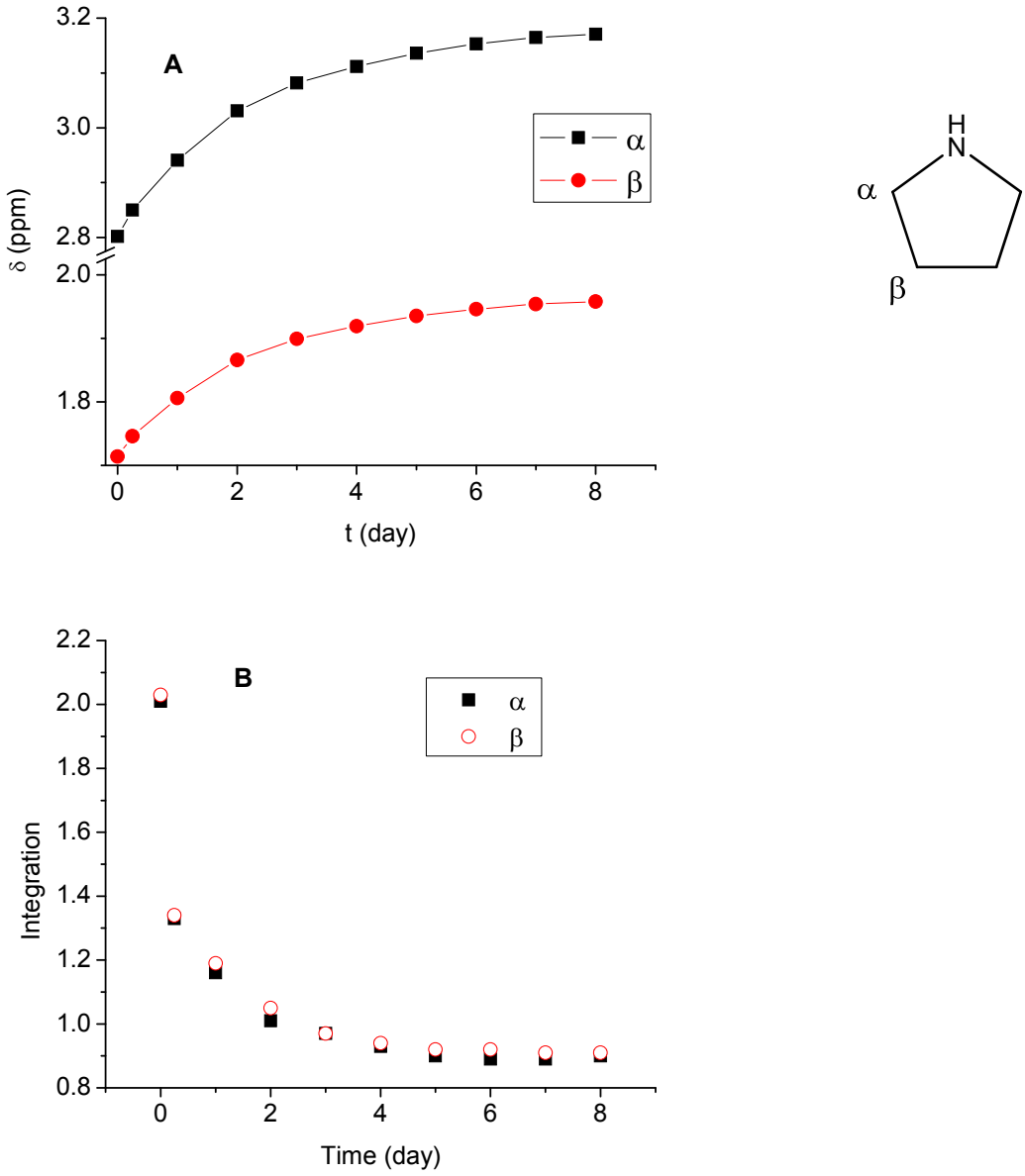

Figure 6.19. Plots of changes in ^{1}H NMR chemical shift (A) and signal integration (B) for the α- and β-hydrogen in pyrrolidine.

The moving of NMR shifts of the α and β protons of pyrrolidine is consistent with the protonation of pyrrolidine. Figure 6.20 shows the change in the ^{1}H NMR spectrum of pyrrolidine

as a result of titration with trifluoacetic acid (TFA), conducted by Daniel Resch. The NMR shifts for the α and β protons of pyrrolidine move to higher frequencies instantly upon adding the acid, indicating that the protonation is a possible mechanism for the NMR change shown in Figure 6.20. However, the observed change when in the presence of PIDA is much slower, suggesting that protons are generated slowly during the reaction between the base and PIDA.

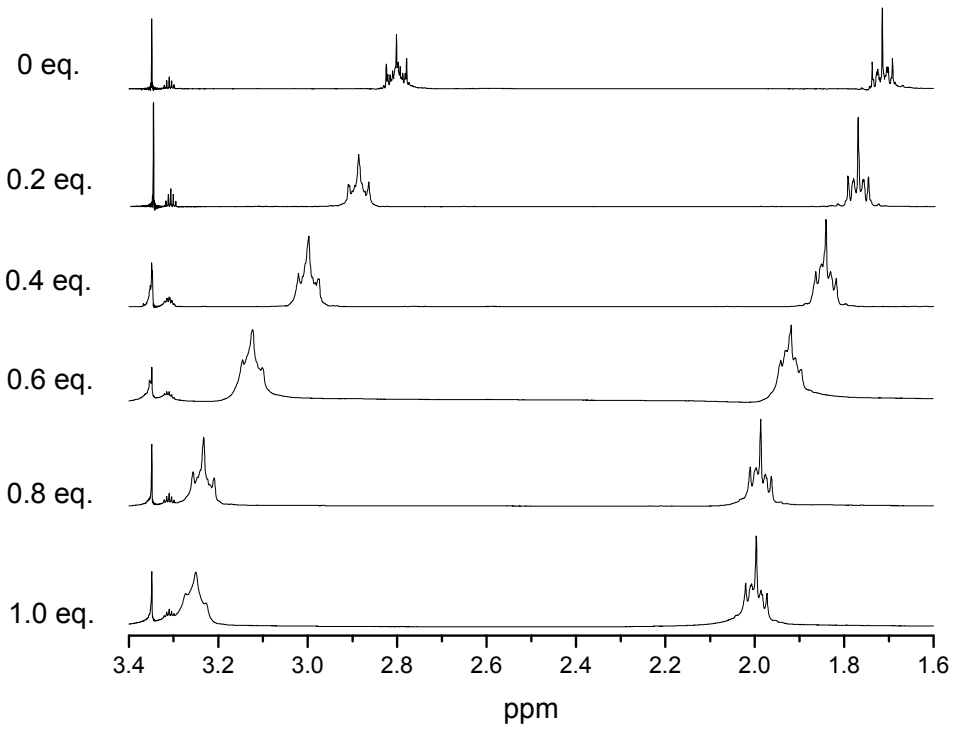

Figure 6.20. ^{1}H NMR change of pyrrolidine upon addition of trifluoacetic acid (TFA). The relative amounts of added TFA are listed to the left of the spectra.

To identify the pyrrolidine product in the reaction, the mixture was subjected to centrifugation after reacting for 2 days. The supernatant layer was collected, and mass spectroscopy (EIMS) exhibits two major peaks at m/z of 71.96 and 100.01, as shown in Figure 6.21. The EIMS spectrum of reaction residue after 9 days is more complicated, with many unidentified peaks, but it still contains the two peaks shown in Figure 6.21.

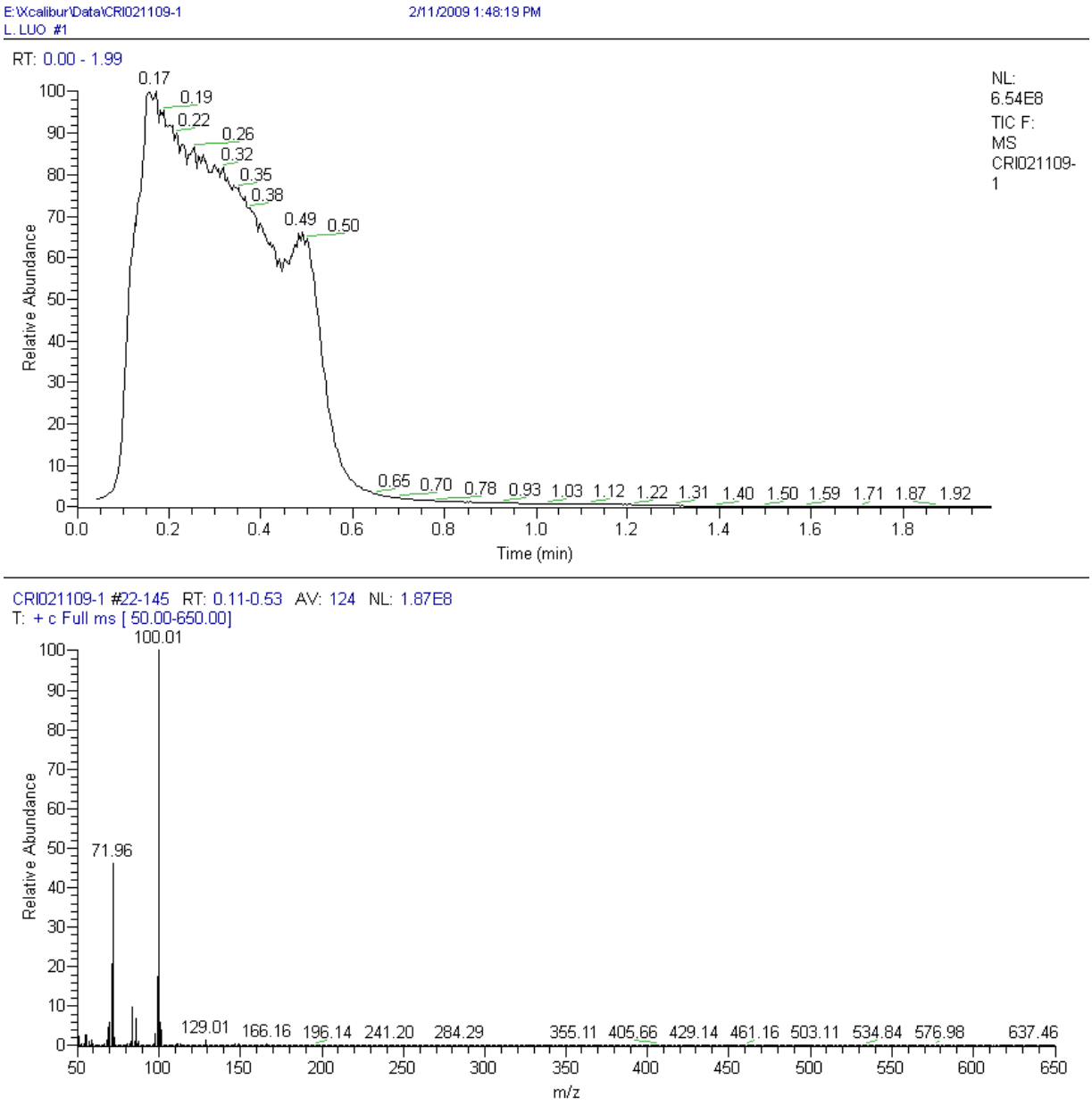

Figure 6.21. EIMS spectrum of supernatant layer of PIDA/pyrrolidine mixture after reacting for 2 days.

The appearance of a new ^{1}H NMR peak at 7.90 ppm, and the m/z peak at 100.01 in EIMS both indicate the formation of *N*-formylpyrrolidine during the reaction. Based on the research of Cruickshank and Benson studied the reaction of molecular iodine and methanol in the gas phase,[124] and found that they react slowly to form CO. Similarly, as shown in Scheme 6.1 A, the

PIDA-generated iodine atoms can react with methanol to produce CO, and further reaction with pyrrolidine can produce *N*-formylpyrrolidine. However, it is difficult to explain the gradual change in the ^{1}H NMR spectrum based on formation of *N*-formylpyrrolidine. Such a gradual change would be expected only from a shifting equilibrium occurring on the NMR timescale, while during NMR titrations, while the transformation from pyrrolidine to *N*-formylpyrrolidine, i.e, the formation of the N-Carbonyl bond should be irreversible.

On the other hand, the CD_3OD oxidation will also lead to formation of DI, and pyrrolidine will react with the acid to make the ammonium ion, as shown in Scheme 6.1 B. The exchange of protons between pyrrolidine and pyrrolidinium can happen easily on the NMR timescale, which is consistent with the gradual change of NMR shifts. In addition, pyrrolidine can also form a halogen-bond complex with iodine, as introduced in Scheme 6.1.

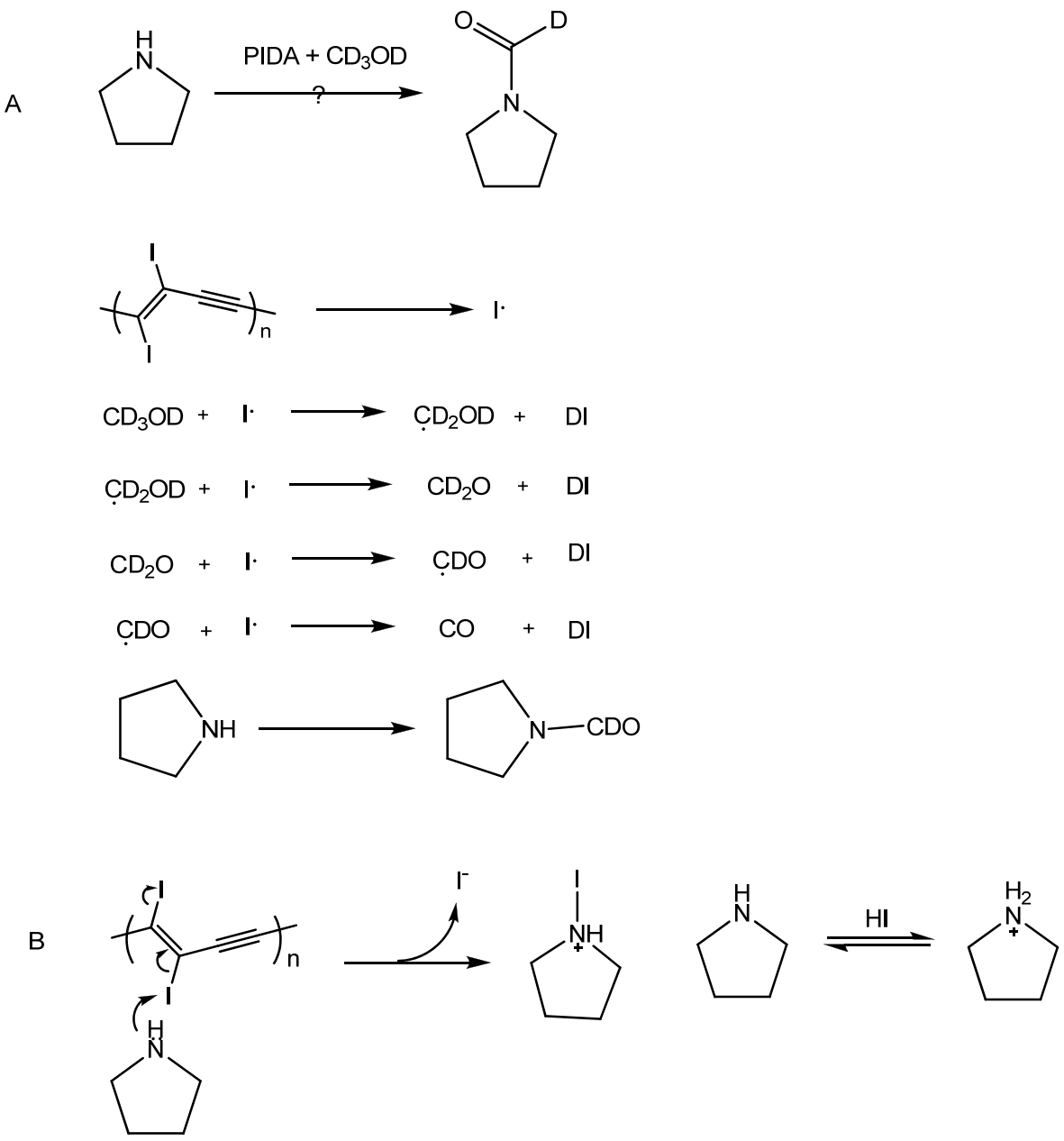

Scheme 6.1. Hypothetical mechanism between PIDA and pyrrolidine based on above stoichiometric reaction.

The stoichiometric reaction between pyridine and PIDA in methanol-d4 is different from the reaction between pyrrolidine and PIDA. As shown in Figure 6.22 A, the hydrogen atoms in pyridine remain at the same chemical shifts even after 6 days of mixing. However, the NMR shifts for the protons of pyridine move to higher frequencies instantly upon adding the TFA

(done with the help of Dan Resch), as shown in Figure 6.22 B. In addition, the reaction between pyridine and PIDA generates molecular iodine rather than iodide. The EIMS spectrum of the supernatant layer, as shown in Figure 6.23, confirms the formation of I_2 and DI.

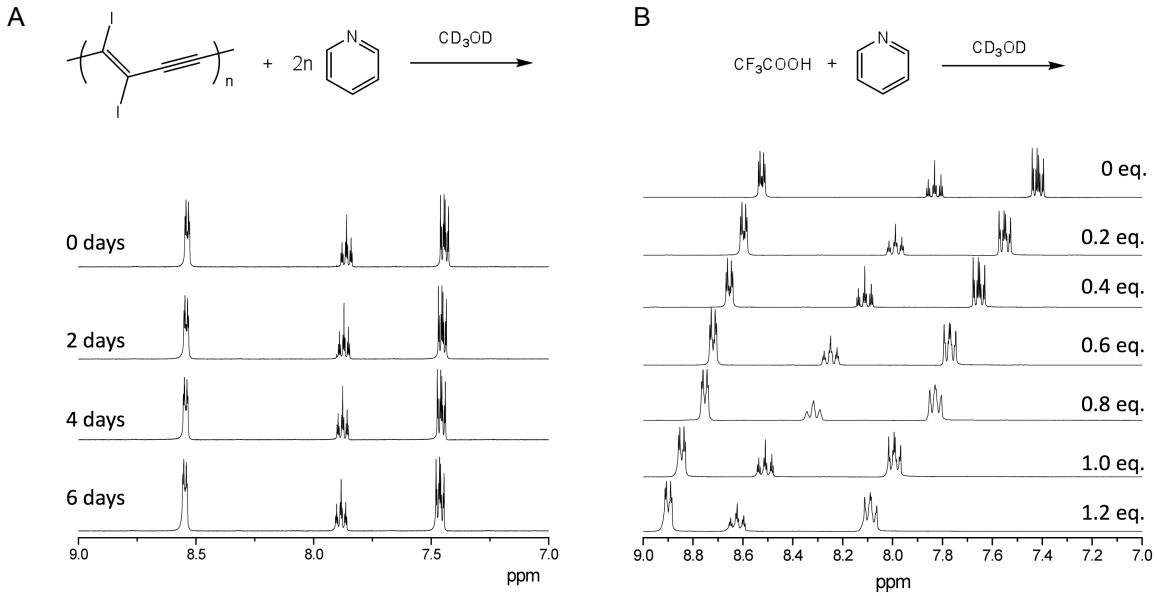

Figure 6.22. Change of ^{1}H NMR chemical shift of pyridine during its interaction with PIDA (A) and upon addition of TFA (B).

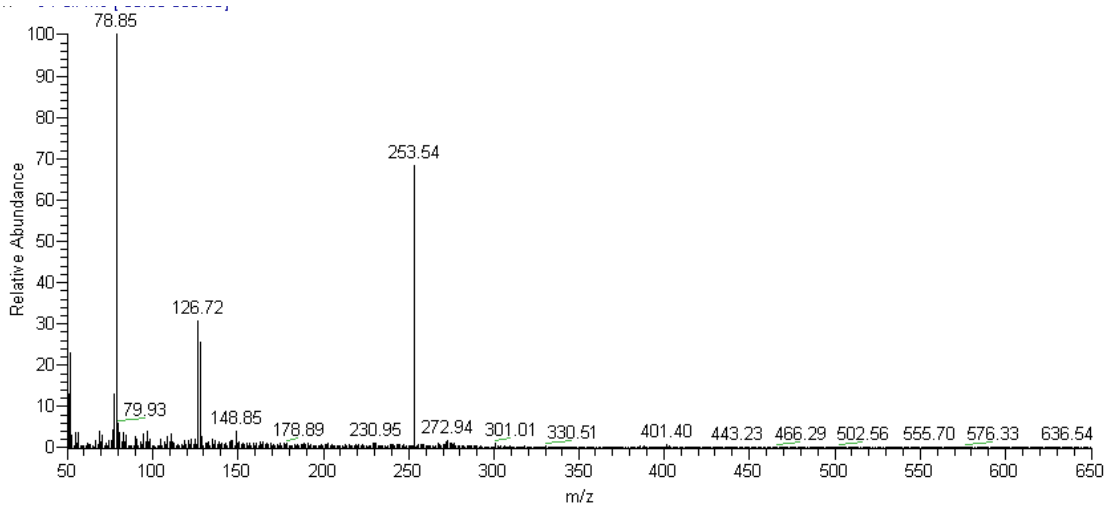

Figure 6.23. EIMS spectrum of reaction mixture of PIDA and pyridine after reacting for 6 days.

6.5. Morphology and elemental compositions

In addition to understanding the chemistry of the reaction between PIDA and Lewis bases, it is of great interest to characterize the new material generated from base-treated PIDA. After PIDA reacts with Lewis bases, new solid materials are isolated by centrifugation from. The base-treated materials appear more amorphous and lose the previous metallic sheen, as illustrated in Figure 6.24.

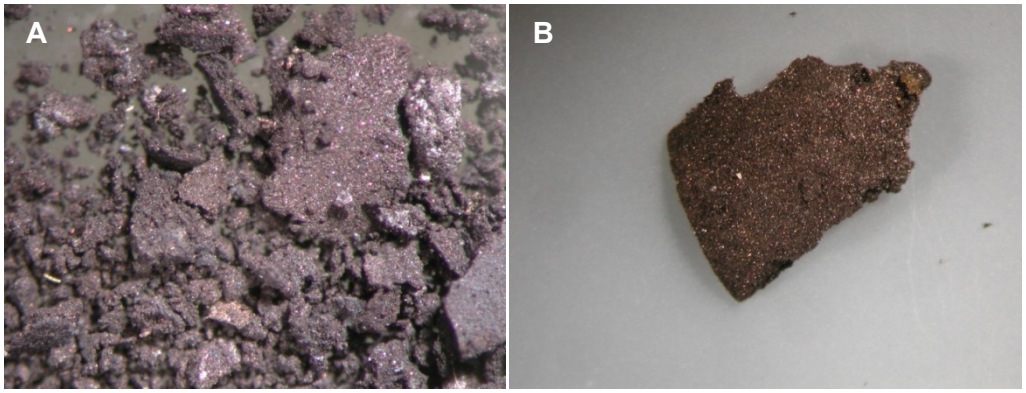

Figure 6.24. Optical microscope images of (A) pyrrolidine-treated PIDA and (B) pyridine-treated PIDA.

Although the macroscopic solids appear to be amorphous, on the microscopic level the base-treated PIDA maintains the fibrous morphology of pristine PIDA, as illustrated by the TEM images in Figure 6.25. The diameter of the base-treated PIDA fibers can be as low as 50 – 100 nm, promoting interest in studying indicating that to study charge transport in the nano-scale. In addition, as described in the previous section 6.2, other experiments indicate that PIDA is losing iodine during the reaction with Lewis bases. This result suggests a potential novel method to prepare carbon nanofibers by carbonization of PIDA through a mild organic reaction at room temperature.

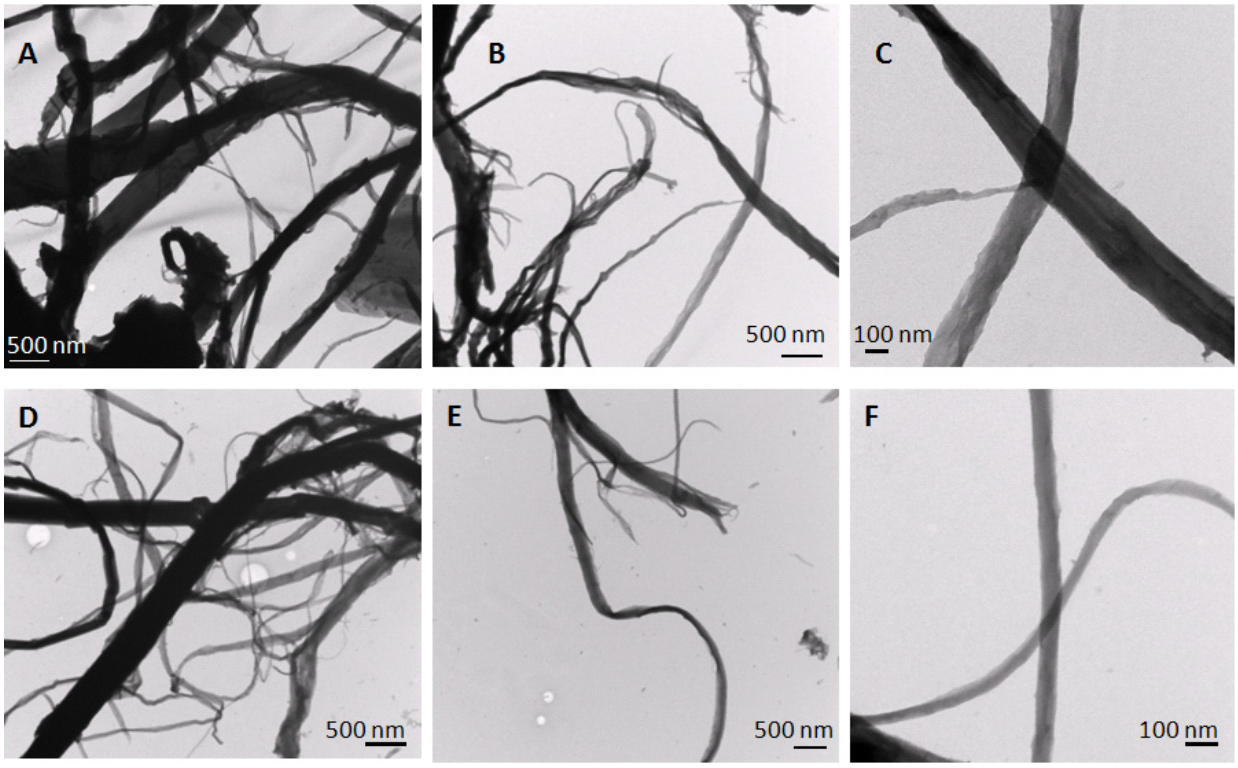

Figure 6.25. TEM images of base-treated PIDA fibers. A, B, and C: pyrrolidine-treated PIDA; D, E, and F: pyridine-treated PIDA.

High-resolution (HR) TEM images, performed with the help of Dr. More at ORNL, reveal that base-treated PIDA fibers are still amorphous at the nano-scale. There is no long-range ordered structure observed within these fibers, as show in Figure 6.26. Energy dispersive spectroscopy (EDS) spectra indicate that these fibers still contain some iodine. However, it is difficult to quantify their elemental composition due to the limitation of the method.

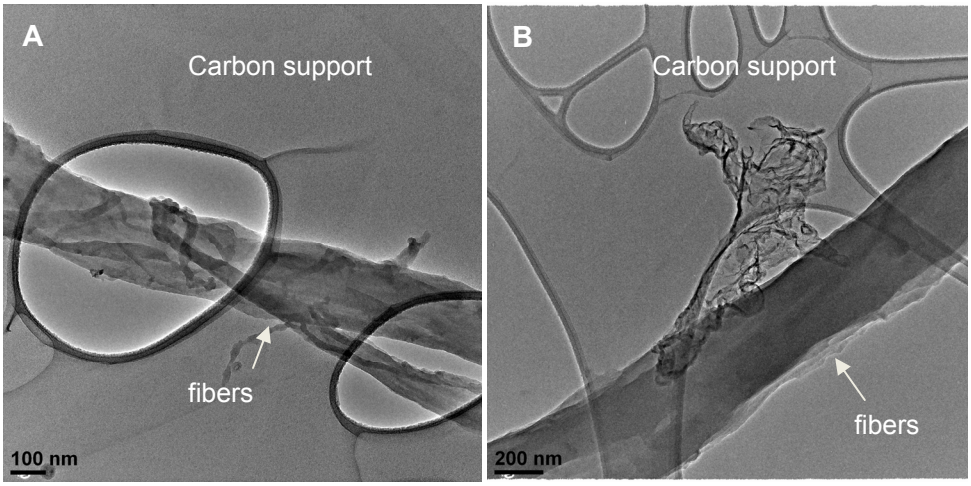

Figure 6.26. HR TEM images of base-treated PIDA fibers. A: pyridine-treated PIDA; B: pyrrolidine-treated PIDA. The fibers are loaded on top of a carbon support for every experiment.

The change in elemental composition change of PIDA by the treatment of Lewis bases is demonstrated by the elemental analysis reuslts of PIDA-related materials (performed by Elemental Analysis, Inc.), as listed in Table 6.1. Sample EA1 is isolated PIDA, which contains mainly of carbon and iodine plus trace amount of hydrogen and nitrogen. However, the sum of all listed elemental compositions is 95.81 %. The possible reason that it is less than 100 % is the inhomogenity of the PIDA sample, and there could also cotain other elements such as O. Sample EA2 is pyridine-treated PIDA, while EA3 is pyrrolidine-treated PIDA. Both EA2 and EA3 were taken from the reaction between PIDA and the Lewis base at the point when PIDA first lost its visible absorption, but remained the PDA backbone features, as identified by Raman. Although there is still inhomogenity problems, it clearly shows that the iodine composition starts to decrease at a very initial stage during the reaction. EA4 is the materials resulted from extensively washing PIDA by large excess of pyrroline. The significantly higher composition of nitrogen in EA4 possibly indicates that pyrrolidine is binded to the polymer, given that the observation from NMR titration experiment that soluble pyrrolidine is decreasing during the reaction. Unfortunately, the amount of this sample was too small to obtain iodine content information.

Table 6.1. lists the elemental analysis of various PIDA-related materials.

Sample*	Carbon (wt %)	Hydrogen (wt %)	Nitrogen (wt %)	Iodine (wt %)
EA1	18.42	0.34	0.44	76.61
EA2	26.55	1.37	2.18	70.55
EA3	26.80	1.08	2.31	63.84
EA4	51.74	4.95	8.46	N/A

*EA1: Isolated PIDA; EA2: isolated PIDA treated by neat pyridine; EA3: isolated PIDA treated by stroichiometric pyrrolidine in a media of methanol; EA4: isolated PIDA treated by large excess of pyrrolidine in a media of methanol.

6.6. Raman

The products of the reactions between PIDA and Lewis bases were subjected to Raman spectroscopy. Interestingly, these products exhibit Raman spectra similar to graphitic carbon. After treatment of PIDA in neat pure pyridine for three days, the resulting material gives an initial Raman spectrum that contains no structural information, using a 785 nm laser. Continuous exposure of the same area of the sample under the laser beam quenches some of the large fluorescence background in the Raman spectrum and reveals two very broad peaks centered at 1380 and 1560 cm^{-1}, as shown in Figure 6.27 A. The Raman spectrum of pyrrolidine-treated PIDA, obtained after stoicheometric reaction of PIDA and pyrrolidine over 9 days, demonstrates the same spectroscopic change as pyridine-treated PIDA. Shown in Figure 6.27 B, the broad peaks in the final spectrum of the new material are consistent with those of commercial graphite (Figure 6.27 C), indicating that base-treated PIDA generates sp^2-hybridized carbon within it.

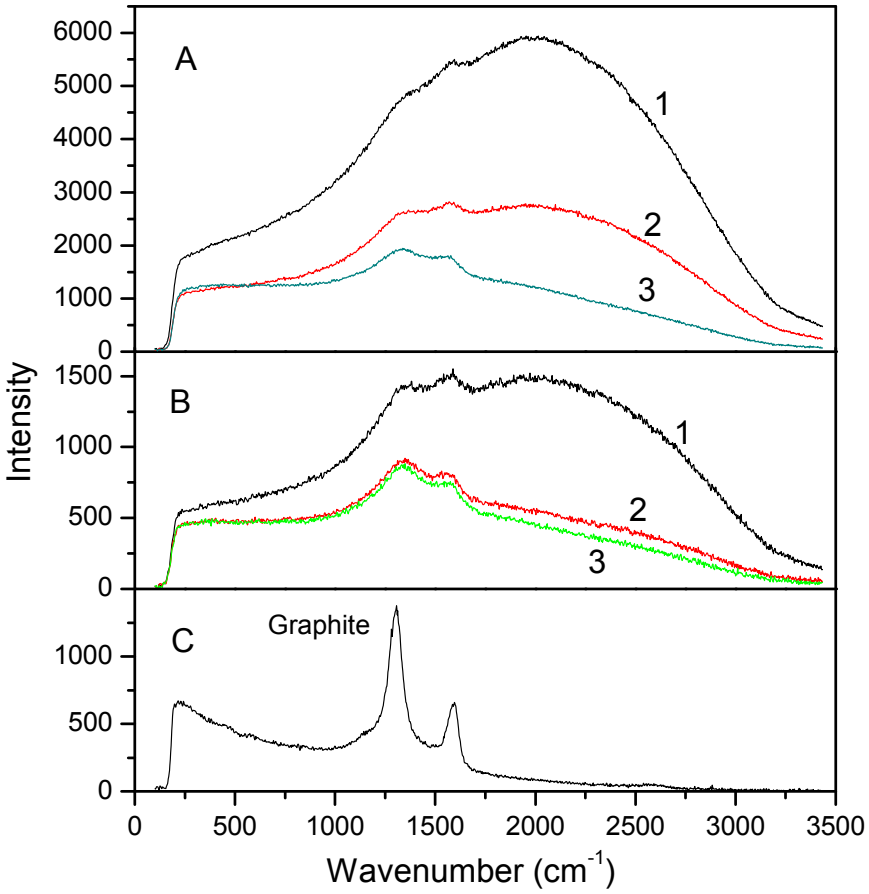

Figure 6.27. Raman spectra of base-treated PIDA materials using a 785 nm laser beam. A: Neat pyridine-treated PIDA; B: pyrrolidine-treated PIDA by a reaction of PIDA and stoichiometric pyrrolidine in methanol-d4; C: commercial graphite as a reference. Curves 1, 2, and 3 are the Raman spectra taken one after another on a selected area of the material.

Polarized Raman measurements, performed at Oak Ridge National Laboratory in collaboration with Dr. David B. Geohegan and Dr. Ilia Ivanov, further elucidate the change in PIDA materials upon base treatment. A sample of PIDA, after being dispersed in pure pyridine for one week, gives similar polarized Raman spectra in different areas and at different orientations, shown in Figure 6.28, indicating that the material becomes isotropic upon the treatment. There is a large fluorescence background signal in each Raman spectrum, making it difficult to obtain structural information from these spectra.

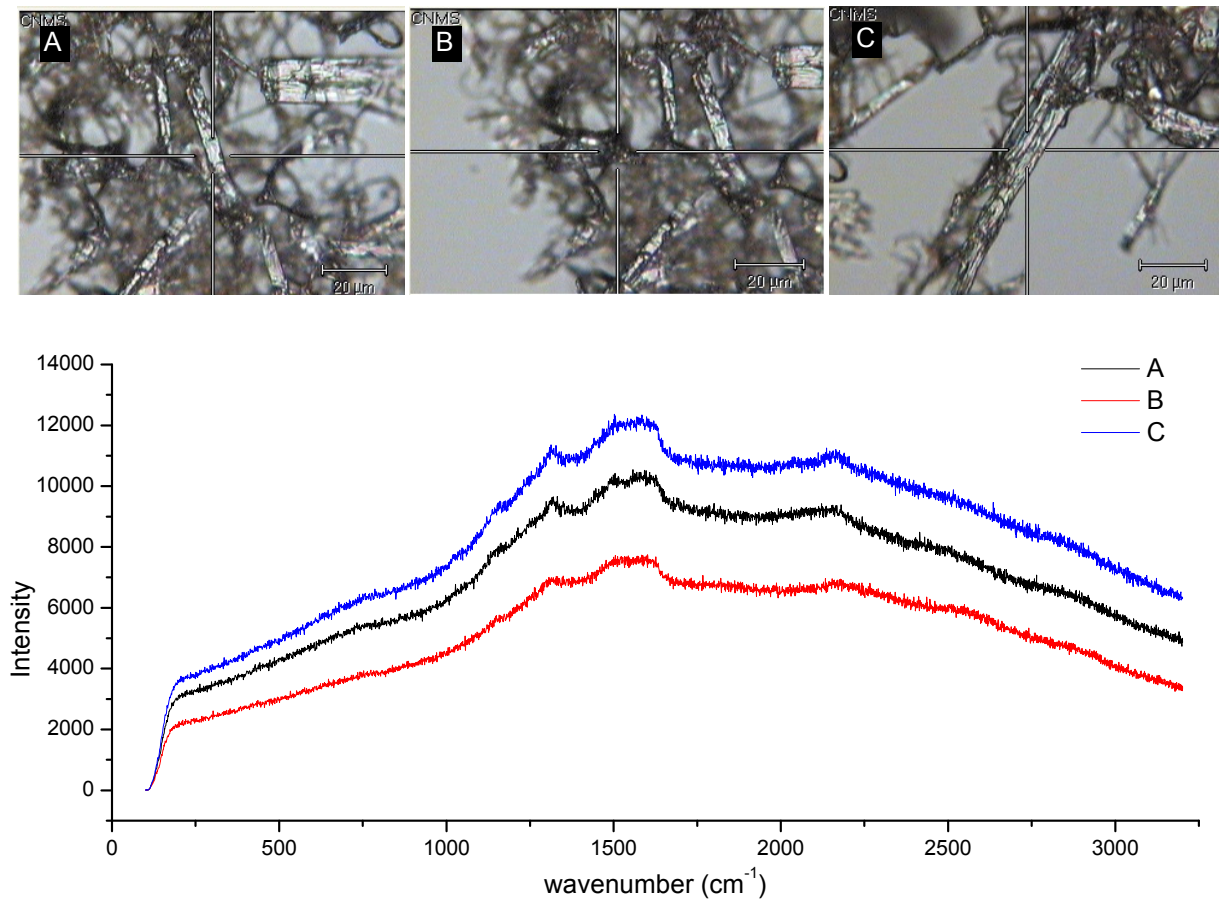

Figure 6.28. Polarized Raman spectra of pyridine-treated PIDA. A, B, C are different selected areas for the measurements.

The polarized Raman spectra of pyrrolidine-treated PIDA are more interesting. Different from pyridine case, the pyrrolidine-treated PIDA sample for polarized Raman measurements was prepared by the stoichiometric reaction of PIDA and pyrrolidine. The solid was collected by centrifuge after one week of reaction. The polarized Raman spectra of the sample show different features in different selected area. In some locations, such as one shown in Figure 6.29 A, matches pristine PIDA, while in others, it resembles sp^2-hybridized carbon, as shown in Figure 6.29 B.

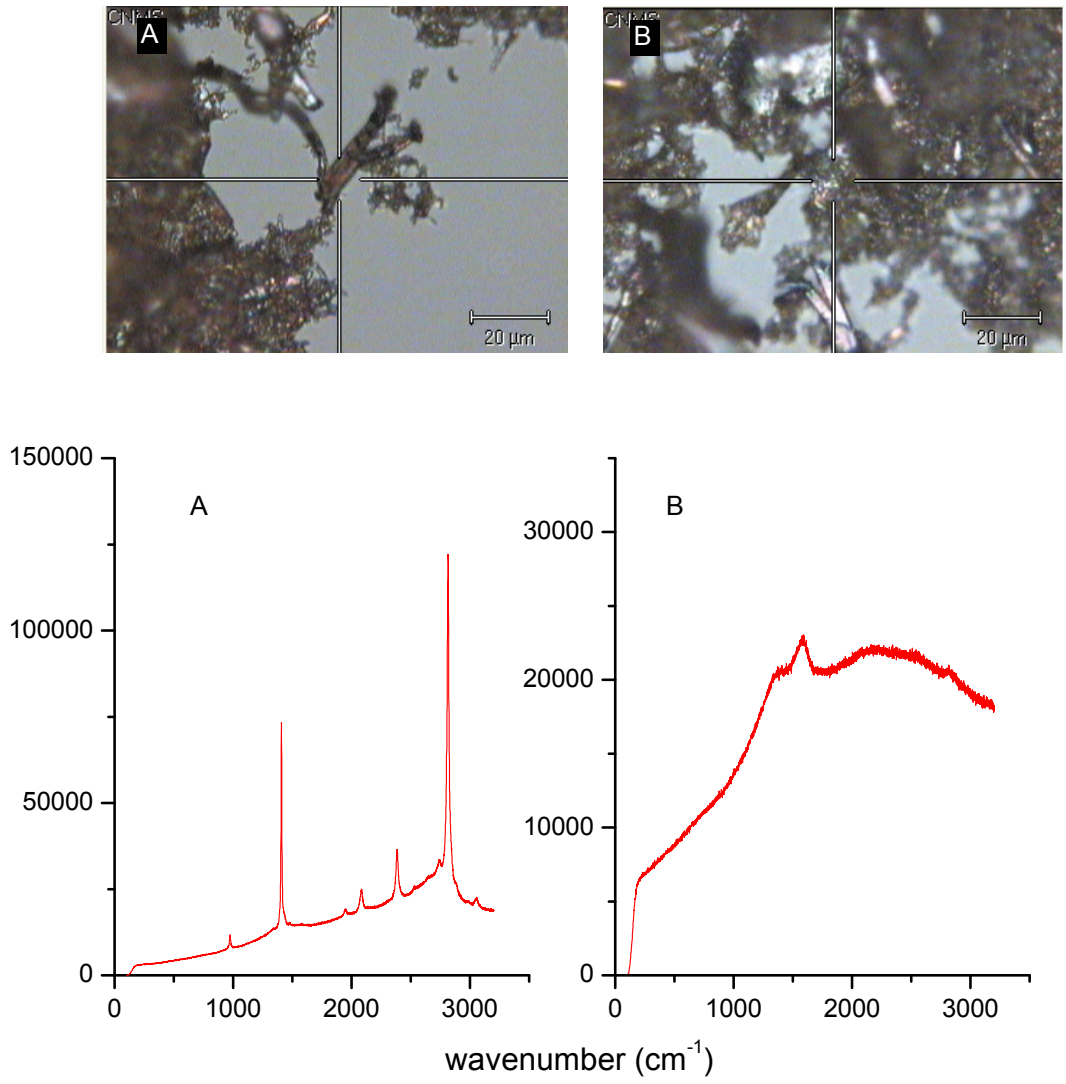

Figure 6.29. Polarized Raman spectra of pyrrolidine-treated PIDA. A and B are different selected areas for the measurements.

Raman mapping of the selected area in Figure 6.30 A indicates the structural transformation of the fiber. Using the selected frequency range in Figure 30 D, the double-bond streching band of PIDA, as a reference, the intensity of this band in the fiber is relatively low, as represented by the dark colors.

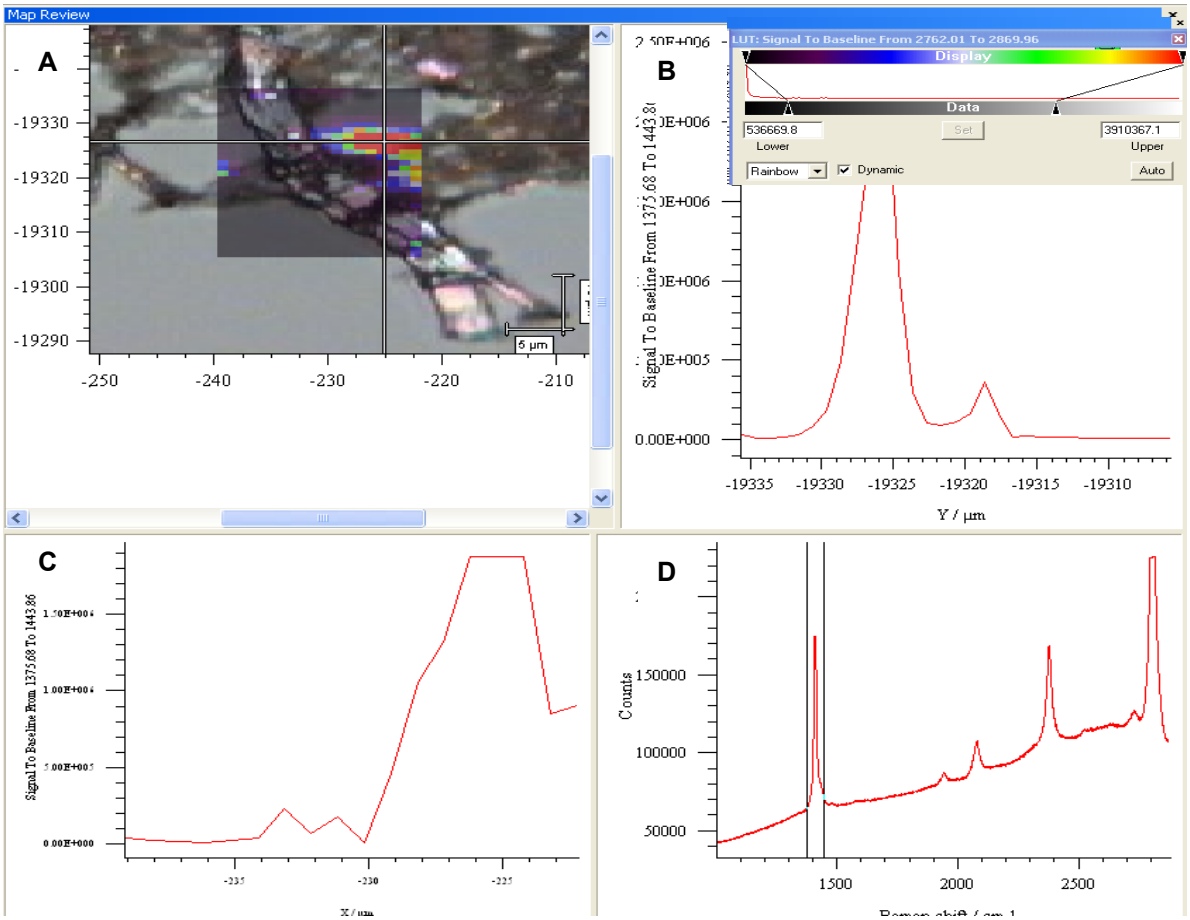

Figure 6.30. Raman mapping of selected area on a pyrrolidine-treated PIDA fiber, referenced by double bond stretching of PIDA (1407 cm^{-1}). A: Raman scattering intensity at each point represented by the color of that pixel; B: the scale of the scattering intensity represented by different colors; C: Raman scattering intensity along the x-axis of the area; D: The referenced frequency range, containing double-bond stretching of PIDA (1407 cm^{-1}).

However, if using the peak at 1600 cm^{-1} (sp^2-hybridized carbon) as a reference, shown in Figure 6.31 D, the scattering intensity of the fiber becomes much stronger (Figure 6.31 A). This observation indicates that the fiber has been carbonized already during the reaction between PIDA and pyrrolidine.

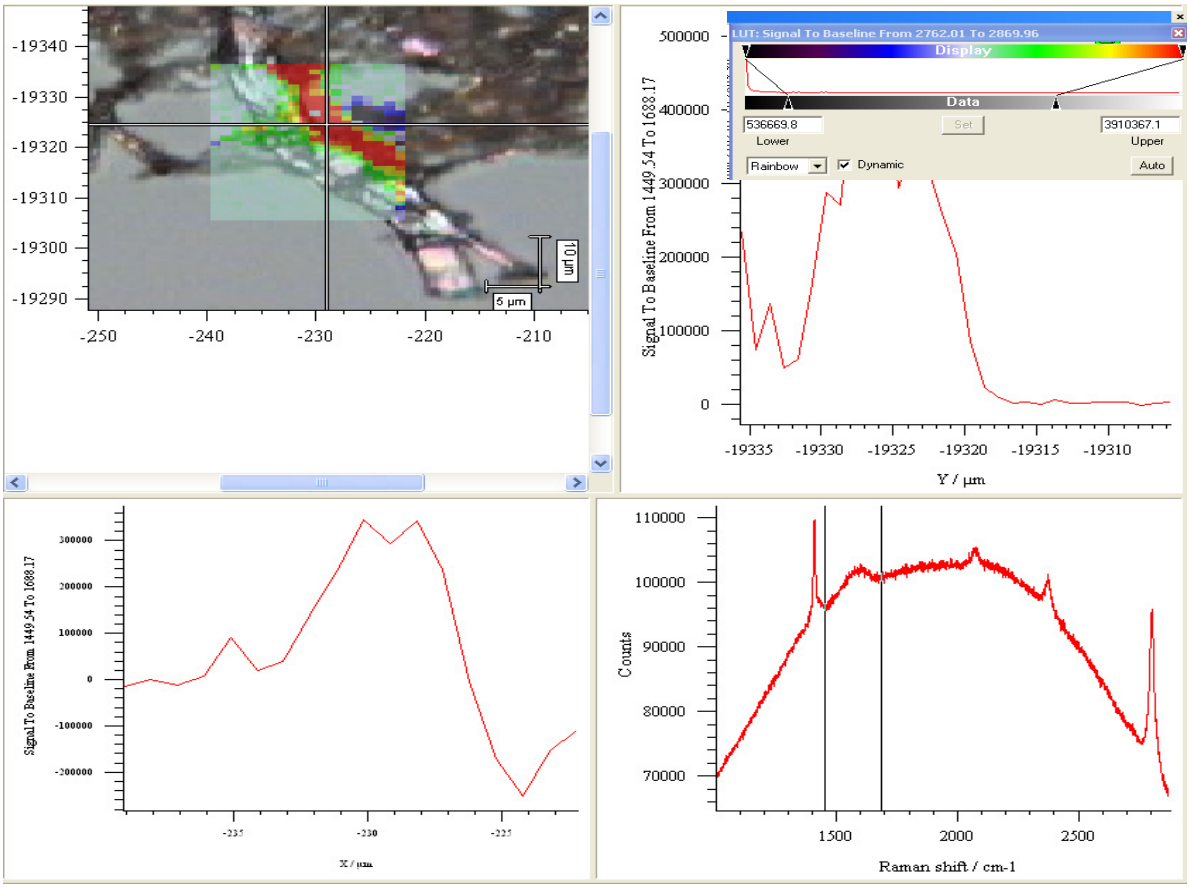

Figure 6.31. Raman mapping of selected area on a pyrrolidine-treated PIDA fiber, referenced by sp^2-hybridized carbon peak at 1600 cm^{-1}. A: Raman scattering intensity at each point represented by the color of that pixel; B: the scale of the scattering intensity represented by different colors; C: Raman scattering intensity along the x-axis of the area; D: The referenced frequency range, containing double-bond stretching sp^2-hybridized carbon peak of 1600 cm^{-1}.

Annealing of base-treated PIDA materials at 900 ^{o}C leads to complete carbonization of the material. The Raman spectra of annealed pyrrolidine-treated PIDA and pyridine-treated PIDA are similar to that of graphite, as shown in Figure 6.32. EDS spectra of both samples exhibit that all iodine has been dissociated by annealing.

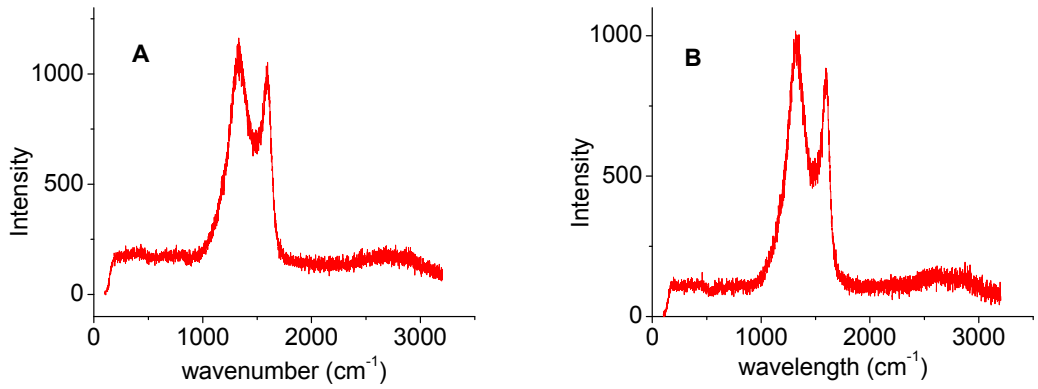

Figure 6.32. Polarized Raman spectra of annealed base-treated PIDA. A: pyrrolidine-treated PIDA; B: pyridine-treated PIDA.

In addition, HR TEM images of annealed pyrrolidine-treated PIDA show that turbostratic carbon[125] is formed during the treatment (Figure 6.33). This type of carbon, formed by carbon sheets that are haphazardly folded or crumbled, tends to have very strong tensile strength. The difference between annealed PIDA and annealed pyrrolidine-treated PIDA further illustrates the function of pyrrolidine on PIDA.

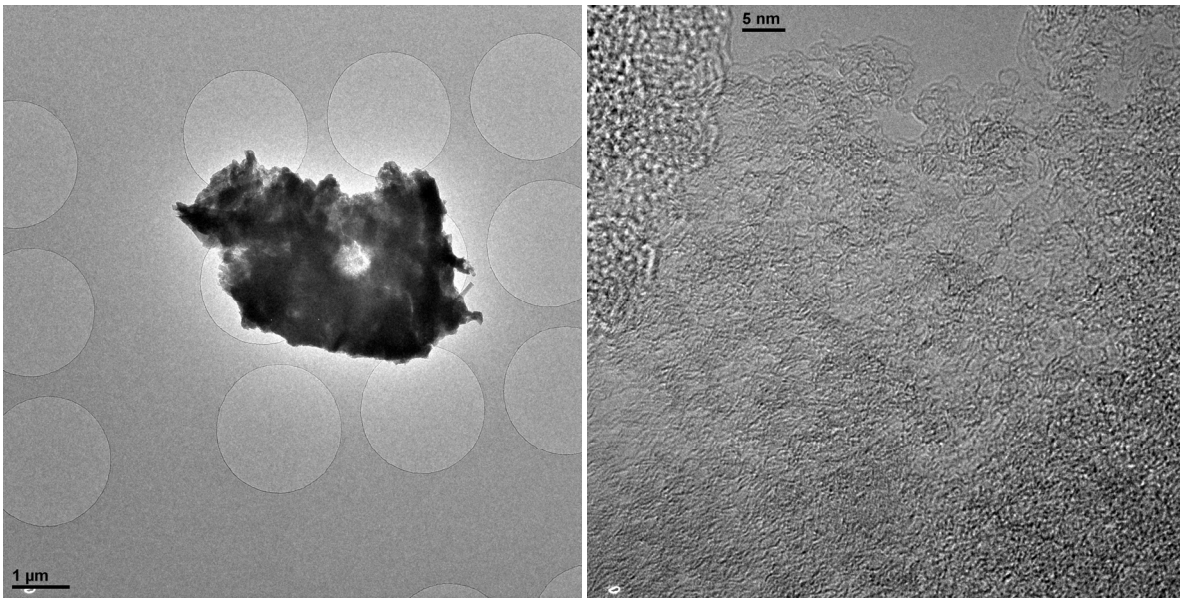

Figure 6.33. HR TEM images of annealed pyrrolidine-treated PIDA.

6.7. ^{13}C MAS NMR

Colleague Christopher Wilhelm has measured the ^{13}C MAS NMR of base-treated PIDA materials. Interestingly, the pyrrolidine-treated PIDA materials cannot spin in high magnetic field until dilute by $NaNO_3$. This phenomenon can be attributed to the generation of eddy current,[126] which is caused when a conductor is exposed to a changing magnetic field due to relative motion of the field source and the conductor; or due to variations of the field with time.[126] It suggests that the conductivity of PIDA has been significantly enhanced by treating with Lewis bases, consistent with the observation of UV/Vis/NIR transmittance spectroscopy.

The ^{13}C MAS NMR spectra of the solid residues obtained from the reaction of PIDA with pyrrolidine and with pyridine have been measured after they were diluted by $NaNO_3$. These spectra suggest properties distinct from the starting polymer (Figure 6.34). The original sp^2 and sp carbon peaks in PIDA are no longer distinguishable after the reactions, replaced by very broad peaks from ~50 – 150 ppm. These broad peaks are indicative of paramagnetic species present in the samples.

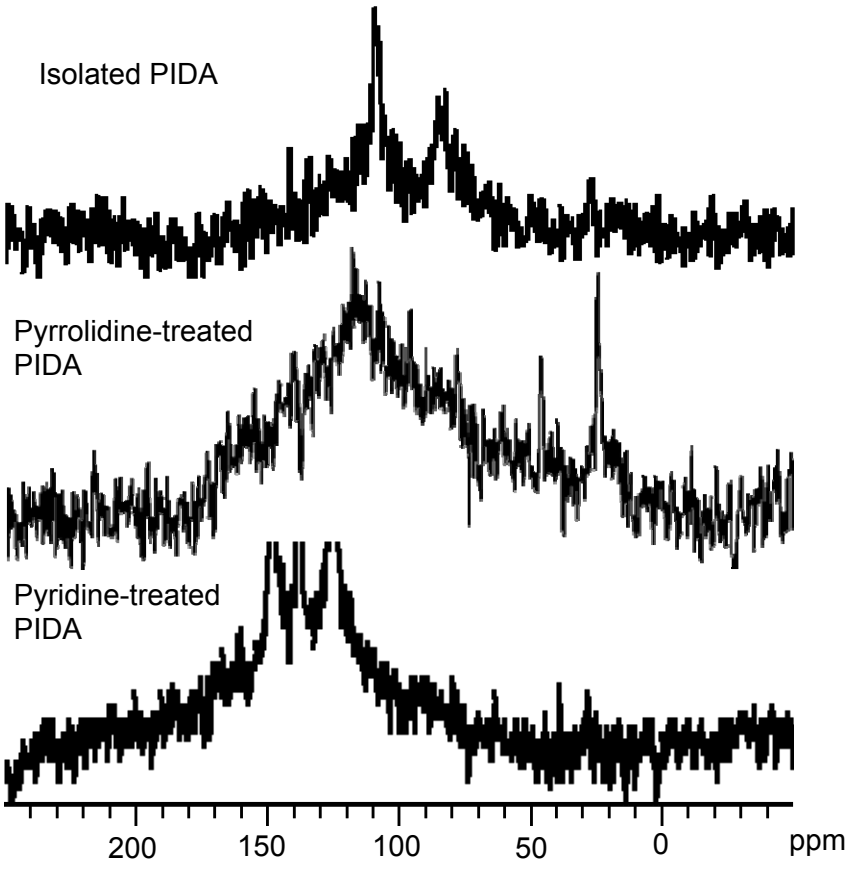

Figure 6.34. ^{13}C MAS NMR of isolated PIDA, pyrrolidine treated PIDA, and pyridine treated PIDA, conducted by Christopher Wilhelm.

6.8.Impedance studies

For conjugated polymers, charge mobility is often an important property. The observation that the pyrrolidine-treated PIDA sample dose not spin in high magnetic field made it especially interesting to study the electronic properties of pristine PIDA and base-treated PIDA. In collaboration with Prof. Richard J. Gambino of Department of the Material Sciences and Engineering at Stony Brook University, we have begun to measure the resistivity and capacitance of these samples.

Figure 6.35 shows a schematic representative of the circuit board used for these experiments. The circuit board is composed of two parts; a flexible Kapton (polyimide) substrate with a pattern of gold contacts made by laser micromachining at the left side, and a plastic chip with metallic bridges on the right. Isolated PIDA has been deposited on top of the gold electrodes by drop-casting suspensions. In each of the metallic bridges, one side is connected with a corresponding gold electrode by a fine copper wire, and the other side can be connected to various instruments to perform different types of measurements on the samples.

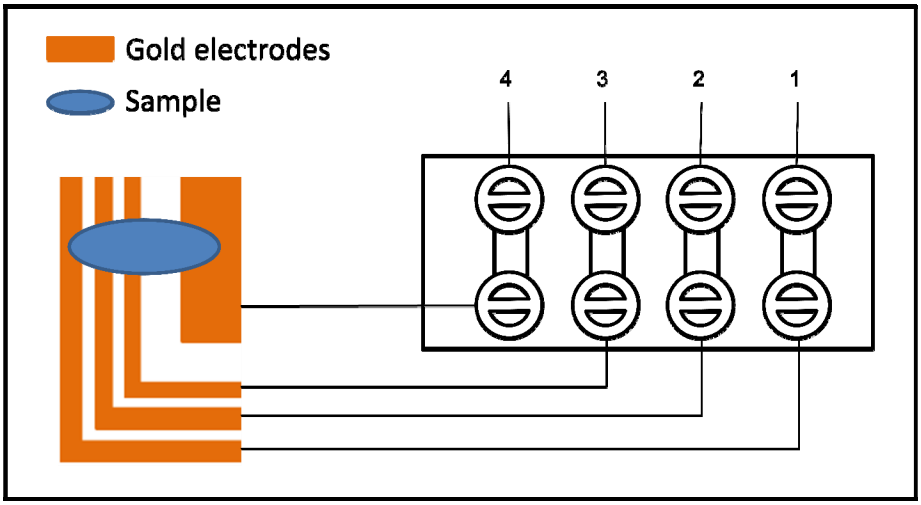

Figure 6.35. Schema of a circuit board used to measure the electronic properties of deposited film samples. The gaps between gold electrodes 1 and 2 and between electrodes 2 and 3 are 0.2 mm each and that between 3 and 4 is 1 mm.

The samples were first submitted to DC current-voltage measurement to obtain basic resistivity information, as shown in Figure 6.36. The current-voltage curves for both contacts 1-2 and 3-4 are almost linear, with measured resistance of about 9.5 MΩ. However, the gap distance between electrodes 3 and 4 is 5 times larger than between electrodes 1 and 2, and therefore the resistance between electrodes 1 and 2 should be around 5 times as that for electrodes 3 and 4, given that they have similar widths and heights. A concern is that the resistance of the isolated PIDA sample is so high that the measured resistance is that of the ohm meter. The same

experiment on a blank circuit board (only the ohm meter is connected) gives a similar resistance, indicating that the resistance of PIDA obtained is inaccurate.

The sample between electrodes 1 and 2

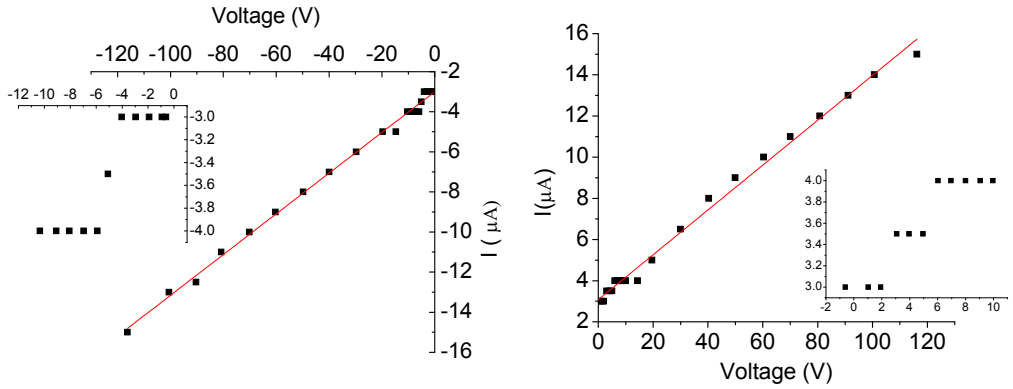

The sample between electrodes 3 and 4

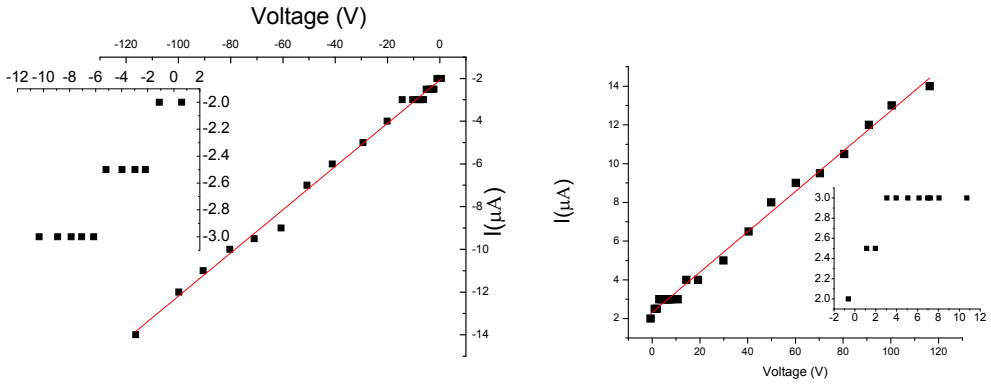

Figure 6.36. DC I-V curves of isolated PIDA samples between different electrodes.

Then the circuit board was connected to a LCR meter to perform the impedance studies on the materials. Impedance (Z) refers to the total opposition a device or circuit offers to the flow of an alternative current (AC) at a given frequency. The relationship between the amplitude of AC and Z was measured at a fixed frequency of either 500 KHz or 1 MHz. In general, the impedance

does not change significantly under different amplitudes of current. However, the resistances at 500 KHz are always higher than those at 1MHz, as shown in Figure 6.37.

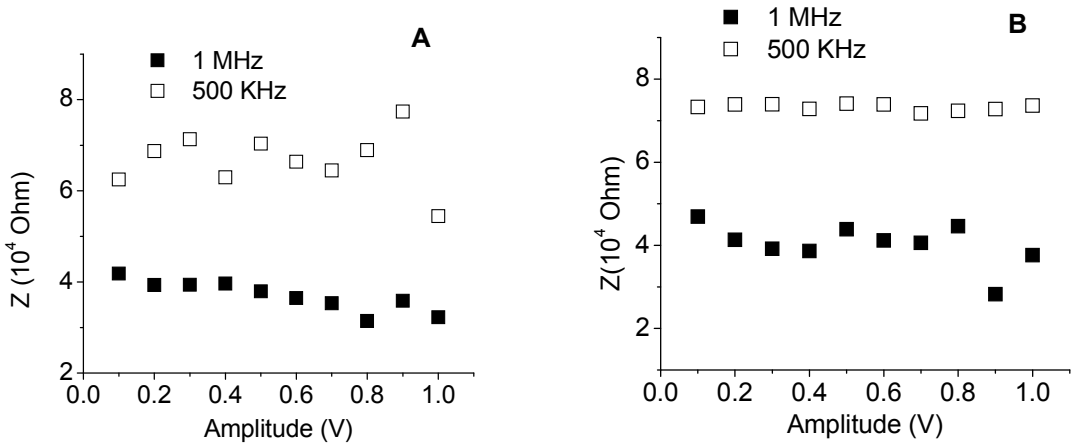

Figure 6.37. The relationships between Z and amplitude of AC for the isolated PIDA samples. A: Measurement of the sample between electrodes 1 and 2; B: measurement of the sample between electrodes 3 and 4.

Further impedance studies were performed as a function of frequency at fixed AC amplitude of 1.0 V. Figure 6.38 shows the change in Z as a function of frequency in the range of 1 KHz to 1MHz. The impedance of PIDA sample decreases with increasing frequency, linearly on a log scale. However, the measured resistivity values for the material are below zero. These non-physical values indicate that the large resistivity may be caused by the poor contact between the sample and electrodes.

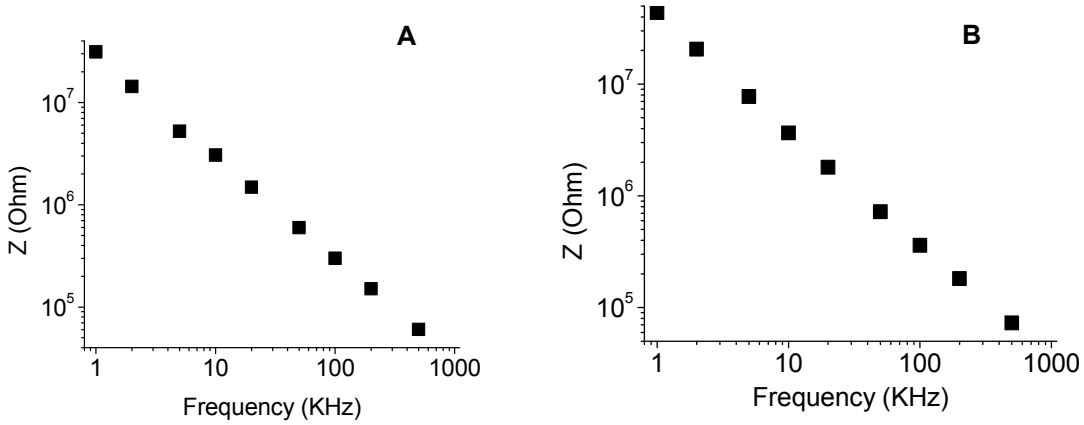

Figure 6.38. The relationship between Z and frequency of AC measured for isolated PIDA samples. A: Measurement of the sample between electrodes 1 and 2; B: measurement of the sample between electrodes 3 and 4.

To reduce the contact resistance, the PIDA-related samples have been studied in a new device, in which two copper tapes with conductive adhesives were connected to top and bottom sides of the PIDA sample, as schemed in Figure 6.39.

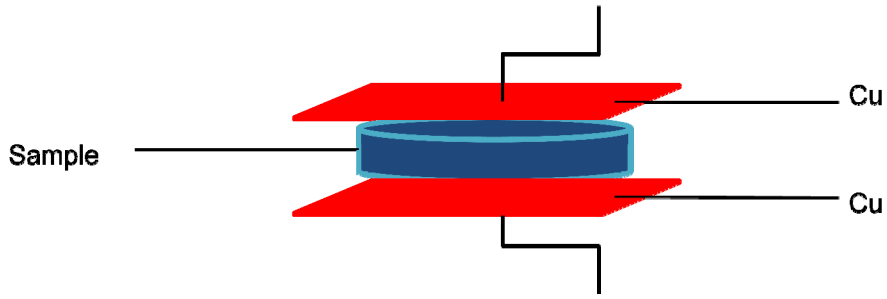

Figure 6.39. A schematic diagram of the top bottom contact mode.

The top bottom contact was submitted to experiments like those described above to characterize the impedance changes with frequency at a fixed amplitude of 1.0 V. The results shown in Figure 6.40 indicate that the resistivity of base-treated PIDA is apparently lower than pristine PIDA, as predicted from other experimental results. The resistivity ρ_Z of pyridine-treated PIDA is 10 times lower than that of the pristine PIDA at a given AC frequency, while

pyrrolidine-treated PIDA is 10^4 times lower than that of the pristine PIDA, as shown in Figure 6.40 A. Using the sample as a serial resistor, the obtain conductivities of pyrrolidine-treated PIDA is as high as 1 $S \cdot cm^{-1}$ when the AC frequency is 1 MHz, suggesting that the conductivity of PIDA has be significantly increased by treatment with pyrrolidine.

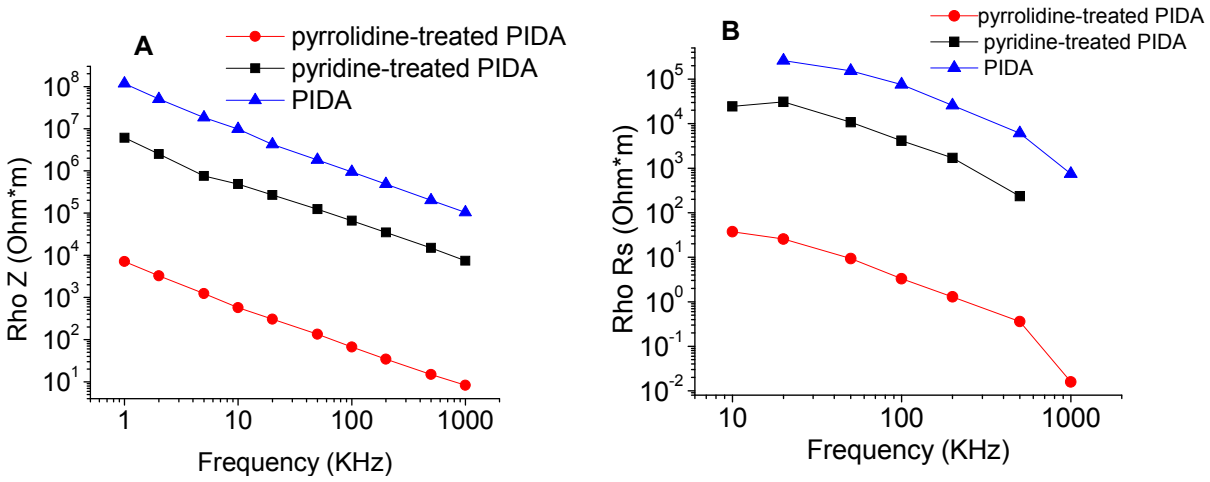

Figure 6.40. Resistivity of PIDA and base-treat PIDA obtained from impedance studies. A: resistivity obtained from impedance of the materials; B: resistivity obtained using the sample as a resistor Rs.

6.9. Summary and future work

In summary, the reaction between PIDA and Lewis bases has been studied by a variety of spectroscopic methods. This system is too messy for us to make general conclusions from what we observed here. However, it is still very interesting because of the potential for making new carbon-rich materials in a controlled way, under mild conditions. Future work will focus on optimizing the conditions and used bases to obtain full dissociation of iodine.

6.10. Experimental details

Preparation of pyridine-treated PIDA samples: Solid isolated PIDA can be obtained after centrifuging a blue PIDA suspension and decanting the supernatant. The solid isolated PIDA was dried in air, before it was dispersed in pyridine. UV/Vis absorption spectroscopy was used to

monitor the progress of the reaction. Neat pyridine was used in all the cases except for the stoichometric reaction, where calculated amount of pyridine was added dropwise through a micro-syringe to the PIDA suspension in methanol-d4. Centrifuging the PIDA/pyridine suspension and decanting the supernatant gave black wet solid at the bottom of the centrifuge tubes. The materials were dried in air before being subjected to other studies.

Preparation of pyrrolidine-treated PIDA samples: Pyrrolidine was added to the blue PIDA suspension in methanol or THF to prepare pyrrolidine-treated PIDA. Chloroform should be avoided due to the reaction between pyrrolidine and chloroform. In stoichiometric reactions, calculated amount of pyrrolidine was added to the PIDA suspension in methanol-d4 by a micro-syringe. In other situations, excess amount of pyrrolidine was added by a pipet to the PIDA suspensions. UV/Vis absorption spectroscopy was used to monitor the progress of the reaction. Centrifuging the PIDA/pyridine suspension and decanting the supernatant gave black wet solid at the bottom of the centrifuge tubes. The materials were dried in air before being subjected to other studies.

The instrumental methods of ^{13}C MAS NMR, Raman, polarized Raman, UV/Vis absorption spectroscopy, ESR, and electronic microscopy have been introduced in previous chapters.

UV/Vis/NIR: UV/Vis/NIR spectra of all suspensions were recorded in 1-cm cells using a Varian Cary 5E spectrometer, located in College of Chemistry, Georgia Institute of Technology. UV/Vis/NIR transmittance spectra of PIDA-related fibers were recorded using a Cary 5000 UV/Vis/NIR absorption spectrometer. Each sample of the fibers was prepared by drop-casting the corresponding suspension to a quartz slide. The slide was loaded onto the support for the transmittance measurements.

Impedance studies: The preparation methods of samples have been introduced in Section 6.9. The impedance studies of the aligned circuits shown in Figure 6.35 and 6.39 were carried out using a 1920 Precision LCR meter, which recorded the total opposition a device or circuit offers to the flow of an alternating current (AC) at a given frequency.

Chapter 7. Topochemical Polymerization of Polyynes

7.1. Introduction

7.1.1. Synthetic background of polyynes

Polyynes, molecules that contain two or more conjugated triple bonds, have attracted great interest in recent years due to their interesting properties and the synthetic challenge.[62,63] Compared to diamond and graphite, which represent three-dimensional sp^3 polymeric carbon and two-dimensional sp^2 polymeric carbon respectively, one-dimensional polymeric *sp* carbon, named carbyne, is much less stable. This makes carbyne present a significant synthetic challenge to date.

Researchers have developed many useful methodologies for synthesizing polyynes. In 1972, Walton built end-capped polyyne rods by the Cadiot-Chodkiewicz and Hay coupling reactions, using trialkylsilyl protecting groups.[127] Using the route shown in Scheme 7.1, Walton and coworkers prepared silyl-protected alkynes with up to 24 sp carbons.

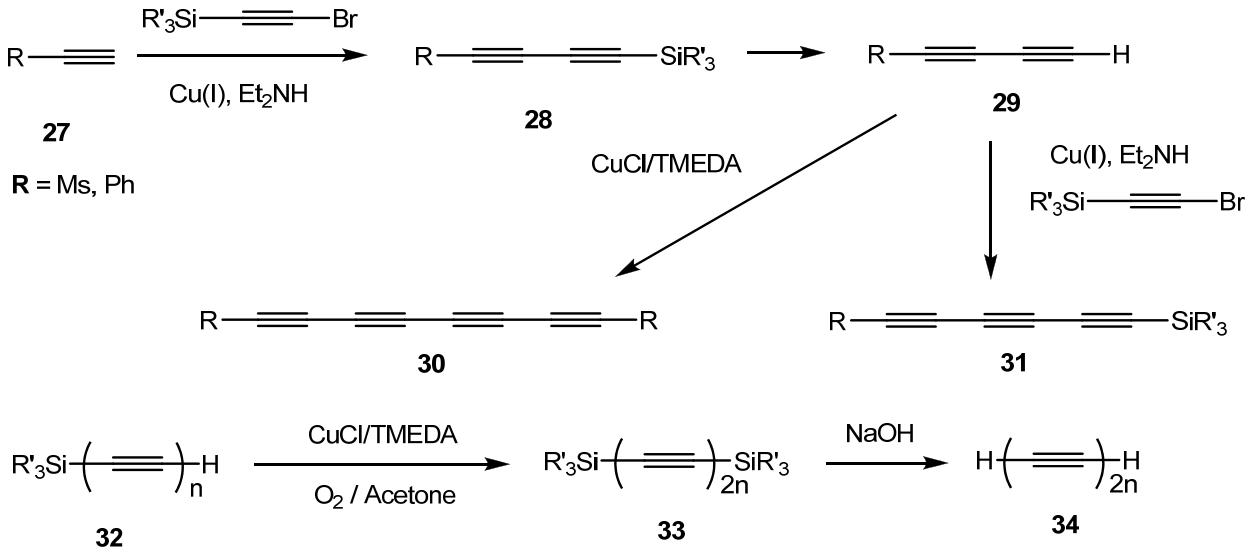

Scheme 7.1. Walton's routes toward polyynes.

Diederich and coworkers developed an alternative route to synthesize asymmetric polyynes, using a solution-spray flash vacuum pyrolysis technique (SS-FVP). As shown in Scheme 7.2, the asymmetric cyclobutenedione precursor **37** can readily lose two equivalents of carbon monoxide to give an asymmetric polyyne under SS-FVP conditions. This method has also been used to synthesize symmetric polyynes such as 1,10-diphenyl-1,3,5,7,9-decapentayne.[128]

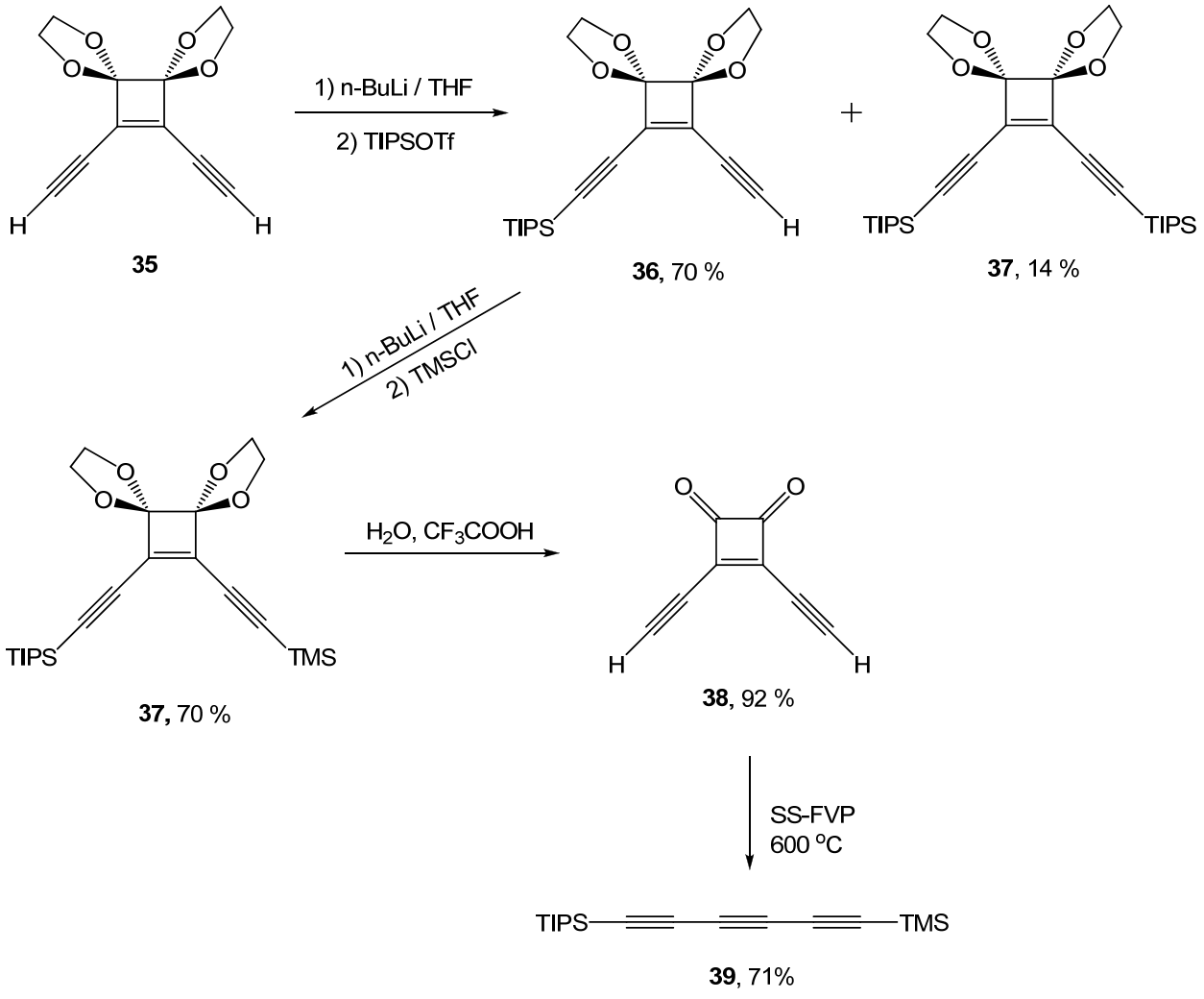

Scheme 7.2. The route to polyynes via a SS-FVP method.

Tykwinski and coworkers developed a new route to construct end-capped polyyne rods by combining the Hay-coupling reaction and the Fristsch-Buttenberg-Wiechell (FBW) rearrangement of dibromoolefin precurs.[129] As an example shown in Scheme 8.3, the dibromoolefin precursor **43** was prepared from Hay coupling of **42**, which was produced from acetyl chloride **40**. Reaction with n-BuLi at -78 ^{o}C converts **43** to desired octayne **44** through the FBW rearrangement.

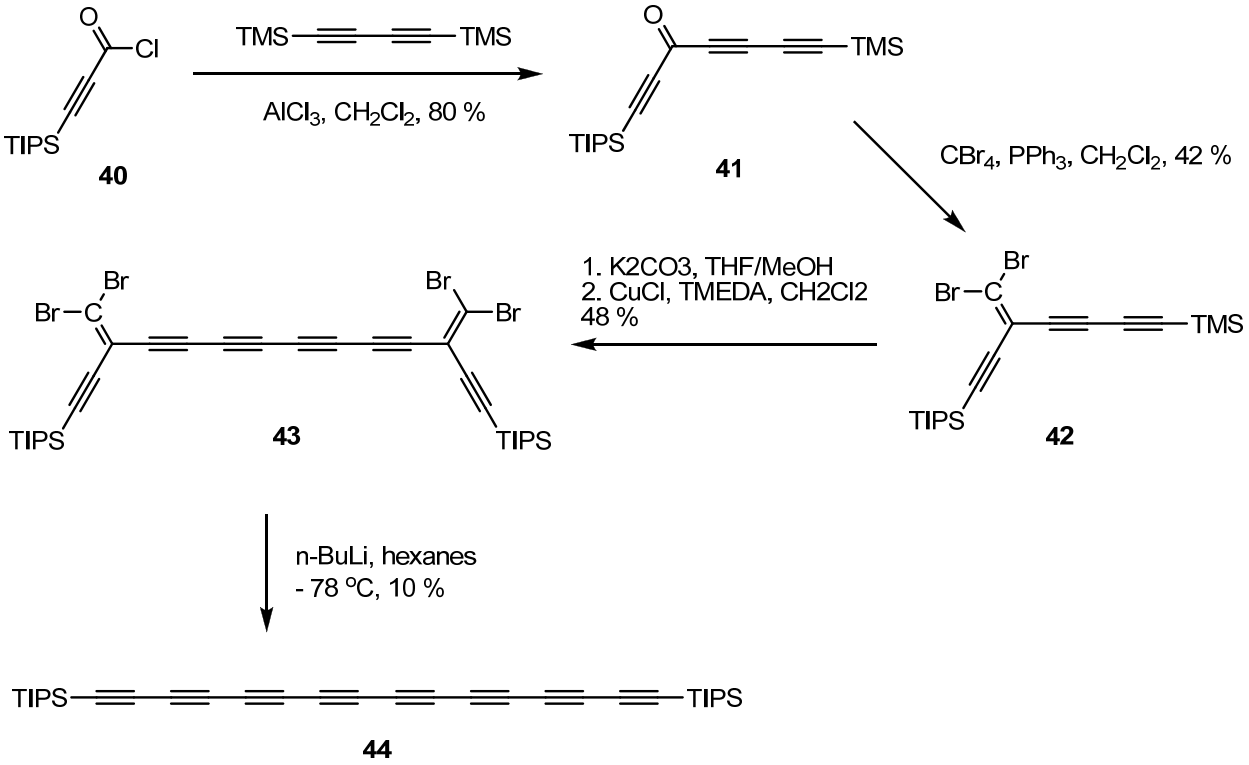

Scheme 7.3. Approaching polyynes through FBW rearrangement.

Li and Goroff have developed a new iterative synthetic strategy to synthesize polyynes. This method can be used to prepare symmetric polyynes in high yield under mild conditions, as shown in Scheme 8.4.[130] To synthesize long-chain polyynes, shorter iodo-capped polyyne **45** reacts at both ends with silyl-protected metal alkylides via palladium-catalyzed coupling reactions. The resulting longer symmetric silyl-protected polyyne rod **46** can be iodinated and

carried through the next coupling reaction. By recursive iteration of this method, the length of the polyyne increases four *sp* carbons every two steps. This strategy makes it possible to lengthen the polyyne symmetrically from both ends. It avoids the generation of terminal alkynes, which decomposes quickly and leads to low yields. Compared to the FBW rearrangement method, this strategy requires fewer steps, and produces polyynes in a higher yield, and the required conditions are much milder than the SS-FVP method. We will use this methodology to prepare polyynes for the desired topochemical polymerization.

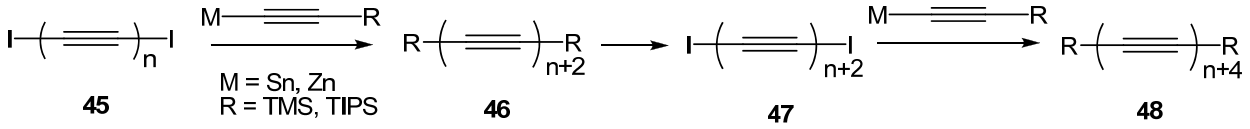

Scheme 7.4. Iterative synthesis toward symmetric polyynes.

7.1.2. Topochemical polymerization of polyynes

Despite the challenge in their synthesis, polyynes are interesting structures for materials chemistry, molecular electronics and carbon science.[131] Polyynes are found in interstellar space, plants, fungi, and marine organisms.[132,133] In addition, polyynes are assumed to be precursors of fullerenes[134] and carbon nanotubes.[135] Polyynes higher than ethyne are unstable and explosive unless they are end-capped with suitable substituents, such as silyl groups and transition metal complexes.[63] However, the inherent instability of polyynes can also be utilized for soft-chemical synthesis of nanocarbons, including multiwall carbon nanotubes[136] and onions.[137]

Shuji Okada and coworkers reported the 1,4-topochemical polymerization of octatetrayne and dodecahexayne in 1994.[138] They proposed that the polymerization of these polyynes proceed in two steps (Scheme 7.5). In the first step, the monomers are polymerized by the reaction at the

1 and 4 positions to give poly(diacetylene)s with butadiyne (for octatetrayne) or octatetrayne (for dodecahexayne) side groups. In the second step, a second topochemical polymerization occurs, involving the polyyne substituents, to give ladder polymers with two parallel poly(diacetylene) chains, as shown in Scheme 7.5.

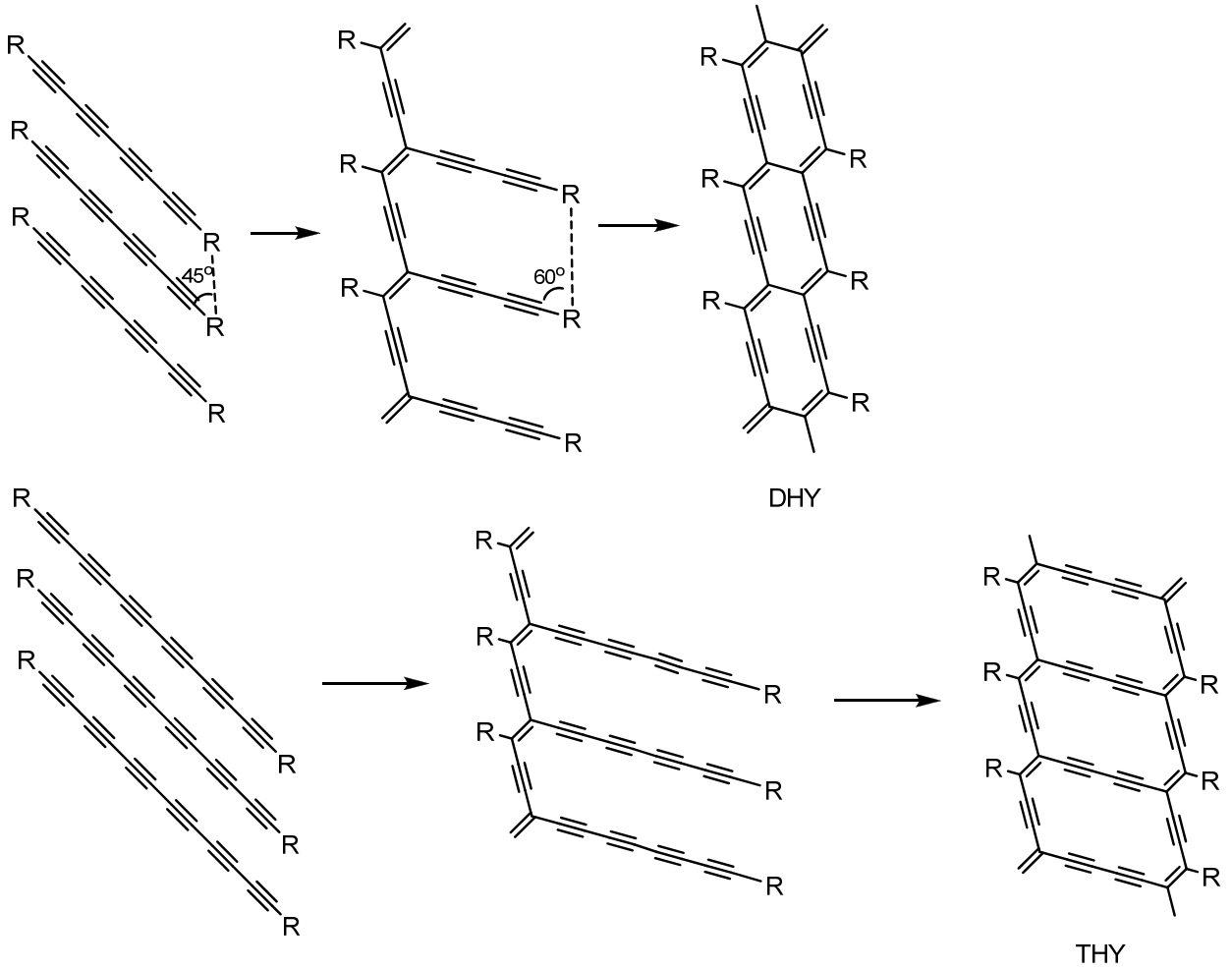

Scheme 7.5. Solid-state 1,4-polymerization of octatetrayne (DHY) and tetracontahexayne (THY) developed by Shuji Okada.[138]

Absorption spectra of the products show that there are Vis/NIR absorption peaks, as shown in Figure 8.5 A. ^{13}C MAS NMR has also been used to characterize the insoluble products. The newly appeared multiple broad peaks in a range from 50 – 200 ppm in the NMR spectra have been assigned to the backbones of the laddered polymers (Figure 8.5 B). Although the packed

geometries for the polyyne substituents have changed significantly after the first step, it is still possible for another topochemical polymerization to take place within the formed polydiacetylene, if the packing of the polyynes is not so regular in the solid state. In addition, if the laddered bi-PDAs is formed, it will continue to generate graphitic ribbon structures, which have a much lower energy than the ladder intermediate.

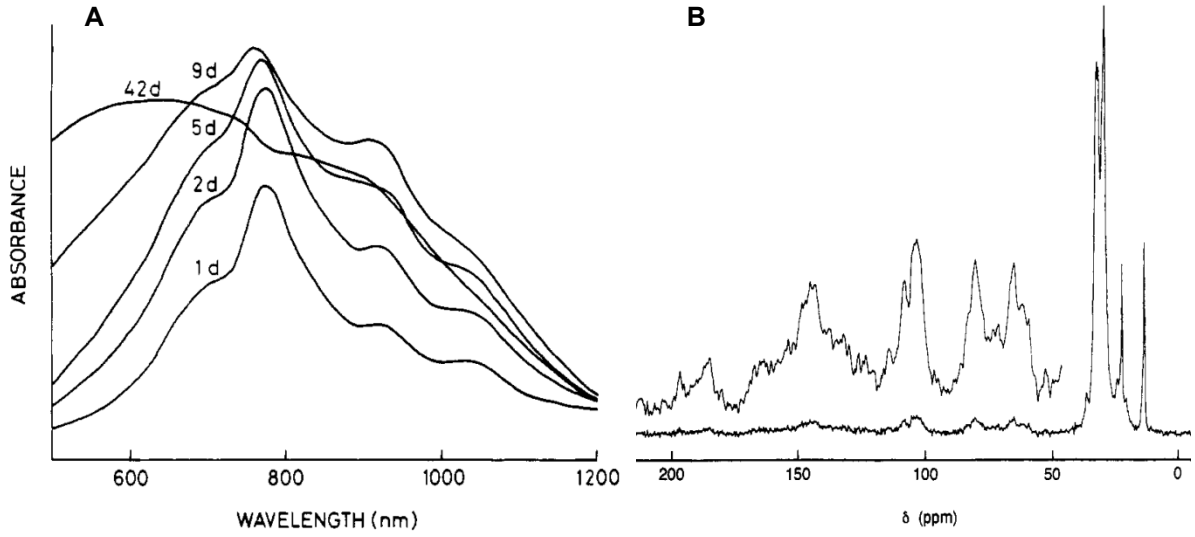

Figure 7.1. A: Vis/NIR spectral changes of aligned hexayne monomers in the course of solid-state polymerization at ambient temperature; B: ^{13}C MAS NMR spectrum of THY in Scheme 7.5.

Susan Olesik and coworkers prepared polymer nanospheres and carbon nanospheres using the cross-linking reaction of aligned 1,8-dihydroxylmethyl-1,3,5,7-octatetrayne films.[139] Carbon nanophase materials can be obtained by pyrolysis of the cross-linked polymers at 800 ^{o}C. The XPS data confirmed that 46 % of carbon in the product was found to be involved in carbon-carbon double bonds. The Raman spectrum of carbonized cross-linked polymers after pyrolysis is similar to that of glassy carbon or microcrystalline graphite.

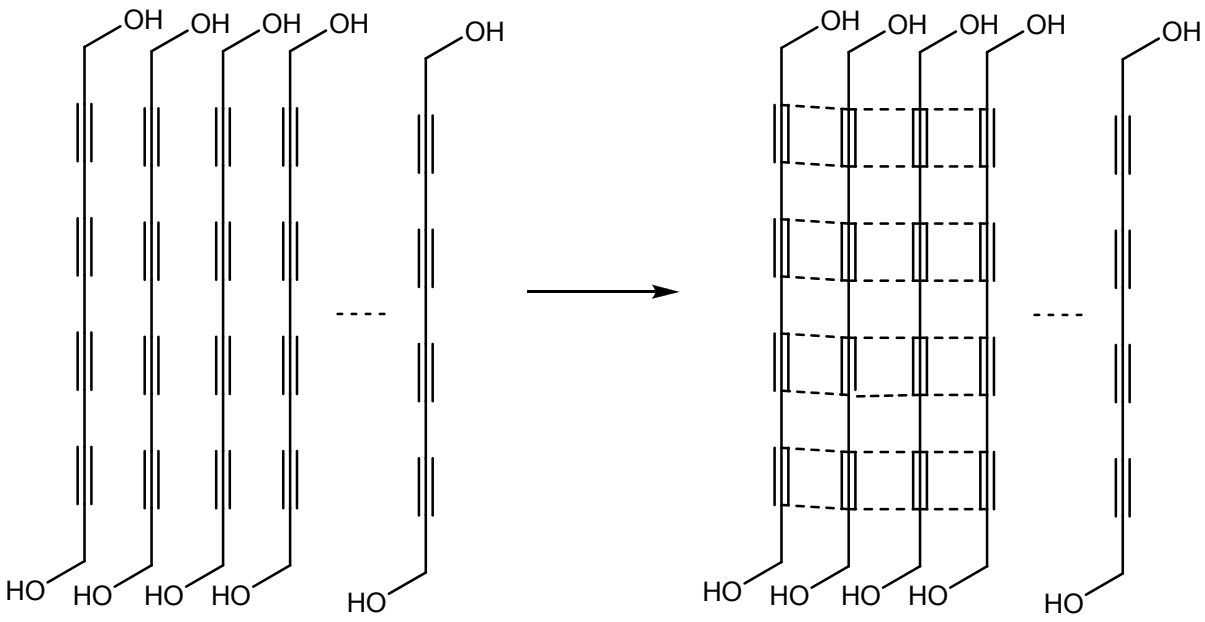

Scheme 7.6. Formation of cross-linked poly(tetrayne) ultrathin films.

Although the topochemical polymerization of butadiyne has been extensively studied over the decades, the topochemical polymerization of elongated polyynes is more limited, possibly because that the monomer polyyynes are less stable and the polymerization is more complicated. However, it is of great interest to investigate the possible topochemical polymerization of aligned polyynes, which will provide a potential method to approach novel carbon-rich or graphitic materials. In our work, we propose to take the advantage of the host-guest co-crystal strategy that has been well developed in our group. Iodo-capped polyynes can form co-crystals with hosts containing terminal nitrogen atoms. The well-defined alignment of polyynes within the co-crystals will help to rationalize the inherent polymerization procedures, and produce novel materials with clearly resolved structures.

7.2. Synthesis of polyynes via the iterative strategy

To synthesis bis(triisopropylsilyl)-1,3,5,7,9-pentayne **49** through the iterative synthetic methodology, trimetyhlsilyl acetylene **49** was iodinated to diiodoacetylene **51**. Two more steps

produce diiodohexatriyne **53**, adding two triple bonds to the polyynes. Hexatriyne **53** can be further elongated to pentayne **58** using the same strategy, which will be performed by another Goroff group member Raquel Campo.

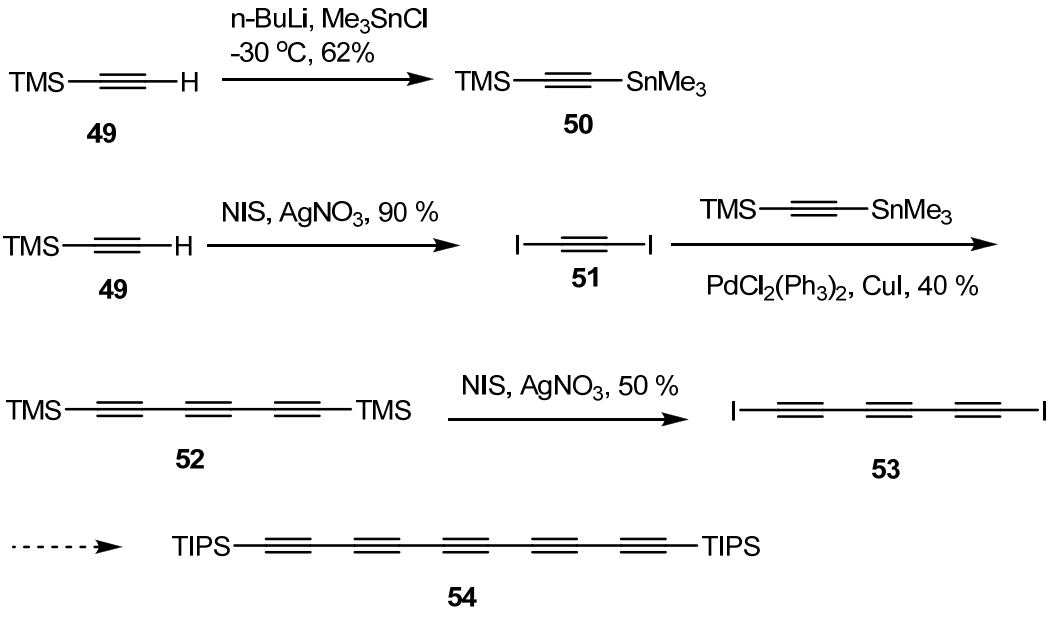

Scheme 7.7. Approaching pentayne **58** starting from trimethylsilyl acetylene **53**.

An alternative method to prepare diiodotriyne **53** was developed by Gao and Goroff.[74] Using a method developed by Rubin,[140] bis(trimethylsilyl) hexatriyne **52** can be obtained by the reaction between bis(tosyl) ester of 2,4-hexadiyne-1,6-diol **55** and n-BuLi in the presence of an excess of chlorotrimethylsilane. This method starts from a cheaper starting material and produces the desired product in one step. However, the conversion was not very high even after several trials. The latest results from Campo indicate that it is essential to use fresh n-BuLi, because any contaminated lithium hydroxide in the n-BuLi may possibly ruin the reaction by substituting at thetosylate group and generate dimerized impurities.

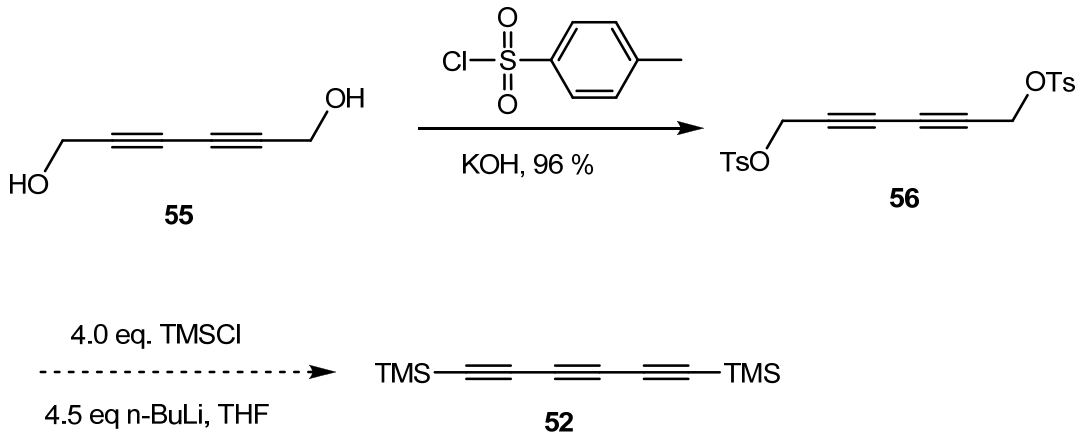

Scheme 7.8. Alternative preparation method for bis(trimethylsilyl) hexatriyne **56**.

To prepare diiodooctatetrayne **60**, and other polyynes with even number of triple bonds, we starts from Diiodobutadiyne **1**, the monomer of PIDA. A palladium catalyzed coupling reaction between **1** and acetylide **49** produces silyl-capped octatetrayne **58**, which can be iodinated to generate **60**. This iterative synthetic method is expected to produce symmetric polyynes with up to 20 sp carbons. This work will be continued by Raquel Campo.

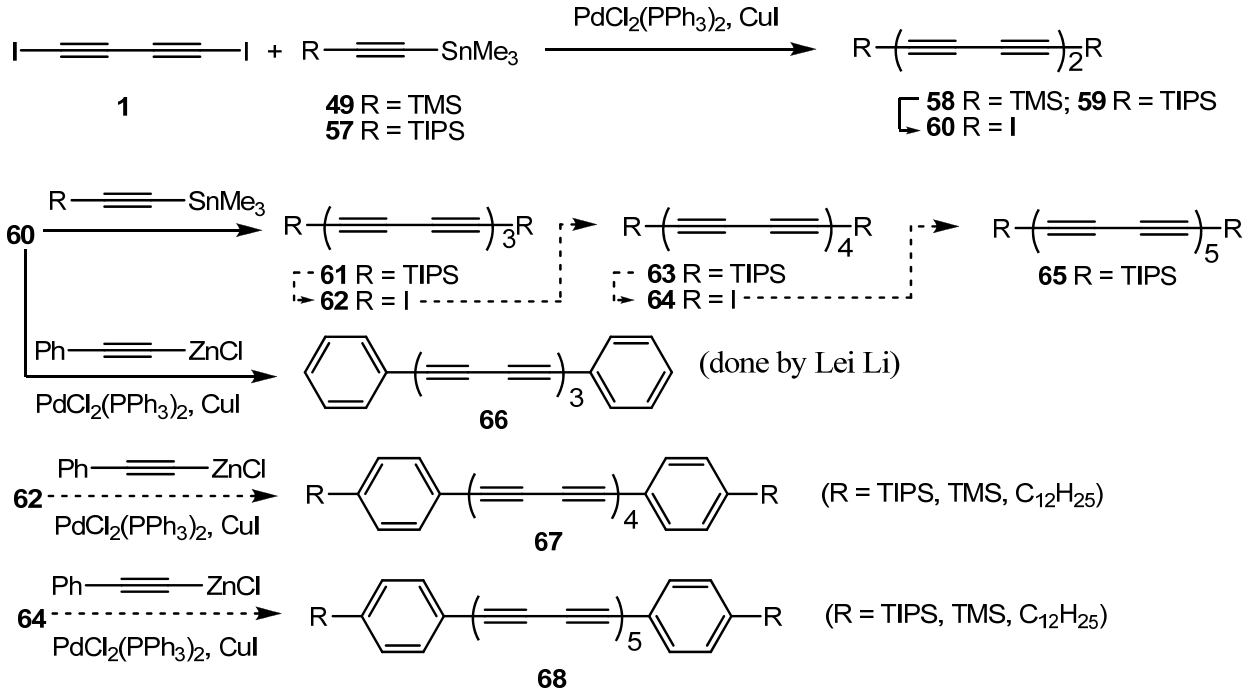

Scheme 7.9. Synthetic routes toward polyynes with even number of triple bonds.

7.3. Building co-crystals of iodo-capped polyynes

The preliminary attempt to build co-crystals of extended iodine capped alkynes was carried out by Webb and coworkers.[93] Diiodohextriyne **53** can form co-crystal with N,N'-bis(3-pyridylmethyl)-oxalamide (host **3**), similar to what we observed on co-crystals of diyne **1**. The repeat distance *r* of aligned triynes is a little larger than the optimal value. However, the C1-C4 contact distance *d* and tilt angle θ are very suitable for a 1-4-polymerization. Unfortunately, previous attempts to induce the polymerization within the co-crystal failed to produce polymer with a clear structure.

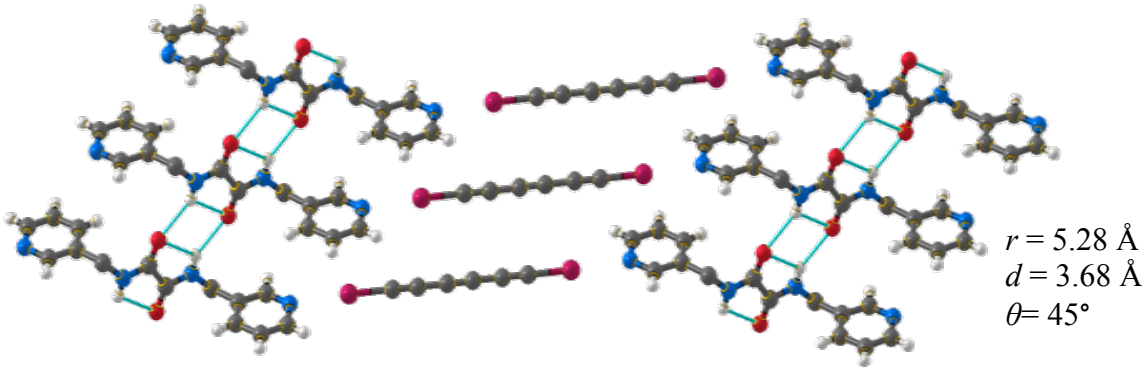

Figure 7.2. Crystal structure of co-crystal **3·53**.[93]

Polyyne1,8-diiodooctatetrayne **60** was attempted to build co-crystals with previous developed hosts. The conditions for growing tetrayne co-crystals are similar to those for growing PIDA co-crystal, except for a lower temperature of 4 ^{o}C. Of the hosts we have attempted, host **3**, host **4**, and N, N'-bis(3-pyridylethyl)-oxalamide **69** give XRD quality co-crystals with C_8I_2. Allison Black in our group has demonstrated that the co-crystal **3·60** can also grow at -20 ^{o}C. Figure 7.3 shows the morphology of co-crystal **3·60**, which appears green yellow when it forms at -20 ^{o}C but turns green quickly when exposed to room temperature. Staying at room

temperature for a longer time causes the co-crystals to turn darker and to gradually lose crystallinity.

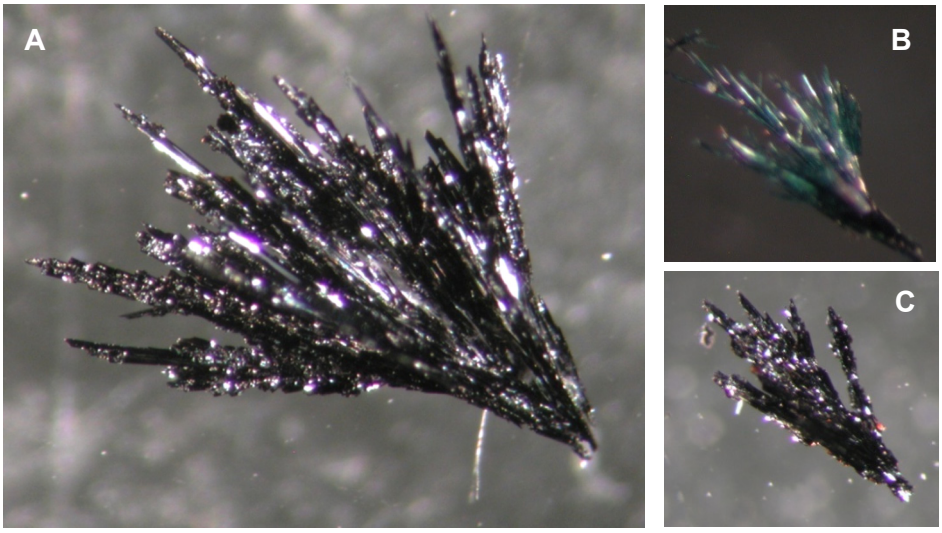

Figure 7.3. Optical microscope images of co-crystal **3·60.** A: The co-crystals after staying at room temperature for 1 week; B: The co-crystals after staying at room temperature for 1 min.; C: The co-crystals in B that stayed at room temperature for 1 week.

Host **69** can also form co-crystals with tetrayne **60**. The formed co-crystals between **69** and **60** contain two different crystal morphologies, as shown in Figure 7.4. One type of crystals appears reddish yellow, and the other one has a similar appearance as co-crystal **3·60**. Both types of crystals turn dark quickly at room temperature and lose crystallinity.

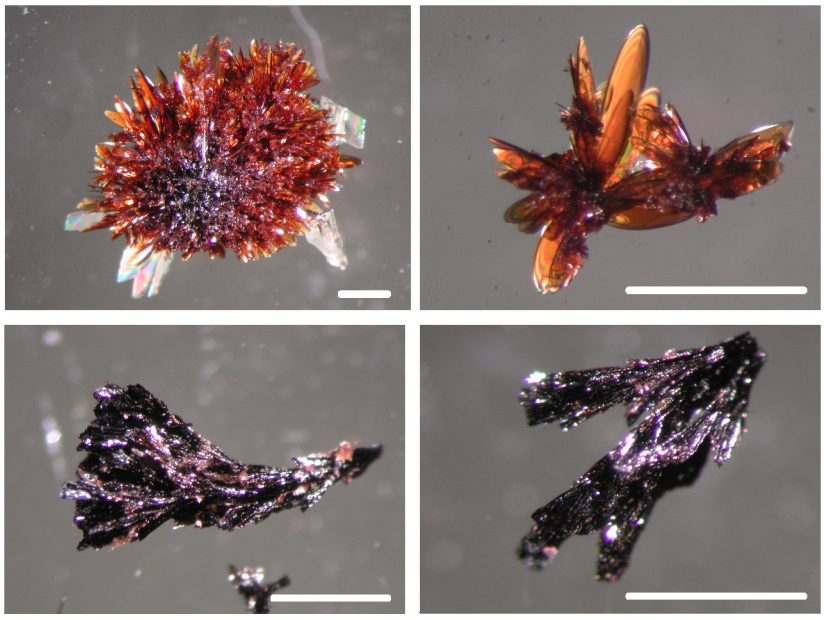

Figure 7.4. Co-crystals formed between host **69** and guest **60**. The top two have the same reddish yellow color, while the bottom two have the dark blue appearance. The scale bars are all 1 mm.

The SEM images of the blue crystals of co-crystal **69·60** were taken without a coating of Au, as shown in Figure 7.5. The fact that SEM images can still be obtained with a high energy electron beam at 20 kV suggests that there is good electron transport at the surface of the material.

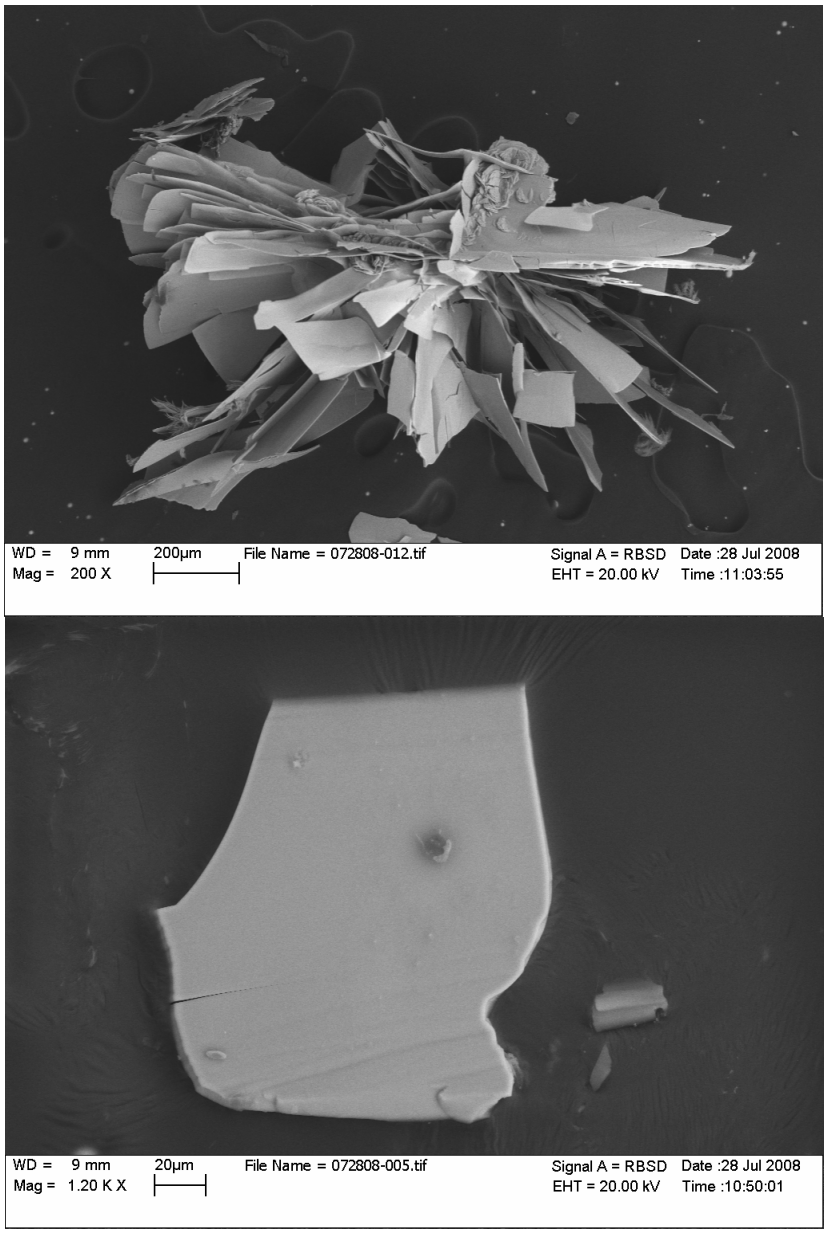

Figure 7.5. SEM images of blue form co-crystal **69·60**.

The crystal structures of co-crystals **3·60** and **4·60** are shown in Figure 7.6 and 7.7. The geometry parameters of the aligned monomers within co-crystal **3·60** are close to the ideal values for polymerization. The repeat distance of the monomers is 5.02 Å, the C1-C4 contact distance is 3.71 Å, the C3-C6 contact distance is 3.63 Å, and the tilt angle is 47^{o}.

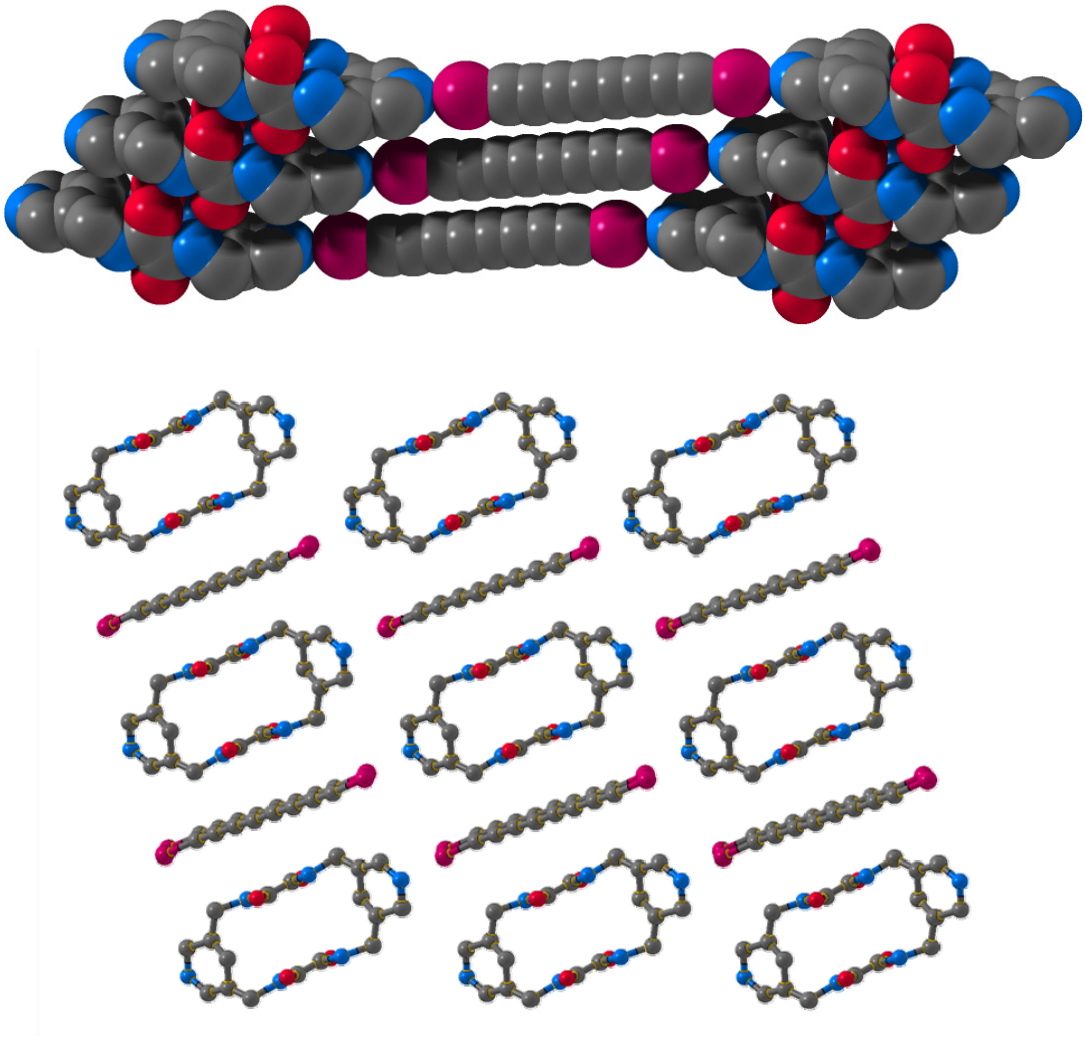

Figure 7.6. Crystal tructure of co-crystal **3·60**. Top: Side view; Bottom: top view.

Within co-crystal **3·60**, the alignment of host **3** is disordered, as illustrated from the top view of the crystals. The possible reason is that two sets of oppositely aligned hosts are distributed alternatively in the co-crystals, and their positions have been averaged by the reflection of the X-rays. This is similar to a "racemic" mixture of two "enantiomers", which are composed of two equal amounts of oppositely aligned hosts.

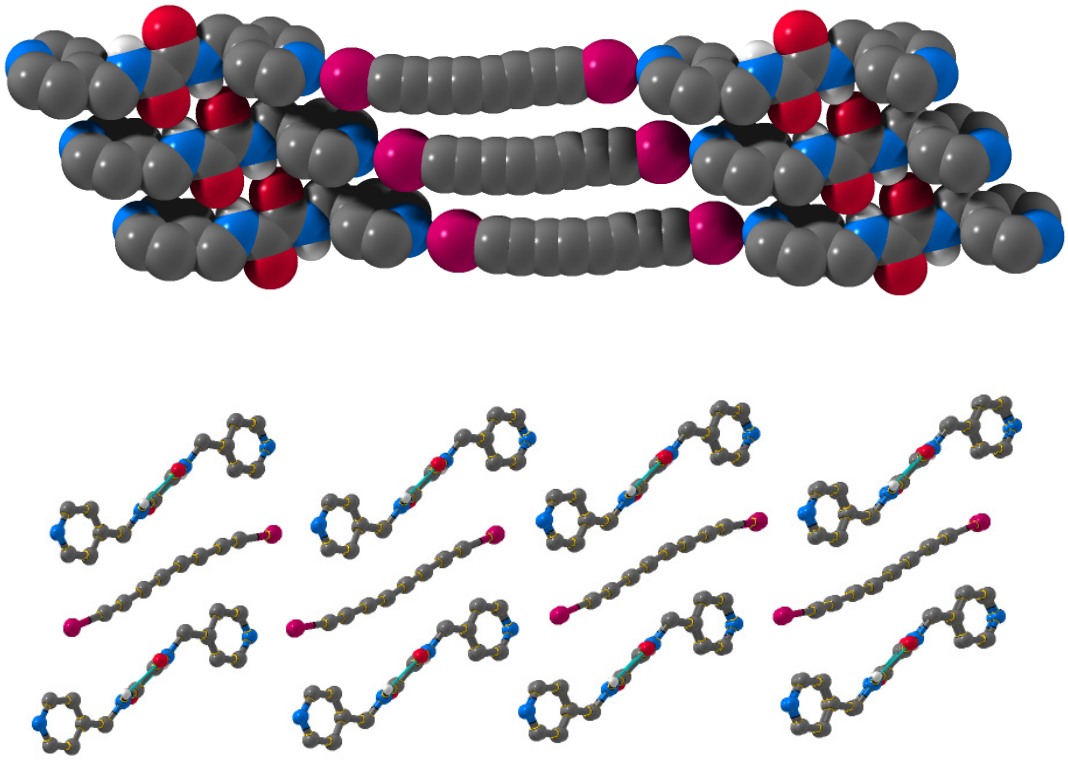

Figure 7.7. Crystal structure of co-crystal **4·60**. Top: Side view; Bottom: top view.

The alignment of co-crystal **4·60** is what we designed. The alignment of the hosts through hydrogen bonding provides the scaffold for the guest, connected by the halogen bonds. The repeat distance is 4.98 Å, favorable for a topochemical polymerization. However, the tilt angle for the guest monomers is 59.9^{o} and the C1-C4 distance is 4.30 Å, making the desired polymerization difficult to proceed.

7.4. Topochemical polymerization of tetrayne within co-crystals

The geometry parameters of the aligned monomers within co-crystal **3·60** are close to the ideal values for their polymerization. After an extended time at room temperature, the repeat distance of the monomers kept on decreasing, and the unit cell changed toward the direction that favors the topochemical polymerization. (Table 8.1)

Table 7.1. Unit cell change of co-crystal **3·60** according to the time that the co-crystal stays at room temperature.

Time (day)	a (Å)	b (Å)	c (Å)	α (°)	β (°)	γ (°)	V (Å^3)
0	5.019	10.529	12.557	74.871	81.26	83.59	631.28
4	4.988	10.510	12.611	74.85	80.98	83.86	628.65
6	4.971	10.482	12.619	74.84	80.95	83.98	625.41
7	4.964	10.474	12.626	74.81	80.89	84.10	624.30
8	4.959	10.485	12.683	74.80	80.86	84.16	626.98
12	4.855	10.465	12.748	74.35	80.90	85.16	609.93
20	4.807	10.344	12.794	74.11	80.66	85.80	603.47

The **3·60** co-crystal remains crystalline even after it decomposes. Before it completely loses crystallinity, we are able to analyze structural information from the diffraction data. The crystal structure becomes disordered gradually during the decomposition. The monomer **60** polymerizes during the decomposition, and it undergoes several polymerization modes at the same time. Figure 7.8 lists two series of intermediate atomic positions of the monomers during the polymerization, deduced from the same X-ray diffraction data.

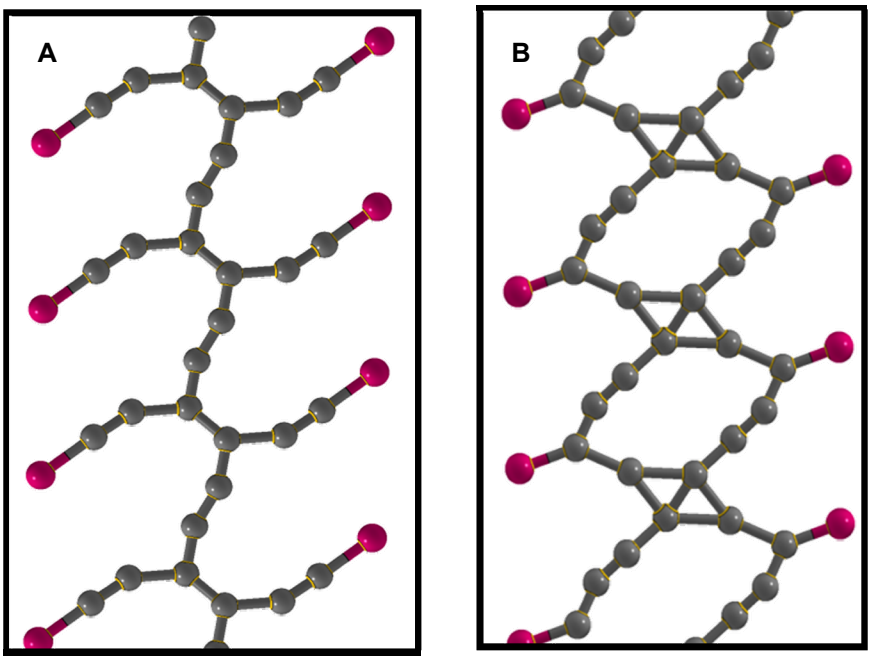

Figure 7.8. Polymerization intermediate structures deduced from X-ray diffraction data of decomposed **3·60** co-crystal. A and B are two sets of atomic positions deduced from one set of XRD data.

Series A in Figure 7.8 suggests a polymerization mode with the middle two triple bonds of the tetrayne. The hypothetical polymer product is a poly(diacetylene) with acetylene side chains, as shown in Scheme 7.9 A. Series B suggests a polymerization mode leading to a laddered bi-poly(diacetylene) (Scheme 7.9 B), where the topochemical polymerization takes place at both 1,4- and 5,8- positions. In addition, it is also possible that the aligned tetrayne monomers undergo polymerization on one side, forming the poly(diacetylene)s shown in either Scheme 7.9 C or Scheme 7.9 D. The overlap of these two structures may also appear as a crystal structure shown in Figure 7.8 B.

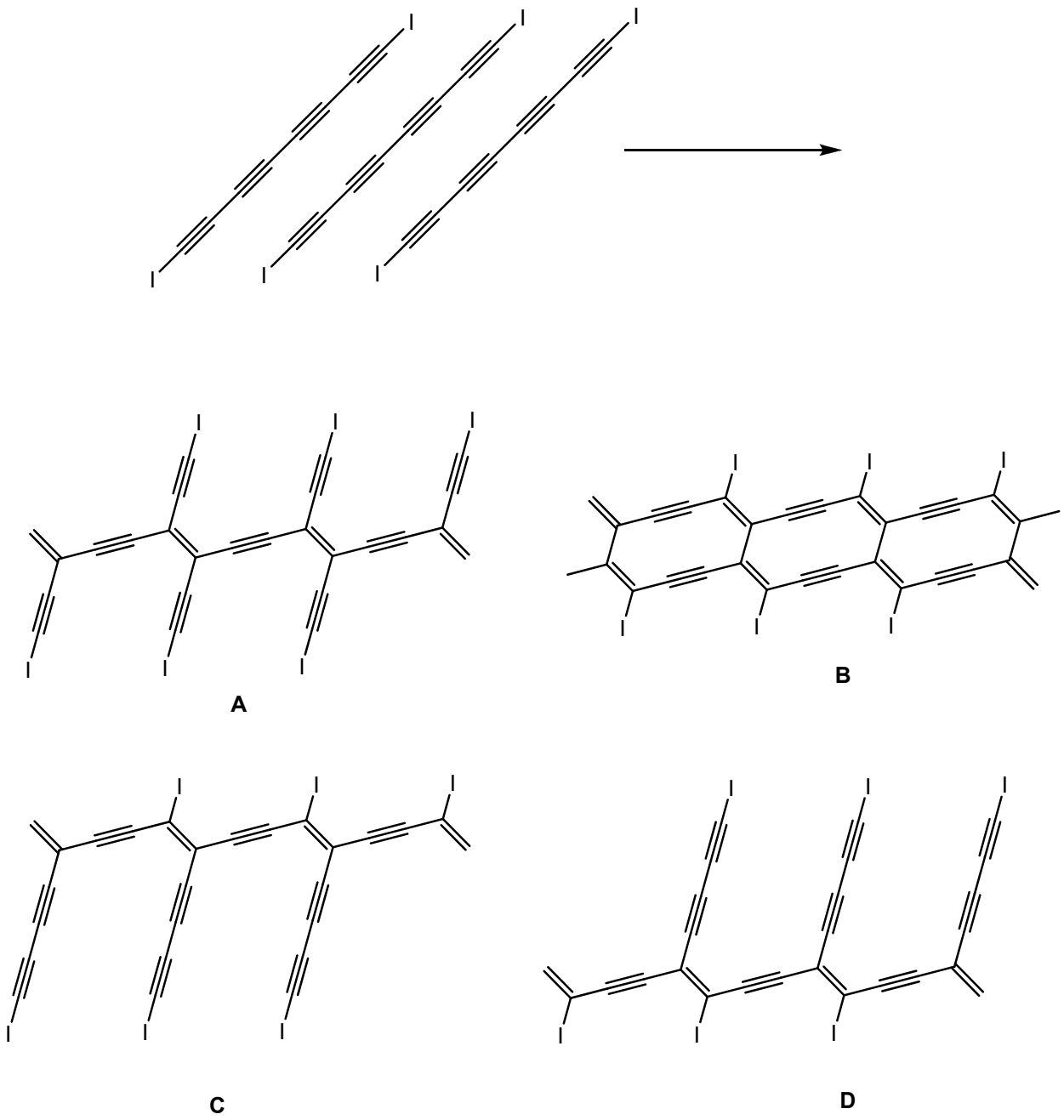

Scheme 7.10. Possible poly(diacetylene) products resulted from the topochemical polymerization of tetrayne **60**.

The Raman spectrum of the final product shows the similar features as poly(diacetylene)s under 785 nm laser, as shown in Figure 7.9. The multiple peaks in the range of double-bond

stretching indicate that topochemical polymerization proceeds in different modes within the o-crystals.

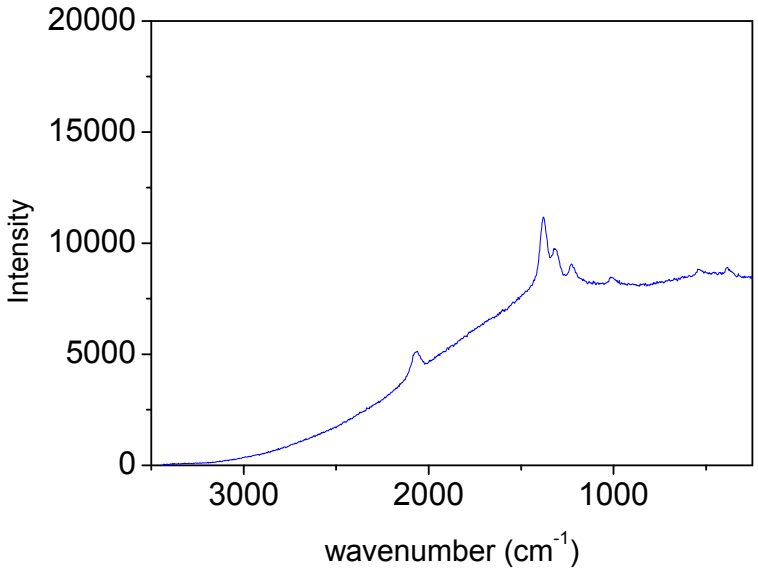

Figure 7.9. Raman spectra of co-crystal **3·60** using laser beams of 785 nm.

However, if using a higher energy laser beam of 532 nm, the Raman spectrum becomes completely different to what is shown in Figure 7.9. However, the new spectrum is similar to that of graphite with all sp^2-hybridized carbon, indicating that graphite ribbons or pieces could be involved, as shown in Figure 7.10.

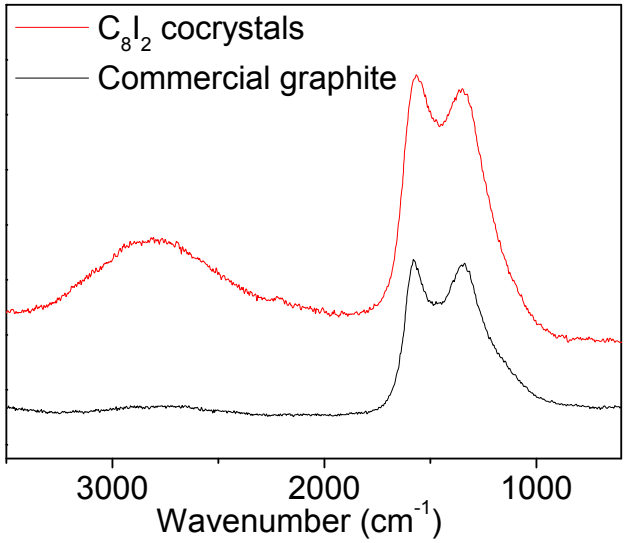

Figure 7.10. Raman spectra of co-crystal **3·60** and commercial graphite using a laser beam of 532 nm.

The Raman spectrum of decomposed **3·60** co-crystals under 532 nm laser beam indicates the potential conversion from polyynes to graphitic carbon. The shiny appearance of the decomposed co-crystals and the high electron transportation suggested by the SEM results provide further evidence for the formation of graphitic materials. However, the poly(diacetylene) products shown in Scheme 7.10 can only form graphitic structures with open shells, as shown in Figure 7.11 A and B. The paramagnetic electrons on the sp^2 carbons are highly reactive and can easily destroy the structure by trapping external atoms, such as H and O. A closed-shell graphitic structure with a repeat unit is shown in Figure 7.11 C. However, to form this structure requires close contact of the monomers, which is disfavored by the big iodine atoms.

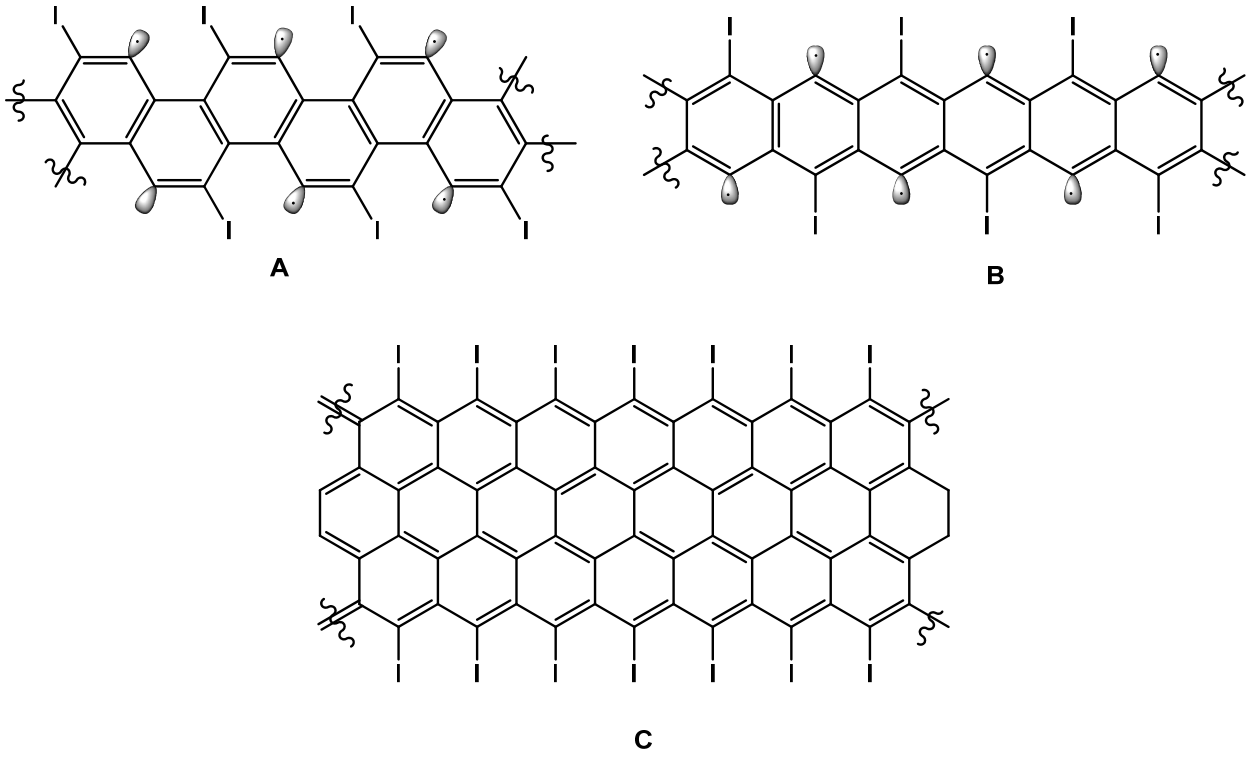

Figure 7.11. Graphitic structures with a repeat unit of C_8I_2.

The ESR spectrum of decomposed co-crystal **3·64**, taken with the help of Dr. Susan A. Odom in Marder's Group at Georgia Tech, indicates that the co-crystal contains paramagnetic electrons, as shown in Figure 7.12. The line shape is different from that of PIDA co-crystals and isolated PIDA. The source of the paramagnetic electrons may be attributed to delocalized polarons generated during the polymerization or graphitization, but will be further investigated by other Goroff group members.

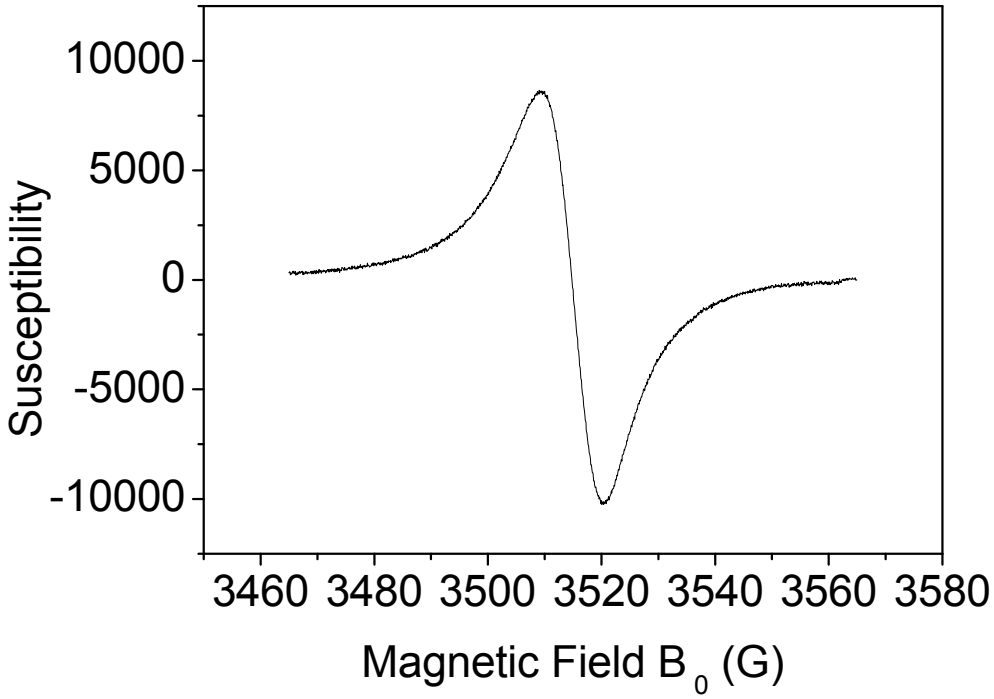

Figure 7.12. ESR **s**pectrum of co-crystal **3·60**.

In summary, we have successfully prepared the co-crystals of diiodooctatetrayne for their 1,4-topochemical polymerization. Further packing for tetraynes, such as 1,2-polymerization, will be explored to approach the graphtic materials with well-defined structures.

7.5. Experimental details

7.5.1. Synthesis of organic compounds.

Trimethylsilyl-trimethylstannyl-ethyne (**50**):[130]

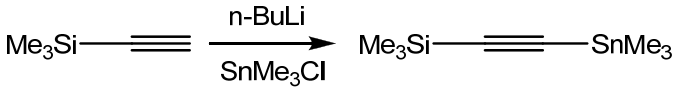

Trimethylsilyl acetylene **49** (1.180 g, 12 mmol) was dissolved by 25 mL anhydrous THF. This solution was cooled down to -30 ^{o}C and n-BuLi (7.5 mL, 12 mmol, 1.6M in hexanes) was added dropwise. The solution was stirred at -30 ^{o}C for 15 min and at the same temperature

trimethyltin chloride (12 mmol, 12 mL, 1M in THF) was added dropwise. After stirring at -30 °C for 30 min and at room temperature for 1 h, 100 mL hexanes was added. The solid suspension was filled out and the solvent was removed under reduced pressure. Trimethylsilyl-trimethylstannyl-ethyne **50** was obtained as colorless oil after vacuum distillation. (1.886 g, 7.2 mmol, yield 60.2 %) B. p. 36 °C, 7 torr. ^{1}H NMR (400 MHz, $CDCl_3$) δ 0.16 (s, 9H), 0.28 (s, 9H). ^{13}C NMR (400 MHz, $CDCl_3$) -7.6, 0.2, 113.2, 117.5. UV and PMA inactive.

Triisopropylsilyl-trimethylstannyl-ethyne (**57**):[130]

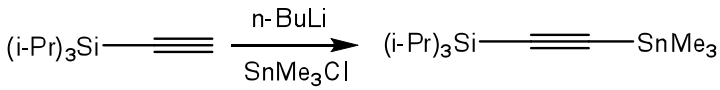

Triisopropylsilyl acetylene **49** (4.50 g, 25 mmol) was dissolved by 50 mL anhydrous THF. This solution was cooled down to -30 °C and n-BuLi (15 mL, 25 mmol, 1.6M in hexanes) was added dropwise. The solution was stirred at -30 °C for 15 min and at the same temperature trimethyltin chloride (25 mmol, 25 mL, 1M in THF) was added dropwise. After stirring at -30 °C for 30 min and at room temperature for 1 h, 100 mL hexanes was added. The solid suspension was filled out and the solvent was removed under reduced pressure. Trimethylsilyl-trimethylstannyl-ethyne **57** was obtained as colorless oil after vacuum distillation. (4.8 g, 14 mmol, yield 56 %) B. p. 90 °C, 7 torr. ^{1}H NMR (500 MHz, $CDCl_3$) δ 0.27 (s, 9H), 1.06-1.07 (bs, 21H). ^{13}C NMR (500 MHz, $CDCl_3$) -7.6, 11.2, 18.6, 113.6, 115.2. UV and PMA inactive.

Diiodoethyne (**51**):[76]

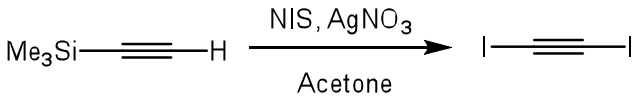

Trimethylsilyl acetylene **49** (0.5 g, 5.1 mmol) was dissolved in 250 ml acetone. The solution was added NIS (2.831 g, 12.6 mmol) and $AgNO_3$ (0.687 g, 6.1 mmol). The solution was stirred

under dark for 4 h and then partitioned between 100 mL ice water and 100 mL cold hexane. The aqueous layer was extracted with hexane (3×50 mL) and the combined organic layer was dried with $MgSO_4$. The solvent was removed at 0 ^oC in dark to give 1.276 g (4.6 mmol) **51** as white solid (yield 90.0 %). ^{13}C NMR (400 MHz, $CDCl_3$) δ 0.38.

1,6-Bis(trimethylsilyl)-1,3,5-hextriyne (52):[140]

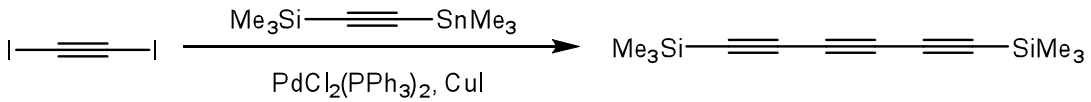

A 100-mL round-bottom flask was charged with a magnetic stir bar, anhydrous THF (8 mL), $PdCl_2(PPh_3)_2$ (35 mg, 0.1 mmol, 5.0 mol %), and CuI (19 mg, 0.10 mmol, 5.0 mol %). The mixture was stirred at room temperature. In another 50-mL round-bottom flask charged with a magnetic stir bar, trimethylsilyl-trimethylstannyl-ethyne **50** (560 mg, 2.2 mmol, 0.44 mL) and C_2I_2 **51** (280 mg, 1.0 mmol) were dissolved in 15 mL anhydrous THF. This solution was stirred at room temperature and added dropwise to the catalyst solution via a gradual additional funnel with a pace of 20-30 seconds per drop. After addition the mixture was stirred for another 2 h and the solvent was removed under reduced pressure. The residue was purified by short column chromatography (Al_2O_3, hexanes), and colorless or light yellow crystals were obtained. Further purifying by diffusion pump at 0.1 Torr for 0.5 h gives 76 mg **52** as dark yellow solid (yield 35.9%). ^1H NMR (400 MHz, $CDCl_3$) δ 0.20. ^{13}C NMR (400 MHz, $CDCl_3$) δ 87.9, 87.4, 61.9, -0.6.

1,6-diiodohexatriyne (53)[74]

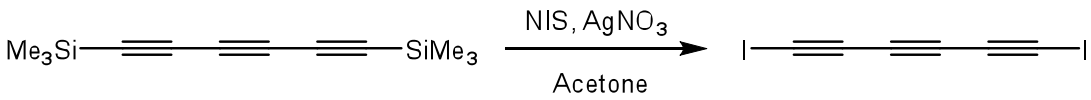

1,6-Bis(trimethylsilyl)-1,3,5-hextriyne **52** (80.0 mg, 0.37 mmol) was dissolved in 250 ml acetone. The solution was added NIS (187.5 mg, 0.85 mmol) and $AgNO_3$ (67.6 mg, 0.40 mmol). The solution was stirred under dark for 4 h and then partitioned between 250 mL ice water and 200 mL cold hexane. The aqueous layer was extracted with hexane (3×100 mL) and the combined organic layer was dried with $MgSO_4$. The solvent was removed at 0 ^oC in dark. After flash chromatography, 60.5 mg **53** was obtained as light yellow solid (yield 50.3%). ^{13}C NMR (400 MHz, $CDCl_3$) δ 78.5, 59.7, 0.9.

1,6-Bis(p-toluenesulfonyloxy)-2,4-hexadiyne (56):[140]

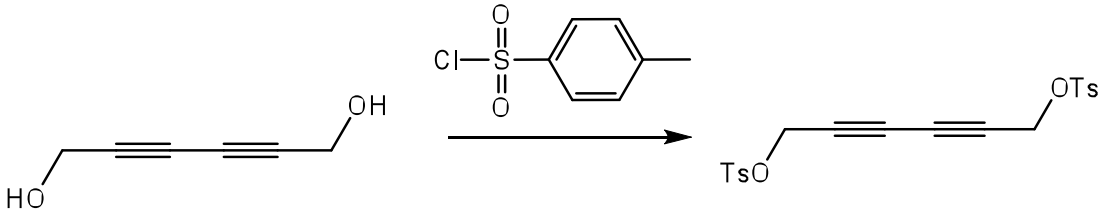

To a solution of 0.50 g (4.5 mmol) of 2,4-hexadiyne-1,6-diol **55** in 9.0 mL THF was added 1.98 g (10.4 mmol) of *p*-tosylchloride. The solution was kept at -15 ^oC and a cold solution (0 ^oC) of 0.58 g (10.4 mmol) KOH in 2 ml water was added dropwise. After 2 h, ice-cold water was added and the product was precipitated. 1.80 g of **56** was obtained after filtration as unstable pink crystals (yield 94.5 %). ^1H NMR (300 MHz, $CDCl_3$) δ 2.45 **(**s**,** 6 H, CH_3), 4.73 **(**s**,** 4 H, CH_2), 7.36 (d, 4 H, J = 8.2 Hz, 3,5-H ph), 7.79 (d, 4 H, J = 8.2 Hz, 2.6-H ph)

1,6-Bis(trimethylsilyl)-1,3,5-hexatriyne (52)

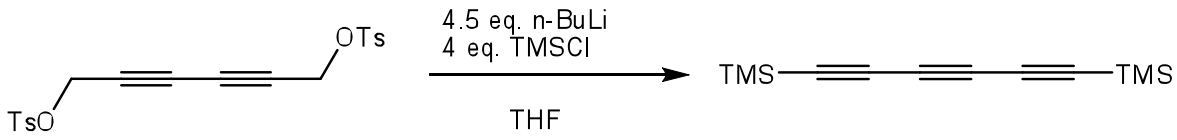

To a solution of 1.71 g (4 mmol) of **26** and 2.22 g (20.5 mmol, 2.6 mL) of Me_3SiCl in 60 mL of dry THF at -78 ^oC was added 12 mL (19.2 mmol) of a 1.6 M solution of n-BuLi in hexane

over 3 h. The brown solution was allowed to warm to -30 ^{o}C and quenched with saturated NH_4Cl. Removing solvent under reduced pressure afford yellow solid. ^{13}C NMR indicating that desired product was included with low partition.

1,8-Bis(trimethylsilyl)-1,3,5,7-octatetrayne (58): [130]

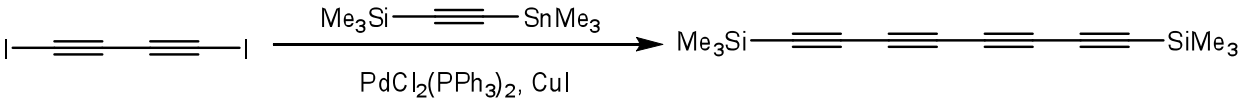

A 100-mL round-bottom flask was charged with a magnetic stir bar, anhydrous THF (8 mL), $PdCl_2(PPh_3)_2$ (35 mg, 0.1 mmol, 5.0 mol %), and CuI (19 mg, 0.10 mmol, 5.0 mol %). The mixture was stirred at room temperature. In another 50-mL round-bottom flask charged with a magnetic stir bar, trimethylsilyl-trimethylstannyl-ethyne **49** (280 mg, 1.1 mmol, 0.22 mL) and C_4I_2 **1** (150 mg, 0.50 mmol) were dissolved in 15 mL anhydrous THF. This solution was stirred at room temperature and added dropwise to the catalyst solution via a double-tipped needle over 10 h. After addition the mixture was stirred overnight and the solvent was removed under reduced pressure. The residue was purified by short column chromatography (Al_2O_3, hexanes), and colorless or light yellow crystals were obtained. ^{1}H NMR (400 MHz, $CDCl_3$) δ 0.20, 0.21. ^{13}C NMR (400 MHz, $CDCl_3$) -0.6, -0.5, 62.1, 85.9, 87.8, 88.0.

The crystals are the mixture of **62** and 1,4-bis(trimethylsilyl)-1,3-butadiyne with a ratio of around 1:1, determined by mole ratios of 1H NMR. Separating by-product by pumping this mixture at 0.1 torr in a sublimation apparatus, followed by going through an Al_2O_3 column (2 cm) gives 42.5 mg desired product **58** (yield 39.5 %).

1,8-Bis(trimethylsilyl)-1,3,5,7-octatetrayne (59):[130]

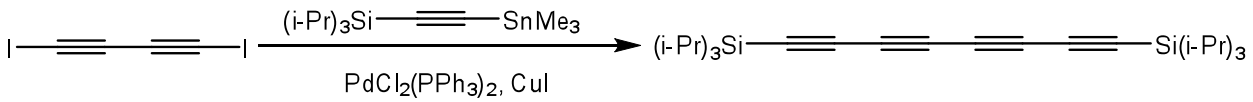

A 100-mL round-bottom flask was charged with a magnetic stir bar, anhydrous THF (8 mL), $PdCl_2(PPh_3)_2$ (35 mg, 0.1 mmol, 5.0 mol %), and CuI (19 mg, 0.10 mmol, 5.0 mol %). The mixture was stirred at room temperature. In another 50-mL round-bottom flask charged with a magnetic stir bar, trimethylsilyl-trimethylstannyl-ethyne **57** (2.2 mmol, 0.62 mL) and C_4I_2 **1** (302 mg, 1 mmol) were dissolved in 15 mL anhydrous THF. This solution was stirred at room temperature and added dropwise to the catalyst solution via a double-tipped needle over 10 h. After addition the mixture was stirred overnight and the solvent was removed under reduced pressure. The residue was purified by short column chromatography (Al_2O_3, hexanes), and yellow solid containing **57** and by-product 1,4-bis(triisopropyl)-1,3-butadiyne was obtained. ^{13}C NMR (400 MHz, $CDCl_3$) 11.30, (11.34), 18.49, (18.56), 61.36, 62.20, (81.53), 85.54, 89.67, (90.51).

1,8-diiodo-1,3,5,7-octatetrayne (64):[130]

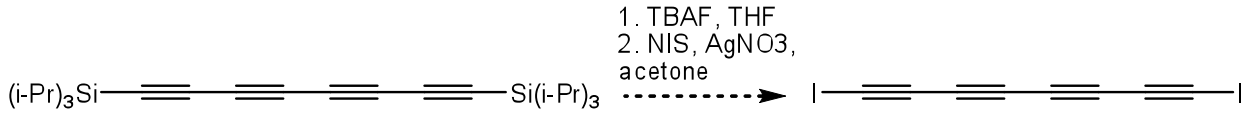

63

The mixture of **57** and 1,4-bis(triisopropylsilyl)-1,3-butadiyne (240 mg) was dissolved in 250 mL THF, and 5 mL tetrabutylammonium fluride solution (1M in THF) was added dropwise. The mixture turned dark immediately upon the addition of TBAF. This solution was allowed to stir at room temperature for 3 h until no starting material showing in TLC. Then the solution was partitioned between 250 mL ice water and 200 mL cold hexane. The aqueous layer was extracted by hexane (3×100 mL) and the combined organic phase was dried with $MgSO_4$.

The solvent was partially removed at 0 ^{o}C and actone (250 mL) was added. The solution was added NIS (330 mg, 1.5 mmol) and $AgNO_3$ (105 mg, 1.1 mmol). The solution was stirred under dark for 2 h and then partitioned between 250 mL ice water and 200 mL cold hexane. The aqueous layer was extracted with hexane (3×100 mL) and the combined organic layer was dried with $MgSO_4$. The solvent was removed at 0 ^{o}C in dark. There is no desired product **60** obtained. This reaction was reproduced twice, both failed in obtaining an unidentified mixtures. The possible reason is that triisopropyl group is hard to cleave and mixtures of non-deprotected, mono-deprotected, and full-deprotected octatetraynes were obtained.

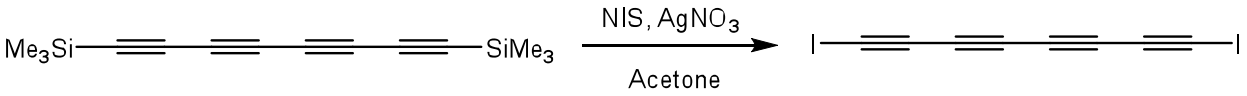

62

1,8-Bis(trimethylsilyl)-1,3,5,7-octatetrayne 58 (40 mg, 0.16 mmol) was dissolved in 250 ml acetone. The solution was added NIS (88 mg, 0.4 mmol) and $AgNO_3$ (20 mg, 0.2 mmol). The solution was stirred under dark for 4 h and then partitioned between 250 mL ice water and 200 mL cold hexane. The aqueous layer was extracted with hexane (3×100 mL) and the combined organic layer was dried with $MgSO_4$. The solvent was removed at 0 ^{o}C in dark. After flash chromatography, 42 mg **60** was obtained as light yellow solid (yield 80.1%). ^{13}C NMR (400 MHz, $CDCl_3$) δ 78.1, 62.0, 58.8, 1.9.

7.5.2. Growing co-crystals

Co-crystals between hosts **3**, **4**, and **69** and monomer **60** were prepared by slow evaporation. To a 0.02 mM methanol solution of host, fresh made **60** was added with a host/guest stoichiometry of 1:1. The solution was centrifuged to remove any undissolved particles. The supernatant layer was transferred into a 50 ml crystallization dish. The dish was then covered

tightly by an aluminum foil, with 10 – 15 needle holes on it. Leaving the dish at low temperature (4 ^{o}C or -20 ^{o}C) with no disturbance would produce the desired crystals when all the solvent evaporated.

Bibliography

(1) Marder, S. R.; Cheng, L. T.; Tiemann, B. G.; Friedli, A. C.; Blancharddesce, M.; Perry, J. W.; Skindhoj, J. Large 1st hyperpolarizabilities in push-pull polyenes by tuning of the bond-length alternation and aromaticity. *Science* **1994**, *263*, 511-514.

(2) Reynolds, J. R.; Ruiz, J. P.; Child, A. D.; Nayak, K.; Marynick, D. S. Electrically conducting polymers containing alternating substituted phenylene and bithiophene repeat units. *Macromolecules* **1991**, *24*, 678-687.

(3) Halls, J. J. M.; Pichler, K.; Friend, R. H.; Moratti, S. C.; Holmes, A. B. Exciton diffusion and dissociation in a poly(p-phenylenevinylene)/C-60 heterojunction photovoltaic cell. *Applied Physics Letters* **1996**, *68*, 3120-3122.

(4) Hush, N. S. An overview of the first half-century of molecular electronics. *Annuals of the New York Academy of Sciences* **2003**, 1-20.

(5) Bolto, B. A.; McNeill, R.; Weiss, D. E. Electronic conduction in polymers. 3. Electronic properties of polypyrrole. *Australian Journal of Chemistry* **1963**, *16*, 1090-1103.

(6) Bolto, B. A.; Weiss, D. E. Electronic conduction in polymers. 2. Electrochemical reduction of polypyrrole at controlled potential. *Australian Journal of Chemistry* **1963**, *16*, 1076-1089.

(7) McNeill, R.; Weiss, D. E.; Wardlaw, J. H.; Siudak, R. Electronic conduction in polymers. 1. Chemical structure of polypyrrole. *Australian Journal of Chemistry* **1963**, *16*, 1056-1075.

(8) Chiang, C. K.; Fincher, C. R.; Park, Y. W.; Heeger, A. J.; Shirakawa, H.; Louis, E. J.; Gau, S. C.; Macdiarmid, A. G. Electrical-conductivity in doped polyacetylene. *Physical Review Letters* **1977**, *39*, 1098-1101.

(9) Mele, G.; Epstein, A. Special issue - Celebrating the year 2000 Nobel Prize in Chemistry to Alan Heeger, Alan MacDiarmid and Hideki Shirakawa for the discovery and development of conductive polymers - Foreword. *Synthetic Metals* **2001**, *125*, 1-1.

(10) Samuel, I. D. W.; Turnbull, G. A. Organic semiconductor lasers. *Chemical Reviews* **2007**, *107*, 1272-1295.

(11) Gunes, S.; Neugebauer, H.; Sariciftci, N. S. Conjugated polymer-based organic solar cells. *Chemical Reviews* **2007**, *107*, 1324-1338.

(12) Zaumseil, J.; Sirringhaus, H. Electron and ambipolar transport in organic field-effect transistors. *Chemical Reviews* **2007**, *107*, 1296-1323.

(13) Anslyn, E. V.; Dougherty, D. A., Chapter 17: Electronic organic materials In *Mordern Physical Organic Chemistry*; University Science Books: Sausalito, California, **2004**, p1001-1046.

(14) Baumgartner, T.; Reau, R. Organophosphorus pi-conjugated materials. *Chemical Reviews* **2006**, *106*, 4681-4727.

(15) Lo, S. C.; Burn, P. L. Development of dendrimers: Macromolecules for use in organic light-emitting diodes and solar cells. *Chemical Reviews* **2007**, *107*, 1097-1116.

(16) Menard, E.; Meitl, M. A.; Sun, Y. G.; Park, J. U.; Shir, D. J. L.; Nam, Y. S.; Jeon, S.; Rogers, J. A. Micro- and nanopatterning techniques for organic electronic and optoelectronic systems. *Chemical Reviews* **2007**, *107*, 1117-1160.

(17) Saragi, T. P. I.; Spehr, T.; Siebert, A.; Fuhrmann-Lieker, T.; Salbeck, J. Spiro compounds for organic optoelectronics. *Chemical Reviews* **2007**, *107*, 1011-1065.

(18) McQuade, D. T.; Pullen, A. E.; Swager, T. M. Conjugated polymer-based chemical sensors. *Chemical Reviews* **2000**, *100*, 2537-2574.
(19) Thomas, S. W.; Joly, G. D.; Swager, T. M. Chemical sensors based on amplifying fluorescent conjugated polymers. *Chemical Reviews* **2007**, *107*, 1339-1386.
(20) Burroughes, J. H.; Bradley, D. D. C.; Brown, A. R.; Marks, R. N.; Mackay, K.; Friend, R. H.; Burns, P. L.; Holmes, A. B. Light-emitting-diodes based on conjugated polymers. *Nature* **1990**, *347*, 539-541.
(21) Bernius, M. T.; Inbasekaran, M.; O'Brien, J.; Wu, W. S. Progress with light-emitting polymers. *Advanced Materials* **2000**, *12*, 1737-1750.
(22) McCullough, R. D.; Lowe, R. D. Enhanced electrical-conductivity in regioselectively synthesized poly(3-alkylthiophenes). *Journal of the Chemical Society-Chemical Communications* **1992**, 70-72.
(23) Zhou, Q.; Swager, T. M. Fluorescent Chemosensors Based on Energy Migration in Conjugated Polymers: The Molecular Wire Approach to Increased Sensitivity. *Journal of the American Chemical Society* **1995**, *117*, 12593-12602.
(24) Abe, S.; Schreiber, M.; Su, W. P.; Yu, J. Excitons and Nonlinear Optical-Spectra in Conjugated Polymers. *Physical Review B* **1992**, *45*, 9432-9435.
(25) Carter, G. M.; Thakur, M. K.; Chen, Y. J.; Hryniewicz, J. V. Time and Wavelength Resolved Nonlinear Optical Spectroscopy of a Polydiacetylene in the Solid-State Using Picosecond Dye-Laser Pulses. *Applied Physics Letters* **1985**, *47*, 457-459.
(26) Guo, D.; Mazumdar, S.; Dixit, S. N.; Kajzar, F.; Jarka, F.; Kawabe, Y.; Peyghambarian, N. Role of the Conduction-Band in Electroabsorption, 2-Photon Absorption, and 3rd-Harmonic Generation in Polydiacetylenes. *Physical Review B* **1993**, *48*, 1433-1459.
(27) Charych, D. H.; Nagy, J. O.; Spevak, W.; Bednarski, M. D. Direct Colorimetric Detection of a Receptor-Ligand Interaction by a Polymerized Bilayer Assembly. *Science* **1993**, *261*, 585-588.
(28) Jonas, U.; Shah, K.; Norvez, S.; Charych, D. H. Reversible color switching and unusual solution polymerization of hydrazide-modified diacetylene lipids. *Journal of the American Chemical Society* **1999**, *121*, 4580-4588.
(29) Mino, N.; Tamura, H.; Ogawa, K. Analysis of Color Transitions and Changes on Langmuir-Blodgett-Films of a Polydiacetylene Derivative. *Langmuir* **1991**, *7*, 2336-2341.
(30) Reppy, M. A.; Pindzola, B. A. Biosensing with polydiacetylene materials: structures, optical properties and applications. *Chemical Communications* **2007**, 4317-4338.
(31) Baughman, R. H. Solid-State Synthesis of Large Polymer Single-Crystals. *Journal of Polymer Science Part B-Polymer Physics* **1974**, *12*, 1511-1535.
(32) Enkelmann, V. Crystal-structure of loew-temperature phase of poly[1,2-bis(p-tolylsulfphonyloxymethtlene)-1-buten-3-ynylene]. *Acta Crystallographica Section B-Structural Science* **1977**, *33*, 2842-2846.
(33) Xi, O. Y.; Fowler, F. W.; Lauher, J. W. Single-crystal-to-single-crystal topochemical polymerizations of a terminal diacetylene: Two remarkable transformations give the same conjugated polymer. *Journal of the American Chemical Society* **2003**, *125*, 12400-12401.
(34) Kuriyama, K.; Kikuchi, H.; Kajiyama, T. Chromatic phase of polydiacetylene Langmuir-Blodgett film. *Langmuir* **1998**, *14*, 1130-1138.
(35) Okada, S.; Peng, S.; Spevak, W.; Charych, D. Color and chromism of polydiacetylene vesicles. *Accounts of Chemical Research* **1998**, *31*, 229-239.

(36) Xu, R.; Gramlich, V.; Frauenrath, H. Alternating diacetylene copolymer utilizing perfluorophenyl-phenyl interactions. *Journal of the American Chemical Society* **2006**, *128*, 5541-5547.
(37) Cheng, Q.; Yamamoto, M.; Stevens, R. C. Amino acid terminated polydiacetylene lipid microstructures: Morphology and chromatic transition. *Langmuir* **2000**, *16*, 5333-5342.
(38) Dautel, O. J.; Robitzer, M.; Lere-Porte, J. P.; Serein-Spirau, F.; Moreau, J. J. E. Self-organized ureido substituted diacetylenic organogel. Photopolymerization of one-dimensional supramolecular assemblies to give conjugated nanofibers. *Journal of the American Chemical Society* **2006**, *128*, 16213-16223.
(39) Exarhos, G. J.; Risen, W. M.; Baughman, R. H. Resonance raman study of thermochromic phase-transition of a polydiacetylene. *Journal of the American Chemical Society* **1976**, *98*, 481-487.
(40) Chu, B.; Xu, R. L. Chromatic Transition of Polydiacetylene in Solution. *Accounts of Chemical Research* **1991**, *24*, 384-389.
(41) Oikawa, H.; Korenaga, T.; Okada, S.; Nakanishi, H. Chromatic transition of pi-conjugated polydiacetylene and the subsequent aggregation phenomena. *Polymer* **1999**, *40*, 5993-6001.
(42) Wang, G. J.; Hollingsworth, R. I. Synthesis and properties of chiral self-assembling lamellar polydiacetylene systems with very-long-range order. *Langmuir* **1999**, *15*, 3062-3069.
(43) Kew, S. J.; Hall, E. A. H. Structural effect of polymerisation and dehydration on bolaamphiphilic polydiacetylene assemblies. *Journal of Materials Chemistry* **2006**, *16*, 2039-2047.
(44) Singh, A.; Thompson, R. B.; Schnur, J. M. Reversible thermochromism in photopolymerized phosphatidylcholine vesicles. *Journal of the American Chemical Society* **1986**, *108*, 2785-2787.
(45) Yuan, Z. Z.; Lee, C. W.; Lee, S. H. Reversible thermochromism in hydrogen-bonded polymers containing polydiacetylenes. *Angewandte Chemie-International Edition* **2004**, *43*, 4197-4200.
(46) Yoon, J.; Chae, S. K.; Kim, J. M. Colorimetric sensors for volatile organic compounds (VOCs) based on conjugated polymer-embedded electrospun fibers. *Journal of the American Chemical Society* **2007**, *129*, 3038-3039.
(47) Bloor, D. Dissolution and spectroscopic properties of the polydiacetylene poly(10,12-docosadiyne-1,12-diol-bisethylurethane). *Macromolecular Chemistry and Physics* **2001**, *202*, 1410-1423.
(48) Nallicheri, R. A.; Rubner, M. F. Investigations of the mechanochromic behavior of poly(urethane diacetylene) segmented copolymers. *Macromolecules* **1991**, *24*, 517-525.
(49) Ma, Z. F.; Li, J. R.; Liu, M. H.; Cao, J.; Zou, Z. Y.; Tu, J.; Jiang, L. Colorimetric detection of Escherichia coli by polydiacetylene vesicles functionalized with glycolipid. *Journal of the American Chemical Society* **1998**, *120*, 12678-12679.
(50) Lee, S. W.; Kang, C. D.; Yang, D. H.; Lee, J. S.; Kim, J. M.; Ahn, D. J.; Sim, S. J. The development of a generic bioanalytical matrix using polydiacetylenes. *Advanced Functional Materials* **2007**, *17*, 2038-2044.
(51) Dobrosavljevic, V.; Stratt, R. M. Role of conformational disorder in the electronic-structure of conjugated polymers - substituted polydiacetylenes. *Physical Review B* **1987**, *35*, 2781-2794.

(52) Schott, M. The colors of polydiacetylenes: a commentary. *Journal of Physical Chemistry B* **2006**, *110*, 15864-15868.
(53) Dei, S.; Matsumoto, A. Thermochromism of polydiacetylenes in the solid state and in solution by the self-organization of polymer chains containing no polar group. *Macromolecules* **2008**, *41*, 2467-2473.
(54) Ahn, D. J.; Kim, J. M. Fluorogenic polydiacetylene supramolecules: Immobilization, micropatterning, and application to label-free chemosensors. *Accounts of Chemical Research* **2008**, *41*, 805-816.
(55) Wang, C. G.; Ma, Z. F. Colorimetric detection of oligonucleotides using a polydiacetylene vesicle sensor. *Analytical and Bioanalytical Chemistry* **2005**, *382*, 1708-1710.
(56) Cheng, Q.; Stevens, R. C. Coupling of an induced fit enzyme to polydiacetylene thin films: Colorimetric detection of glucose. *Advanced Materials* **1997**, *9*, 481.
(57) Kolusheva, S.; Shahal, T.; Jelinek, R. Cation-selective color sensors composed of ionophore-phospholipid-polydiacetylene mixed vesicles. *Journal of the American Chemical Society* **2000**, *122*, 776-780.
(58) Okada, S. Y.; Jelinek, R.; Charych, D. Induced color change of conjugated polymeric vesicles by interfacial catalysis of phospholipase A(2). *Angewandte Chemie-International Edition* **1999**, *38*, 655-659.
(59) Gill, I.; Ballesteros, A. Immunoglobulin-polydiacetylene sol-gel nanocomposites as solid-state chromatic biosensors. *Angewandte Chemie-International Edition* **2003**, *42*, 3264-3267.
(60) Zimmermann, B.; Baranovic, G. Two-dimensional infrared correlation spectroscopic study on thermal polymerization of diphenylbutadiyne. *Vibrational Spectroscopy* **2006**, *41*, 126-135.
(61) Diederich, F. Carbon scaffolding - Building acetylenic all-carbon and carbon-rich compounds. *Nature* **1994**, *369*, 199-207.
(62) Szafert, S.; Gladysz, J. A. Carbon in one dimension: Structural analysis of the higher conjugated polyynes. *Chemical Reviews* **2003**, *103*, 4175-4205.
(63) Szafert, S.; Gladysz, J. A. Update 1 of: Carbon in one dimension: Structural analysis of the higher conjugated polyynes. *Chemical Reviews* **2006**, *106*, PR1-PR33.
(64) Berlinsky, A. J.; Wudl, F.; Lim, K. C.; Fincher, C. R.; Heeger, A. J. Theory of the rod-to-coil transition in polydiacetylene *Journal of Polymer Science Part B-Polymer Physics* **1984**, *22*, 847-852.
(65) Lauher, J. W.; Fowler, F. W.; Goroff, N. S. Single-crystal-to-single-crystal topochemical polymerizations by design. *Accounts of Chemical Research* **2008**, *41*, 1215-1229.
(66) Nguyen, T. L.; Fowler, F. W.; Lauher, J. W. Commensurate and incommensurate hydrogen bonds. An exercise in crystal engineering. *Journal of the American Chemical Society* **2001**, *123*, 11057-11064.
(67) Metrangolo, P.; Neukirch, H.; Pilati, T.; Resnati, G. Halogen bonding based recognition processes: A world parallel to hydrogen bonding. *Accounts of Chemical Research* **2005**, *38*, 386-395.
(68) Guthrie, F. On the iodide of Iodammonium. *J. Chem. Soc.* **1863**, *16*, 239-244.
(69) Bent, H. A. Structure chemistry of donor-acceptor interactions. *Chemical Reviews* **1968**, *68*, 587.

(70) Legon, A. C. Prereactive complexes of dihalogens XY with Lewis bases B in the gas phase: A systematic case for the halogen analogue B - XY of the hydrogen bond B - HX. *Angewandte Chemie-International Edition* **1999**, *38*, 2687-2714.
(71) Metrangolo, P.; Resnati, G. Halogen bonding: A paradigm in supramolecular chemistry. *Chemistry-a European Journal* **2001**, *7*, 2511-2519.
(72) Laurence, C.; Queigneccabanetos, M. The acid strength of iodine cyanide. *Journal of the Chemical Society-Dalton Transactions* **1981**, 2144-2146.
(73) Laurence, C.; Queigneccabanetos, M.; Dziembowska, T.; Queignec, R.; Wojtkowiak, B. 1-Iodoacetylenes.1. Spectroscopic evidence of their complexes with Lewis-bases - A spectroscopic scale of soft basicity. *Journal of the American Chemical Society* **1981**, *103*, 2567-2573.
(74) Gao, K.; Goroff, N. S. Two new iodine-capped carbon rods. *Journal of the American Chemical Society* **2000**, *122*, 9320-9321.
(75) Rege, P. D.; Malkina, O. L.; Goroff, N. S. The effect of Lewis bases on the C-13 NMR of lodoalkynes. *Journal of the American Chemical Society* **2002**, *124*, 370-371.
(76) Webb, J. A.; Klijn, J. E.; Hill, P. A.; Bennett, J. L.; Goroff, N. S. Experimental studies of the C-13 NMR of iodoalkynes in Lewis-basic solvents. *Journal of Organic Chemistry* **2004**, *69*, 660-664.
(77) Moss, W. N.; Goroff, N. S. Theoretical analysis of the C-13 NMR of iodoalkynes upon complexation with Lewis bases. *Journal of Organic Chemistry* **2005**, *70*, 802-808.
(78) C. R. C. handbook of Chemistry and Physics; 70 ed.; CRC Press: Boca Raton, FL, p1989-1990.
(79) Gutmann, V., *The donor-acceptor approach to molecular interactions*. Plenum Press: New York, **1978**.
(80) Reichardt, C., *Solvents and solvent effects in organic chemistry*. 2nd ed.; VCH: New York, **1990**.
(81) Taft, R. W.; Kamlet, M. J. Linear solvation energy relationships. 8. Solvent effects on NMR spectral shifts and coupling-constants. *Organic Magnetic Resonance* **1980**, *14*, 485-493.
(82) Taft, R. W.; Abboud, J. L. M.; Kamlet, M. J. Solvatochromic comparison method. 20. Linear solvation energy relationships. 12. The D-delta-term in the solvatochromic equations. *Journal of the American Chemical Society* **1981**, *103*, 1080-1086.
(83) Martin, M. Etude de complexations par resonance magetique necleaire -deplacement chimique et basicities. *Annales De Physique* **1962**, *7*, 35.
(84) Ramsey, N. F. Magnetic shielding of neclei in molecules. *Physical Review* **1950**, *78*, 699-703.
(85) Steed, J. W.; Atwood, J. L., *Supramolecular Chemistry*. Wiley: Chichester, **2000**.
(86) Sun, A. W.; Lauher, J. W.; Goroff, N. S. Preparation of poly(diiododiacetylene), an ordered conjugated polymer of carbon and iodine. *Science* **2006**, *312*, 1030-1034.
(87) Luo, L.; Wilhelm, C.; Sun, A.; Grey, C. P.; Lauher, J. W.; Goroff, N. S. Poly(diiododiacetylene): Preparation, Isolation, and Full Characterization of a Very Simple Poly(diacetylene). *Journal of the American Chemical Society* **2008**, *130*, 7702-7709.
(88) Baeyer, A. *Chem. Ber.* **1885**, *18*, 2269-2281.
(89) Nishikawa, T.; Shibuya, S.; Hosokawa, S.; Isobe, M. One Pot Synthesis of Haloacetylenes from Trimethylsilylacetylenes. *Synlett* **1994**, *1994*, 485-486.

(90) Schauer, C. L.; Matwey, E.; Fowler, F. W.; Lauher, J. W. Controlled Spacing of Metal Atoms via Ligand Hydrogen Bonds. *Journal of the American Chemical Society* **1997**, *119*, 10245-10246.
(91) Ballini, R.; Fiorini, D.; Maggi, R.; Righi, P.; Sartori, G.; Sartorio, R. TBD-catalysed solventless synthesis of symmetrically N,N '-substituted ureas from primary amines and diethyl carbonate. *Green Chemistry* **2003**, *5*, 396-398.
(92) Fringuelli, F.; Pizzo, F.; Vaccaro, L. Cobalt(II) chloride-catalyzed chemoselective sodium borohydride reduction of azides in water. *Synthesis-Stuttgart* **2000**, 646-650.
(93) Goroff, N. S.; Curtis, S. M.; Webb, J. A.; Fowler, F. W.; Lauher, J. W. Designed cocrystals based on the pyridine-iodoalkyne halogen bond. *Organic Letters* **2005**, *7*, 1891-1893.
(94) Wilhelm, C.; Boyd, S. A.; Chawda, S.; Fowler, F. W.; Goroff, N. S.; Halada, G. P.; Grey, C. P.; Lauher, J. W.; Luo, L.; Martin, C. D.; Parise, J. B.; Tarabre, C.; Webb, J. A. Pressure-Induced Polymerization of Diiodobutadiyne in Assembled Co-Crystals. *Journal of the American Chemical Society* **2008**, *130*, 4415-4420.
(95) Wilhelm, C. *1,4-Poly(diiododicatylene): Preparation and characterization* Ph. D Dissertation, the State University of New York at Stony Brook, **2008**.
(96) Carboni, B.; Vaultier, M.; Carrie, R. Chemoselectivity of the reaction of dichloroboranes with functional azides - efficient functionalized secondary amine synthesis. *Tetrahedron* **1987**, *43*, 1799-1810.
(97) Weiser, G. Stark-effect of one-dimensional wannier excitons in polydiacetylene single-crystals. *Physical Review B* **1992**, *45*, 14076-14085.
(98) Fujita, N.; Sakamoto, Y.; Shirakawa, M.; Ojima, M.; Fujii, A.; Ozaki, M.; Shinkai, S. Polydiacetylene nanofibers created in low-molecular-weight gels by post modification: Control of blue and red phases by the odd-even effect in alkyl chains. *Journal of the American Chemical Society* **2007**, *129*, 4134-4135.
(99) Tachibana, H.; Kumai, R.; Hosaka, N.; Tokura, Y. Crystal structures, polymerization, and thermochromic phase changes in urethane-substituted diacetylenes crystals with varying alkyl chain lengths. *Chemistry of Materials* **2001**, *13*, 155-158.
(100) Liu, Y. The supramolecular synthesis of polydiacetylene and polytriacetylene. *M.S. Thesis, the State Unicersity of New York at Stony Brook* **2001**.
(101) Weiser, G.; Berrehar, J. Polariton induced transparency at low light level: Polymer chains dispersed in a monomer single crystal. *Physical Review Letters* **2007**, *99*.
(102) Horvath, A.; Weiser, G.; LapersonneMeyer, C.; Schott, M.; Spagnoli, S. Wannier excitons and Franz-Keldysh effect of polydiacetylene chains diluted in their single crystal monomer matrix. *Physical Review B* **1996**, *53*, 13507-13514.
(103) Spagnoli, S.; Berrehar, J.; Lapersonnemeyer, C.; Schott, M. Polydiacetylene Chains Diluted in Their Single-Crystal Monomer Matrix. *Journal of Chemical Physics* **1994**, *100*, 6195-6202.
(104) Barisien, T.; Legrand, L.; Weiser, G.; Deschamps, J.; Balog, M.; Boury, B.; Dutremez, S. G.; Schott, M. Exciton spectroscopy of red polydiacetylene chains in single crystals. *Chemical Physics Letters* **2007**, *444*, 309-313.
(105) Katagi, H.; Kasai, H.; Okada, S.; Oikawa, H.; Komatsu, K.; Matsuda, H.; Liu, Z. F.; Nakanishi, H. Size control of polydiacetylene microcrystals. *Japanese Journal of Applied Physics Part 2-Letters* **1996**, *35*, L1364-L1366.

(106) Wang, X.; Yang, K.; Ye, H.; Wang, Y. P.; Lee, J. S.; Sandman, D. J. Methods for the preparation of micro- and nanocrystals of urethane-substituted polydiacetylenes. *Journal of Macromolecular Science Part a-Pure and Applied Chemistry* **2006**, *43*, 1937-1943.
(107) Bucar, D. K.; MacGillivray, L. R. Preparation and reactivity of nanocrystalline cocrystals formed via sonocrystallization. *Journal of the American Chemical Society* **2007**, *129*, 32-33.
(108) Iida, R.; Kamatani, H.; Kasai, H.; Okada, S.; Oikawa, H.; Matsuda, H.; Kakuta, A.; Nakanishi, H. Solid-state polymerization of diacetylene microcrystals. *Molecular Crystals and Liquid Crystals Science and Technology Section a-Molecular Crystals and Liquid Crystals* **1995**, *267*, 95-100.
(109) Takahashi, S.; Miura, H.; Kasai, H.; Okada, S.; Oikawa, H.; Nakanishi, H. Single-crystal-to-single-crystal transformation of diolefin derivatives in nanocrystals. *Journal of the American Chemical Society* **2002**, *124*, 10944-10945.
(110) Song, K.; Rabolt, J. F. Polarized Raman measurements of uniaxially oriented poly(epsilon-caprolactam). *Macromolecules* **2001**, *34*, 1650-1654.
(111) Frisk, S.; Ikeda, R. M.; Chase, D. B.; Kennedy, A.; Rabolt, J. F. Structural analysis of poly(trimethylene terephthalate) fibers and films using polarized Raman spectroscopy. *Macromolecules* **2004**, *37*, 6027-6036.
(112) Frisk, S.; Ikeda, R. M.; Chase, D. B.; Rabolt, J. F. Determination of the molecular orientation of poly(propylene terephthalate) fibers using polarized raman spectroscopy: A comparison of methods. *Applied Spectroscopy* **2004**, *58*, 279-286.
(113) Yamamoto, T.; Komarudin, D.; Arai, M.; Lee, B. L.; Suganuma, H.; Asakawa, N.; Inoue, Y.; Kubota, K.; Sasaki, S.; Fukuda, T.; Matsuda, H. Extensive studies on pi-stacking of poly(3-alkylthiophene-2,5-diyl)s and poly(4-alkylthiazole-2,5-diyl)s by optical spectroscopy, NMR analysis, light scattering analysis, and X-ray crystallography. *Journal of the American Chemical Society* **1998**, *120*, 2047-2058.
(114) Chu, Q. H.; Pang, Y. Molecular aggregation of poly[(1,3-phenyleneethynylene)-alt-oligo(2,5-dialkoxy-1,4-phenyleneethyn ylene)]: Effects of solvent, temperature, and polymer conformation. *Macromolecules* **2003**, *36*, 4614-4618.
(115) Bondi, A. Van der Waals volumes + radii. *Journal of Physical Chemistry* **1964**, *68*, 441-&.
(116) Lu, Y. F.; Yang, Y.; Sellinger, A.; Lu, M. C.; Huang, J. M.; Fan, H. Y.; Haddad, R.; Lopez, G.; Burns, A. R.; Sasaki, D. Y.; Shelnutt, J.; Brinker, C. J. Self-assembly of mesoscopically ordered chromatic polydiacetylene/silica nanocomposites. *Nature* **2001**, *410*, 913-917.
(117) Dyson, F. J. Electron spin resonance absorption in metals. 2. Theory of electron diffusion and the skin effect. *Physical Review* **1955**, *98*, 349-359.
(118) Wilamowski, Z.; Oczkiewicz, B.; Kacman, P.; Blinowski, J. Asymmetry of the electron-paramagnetic resonance absorption line in CdF_2. *Physica Status Solidi B-Basic Research* **1986**, *134*, 303-306.
(119) Goldberg, I. B.; Crowe, H. R.; Newman, P. R.; Heeger, A. J.; Macdiarmid, A. G. Electron-spin resonance of polyacetylene and AsF_5-doped polyacetylene. *Journal of Chemical Physics* **1979**, *70*, 1132-1136.
(120) Kanemoto, K.; Kato, T.; Aso, Y.; Otsubo, T. ESR studies on polarons in long oligothiophenes. *Physical Review B* **2003**, *68*.

(121) Kanemoto, K.; Furukawa, K.; Negishi, N.; Aso, Y.; Otsubo, T. Polaron dynamics in two types of long oligothiophenes revealed by Q- and X-band ESR measurements. *Physical Review B* **2007**, *76*.
(122) Goldenberg, L. M.; Pelekh, A. E.; Krinichnyi, V. I.; Roshchupkina, O. S.; Zueva, A. F.; Lyubovskaya, R. N.; Efimov, O. N. Investigation of poly(p-phenylene) obtained by electrochemical oxidation of benzene in a BupyCl-$AlCl_3$ melt. *Synthetic Metals* **1990**, *36*, 217-228.
(123) Takami, K.; Kuwahara, Y.; Ishii, T.; Akai-Kasaya, M.; Saito, A.; Aono, M. Significant increase in conductivity of polydiacetylene thin film induced by iodine doping. *Surface Science* **2005**, *591*, L273-L279.
(124) Cruicksh.Fr; Benson, S. W. Carbon-hydrogen bond dissociation energy in methanol. *Journal of Physical Chemistry* **1969**, *73*, 733-737.
(125) Harris, P. J. F. New perspectives on the structure of graphitic carbons. *Critical Reviews in Solid State and Materials Sciences* **2005**, *30*, 235-253.
(126) Sears, F. W.; Zemansky, M. W., University Physics; 2nd ed.; Addison-Wesley: Reading, **1955**, p616-618.
(127) Johnson, T. R.; Walton, D. R. M. Silylation as a protective method in acetylene chemistry - polyyne chain extensions using reagents $Et_3Si(CC)_mH$ (m= 1,2,4) in mixed oxidative couplings. *Tetrahedron* **1972**, *28*, 5221-5236.
(128) Rubin, Y.; Diederich, F. Precursors to the cyclo[n] carbons - [4n+2] annulene and [4n] annulene with unusual stabilies. *Journal of the American Chemical Society* **1989**, *111*, 6870-6871.
(129) Eisler, S.; Slepkov, A. D.; Elliott, E.; Luu, T.; McDonald, R.; Hegmann, F. A.; Tykwinski, R. R. Polyynes as a model for carbyne: Synthesis, physical properties, and nonlinear optical response. *Journal of the American Chemical Society* **2005**, *127*, 2666-2676.
(130) Li, L. *From small halogenated carbon-rich molecules to conjugated polymers: Chemistry and synthetic methodologies*. Ph. D Dissertation, State University of New York at Stony Brook **2006**.
(131) Heimann, R. B.; Evsyukov, S. E.; Kavan, L., *Carbyne and Carbyneoid Structures*. Kluwer Academic Publishers: Dordrecht, **1999**; Vol. 21.
(132) Cataldo, F., *Polyynes: Synthesis, properties, and applications*. Taylor & Francis: Boca Raton, FL, **2006**.
(133) Diederich, F.; Stang, P. J.; Tykwinski, R. R., *Acetylene Chemistry: Chemistry, Biology, and Material Science*. Wiley-VCH: Weinhelm, **2005**.
(134) Goroff, N. S. Mechanism of fullerene formation. *Accounts of Chemical Research* **1996**, *29*, 77-83.
(135) Dresselhaus, M. S.; Dresselhaus, G.; Eklund, P. C., Science of fullerenes and carbon nanotubes; Academic Press: San Diego, **1996**.
(136) Hlavaty, J.; Kavan, L.; Kasahara, N.; Oya, A. Polymerisation of 1-iodohexa-1,3,5-triyne and hexa-1,3,5-triyne: a new synthesis of carbon nanotubes at low temperatures. *Chemical Communications* **2000**, 737-738.
(137) Hlavaty, J.; Kavan, L.; Kubista, J. Carbonaceous materials from end-capped alkynes. *Carbon* **2002**, *40*, 345-349.

(138) Okada, S.; Hayamizu, K.; Matsuda, H.; Masaki, A.; Minami, N.; Nakanishi, H. Solid-state polymerization of 15,17,19,21,23,25-tetracontahexayne. *Macromolecules* **1994**, *27*, 6259-6266.
(139) Ding, L.; Olesik, S. V. Synthesis of polymer nanospheres and carbon nanospheres using the monomer 1,8-dihydroxymethyl-1,3,5,7-octatetrayne. *Nano Letters* **2004**, *4*, 2271-2276.
(140) Rubin, Y.; Lin, S. S.; Knobler, C. B.; Anthony, J.; Boldi, A. M.; Diederich, F. Solution-spray flash vacuum pyrolysis - A new method for the synthesis of linear polyynes with odd numbers of CC bonds from substituted 3,4- dialkynyl-3-cyclobutene-1,2-diones. *Journal of the American Chemical Society* **1991**, *113*, 6943-6949.

Appendix I Crystallography Data

Crystal urea host **5**

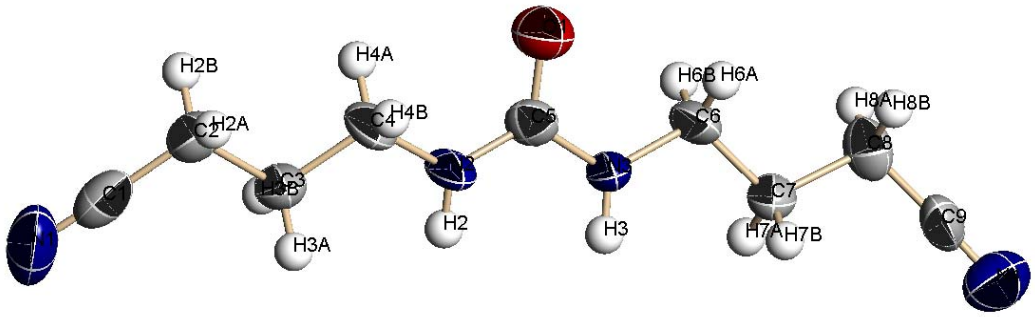

Table 1. Crystal data and structure refinement for luat.

Identification code	luat	
Empirical formula	C9 H14 N4 O	
Formula weight	194.24	
Temperature	273(2) K	
Wavelength	0.71073 Å	
Crystal system	Orthorhombic	
Space group	Pbc2(1)	
Unit cell dimensions	a = 4.6500(19) Å	α = 90°.
	b = 12.098(5) Å	β = 90°.
	c = 18.191(8) Å	γ = 90°.
Volume	1023.3(7) $Å^3$	
Z	4	
Density (calculated)	1.261 Mg/m^3	
Absorption coefficient	0.087 mm^{-1}	
F(000)	416	
Crystal size	? x ? x ? mm^3	
Theta range for data collection	2.24 to 28.48°.	
Index ranges	-6<=h<=6, -11<=k<=15, -20<=l<=23	
Reflections collected	4619	
Independent reflections	2015 [R(int) = 0.2898]	
Completeness to theta = 28.48°	91.8 %	
Absorption correction	None	

Refinement method	Full-matrix least-squares on F^2
Data / restraints / parameters	2015 / 1 / 127
Goodness-of-fit on F^2	0.694
Final R indices [I>2sigma(I)]	R1 = 0.0741, wR2 = 0.1705
R indices (all data)	R1 = 0.3557, wR2 = 0.2544
Absolute structure parameter	-7(10)
Largest diff. peak and hole	0.202 and -0.269 e.Å^{-3}

Table 2. Atomic coordinates (x 10^4) and equivalent isotropic displacement parameters (Å^{2}x 10^3)
for luat. U(eq) is defined as one third of the trace of the orthogonalized U^{ij} tensor.

	x	y	z	U(eq)
N(2)	2140(20)	9473(9)	1539(6)	58(3)
N(3)	2234(19)	7932(8)	2279(6)	57(3)
C(3)	2680(30)	11140(11)	818(7)	60(4)
C(7)	3000(30)	6302(10)	3012(6)	50(3)
C(1)	3120(30)	12891(13)	87(8)	70(4)
C(4)	710(30)	10262(12)	1070(9)	61(4)
C(5)	740(30)	8729(16)	1906(13)	50(3)
O(1)	-1964(17)	8709(12)	1928(9)	73(2)
C(2)	1080(30)	12002(11)	324(7)	63(4)
C(6)	900(30)	7176(12)	2781(8)	60(5)
N(4)	5360(30)	3947(13)	3875(13)	86(6)
C(8)	1660(30)	5438(10)	3517(7)	61(4)
C(9)	3730(40)	4583(12)	3732(8)	67(5)
N(1)	4660(30)	13597(13)	-73(14)	102(7)

Table 3. Bond lengths [Å] and angles [°] for luat.

N(2)-C(5)	1.30(2)
N(2)-C(4)	1.442(17)
N(3)-C(5)	1.37(2)
N(3)-C(6)	1.433(16)
C(3)-C(4)	1.477(17)
C(3)-C(2)	1.566(16)
C(7)-C(6)	1.500(18)
C(7)-C(8)	1.525(15)
C(1)-N(1)	1.152(19)
C(1)-C(2)	1.499(19)
C(5)-O(1)	1.258(12)
N(4)-C(9)	1.111(17)
C(8)-C(9)	1.467(17)

C(5)-N(2)-C(4)	122.2(11)
C(5)-N(3)-C(6)	123.1(11)
C(4)-C(3)-C(2)	111.1(11)
C(6)-C(7)-C(8)	112.7(10)
N(1)-C(1)-C(2)	177(2)
N(2)-C(4)-C(3)	111.9(12)
O(1)-C(5)-N(2)	122.1(15)
O(1)-C(5)-N(3)	118.5(17)
N(2)-C(5)-N(3)	119.4(10)
C(1)-C(2)-C(3)	109.9(11)
N(3)-C(6)-C(7)	110.3(10)
C(9)-C(8)-C(7)	111.9(11)
N(4)-C(9)-C(8)	178(2)

Symmetry transformations used to generate equivalent atoms:

Table 4. Anisotropic displacement parameters ($Å^2 x\ 10^3$) for luat. The anisotropic displacement factor exponent takes the form: $-2\pi^2[h^2 a^{*2} U^{11} + ... + 2 h k a^* b^* U^{12}]$

	U^{11}	U^{22}	U^{33}	U^{23}	U^{13}	U^{12}
N(2)	24(6)	66(7)	82(8)	27(6)	-5(7)	-5(6)
N(3)	33(7)	50(6)	88(9)	24(6)	8(7)	7(5)
C(3)	43(9)	59(8)	78(10)	14(7)	3(8)	6(7)
C(7)	41(8)	49(7)	61(9)	5(7)	-1(7)	0(6)
C(1)	76(13)	63(10)	72(12)	-1(10)	2(10)	28(9)
C(4)	35(9)	63(11)	86(12)	12(9)	-5(9)	-16(8)
C(5)	48(9)	60(7)	43(6)	3(6)	9(13)	3(13)
O(1)	54(6)	83(5)	80(5)	11(4)	2(8)	1(7)
C(2)	58(11)	61(9)	71(11)	7(8)	6(8)	13(8)
C(6)	42(9)	67(12)	71(12)	23(10)	17(9)	-1(8)
N(4)	74(12)	79(14)	104(17)	-14(13)	-2(9)	13(7)
C(8)	80(12)	59(9)	44(10)	12(8)	6(8)	-9(8)
C(9)	74(14)	46(9)	82(11)	9(8)	31(10)	-8(7)
N(1)	145(15)	56(12)	104(16)	18(11)	26(11)	12(8)

Table 5. Hydrogen coordinates (x 10^4) and isotropic displacement parameters ($Å^2$x 10^3) for luat.

	x	y	z	U(eq)
H(2)	3980	9497	1576	69
H(3)	4058	7882	2209	68
H(3A)	4246	10811	541	72
H(3B)	3502	11513	1241	72
H(7A)	4601	6650	3265	61
H(7B)	3753	5937	2578	61
H(4A)	-878	10595	1337	73
H(4B)	-81	9882	646	73
H(2A)	289	11635	-105	76
H(2B)	-501	12327	597	76
H(6A)	-747	6833	2546	72
H(6B)	225	7575	3210	72
H(8A)	926	5799	3955	73
H(8B)	45	5094	3268	73

Crystal urea host **6**

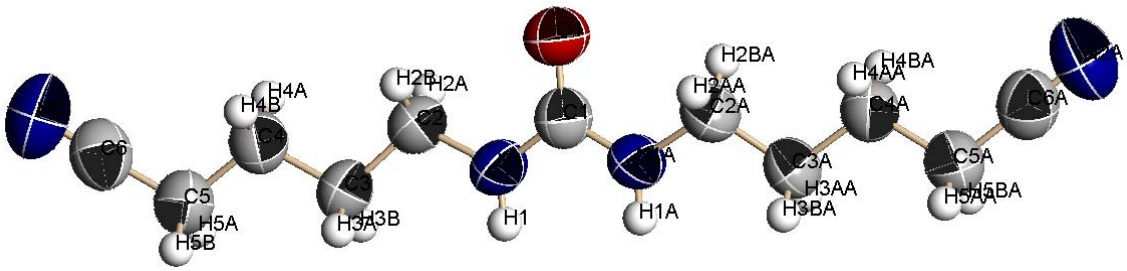

Table 1. Crystal data and structure refinement for lud121.

Identification code	lud121	
Empirical formula	C11 H18 N4 O	
Formula weight	222.29	
Temperature	273(2) K	
Wavelength	0.71073 Å	
Crystal system	Orthorhombic	
Space group	Fdd2	
Unit cell dimensions	a = 13.678(8) Å	α = 90°.
	b = 39.47(2) Å	β = 90°.
	c = 4.602(3) Å	γ = 90°.
Volume	2485(2) $Å^3$	
Z	8	
Density (calculated)	1.189 Mg/m^3	
Absorption coefficient	0.080 mm^{-1}	
F(000)	960	
Crystal size	? x ? x ? mm^3	
Theta range for data collection	2.06 to 23.28°.	
Index ranges	-14<=h<=14, -42<=k<=29, -5<=l<=5	
Reflections collected	2593	
Independent reflections	847 [R(int) = 0.1092]	
Completeness to theta = 23.28°	100.0 %	
Absorption correction	None	
Refinement method	Full-matrix least-squares on F^2	
Data / restraints / parameters	847 / 1 / 74	

Goodness-of-fit on F^2	0.754
Final R indices [I>2sigma(I)]	R1 = 0.0515, wR2 = 0.1134
R indices (all data)	R1 = 0.1463, wR2 = 0.1478
Absolute structure parameter	-8(7)
Largest diff. peak and hole	0.106 and -0.089 e.$Å^{-3}$

Table 2. Atomic coordinates (x 10^4) and equivalent isotropic displacement parameters ($Å^2$x 10^3)
for lud121. U(eq) is defined as one third of the trace of the orthogonalized U^{ij} tensor.

	x	y	z	U(eq)
C(1)	0	5000	6620(30)	92(3)
C(3)	2198(4)	5489(1)	8645(14)	93(2)
C(2)	1405(4)	5367(1)	6648(13)	97(2)
N(1)	664(4)	5169(1)	8166(10)	94(2)
C(4)	3017(4)	5652(1)	6901(13)	97(2)
C(5)	3808(4)	5813(2)	8760(16)	104(2)
C(6)	4607(5)	5946(2)	7002(17)	108(2)
O(1)	0	5000	3918(15)	111(2)
N(2)	5216(4)	6044(2)	5612(18)	146(3)

Table 3. Bond lengths [Å] and angles [°] for lud121.

C(1)-O(1)	1.246(11)
C(1)-N(1)	1.331(7)
C(1)-N(1)#1	1.331(7)
C(3)-C(2)	1.501(7)
C(3)-C(4)	1.520(6)
C(2)-N(1)	1.459(6)
C(4)-C(5)	1.520(7)
C(5)-C(6)	1.456(8)
C(6)-N(2)	1.121(9)
O(1)-C(1)-N(1)	122.2(5)
O(1)-C(1)-N(1)#1	122.2(5)
N(1)-C(1)-N(1)#1	115.6(10)
C(2)-C(3)-C(4)	110.1(5)
N(1)-C(2)-C(3)	112.4(5)
C(1)-N(1)-C(2)	119.2(6)
C(3)-C(4)-C(5)	113.8(5)
C(6)-C(5)-C(4)	111.8(6)
N(2)-C(6)-C(5)	178.8(9)

Symmetry transformations used to generate equivalent atoms:
#1 -x,-y+1,z

Table 4. Anisotropic displacement parameters ($Å^2 x\ 10^3$) for lud121. The anisotropic displacement factor exponent takes the form: $-2\pi^2[h^2 a^{*2} U^{11} + ... + 2 h k a^* b^* U^{12}]$

	U^{11}	U^{22}	U^{33}	U^{23}	U^{13}	U^{12}
C(1)	93(7)	92(7)	91(8)	0	0	-19(5)
C(3)	88(4)	101(5)	91(5)	9(4)	8(4)	-15(4)
C(2)	94(4)	114(5)	84(4)	13(4)	4(4)	-12(4)
N(1)	100(4)	108(4)	74(3)	2(3)	7(3)	-32(3)
C(4)	87(4)	107(5)	98(5)	-9(4)	1(4)	-6(4)
C(5)	89(4)	121(5)	103(5)	3(5)	3(4)	-3(4)
C(6)	99(5)	101(6)	124(6)	-14(5)	-2(5)	-5(4)
O(1)	123(5)	129(5)	83(4)	0	0	-31(4)
N(2)	117(5)	149(6)	173(7)	11(5)	31(5)	-19(4)

Table 5. Hydrogen coordinates ($x\ 10^4$) and isotropic displacement parameters ($Å^2 x\ 10^3$) for lud121.

	x	y	z	U(eq)
H(3A)	2455	5300	9753	112
H(3B)	1932	5653	10001	112
H(2A)	1096	5561	5735	117
H(2B)	1694	5230	5127	117
H(1)	656	5161	10034	113
H(4A)	2740	5823	5640	117
H(4B)	3314	5480	5674	117
H(5A)	3525	5996	9890	125
H(5B)	4064	5646	10104	125

Crystal oxalamide host **8**

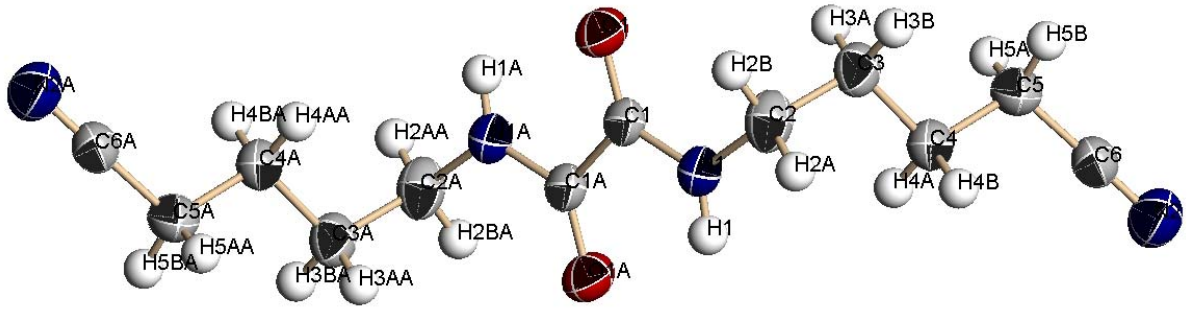

Table 1. Crystal data and structure refinement for loet.

Identification code	loet	
Empirical formula	C12 H14 N4 O2	
Formula weight	246.27	
Temperature	273(2) K	
Wavelength	0.71073 Å	
Crystal system	Orthorhombic	
Space group	Pbca	
Unit cell dimensions	a = 8.0702(10) Å	α = 90°.
	b = 10.8379(13) Å	β = 90°.
	c = 15.038(2) Å	γ = 90°.
Volume	1315.2(3) $Å^3$	
Z	4	
Density (calculated)	1.244 Mg/m^3	
Absorption coefficient	0.088 mm^{-1}	
F(000)	520	
Crystal size	? x ? x ? mm^3	
Theta range for data collection	2.71 to 28.63°.	
Index ranges	-10<=h<=10, -11<=k<=13, -13<=l<=19	
Reflections collected	7574	
Independent reflections	1550 [R(int) = 0.0764]	
Completeness to theta = 28.63°	92.1 %	
Absorption correction	None	
Refinement method	Full-matrix least-squares on F^2	
Data / restraints / parameters	1550 / 0 / 82	

Goodness-of-fit on F^2	0.497
Final R indices [I>2sigma(I)]	R1 = 0.0404, wR2 = 0.1151
R indices (all data)	R1 = 0.1195, wR2 = 0.1794
Largest diff. peak and hole	0.203 and -0.146 e.$Å^{-3}$

Table 2. Atomic coordinates (x 10^4) and equivalent isotropic displacement parameters ($Å^2$x 10^3)
for loet. U(eq) is defined as one third of the trace of the orthogonalized U^{ij} tensor.

	x	y	z	U(eq)
O(1)	263(2)	-435(1)	1111(1)	54(1)
C(4)	148(3)	3782(2)	1183(2)	48(1)
N(1)	1182(2)	1271(2)	392(1)	46(1)
C(1)	391(3)	200(2)	439(1)	40(1)
C(3)	697(3)	2637(2)	1684(2)	50(1)
C(2)	1922(3)	1856(2)	1165(2)	54(1)
C(5)	-1115(3)	4530(2)	1704(2)	53(1)
N(2)	-1715(3)	6637(2)	965(2)	67(1)
C(6)	-1461(3)	5715(2)	1294(2)	49(1)

Table 3. Bond lengths [Å] and angles [°] for loet.

O(1)-C(1)	1.227(2)
C(4)-C(3)	1.518(3)
C(4)-C(5)	1.520(3)
N(1)-C(1)	1.326(3)
N(1)-C(2)	1.452(3)
C(1)-C(1)#1	1.527(4)
C(3)-C(2)	1.517(3)
C(5)-C(6)	1.452(3)
N(2)-C(6)	1.134(3)
C(3)-C(4)-C(5)	112.1(2)
C(1)-N(1)-C(2)	122.52(19)
O(1)-C(1)-N(1)	125.1(2)
O(1)-C(1)-C(1)#1	121.2(2)
N(1)-C(1)-C(1)#1	113.6(2)
C(4)-C(3)-C(2)	113.0(2)
N(1)-C(2)-C(3)	112.77(19)
C(6)-C(5)-C(4)	112.4(2)
N(2)-C(6)-C(5)	179.1(3)

Symmetry transformations used to generate equivalent atoms:
#1 -x,-y,-z

Table 4. Anisotropic displacement parameters ($Å^2 x\ 10^3$) for loet. The anisotropic displacement factor exponent takes the form: $-2\pi^2[h^2 a^{*2} U^{11} + ... + 2 h k a^* b^* U^{12}]$

	U^{11}	U^{22}	U^{33}	U^{23}	U^{13}	U^{12}
O(1)	73(1)	45(1)	45(1)	6(1)	-8(1)	-6(1)
C(4)	54(1)	41(1)	47(1)	-3(1)	2(1)	-1(1)
N(1)	55(1)	36(1)	48(1)	-2(1)	0(1)	-3(1)
C(1)	44(1)	33(1)	44(1)	-1(1)	2(1)	4(1)
C(3)	60(2)	42(1)	47(1)	-6(1)	-11(1)	-3(1)
C(2)	51(1)	45(1)	65(2)	-7(1)	-13(1)	1(1)
C(5)	66(2)	50(1)	43(1)	2(1)	3(1)	4(1)
N(2)	72(2)	52(1)	76(2)	6(1)	11(1)	5(1)
C(6)	54(1)	45(1)	48(1)	-5(1)	6(1)	1(1)

Table 5. Hydrogen coordinates ($x\ 10^4$) and isotropic displacement parameters ($Å^2 x\ 10^3$) for loet.

	x	y	z	U(eq)
H(4A)	-332	3539	618	57
H(4B)	1107	4293	1060	57
H(1)	1259	1632	-115	55
H(3A)	-269	2140	1822	60
H(3B)	1202	2884	2241	60
H(2A)	2835	2374	972	64
H(2B)	2369	1224	1553	64
H(5A)	-2137	4063	1749	64
H(5B)	-702	4664	2302	64

Co-crystal **2·1**

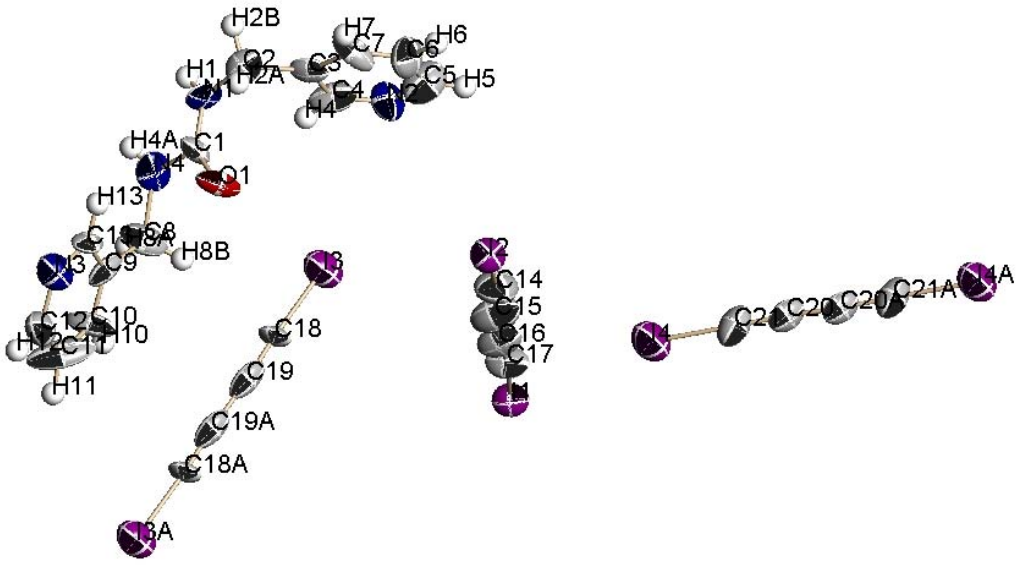

Table 1. Crystal data and structure refinement for liabt.

Identification code	liabt	
Empirical formula	C21 H14 I4 N4 O	
Formula weight	845.96	
Temperature	273(2) K	
Wavelength	0.71073 Å	
Crystal system	Triclinic	
Space group	P-1	
Unit cell dimensions	a = 4.469(2) Å	α = 74.407(8)°.
	b = 16.399(7) Å	β = 84.618(7)°.
	c = 18.116(8) Å	γ = 82.207(7)°.
Volume	1264.8(10) $Å^3$	
Z	2	
Density (calculated)	2.221 Mg/m^3	
Absorption coefficient	4.946 mm^{-1}	
F(000)	776	
Crystal size	? x ? x ? mm^3	
Theta range for data collection	1.17 to 28.48°.	
Index ranges	-5<=h<=5, -17<=k<=21, -23<=l<=18	

Reflections collected	7764
Independent reflections	5471 [R(int) = 0.1359]
Completeness to theta = 28.48°	86.0 %
Absorption correction	None
Refinement method	Full-matrix least-squares on F^2
Data / restraints / parameters	5471 / 0 / 271
Goodness-of-fit on F^2	0.726
Final R indices [I>2sigma(I)]	R1 = 0.0859, wR2 = 0.2168
R indices (all data)	R1 = 0.2690, wR2 = 0.2711
Largest diff. peak and hole	1.285 and -1.640 e.$Å^{-3}$

Table 2. Atomic coordinates (x 10^4) and equivalent isotropic displacement parameters ($Å^2$x 10^3)
for liabt. U(eq) is defined as one third of the trace of the orthogonalized U^{ij} tensor.

	x	y	z	U(eq)
I(1)	-2484(4)	9778(1)	1289(1)	63(1)
I(2)	5703(4)	5505(1)	3596(1)	64(1)
I(3)	758(5)	5105(1)	1925(1)	86(1)
C(15)	2160(70)	7280(20)	2620(20)	98(11)
C(2)	-1070(60)	1795(15)	3736(16)	66(8)
N(3)	4730(50)	1293(14)	446(14)	70(6)
C(19)	4220(50)	5025(15)	355(16)	62(9)
C(13)	2660(50)	1724(15)	846(13)	50(6)
C(10)	2550(60)	2954(17)	-139(15)	74(9)
C(11)	4560(60)	2570(20)	-540(20)	119(16)
C(4)	-1550(60)	3321(16)	3905(17)	75(9)
C(9)	1610(50)	2558(14)	543(16)	53(7)
C(14)	3470(70)	6590(20)	3070(16)	86(10)
C(18)	2880(50)	5027(16)	956(13)	52(7)
C(1)	-710(60)	2375(16)	2419(13)	51(6)
I(4)	2317(5)	9307(2)	3335(1)	93(1)
C(20)	4470(50)	9891(15)	4729(16)	56(7)

C(21)	3660(60)	9667(16)	4190(18)	75(9)
N(1)	-2370(40)	2101(13)	3004(12)	60(6)
C(16)	660(50)	8060(19)	2200(18)	73(9)
C(3)	-680(50)	2462(14)	4157(14)	51(7)
C(17)	-510(60)	8733(15)	1892(15)	68(8)
C(12)	5650(60)	1720(20)	-273(17)	79(9)
N(2)	-1490(50)	3948(14)	4227(13)	67(6)
C(7)	950(60)	2280(20)	4818(14)	69(9)
C(6)	1120(70)	2910(20)	5106(18)	89(10)
C(5)	50(70)	3710(20)	4830(20)	91(11)
O(1)	2030(30)	2447(11)	2389(8)	66(5)
N(4)	-2060(40)	2557(12)	1770(12)	63(6)
C(8)	-640(60)	3085(17)	986(14)	78(9)

Table 3. Bond lengths [Å] and angles [°] for liabt.

I(1)-C(17)	1.92(2)
I(2)-C(14)	1.96(3)
I(3)-C(18)	1.94(2)
C(15)-C(14)	1.31(4)
C(15)-C(16)	1.41(4)
C(2)-N(1)	1.43(3)
C(2)-C(3)	1.53(3)
N(3)-C(13)	1.36(3)
N(3)-C(12)	1.36(3)
C(19)-C(18)	1.19(3)
C(19)-C(19)#1	1.42(6)
C(13)-C(9)	1.36(3)
C(10)-C(11)	1.30(4)
C(10)-C(9)	1.29(3)
C(11)-C(12)	1.37(4)
C(4)-N(2)	1.32(3)
C(4)-C(3)	1.37(3)
C(9)-C(8)	1.55(3)
C(1)-O(1)	1.24(3)

C(1)-N(1)	1.25(3)
C(1)-N(4)	1.32(3)
I(4)-C(21)	1.97(3)
C(20)-C(21)	1.23(3)
C(20)-C(20)#2	1.28(5)
C(16)-C(17)	1.17(3)
C(3)-C(7)	1.40(3)
N(2)-C(5)	1.29(3)
C(7)-C(6)	1.29(4)
C(6)-C(5)	1.32(4)
N(4)-C(8)	1.58(3)

C(14)-C(15)-C(16)	175(3)
N(1)-C(2)-C(3)	117(2)
C(13)-N(3)-C(12)	117(2)
C(18)-C(19)-C(19)#1	177(3)
C(9)-C(13)-N(3)	121(2)
C(11)-C(10)-C(9)	120(3)
C(10)-C(11)-C(12)	122(3)
N(2)-C(4)-C(3)	131(3)
C(10)-C(9)-C(13)	120(3)
C(10)-C(9)-C(8)	116(2)
C(13)-C(9)-C(8)	123(2)
C(15)-C(14)-I(2)	171(3)
C(19)-C(18)-I(3)	176(2)
O(1)-C(1)-N(1)	127(2)
O(1)-C(1)-N(4)	118(2)
N(1)-C(1)-N(4)	114(2)
C(21)-C(20)-C(20)#2	175(4)
C(20)-C(21)-I(4)	179(3)
C(1)-N(1)-C(2)	119(2)
C(17)-C(16)-C(15)	175(3)
C(4)-C(3)-C(7)	111(3)
C(4)-C(3)-C(2)	126(3)
C(7)-C(3)-C(2)	123(2)
C(16)-C(17)-I(1)	173(3)

N(3)-C(12)-C(11)	119(3)
C(5)-N(2)-C(4)	112(3)
C(6)-C(7)-C(3)	116(3)
C(7)-C(6)-C(5)	127(3)
N(2)-C(5)-C(6)	122(3)
C(1)-N(4)-C(8)	123(2)
C(9)-C(8)-N(4)	115(2)

Symmetry transformations used to generate equivalent atoms:
#1 -x+1,-y+1,-z #2 -x+1,-y+2,-z+1

Table 4. Anisotropic displacement parameters ($Å^2 x\ 10^3$) for liabt. The anisotropic displacement factor exponent takes the form: $-2\pi^2[h^2 a^{*2} U^{11} + ... + 2 h k a^* b^* U^{12}]$

	U^{11}	U^{22}	U^{33}	U^{23}	U^{13}	U^{12}
I(1)	52(1)	60(1)	70(1)	-13(1)	-1(1)	3(1)
I(2)	60(1)	65(1)	65(1)	-14(1)	-10(1)	0(1)
I(3)	76(1)	117(2)	68(1)	-28(1)	0(1)	-13(1)
C(15)	70(20)	80(20)	130(30)	-10(20)	20(20)	-11(19)
C(2)	58(17)	54(17)	80(20)	-13(16)	-7(16)	-1(13)
N(3)	55(14)	87(18)	66(17)	-21(15)	-9(13)	3(12)
C(19)	39(19)	41(14)	100(30)	0(20)	-34(17)	-8(13)
C(13)	58(16)	65(18)	20(13)	13(13)	-9(12)	-27(13)
C(10)	80(20)	59(19)	47(18)	21(15)	23(15)	23(16)
C(11)	60(20)	70(20)	160(40)	70(20)	0(20)	4(18)
C(4)	71(19)	44(17)	80(20)	24(17)	-1(16)	2(14)
C(9)	37(13)	38(15)	80(20)	6(15)	-28(14)	-14(11)
C(14)	90(20)	90(20)	60(20)	12(18)	-9(18)	-16(19)
C(18)	42(15)	79(19)	34(16)	-17(14)	22(12)	-19(13)
C(1)	41(16)	84(19)	29(16)	-20(14)	5(13)	-8(13)
I(4)	78(1)	131(2)	76(2)	-39(1)	2(1)	-17(1)
C(20)	28(15)	55(17)	80(30)	-11(16)	-11(14)	-4(11)
C(21)	70(20)	58(19)	100(30)	-18(17)	-25(19)	-15(14)
N(1)	22(10)	93(17)	64(16)	-10(13)	-3(11)	-29(10)
C(16)	40(15)	60(20)	110(20)	-21(18)	27(16)	-1(14)

C(3)	40(14)	46(15)	53(17)	-5(13)	20(13)	10(11)
C(17)	74(18)	33(15)	80(20)	5(14)	10(16)	16(14)
C(12)	80(20)	120(30)	50(20)	-30(20)	-4(17)	-40(19)
N(2)	82(16)	63(16)	53(15)	-8(13)	-27(13)	9(13)
C(7)	54(16)	110(20)	35(17)	-13(16)	-14(13)	38(16)
C(6)	100(20)	110(30)	70(20)	-20(20)	-33(19)	-40(20)
C(5)	80(20)	60(20)	120(30)	0(20)	-30(20)	3(17)
O(1)	22(9)	123(15)	35(10)	9(10)	-5(7)	-3(9)
N(4)	17(10)	93(17)	82(17)	-33(14)	-18(11)	9(9)
C(8)	74(19)	90(20)	44(18)	15(16)	-4(15)	17(17)

Table 5. Hydrogen coordinates (x 10^4) and isotropic displacement parameters (Å^{2}x 10^3) for liabt.

	x	y	z	U(eq)
H(2A)	905	1489	3662	79
H(2B)	-2320	1388	4066	79
H(13)	1946	1445	1335	60
H(10)	1795	3519	-346	88
H(11)	5269	2874	-1016	143
H(4)	-2309	3490	3420	90
H(1)	-4276	2098	2968	71
H(12)	6997	1453	-580	95
H(7)	1863	1732	5036	83
H(6)	2106	2781	5560	107
H(5)	416	4115	5074	109
H(4A)	-3796	2382	1774	75
H(8A)	-2272	3370	658	94
H(8B)	392	3523	1088	94

Co-crystal **3·1**

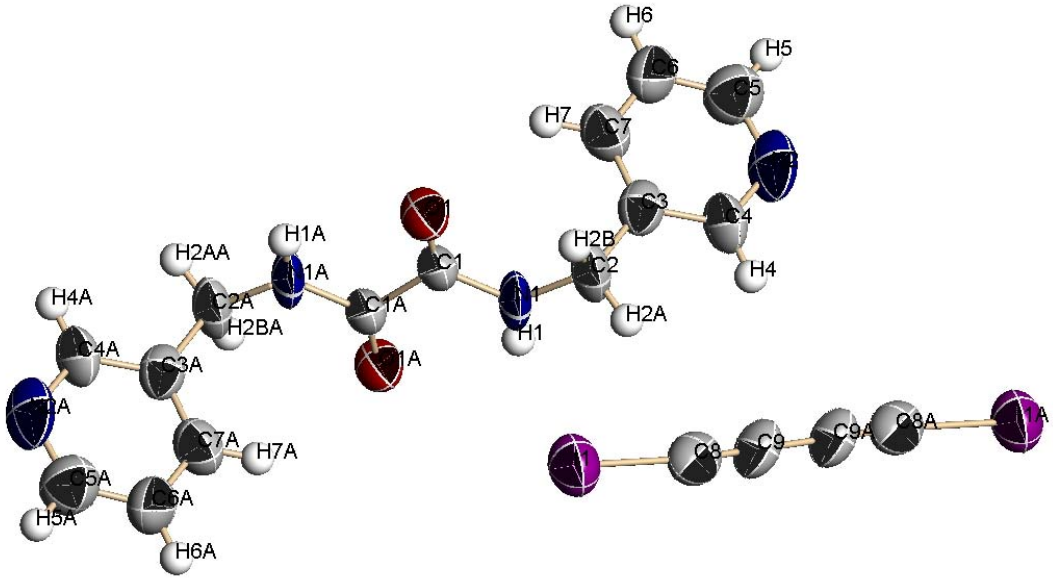

Table 1. Crystal data and structure refinement for low101.

Identification code	low101	
Empirical formula	C18 H14 I2 N4 O2	
Formula weight	572.13	
Temperature	273(2) K	
Wavelength	0.71073 Å	
Crystal system	Triclinic	
Space group	P-1	
Unit cell dimensions	a = 5.077(5) Å	α = 96.110(16)°.
	b = 8.618(7) Å	β = 99.659(13)°.
	c = 11.714(10) Å	γ = 103.666(16)°.
Volume	485.2(7) $Å^3$	
Z	1	
Density (calculated)	1.958 Mg/m^3	
Absorption coefficient	3.260 mm^{-1}	
F(000)	272	
Crystal size	? x ? x ? mm^3	
Theta range for data collection	1.78 to 28.89°.	
Index ranges	-5<=h<=6, -9<=k<=10, -14<=l<=14	
Reflections collected	3061	

Independent reflections	2138 [R(int) = 0.1100]
Completeness to theta = 28.89°	84.0 %
Absorption correction	None
Refinement method	Full-matrix least-squares on F^2
Data / restraints / parameters	2138 / 0 / 118
Goodness-of-fit on F^2	0.764
Final R indices [I>2sigma(I)]	R1 = 0.0747, wR2 = 0.1771
R indices (all data)	R1 = 0.2228, wR2 = 0.2260
Largest diff. peak and hole	1.069 and -0.903 e.$Å^{-3}$

Table 2. Atomic coordinates (x 10^4) and equivalent isotropic displacement parameters ($Å^2$x 10^3)
for low101. U(eq) is defined as one third of the trace of the orthogonalized U^{ij} tensor.

	x	y	z	U(eq)
I(1)	10745(3)	8000(2)	8945(1)	92(1)
O(1)	12700(20)	4389(12)	5810(9)	74(3)
C(1)	10490(40)	4636(16)	5561(13)	59(4)
N(1)	8320(20)	4296(13)	6139(10)	69(3)
C(3)	7450(30)	1850(20)	7072(13)	68(4)
C(2)	8750(30)	3647(17)	7218(13)	77(5)
N(2)	4400(30)	-350(20)	7643(14)	98(5)
C(4)	5540(30)	1250(20)	7724(14)	74(4)
C(8)	7740(40)	6510(20)	9598(14)	79(5)
C(9)	6020(30)	5560(20)	9842(15)	76(5)
C(5)	5100(40)	-1340(20)	6850(19)	96(6)
C(6)	6940(50)	-860(30)	6170(15)	100(6)
C(7)	8090(30)	770(20)	6279(15)	79(5)

Table 3. Bond lengths [Å] and angles [°] for low101.

I(1)-C(8)	2.06(2)
O(1)-C(1)	1.188(15)
C(1)-N(1)	1.379(18)
C(1)-C(1)#1	1.57(3)
N(1)-C(2)	1.439(18)
C(3)-C(4)	1.38(2)
C(3)-C(7)	1.38(2)
C(3)-C(2)	1.51(2)
N(2)-C(5)	1.35(2)
N(2)-C(4)	1.35(2)
C(8)-C(9)	1.15(2)
C(9)-C(9)#2	1.36(4)
C(5)-C(6)	1.35(3)
C(6)-C(7)	1.37(2)

O(1)-C(1)-N(1)	127.9(13)
O(1)-C(1)-C(1)#1	124.1(17)
N(1)-C(1)-C(1)#1	108.0(17)
C(1)-N(1)-C(2)	118.2(13)
C(4)-C(3)-C(7)	117.7(16)
C(4)-C(3)-C(2)	120.4(15)
C(7)-C(3)-C(2)	121.9(14)
N(1)-C(2)-C(3)	112.8(12)
C(5)-N(2)-C(4)	117.4(15)
N(2)-C(4)-C(3)	122.0(16)
C(9)-C(8)-I(1)	172.0(17)
C(8)-C(9)-C(9)#2	179(3)
N(2)-C(5)-C(6)	124.5(18)
C(5)-C(6)-C(7)	117.0(17)
C(6)-C(7)-C(3)	121.4(16)

Symmetry transformations used to generate equivalent atoms:
#1 -x+2,-y+1,-z+1 #2 -x+1,-y+1,-z+2

Table 4. Anisotropic displacement parameters ($Å^2 x\ 10^3$) for low101. The anisotropic displacement factor exponent takes the form: $-2\pi^2[h^2 a^{*2} U^{11} + ... + 2 h k a^* b^* U^{12}]$

	U^{11}	U^{22}	U^{33}	U^{23}	U^{13}	U^{12}
I(1)	89(1)	93(1)	100(1)	33(1)	30(1)	17(1)
O(1)	47(6)	86(8)	102(9)	41(6)	26(6)	23(6)
C(1)	65(10)	52(9)	69(10)	22(7)	27(9)	15(8)
N(1)	80(8)	62(8)	63(8)	22(6)	38(7)	-4(7)
C(3)	61(10)	87(12)	58(10)	21(9)	12(8)	20(9)
C(2)	108(13)	51(9)	61(10)	11(8)	33(9)	-9(9)
N(2)	56(9)	127(15)	113(13)	47(11)	32(9)	7(10)
C(4)	67(10)	67(11)	83(11)	24(9)	23(9)	-4(9)
C(8)	81(13)	99(15)	68(11)	21(10)	13(10)	39(12)
C(9)	57(11)	100(16)	73(12)	13(10)	24(10)	16(11)
C(5)	98(14)	91(14)	98(15)	6(12)	26(13)	21(12)
C(6)	133(17)	113(17)	84(13)	40(12)	53(13)	58(14)
C(7)	90(12)	63(12)	80(12)	18(10)	20(10)	8(10)

Partially polymerized co-crystal **3·1** after heating

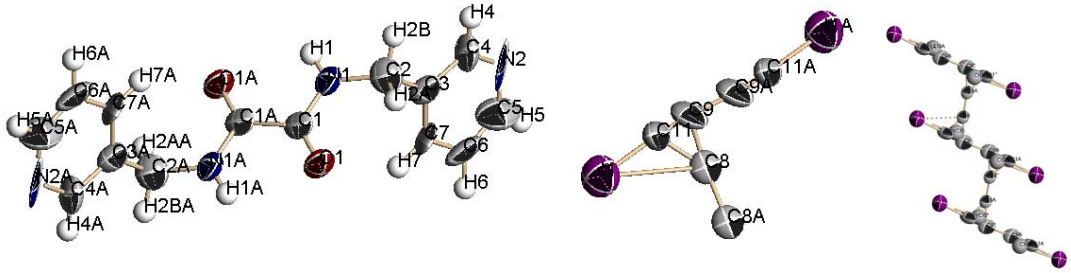

Table 1. Crystal data and structure refinement for liaot.

Identification code	liaot	
Empirical formula	C18 H14 I2 N4 O2	
Formula weight	572.13	
Temperature	273(2) K	
Wavelength	0.71073 Å	
Crystal system	Triclinic	
Space group	P-1	
Unit cell dimensions	a = 4.905(6) Å	α = 96.51(3)°.
	b = 8.324(9) Å	β = 98.46(3)°.
	c = 11.353(15) Å	γ = 103.39(3)°.
Volume	440.8(10) $Å^3$	
Z	1	
Density (calculated)	2.155 Mg/m^3	
Absorption coefficient	3.589 mm^{-1}	
F(000)	272	
Crystal size	? x ? x ? mm^3	
Theta range for data collection	1.84 to 28.51°.	
Index ranges	-3<=h<=6, -8<=k<=8, -15<=l<=9	
Reflections collected	1307	
Independent reflections	1307 [R(int) = 0.0000]	
Completeness to theta = 28.51°	58.2 %	
Absorption correction	None	
Refinement method	Full-matrix least-squares on F^2	
Data / restraints / parameters	1307 / 0 / 118	

Goodness-of-fit on F^2	0.776
Final R indices [I>2sigma(I)]	R1 = 0.0829, wR2 = 0.2207
R indices (all data)	R1 = 0.1819, wR2 = 0.2720
Largest diff. peak and hole	1.176 and -0.819 e.$Å^{-3}$

Table 2. Atomic coordinates (x 10^4) and equivalent isotropic displacement parameters ($Å^2$x 10^3)
for liaot. U(eq) is defined as one third of the trace of the orthogonalized U^{ij} tensor.

	x	y	z	U(eq)
I(1)	5733(3)	2988(2)	3952(2)	94(1)
O(1)	7640(30)	9380(17)	845(11)	61(4)
C(3)	5410(40)	9660(20)	537(17)	49(6)
N(1)	3320(30)	9322(17)	1130(14)	51(4)
C(5)	2420(40)	6800(30)	2007(17)	55(5)
N(2)	-590(40)	4560(30)	2574(19)	92(7)
C(6)	580(50)	6170(30)	2730(20)	72(6)
C(4)	3650(40)	8600(20)	2189(19)	66(6)
C(8)	1910(60)	4050(40)	1180(20)	90(8)
C(2)	1050(50)	670(30)	4826(18)	81(8)
C(7)	50(60)	3510(30)	1770(20)	87(9)
C(1)	2920(50)	1630(30)	4621(18)	75(7)
C(9)	3150(60)	5770(30)	1270(20)	79(7)

Table 3. Bond lengths [Å] and angles [°] for liaot.

I(1)-C(1)	1.88(3)
O(1)-C(3)	1.18(2)
C(3)-N(1)	1.30(2)
C(3)-C(3)#1	1.44(4)
N(1)-C(4)	1.41(3)
C(5)-C(9)	1.28(3)
C(5)-C(6)	1.36(3)
C(5)-C(4)	1.46(3)
N(2)-C(6)	1.31(3)
N(2)-C(7)	1.31(3)
C(8)-C(7)	1.24(4)
C(8)-C(9)	1.40(4)
C(2)-C(1)	1.14(3)
C(2)-C(2)#2	1.47(5)
O(1)-C(3)-N(1)	122.6(19)
O(1)-C(3)-C(3)#1	126(2)
N(1)-C(3)-C(3)#1	111(2)
C(3)-N(1)-C(4)	120.4(18)
C(9)-C(5)-C(6)	118(2)
C(9)-C(5)-C(4)	123.3(19)
C(6)-C(5)-C(4)	118.6(18)
C(6)-N(2)-C(7)	122(2)
N(2)-C(6)-C(5)	120(2)
N(1)-C(4)-C(5)	113.7(16)
C(7)-C(8)-C(9)	122(2)
C(1)-C(2)-C(2)#2	172(4)
C(8)-C(7)-N(2)	119(3)
C(2)-C(1)-I(1)	168(2)
C(5)-C(9)-C(8)	119(2)

Symmetry transformations used to generate equivalent atoms:
#1 -x+1,-y+2,-z #2 -x,-y,-z+1

Table 4. Anisotropic displacement parameters ($Å^2 x\ 10^3$) for liaot. The anisotropic displacement factor exponent takes the form: $-2\pi^2[h^2 a^{*2} U^{11} + ... + 2 h k a^* b^* U^{12}]$

	U^{11}	U^{22}	U^{33}	U^{23}	U^{13}	U^{12}
I(1)	91(1)	87(2)	105(1)	24(1)	21(1)	17(1)
O(1)	39(7)	66(10)	93(10)	35(8)	17(7)	25(8)
C(3)	49(12)	19(12)	84(14)	12(10)	27(12)	4(10)
N(1)	64(9)	30(9)	67(10)	17(8)	22(8)	16(8)
C(5)	43(10)	53(14)	72(12)	14(11)	7(9)	20(10)
N(2)	61(11)	98(17)	126(17)	104(15)	-14(11)	16(13)
C(6)	81(14)	53(15)	94(15)	55(12)	26(12)	15(13)
C(4)	76(14)	45(13)	76(13)	20(11)	17(10)	4(11)
C(8)	110(20)	100(20)	89(17)	27(17)	10(16)	85(19)
C(2)	93(18)	110(20)	54(13)	3(13)	33(12)	38(16)
C(7)	100(18)	100(20)	67(15)	-12(15)	16(14)	46(16)
C(1)	89(17)	110(20)	60(13)	31(14)	19(12)	73(17)
C(9)	140(20)	39(16)	101(17)	47(14)	51(16)	67(16)

Co-crystal **5·1**

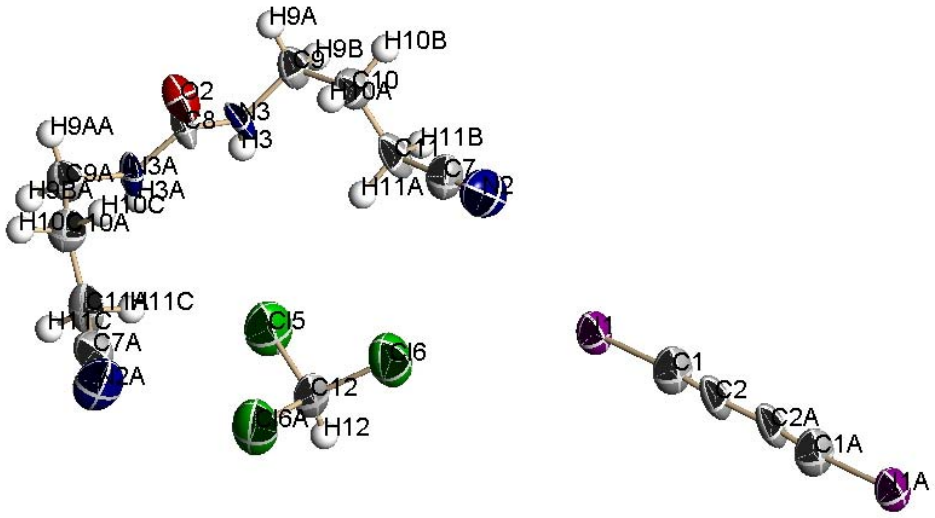

Table 1. Crystal data and structure refinement for lor124.

Identification code	lor124	
Empirical formula	C14 H15 Cl3 I2 N4 O	
Formula weight	615.45	
Temperature	273(2) K	
Wavelength	0.71073 Å	
Crystal system	Monoclinic	
Space group	P2(1)/m	
Unit cell dimensions	a = 4.595(3) Å	α = 90°.
	b = 26.388(13) Å	β = 94.633(11)°.
	c = 8.885(5) Å	γ = 90°.
Volume	1073.7(10) $Å^3$	
Z	2	
Density (calculated)	1.904 Mg/m^3	
Absorption coefficient	3.311 mm^{-1}	
F(000)	584	
Crystal size	? x ? x ? mm^3	
Theta range for data collection	1.54 to 28.22°.	
Index ranges	-6<=h<=5, -23<=k<=26, -4<=l<=11	

Reflections collected	12216
Independent reflections	2066 [R(int) = 0.1003]
Completeness to theta = 28.22°	76.5 %
Absorption correction	None
Refinement method	Full-matrix least-squares on F^2
Data / restraints / parameters	2066 / 0 / 118
Goodness-of-fit on F^2	1.467
Final R indices [I>2sigma(I)]	R1 = 0.1409, wR2 = 0.3660
R indices (all data)	R1 = 0.1940, wR2 = 0.4128
Largest diff. peak and hole	2.879 and -3.902 e.$Å^{-3}$

Table 2. Atomic coordinates (x 10^4) and equivalent isotropic displacement parameters ($Å^2$x 10^3)
for lor124. U(eq) is defined as one third of the trace of the orthogonalized U^{ij} tensor.

	x	y	z	U(eq)
I(1)	8048(3)	4479(1)	6353(1)	65(1)
C(1)	6270(60)	4760(10)	8220(20)	73(7)
C(2)	5460(50)	4895(8)	9350(20)	62(6)
C(10)	1370(40)	3648(9)	80(20)	59(5)
C(11)	3520(40)	3742(9)	1510(20)	62(6)
N(2)	750(50)	4048(10)	3660(20)	94(7)
C(7)	1930(50)	3911(9)	2720(20)	63(6)
N(3)	4230(30)	2938(6)	-919(17)	46(4)
O(2)	-20(40)	2500	-1210(20)	61(5)
C(8)	2590(50)	2500	-1030(30)	42(6)
C(9)	2920(40)	3417(8)	-1210(20)	53(5)
Cl(5)	8720(30)	2500	2842(11)	110(4)
Cl(6)	6060(20)	3043(3)	5184(8)	113(3)
C(12)	8210(100)	2500	4740(30)	85(12)

Table 3. Bond lengths [Å] and angles [°] for lor124.

I(1)-C(1)	2.05(2)
C(1)-C(2)	1.15(3)
C(2)-C(2)#1	1.38(4)
C(10)-C(9)	1.53(2)
C(10)-C(11)	1.56(3)
C(11)-C(7)	1.42(3)
N(2)-C(7)	1.09(3)
N(3)-C(8)	1.38(2)
N(3)-C(9)	1.42(2)
O(2)-C(8)	1.20(3)
C(8)-N(3)#2	1.38(2)
Cl(5)-C(12)	1.72(3)
Cl(6)-C(12)	1.80(3)
C(12)-Cl(6)#2	1.80(3)

C(2)-C(1)-I(1)	174(3)
C(1)-C(2)-C(2)#1	174(3)
C(9)-C(10)-C(11)	111.7(16)
C(7)-C(11)-C(10)	109.5(18)
N(2)-C(7)-C(11)	179(3)
C(8)-N(3)-C(9)	120.8(16)
O(2)-C(8)-N(3)	123.1(10)
O(2)-C(8)-N(3)#2	123.1(10)
N(3)-C(8)-N(3)#2	114(2)
N(3)-C(9)-C(10)	115.8(16)
Cl(5)-C(12)-Cl(6)	109.7(14)
Cl(5)-C(12)-Cl(6)#2	109.7(14)
Cl(6)-C(12)-Cl(6)#2	105(2)

Symmetry transformations used to generate equivalent atoms:
#1 -x+1,-y+1,-z+2 #2 x,-y+1/2,z

Table 4. Anisotropic displacement parameters ($Å^2 x\ 10^3$) for lor124. The anisotropic displacement factor exponent takes the form: $-2\pi^2[h^2 a^{*2} U^{11} + ... + 2 h k a^* b^* U^{12}]$

	U^{11}	U^{22}	U^{33}	U^{23}	U^{13}	U^{12}
I(1)	97(1)	52(2)	51(1)	-3(1)	32(1)	6(1)
C(1)	105(16)	62(19)	55(11)	-4(11)	37(11)	-7(14)
C(2)	98(15)	32(14)	63(13)	0(9)	39(11)	19(11)
C(10)	69(12)	54(15)	57(11)	-2(9)	23(9)	15(10)
C(11)	82(14)	40(16)	71(13)	0(10)	41(11)	27(11)
N(2)	123(17)	100(20)	67(12)	-5(11)	30(12)	33(15)
C(7)	80(14)	55(16)	57(12)	-6(10)	22(10)	-13(11)
N(3)	61(9)	20(11)	61(9)	9(7)	20(7)	14(7)
O(2)	49(12)	42(14)	94(15)	0	21(9)	0
C(8)	51(17)	18(19)	61(14)	0	26(11)	0
C(9)	57(10)	42(15)	61(11)	-7(9)	19(8)	10(10)
Cl(5)	175(11)	91(9)	70(5)	0	49(6)	0
Cl(6)	190(8)	73(6)	81(4)	-3(4)	40(5)	17(5)
C(12)	180(40)	50(20)	29(12)	0	40(17)	0

Table 5. Hydrogen coordinates ($x\ 10^4$) and isotropic displacement parameters ($Å^2 x\ 10^3$) for lor124.

	x	y	z	U(eq)
H(10A)	-180	3422	346	71
H(10B)	478	3967	-244	71
H(11A)	4540	3430	1794	75
H(11B)	4954	3994	1286	75
H(3)	6080	2920	-670	56
H(9A)	1514	3384	-2082	63
H(9B)	4416	3652	-1482	63
H(12)	10100(800)	0(1390000)	5300(400)	102

Co-crystal **8·1**

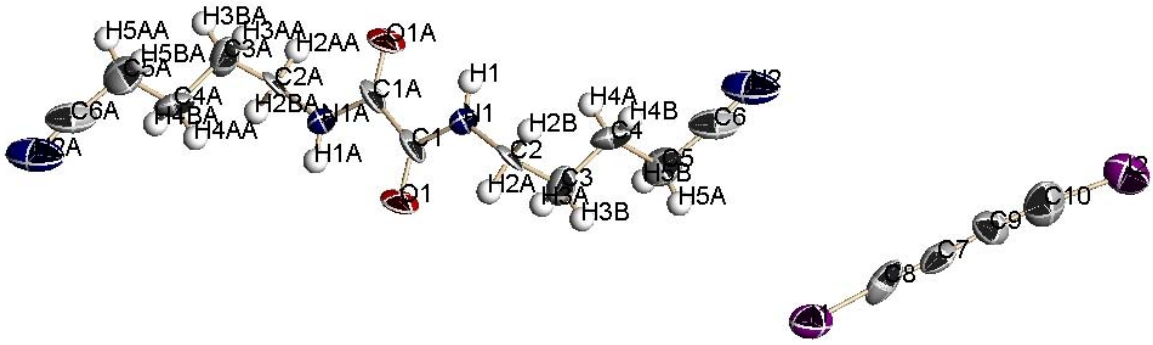

Table 1. Crystal data and structure refinement for liaut.

Identification code	liaut	
Empirical formula	C20 H18 I4 N4 O2	
Formula weight	853.98	
Temperature	273(2) K	
Wavelength	0.71073 Å	
Crystal system	Triclinic	
Space group	P-1	
Unit cell dimensions	a = 4.980(4) Å	α = 92.121(11)°.
	b = 8.509(6) Å	β = 96.382(14)°.
	c = 16.242(12) Å	γ = 97.568(12)°.
Volume	677.0(8) $Å^3$	
Z	1	
Density (calculated)	2.095 Mg/m^3	
Absorption coefficient	4.624 mm^{-1}	
F(000)	394	
Crystal size	? x ? x ? mm^3	
Theta range for data collection	1.26 to 28.37°.	
Index ranges	-6<=h<=6, -10<=k<=10, -9<=l<=21	
Reflections collected	4098	
Independent reflections	2903 [R(int) = 0.1480]	
Completeness to theta = 28.37°	85.4 %	
Absorption correction	None	

Refinement method	Full-matrix least-squares on F^2
Data / restraints / parameters	2903 / 0 / 136
Goodness-of-fit on F^2	0.645
Final R indices [I>2sigma(I)]	R1 = 0.0636, wR2 = 0.1271
R indices (all data)	R1 = 0.3384, wR2 = 0.1741
Largest diff. peak and hole	1.130 and -0.728 e.Å^{-3}

Table 2. Atomic coordinates (x 10^4) and equivalent isotropic displacement parameters (Å^{2}x 10^3)
for liaut. U(eq) is defined as one third of the trace of the orthogonalized U^{ij} tensor.

	x	y	z	U(eq)
C(10)	-980(50)	-1030(30)	1929(15)	93(8)
C(9)	970(50)	-620(20)	2497(15)	60(7)
C(7)	4970(50)	550(20)	3618(13)	73(7)
C(8)	3070(50)	-70(20)	3032(14)	58(6)
I(1)	7741(3)	1563(2)	4391(1)	82(1)
I(2)	-3625(3)	-1800(2)	1014(1)	91(1)
C(3)	8820(40)	6230(20)	7715(12)	67(6)
O(1)	12770(20)	6118(14)	9599(7)	57(4)
N(1)	8310(30)	5926(17)	9203(9)	51(4)
C(1)	10440(40)	5550(20)	9676(11)	48(6)
C(2)	8530(30)	7030(20)	8538(12)	56(6)
N(2)	1880(40)	3240(20)	5660(15)	102(8)
C(6)	3910(50)	3820(30)	5959(17)	74(8)
C(5)	6470(40)	4530(30)	6439(13)	91(8)
C(4)	6150(30)	5310(20)	7273(12)	71(6)

Table 3. Bond lengths [Å] and angles [°] for liaut.

C(10)-C(9)	1.27(2)
C(10)-I(2)	1.91(3)
C(9)-C(8)	1.30(3)
C(7)-C(8)	1.31(2)
C(7)-I(1)	1.86(2)
C(3)-C(2)	1.51(2)
C(3)-C(4)	1.54(2)
O(1)-C(1)	1.221(17)
N(1)-C(1)	1.318(19)
N(1)-C(2)	1.460(19)
C(1)-C(1)#1	1.50(3)
N(2)-C(6)	1.12(3)
C(6)-C(5)	1.46(3)
C(5)-C(4)	1.52(2)

C(9)-C(10)-I(2)	173(2)
C(10)-C(9)-C(8)	174(2)
C(8)-C(7)-I(1)	175.1(17)
C(9)-C(8)-C(7)	173.5(19)
C(2)-C(3)-C(4)	114.3(16)
C(1)-N(1)-C(2)	123.4(14)
O(1)-C(1)-N(1)	122.4(16)
O(1)-C(1)-C(1)#1	126(2)
N(1)-C(1)-C(1)#1	111(2)
N(1)-C(2)-C(3)	113.4(17)
N(2)-C(6)-C(5)	174(3)
C(6)-C(5)-C(4)	114.7(18)
C(5)-C(4)-C(3)	113.7(16)

Symmetry transformations used to generate equivalent atoms:
#1 -x+2,-y+1,-z+2

Table 4. Anisotropic displacement parameters ($Å^2 x\ 10^3$) for liaut. The anisotropic displacement factor exponent takes the form: $-2\pi^2[h^2 a^{*2} U^{11} + ... + 2 h k a^* b^* U^{12}]$

	U^{11}	U^{22}	U^{33}	U^{23}	U^{13}	U^{12}
C(10)	110(20)	75(18)	80(20)	31(16)	4(18)	-8(16)
C(9)	47(16)	60(16)	70(20)	15(15)	3(14)	13(13)
C(7)	140(20)	46(15)	41(16)	15(13)	28(16)	5(15)
C(8)	68(17)	71(18)	48(19)	9(14)	32(14)	33(15)
I(1)	61(1)	98(1)	95(1)	39(1)	21(1)	22(1)
I(2)	77(1)	85(1)	107(2)	-2(1)	9(1)	0(1)
C(3)	86(17)	68(16)	42(15)	14(12)	-1(14)	-9(13)
O(1)	21(7)	77(10)	80(11)	19(8)	13(7)	21(7)
N(1)	41(10)	70(12)	41(11)	17(9)	7(9)	-4(9)
C(1)	26(12)	64(16)	52(17)	0(11)	-17(13)	13(12)
C(2)	12(10)	95(17)	54(15)	17(14)	-15(10)	-6(10)
N(2)	71(16)	97(18)	140(20)	-28(15)	52(17)	1(13)
C(6)	62(19)	54(17)	120(30)	15(16)	40(20)	17(15)
C(5)	80(18)	140(20)	57(18)	-21(16)	27(15)	28(17)
C(4)	51(14)	96(18)	68(17)	22(14)	31(13)	-8(12)

Table 5. Hydrogen coordinates (x 10^4) and isotropic displacement parameters ($Å^2$x 10^3) for liaut.

	x	y	z	U(eq)
H(3A)	10160	5504	7801	81
H(3B)	9518	7034	7354	81
H(1)	6712	5501	9292	61
H(2A)	10102	7828	8691	67
H(2B)	6923	7560	8479	67
H(5A)	7388	5316	6112	109
H(5B)	7638	3708	6532	109
H(4A)	5465	4499	7629	85
H(4B)	4809	6034	7190	85

Partially polymerized Co-crystal **8·1**

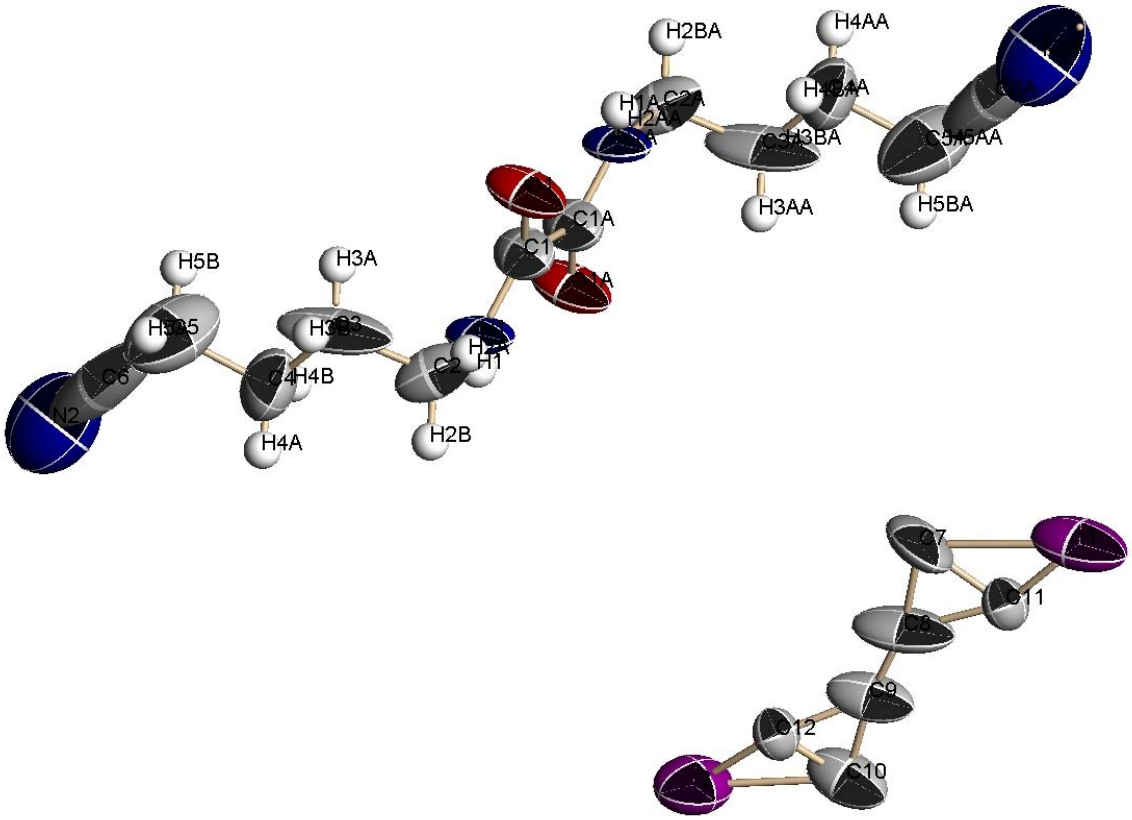

Table 1. Crystal data and structure refinement for liavt.

Identification code	liavt	
Empirical formula	C20 H18 I4 N4 O2	
Formula weight	853.98	
Temperature	273(2) K	
Wavelength	0.71073 Å	
Crystal system	Triclinic	
Space group	P-1	
Unit cell dimensions	a = 4.9460(12) Å	α = 93.940(6)°.
	b = 8.654(2) Å	β = 97.199(6)°.
	c = 15.951(4) Å	γ = 98.220(6)°.
Volume	667.8(3) $Å^3$	
Z	1	
Density (calculated)	2.124 Mg/m^3	
Absorption coefficient	4.688 mm^{-1}	
F(000)	394	
Crystal size	? x ? x ? mm^3	

Theta range for data collection	1.29 to 28.44°.
Index ranges	-6<=h<=6, -10<=k<=11, -9<=l<=20
Reflections collected	4041
Independent reflections	2883 [R(int) = 0.0808]
Completeness to theta = 28.44°	85.2 %
Absorption correction	None
Refinement method	Full-matrix least-squares on F^2
Data / restraints / parameters	2883 / 0 / 136
Goodness-of-fit on F^2	0.668
Final R indices [I>2sigma(I)]	R1 = 0.0919, wR2 = 0.2430
R indices (all data)	R1 = 0.3204, wR2 = 0.3447
Largest diff. peak and hole	2.453 and -1.124 e.$Å^{-3}$

Table 2. Atomic coordinates (x 10^4) and equivalent isotropic displacement parameters ($Å^2$x 10^3)
for liavt. U(eq) is defined as one third of the trace of the orthogonalized U^{ij} tensor.

	x	y	z	U(eq)
I(1)	7745(4)	11277(3)	9203(2)	121(1)
I(2)	-3839(3)	8192(2)	6196(2)	106(1)
O(1)	12830(30)	6030(20)	4593(11)	90(6)
C(9)	640(50)	9530(30)	7600(18)	88(9)
C(7)	5960(50)	9810(40)	7929(18)	101(10)
N(1)	8170(30)	6020(20)	4249(13)	73(6)
C(1)	10340(50)	5640(30)	4673(15)	78(8)
C(8)	3070(50)	9720(40)	7840(20)	115(12)
C(10)	-2130(50)	9430(40)	7451(18)	94(9)
C(2)	8460(50)	7240(30)	3640(18)	84(8)
C(3)	8810(60)	6410(50)	2810(30)	139(16)
C(6)	4100(200)	3920(100)	1040(50)	250(60)
C(4)	6080(60)	5610(40)	2349(18)	104(10)
C(5)	6700(80)	4750(50)	1540(30)	152(19)
N(2)	2090(120)	3350(90)	700(50)	200(30)

Table 3. Bond lengths [Å] and angles [°] for liavt.

I(1)-C(7)	2.32(3)
I(2)-C(10)	2.21(3)
O(1)-C(1)	1.26(3)
C(9)-C(8)	1.20(3)
C(9)-C(10)	1.35(3)
C(7)-C(10)#1	1.35(4)
C(7)-C(8)	1.41(3)
N(1)-C(1)	1.29(3)
N(1)-C(2)	1.48(3)
C(1)-C(1)#2	1.60(5)
C(10)-C(7)#3	1.35(4)
C(2)-C(3)	1.50(5)
C(3)-C(4)	1.50(4)
C(6)-N(2)	1.08(12)
C(6)-C(5)	1.50(10)
C(4)-C(5)	1.54(5)

C(8)-C(9)-C(10)	171(4)
C(10)#1-C(7)-C(8)	138(3)
C(10)#1-C(7)-I(1)	114.6(19)
C(8)-C(7)-I(1)	107(2)
C(1)-N(1)-C(2)	120(2)
N(1)-C(1)-O(1)	129(2)
N(1)-C(1)-C(1)#2	114(3)
O(1)-C(1)-C(1)#2	117(3)
C(9)-C(8)-C(7)	167(4)
C(7)#3-C(10)-C(9)	133(3)
C(7)#3-C(10)-I(2)	114.6(19)
C(9)-C(10)-I(2)	112(2)
N(1)-C(2)-C(3)	106(2)
C(4)-C(3)-C(2)	111(2)
N(2)-C(6)-C(5)	178(9)
C(3)-C(4)-C(5)	106(3)
C(6)-C(5)-C(4)	109(3)

Symmetry transformations used to generate equivalent atoms:
#1 x+1,y,z #2 -x+2,-y+1,-z+1 #3 x-1,y,z

Table 4. Anisotropic displacement parameters ($Å^2 x\ 10^3$) for liavt. The anisotropic displacement factor exponent takes the form: $-2\pi^2[h^2 a^{*2} U^{11} + ... + 2 h k a^* b^* U^{12}]$

	U^{11}	U^{22}	U^{33}	U^{23}	U^{13}	U^{12}
I(1)	58(1)	164(2)	161(2)	77(2)	33(1)	39(1)
I(2)	63(1)	111(2)	141(2)	-3(1)	11(1)	15(1)
O(1)	34(9)	128(15)	115(15)	53(12)	10(9)	14(9)
C(9)	41(14)	100(20)	130(20)	68(18)	28(15)	15(13)
C(7)	43(14)	170(30)	90(20)	20(20)	-14(15)	24(17)
N(1)	38(11)	110(18)	86(16)	33(14)	26(11)	38(11)
C(1)	58(16)	130(30)	60(20)	29(15)	29(14)	33(16)
C(8)	44(16)	140(30)	190(30)	80(20)	44(18)	36(15)
C(10)	50(16)	120(20)	110(20)	60(20)	14(17)	6(16)
C(2)	110(20)	65(19)	100(20)	45(17)	71(18)	33(15)
C(3)	51(18)	190(40)	220(40)	140(30)	70(20)	60(20)
C(6)	490(130)	230(110)	160(90)	130(80)	220(100)	280(100)
C(4)	110(20)	140(30)	70(20)	-11(19)	27(19)	20(20)
C(5)	110(30)	130(30)	210(50)	-30(30)	60(30)	10(20)
N(2)	210(50)	210(40)	190(50)	10(30)	80(40)	30(40)

Co-crystal **8·PIDA**

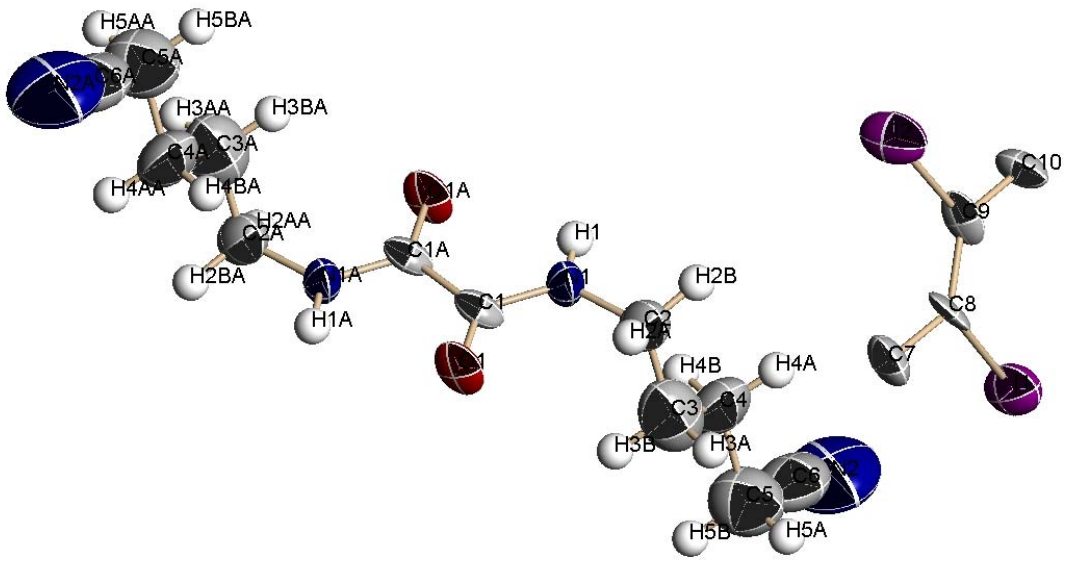

Table 1. Crystal data and structure refinement for liazt.

Identification code	liazt	
Empirical formula	C20 H18 I4 N4 O2	
Formula weight	853.98	
Temperature	273(2) K	
Wavelength	0.71073 Å	
Crystal system	Triclinic	
Space group	P-1	
Unit cell dimensions	a = 4.9395(17) Å	α = 94.874(8)°.
	b = 8.699(3) Å	β = 97.664(6)°.
	c = 15.821(6) Å	γ = 98.583(7)°.
Volume	662.3(4) $Å^3$	
Z	1	
Density (calculated)	2.141 Mg/m^3	
Absorption coefficient	4.727 mm^{-1}	
F(000)	394	
Crystal size	? x ? x ? mm^3	
Theta range for data collection	1.31 to 28.28°.	
Index ranges	-6<=h<=6, -7<=k<=7, -19<=l<=12	

Reflections collected	3473
Independent reflections	1920 [R(int) = 0.0034]
Completeness to theta = 28.28°	58.1 %
Absorption correction	None
Refinement method	Full-matrix least-squares on F^2
Data / restraints / parameters	1920 / 0 / 136
Goodness-of-fit on F^2	0.846
Final R indices [I>2sigma(I)]	R1 = 0.0600, wR2 = 0.1395
R indices (all data)	R1 = 0.1287, wR2 = 0.1687
Largest diff. peak and hole	1.718 and -0.885 e.$Å^{-3}$

Table 2. Atomic coordinates (x 10^4) and equivalent isotropic displacement parameters ($Å^2$x 10^3)
for liazt. U(eq) is defined as one third of the trace of the orthogonalized U^{ij} tensor.

	x	y	z	U(eq)
I(1)	7774(2)	6216(2)	9157(1)	71(1)
I(2)	6067(2)	3197(2)	6232(1)	75(1)
O(1)	-2779(18)	8967(12)	5407(6)	55(3)
C(8)	6050(30)	4900(17)	7975(9)	42(4)
C(9)	7710(30)	4367(18)	7438(9)	46(4)
C(1)	-340(30)	9466(18)	5314(8)	39(4)
N(1)	1740(20)	8898(15)	5707(7)	51(4)
C(2)	1490(30)	7800(20)	6330(10)	68(5)
C(4)	3910(50)	9440(30)	7675(11)	96(7)
C(3)	1300(50)	8580(30)	7193(15)	110(8)
N(2)	8340(70)	11700(30)	9350(16)	161(12)
C(6)	6320(70)	11060(30)	8973(16)	112(9)
C(5)	3580(50)	10240(30)	8571(15)	118(8)
C(10)	10620(30)	4595(19)	7643(9)	50(5)
C(7)	3120(30)	4691(19)	7762(9)	54(5)

Table 3. Bond lengths [Å] and angles [°] for liazt.

I(1)-C(8)	2.110(14)
I(2)-C(9)	2.084(14)
O(1)-C(1)	1.252(15)
C(8)-C(9)	1.355(19)
C(8)-C(7)	1.426(19)
C(9)-C(10)	1.414(19)
C(1)-N(1)	1.309(17)
C(1)-C(1)#1	1.45(3)
N(1)-C(2)	1.437(19)
C(2)-C(3)	1.50(2)
C(4)-C(3)	1.47(3)
C(4)-C(5)	1.56(3)
N(2)-C(6)	1.13(4)
C(6)-C(5)	1.47(3)
C(10)-C(7)#2	1.209(19)
C(7)-C(10)#3	1.209(19)
C(9)-C(8)-C(7)	122.8(13)
C(9)-C(8)-I(1)	120.6(10)
C(7)-C(8)-I(1)	116.4(10)
C(8)-C(9)-C(10)	122.9(13)
C(8)-C(9)-I(2)	121.3(10)
C(10)-C(9)-I(2)	115.8(11)
O(1)-C(1)-N(1)	121.0(13)
O(1)-C(1)-C(1)#1	122.5(18)
N(1)-C(1)-C(1)#1	116.1(16)
C(1)-N(1)-C(2)	124.6(13)
N(1)-C(2)-C(3)	111.5(16)
C(3)-C(4)-C(5)	113.3(19)
C(4)-C(3)-C(2)	115.6(18)
N(2)-C(6)-C(5)	174(3)
C(6)-C(5)-C(4)	108(2)
C(7)#2-C(10)-C(9)	174.4(17)
C(10)#3-C(7)-C(8)	174.5(17)

Symmetry transformations used to generate equivalent atoms:
#1 -x,-y+2,-z+1 #2 x+1,y,z #3 x-1,y,z

Table 4. Anisotropic displacement parameters ($Å^2 x\ 10^3$) for liazt. The anisotropic displacement factor exponent takes the form: $-2\pi^2[h^2 a^{*2} U^{11} + ... + 2 h k a^* b^* U^{12}]$

	U^{11}	U^{22}	U^{33}	U^{23}	U^{13}	U^{12}
I(1)	45(1)	99(1)	65(1)	0(1)	5(1)	12(1)
I(2)	46(1)	93(1)	78(1)	-21(1)	5(1)	2(1)
O(1)	20(5)	61(9)	87(7)	23(6)	12(5)	2(5)
C(8)	26(7)	42(13)	66(9)	5(8)	15(7)	25(8)
C(9)	15(7)	43(13)	79(10)	16(8)	2(7)	-1(7)
C(1)	35(8)	23(12)	60(10)	-5(7)	15(7)	7(8)
N(1)	36(7)	74(13)	52(8)	31(7)	13(6)	19(7)
C(2)	48(10)	100(18)	57(11)	14(11)	6(8)	15(10)
C(4)	95(17)	140(20)	67(13)	34(12)	27(11)	23(15)
C(3)	96(18)	100(20)	140(20)	44(16)	30(15)	20(15)
N(2)	210(30)	130(20)	120(20)	-53(15)	25(19)	20(20)
C(6)	160(30)	100(30)	82(18)	-3(15)	39(18)	40(20)
C(5)	110(20)	120(20)	120(20)	4(16)	19(16)	15(17)
C(10)	31(9)	61(14)	59(9)	-6(8)	13(6)	14(8)
C(7)	32(9)	63(15)	72(11)	14(9)	4(7)	21(9)

Table 5. Hydrogen coordinates (x 10^4) and isotropic displacement parameters ($Å^2$x 10^3) for liazt.

	x	y	z	U(eq)
H(1)	3360	9206	5583	61
H(2A)	3089	7264	6373	81
H(2B)	-147	7015	6142	81
H(4A)	4661	10243	7339	116
H(4B)	5228	8728	7755	116
H(3A)	-13	9307	7118	132
H(3B)	546	7797	7536	132
H(5A)	2281	10967	8505	141
H(5B)	2889	9453	8925	141

Co-crystal **3·64** (The crystal structure is based on the virtual host and guest)

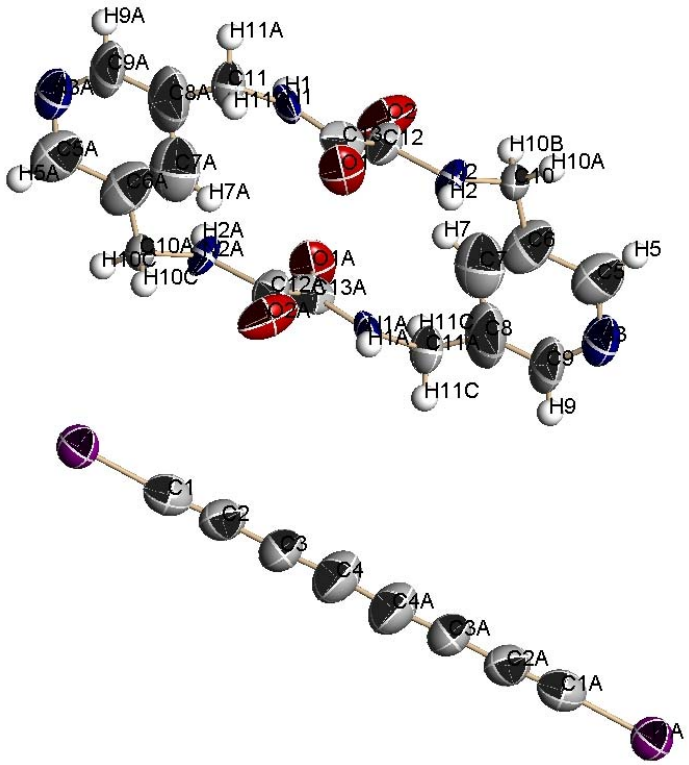

Table 1. Crystal data and structure refinement for tetraynt.

Identification code	tetraynt	
Empirical formula	C26 H18 I2 N6 O4	
Formula weight	732.26	
Temperature	273(2) K	
Wavelength	0.71073 Å	
Crystal system	Triclinic	
Space group	P-1	
Unit cell dimensions	a = 5.0134(14) Å	α = 74.880(5)°.
	b = 10.514(3) Å	β = 81.217(5)°.
	c = 12.549(3) Å	γ = 83.558(4)°.
Volume	629.2(3) $Å^3$	
Z	1	
Density (calculated)	1.932 Mg/m^3	
Absorption coefficient	2.546 mm^{-1}	
F(000)	354	

Crystal size	? x ? x ? mm^3
Theta range for data collection	1.70 to 28.41°.
Index ranges	-6<=h<=6, -14<=k<=10, -16<=l<=13
Reflections collected	3833
Independent reflections	2723 [R(int) = 0.0387]
Completeness to theta = 28.41°	86.0 %
Absorption correction	None
Refinement method	Full-matrix least-squares on F^2
Data / restraints / parameters	2723 / 0 / 172
Goodness-of-fit on F^2	0.933
Final R indices [I>2sigma(I)]	R1 = 0.1083, wR2 = 0.2890
R indices (all data)	R1 = 0.1870, wR2 = 0.3248
Largest diff. peak and hole	1.860 and -0.820 e.$Å^{-3}$

Table 2. Atomic coordinates (x 10^4) and equivalent isotropic displacement parameters ($Å^2$x 10^3)
for tetraynt. U(eq) is defined as one third of the trace of the orthogonalized U^{ij} tensor.

	x	y	z	U(eq)
I(1)	5482(2)	3189(1)	8979(1)	84(1)
N(3)	11710(40)	12270(20)	724(14)	104(6)
C(4)	13860(60)	4860(30)	5350(20)	135(10)
C(1)	8290(60)	3880(20)	7710(20)	120(8)
C(2)	10130(40)	4230(20)	6890(20)	93(6)
N(1)	3810(60)	7640(30)	6020(20)	160(9)
C(3)	12110(50)	4570(19)	6135(18)	95(6)
C(6)	6270(60)	8040(30)	5240(30)	141(10)
O(1)	8580(50)	8270(40)	5280(40)	300(30)
C(13)	10150(50)	13020(30)	1297(16)	110(8)
C(10)	7640(60)	12040(40)	2213(19)	138(14)
C(9)	8670(60)	10720(30)	1980(20)	145(12)
C(12)	11270(50)	11170(40)	980(20)	134(11)
C(8)	8320(70)	9230(20)	2290(20)	152(12)

C(7)	5200(100)	8570(20)	4440(30)	161(18)
O(2)	3560(50)	8740(20)	4110(30)	205(15)
N(2)	8330(50)	8800(20)	3505(18)	138(8)
C(5)	3700(60)	6860(30)	7200(20)	136(10)
C(14)	7760(180)	12990(50)	1860(40)	300(30)

Table 3. Bond lengths [Å] and angles [°] for tetraynt.

I(1)-C(1)	2.00(3)
N(3)-C(12)	1.16(4)
N(3)-C(13)	1.32(3)
C(4)-C(3)	1.21(3)
C(4)-C(4)#1	1.34(5)
C(1)-C(2)	1.28(3)
C(2)-C(3)	1.28(3)
N(1)-C(6)	1.49(4)
N(1)-C(5)	1.49(4)
C(6)-O(1)	1.22(3)
C(6)-C(7)	1.19(4)
C(13)-C(14)	1.29(8)
C(13)-C(10)	1.79(5)
C(10)-C(14)	0.98(5)
C(10)-C(9)	1.52(5)
C(10)-C(5)#2	1.56(4)
C(9)-C(8)	1.53(4)
C(9)-C(12)	1.68(4)
C(8)-N(2)	1.47(3)
C(7)-O(2)	0.96(3)
C(7)-N(2)	1.81(5)
C(5)-C(14)#2	1.32(7)
C(5)-C(10)#2	1.56(4)
C(14)-C(5)#2	1.32(7)
C(12)-N(3)-C(13)	115(2)
C(3)-C(4)-C(4)#1	167(4)

C(2)-C(1)-I(1)	175.5(19)
C(1)-C(2)-C(3)	175(2)
C(6)-N(1)-C(5)	127(3)
C(4)-C(3)-C(2)	174(3)
O(1)-C(6)-C(7)	120(5)
O(1)-C(6)-N(1)	138(4)
C(7)-C(6)-N(1)	98(3)
N(3)-C(13)-C(14)	137(3)
N(3)-C(13)-C(10)	108(2)
C(14)-C(13)-C(10)	32(2)
C(14)-C(10)-C(9)	139(6)
C(14)-C(10)-C(5)#2	57(5)
C(9)-C(10)-C(5)#2	163(3)
C(14)-C(10)-C(13)	45(6)
C(9)-C(10)-C(13)	98.3(19)
C(5)#2-C(10)-C(13)	96(3)
C(10)-C(9)-C(8)	146(3)
C(10)-C(9)-C(12)	101(2)
C(8)-C(9)-C(12)	113(3)
N(3)-C(12)-C(9)	117(3)
C(9)-C(8)-N(2)	106(2)
O(2)-C(7)-C(6)	147(6)
O(2)-C(7)-N(2)	117(4)
C(6)-C(7)-N(2)	95(3)
C(7)-N(2)-C(8)	121(2)
C(14)#2-C(5)-N(1)	133(4)
C(14)#2-C(5)-C(10)#2	39(2)
N(1)-C(5)-C(10)#2	99(2)
C(10)-C(14)-C(5)#2	84(5)
C(10)-C(14)-C(13)	103(8)
C(5)#2-C(14)-C(13)	146(5)

Symmetry transformations used to generate equivalent atoms:

#1 -x+3,-y+1,-z+1 #2 -x+1,-y+2,-z+1

Table 4. Anisotropic displacement parameters ($Å^2 x\ 10^3$) for tetraynt. The anisotropic displacement factor exponent takes the form: $-2\pi^2[h^2 a^{*2} U^{11} + ... + 2 h k a^* b^* U^{12}]$

	U^{11}	U^{22}	U^{33}	U^{23}	U^{13}	U^{12}
I(1)	97(1)	78(1)	73(1)	-13(1)	-11(1)	-7(1)
N(3)	129(15)	106(13)	55(9)	20(9)	0(9)	-31(11)
C(4)	160(20)	122(19)	98(17)	2(14)	35(16)	-42(17)
C(1)	129(19)	82(13)	180(20)	-62(14)	-89(19)	32(13)
C(2)	69(12)	121(16)	98(15)	-38(12)	-2(12)	-24(12)
N(1)	210(30)	170(20)	118(18)	-71(16)	-8(17)	-57(19)
C(3)	102(15)	68(11)	101(14)	-5(10)	11(13)	-18(11)
C(6)	93(18)	130(20)	220(30)	-90(20)	-10(20)	37(16)
O(1)	174(19)	360(40)	540(60)	-390(50)	-190(30)	130(20)
C(13)	114(17)	180(30)	28(9)	-20(12)	13(9)	-38(16)
C(10)	130(20)	230(40)	45(13)	-45(18)	-32(14)	80(30)
C(9)	180(30)	150(20)	82(15)	63(15)	-65(17)	-60(20)
C(12)	86(16)	210(30)	87(16)	4(19)	-14(12)	-21(18)
C(8)	240(30)	95(16)	102(17)	-28(13)	73(19)	-34(18)
C(7)	310(50)	44(11)	170(30)	-9(12)	-180(40)	21(18)
O(2)	138(18)	120(15)	370(50)	-40(20)	-110(20)	9(13)
N(2)	125(16)	144(19)	109(15)	13(13)	14(13)	-3(14)
C(5)	190(30)	150(20)	79(16)	-24(14)	-43(16)	10(20)
C(14)	670(100)	170(40)	100(30)	-20(30)	-60(40)	-170(50)

Co-crystal **4·64**

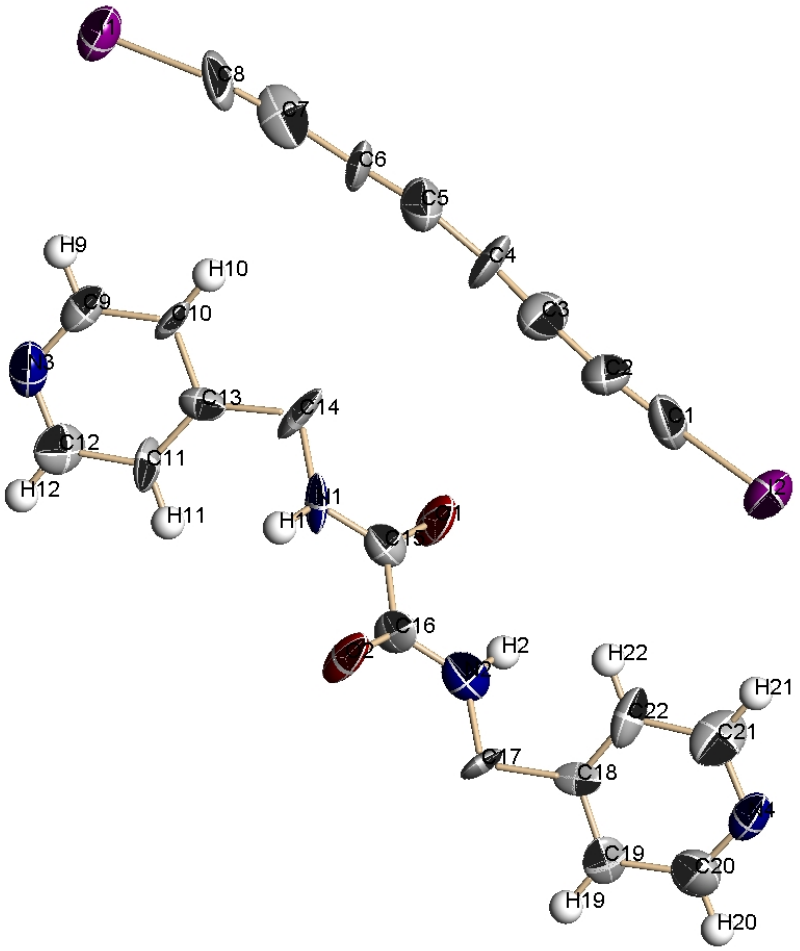

Table 1. Crystal data and structure refinement for liang23t.

Identification code	liang23t	
Empirical formula	C22 H14 I2 N4 O2	
Formula weight	620.17	
Temperature	273(2) K	
Wavelength	0.71073 Å	
Crystal system	Triclinic	
Space group	P-1	
Unit cell dimensions	a = 4.9867(18) Å	α = 83.165(8)°.
	b = 9.624(4) Å	β = 89.947(9)°.
	c = 24.076(10) Å	γ = 80.875(10)°.
Volume	1132.6(7) Å^3	

Z	2
Density (calculated)	1.818 Mg/m^3
Absorption coefficient	2.802 mm^{-1}
F(000)	592
Crystal size	? x ? x ? mm^3
Theta range for data collection	0.85 to 28.63°.
Index ranges	-6<=h<=4, -12<=k<=12, -27<=l<=30
Reflections collected	7285
Independent reflections	5010 [R(int) = 0.1550]
Completeness to theta = 28.63°	86.2 %
Absorption correction	None
Refinement method	Full-matrix least-squares on F^2
Data / restraints / parameters	5010 / 0 / 271
Goodness-of-fit on F^2	0.517
Final R indices [I>2sigma(I)]	R1 = 0.0625, wR2 = 0.1520
R indices (all data)	R1 = 0.3611, wR2 = 0.2856
Largest diff. peak and hole	0.604 and -0.654 $e.Å^{-3}$

Table 2. Atomic coordinates (x 10^4) and equivalent isotropic displacement parameters ($Å^2$x 10^3)
for liang23t. U(eq) is defined as one third of the trace of the orthogonalized U^{ij} tensor.

	x	y	z	U(eq)
I(1)	11234(3)	7550(2)	4696(1)	69(1)
I(2)	-170(3)	2805(2)	715(1)	83(1)
N(4)	7280(40)	2200(20)	9761(8)	57(5)
C(8)	9040(50)	7270(20)	4007(9)	64(7)
C(18)	3760(40)	2170(20)	8873(9)	38(5)
C(13)	1830(40)	2260(20)	3547(9)	49(6)
N(1)	470(30)	1202(17)	2730(6)	46(4)
N(2)	-2390(30)	-1018(18)	1935(6)	54(5)
O(1)	-3850(30)	955(15)	2601(6)	73(5)
C(15)	-1470(40)	670(20)	2515(9)	49(6)

C(12)	4980(50)	1040(20)	4236(9)	70(7)
O(2)	1930(30)	-816(15)	2081(6)	66(5)
C(10)	2350(40)	3530(20)	3722(8)	54(6)
C(16)	-440(40)	-480(20)	2159(8)	42(5)
C(19)	4100(40)	3410(20)	9057(8)	54(6)
C(11)	3230(40)	1050(20)	3789(8)	57(6)
C(1)	1350(50)	3500(30)	1367(10)	76(8)
C(21)	6740(50)	1000(30)	9596(10)	76(8)
C(2)	2420(50)	4050(20)	1722(12)	82(9)
C(22)	5000(50)	950(30)	9128(9)	64(7)
C(6)	6470(40)	6460(20)	3238(10)	74(8)
C(9)	4200(50)	3410(30)	4171(10)	61(7)
C(3)	3310(50)	4710(20)	2115(10)	81(8)
N(3)	5540(40)	2230(20)	4431(8)	73(7)
C(4)	4180(50)	5360(30)	2475(11)	87(9)
C(5)	5430(40)	6090(20)	2862(11)	71(7)
C(20)	6050(50)	3300(30)	9500(11)	83(9)
C(14)	-230(40)	2400(20)	3078(9)	62(7)
C(17)	1720(40)	2240(20)	8398(9)	55(6)
C(7)	7870(50)	6910(20)	3658(11)	69(7)

—

Table 3. Bond lengths [Å] and angles [°] for liang23t.

I(1)-C(8)	2.05(2)
I(2)-C(1)	1.97(2)
N(4)-C(21)	1.33(3)
N(4)-C(20)	1.24(3)
C(8)-C(7)	1.15(3)
C(18)-C(19)	1.36(2)
C(18)-C(22)	1.32(3)
C(18)-C(17)	1.52(3)
C(13)-C(11)	1.33(3)
C(13)-C(10)	1.41(2)
C(13)-C(14)	1.50(3)
N(1)-C(15)	1.298(19)
N(1)-C(14)	1.50(2)
N(2)-C(16)	1.32(2)
N(2)-C(17)#1	1.50(2)
O(1)-C(15)	1.20(2)
C(15)-C(16)	1.50(3)
C(12)-N(3)	1.36(3)
C(12)-C(11)	1.38(3)
O(2)-C(16)	1.200(19)
C(10)-C(9)	1.40(3)
C(19)-C(20)	1.43(3)
C(1)-C(2)	1.22(3)
C(21)-C(22)	1.44(3)
C(2)-C(3)	1.31(3)
C(6)-C(5)	1.16(3)
C(6)-C(7)	1.38(3)
C(9)-N(3)	1.31(3)
C(3)-C(4)	1.25(3)
C(4)-C(5)	1.42(3)
C(17)-N(2)#1	1.50(2)
C(21)-N(4)-C(20)	115(2)
C(7)-C(8)-I(1)	170(2)

C(19)-C(18)-C(22)	121(2)
C(19)-C(18)-C(17)	117.3(19)
C(22)-C(18)-C(17)	121.5(18)
C(11)-C(13)-C(10)	118.1(19)
C(11)-C(13)-C(14)	125.9(19)
C(10)-C(13)-C(14)	116.0(19)
C(15)-N(1)-C(14)	119.5(16)
C(16)-N(2)-C(17)#1	120.6(17)
O(1)-C(15)-N(1)	127(2)
O(1)-C(15)-C(16)	120.4(15)
N(1)-C(15)-C(16)	112.9(17)
N(3)-C(12)-C(11)	124(2)
C(13)-C(10)-C(9)	116(2)
O(2)-C(16)-N(2)	124.5(18)
O(2)-C(16)-C(15)	121.9(16)
N(2)-C(16)-C(15)	113.6(17)
C(18)-C(19)-C(20)	116(2)
C(13)-C(11)-C(12)	121(2)
C(2)-C(1)-I(2)	172(3)
N(4)-C(21)-C(22)	124(2)
C(1)-C(2)-C(3)	174(3)
C(18)-C(22)-C(21)	117(2)
C(5)-C(6)-C(7)	176(3)
N(3)-C(9)-C(10)	126.9(19)
C(4)-C(3)-C(2)	178(3)
C(9)-N(3)-C(12)	114.0(19)
C(3)-C(4)-C(5)	174(3)
C(6)-C(5)-C(4)	168(3)
N(4)-C(20)-C(19)	127(2)
N(1)-C(14)-C(13)	109.8(17)
N(2)#1-C(17)-C(18)	111.8(15)
C(8)-C(7)-C(6)	179(3)

Symmetry transformations used to generate equivalent atoms:

#1 -x,-y,-z+1

Table 4. Anisotropic displacement parameters ($Å^2 x\ 10^3$) for liang23t. The anisotropic displacement factor exponent takes the form: $-2\pi^2[h^2 a^{*2} U^{11} + ... + 2 h k a^* b^* U^{12}]$

	U^{11}	U^{22}	U^{33}	U^{23}	U^{13}	U^{12}
I(1)	58(1)	89(1)	66(1)	-26(1)	-10(1)	-19(1)
I(2)	86(1)	79(1)	89(2)	-37(1)	-26(1)	-10(1)
N(4)	41(12)	68(15)	70(15)	-32(12)	0(10)	-15(11)
C(8)	73(17)	68(17)	50(16)	-3(13)	-25(13)	-11(13)
C(18)	18(11)	40(15)	61(16)	-9(13)	22(11)	-14(11)
C(13)	37(13)	46(15)	64(17)	-13(13)	10(12)	3(12)
N(1)	28(9)	81(13)	34(10)	-16(9)	-1(8)	-19(9)
N(2)	55(11)	94(14)	19(10)	-6(9)	-22(8)	-35(11)
O(1)	20(8)	96(12)	113(14)	-55(10)	-5(8)	-11(8)
C(15)	5(11)	71(16)	78(16)	-10(13)	-18(11)	-31(11)
C(12)	100(20)	72(18)	32(15)	4(13)	2(14)	-3(16)
O(2)	20(8)	104(12)	88(12)	-63(10)	10(8)	-14(8)
C(10)	38(13)	68(16)	64(16)	-45(13)	-11(11)	-8(11)
C(16)	23(12)	49(15)	58(16)	-18(11)	3(11)	-12(11)
C(19)	73(16)	50(15)	35(14)	-17(11)	-2(12)	14(12)
C(11)	66(16)	82(19)	23(13)	12(12)	-19(12)	-25(14)
C(1)	83(19)	73(18)	64(18)	-20(14)	-12(15)	22(15)
C(21)	87(19)	67(19)	71(19)	24(15)	-22(15)	-31(15)
C(2)	78(19)	58(18)	120(20)	-23(17)	-22(17)	-21(15)
C(22)	75(18)	74(19)	46(16)	-4(14)	-8(13)	-27(15)
C(6)	55(15)	100(20)	78(18)	-45(15)	-42(14)	-8(14)
C(9)	65(17)	69(18)	66(18)	-36(14)	5(14)	-36(15)
C(3)	110(20)	68(18)	70(19)	-18(15)	-15(17)	-21(16)
N(3)	46(13)	98(19)	73(16)	-20(15)	-21(11)	3(13)
C(4)	87(19)	100(20)	90(20)	-31(17)	-36(16)	-30(16)
C(5)	47(15)	74(18)	90(20)	-7(15)	-18(14)	-2(13)
C(20)	70(20)	90(20)	80(20)	-39(17)	-19(16)	15(16)
C(14)	54(15)	87(18)	62(16)	-35(14)	4(12)	-41(13)
C(17)	51(14)	42(14)	76(17)	-21(12)	-13(12)	-11(11)
C(7)	75(19)	68(18)	70(20)	7(15)	22(16)	-41(15)

Appendix II NMR spectra

-3.422
79.714
77.318
77.000
76.682
1
150
100
50
0
ppm (f1)

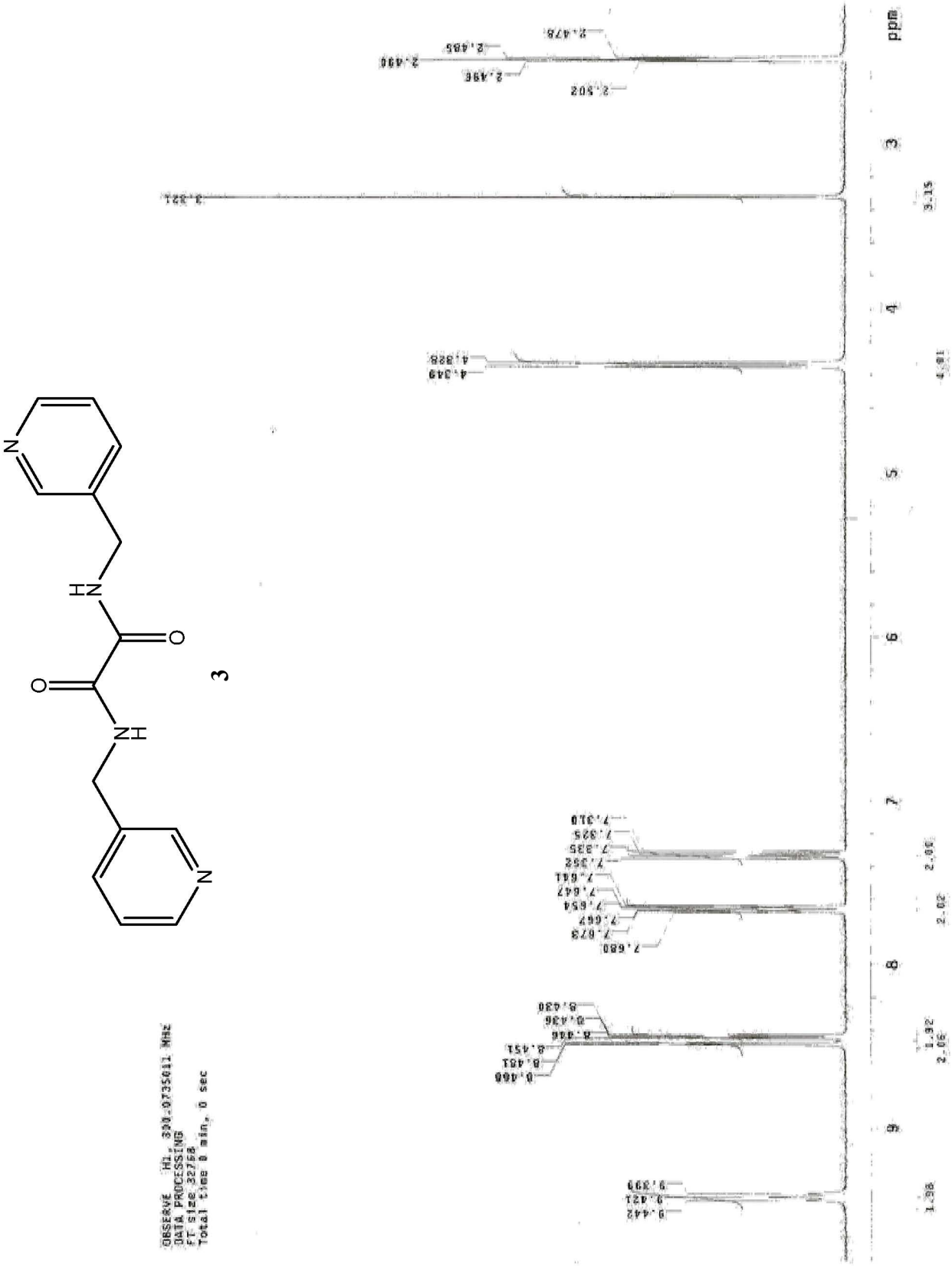
3
OBSERVE H1, 399.9735611 MHz
DATA PROCESSING
FT size 32768
Total time 8 min, 0 sec
ppm

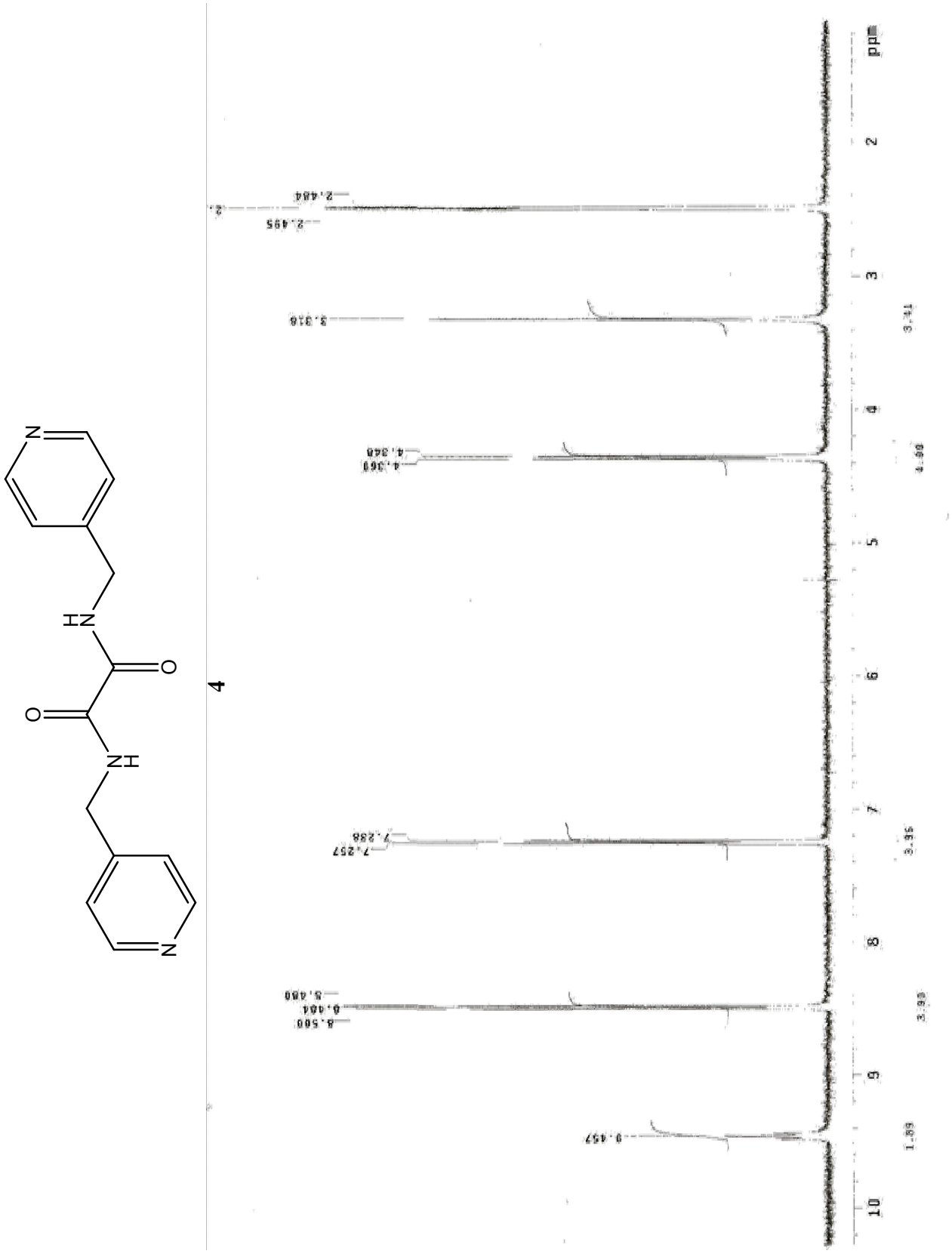
4
8.500
8.484
5.480
7.257
7.238
4.368
4.348
3.316
2.495
2.484
0.157
ppm

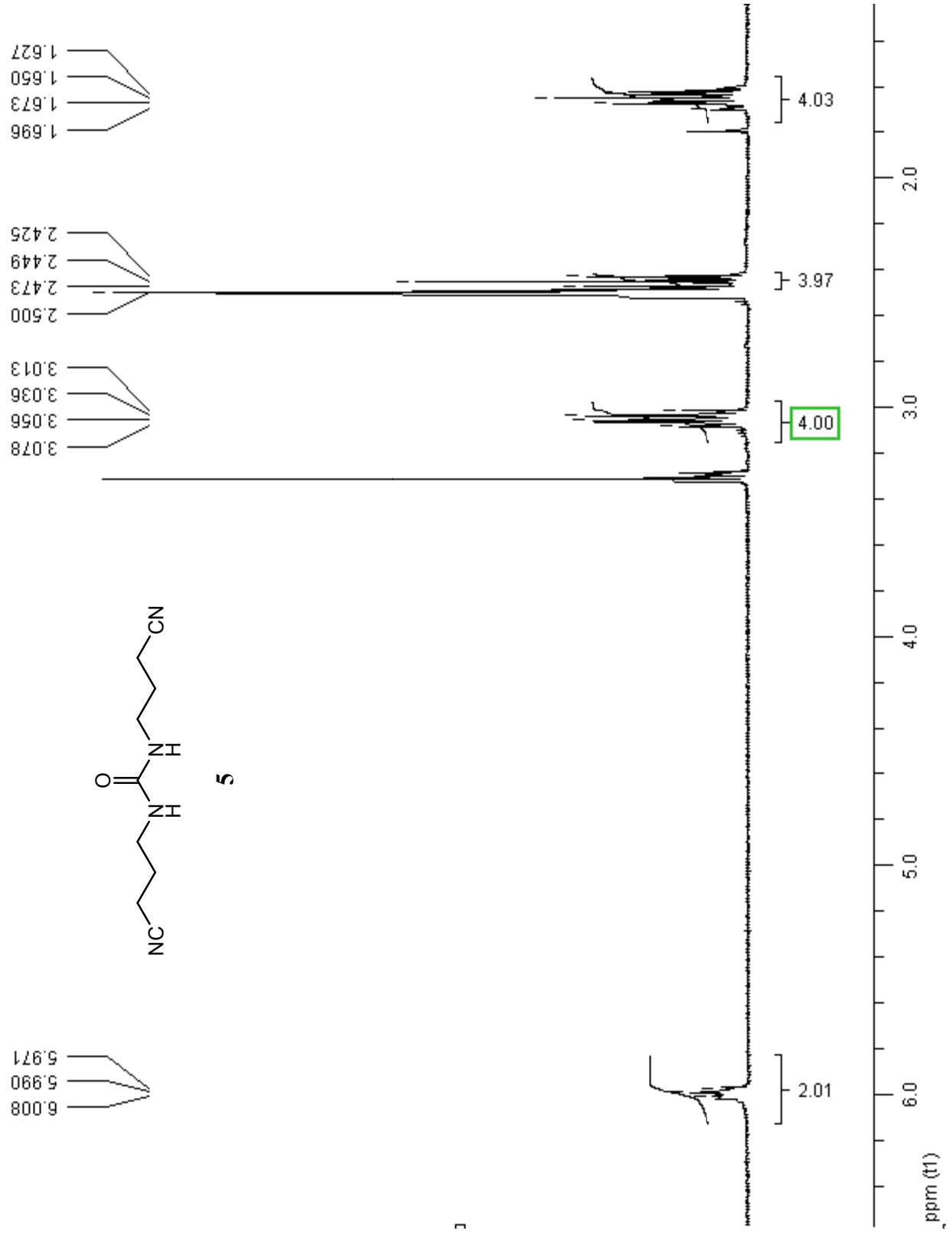
1.627
1.650
1.673
1.696
2.425
2.449
2.473
2.500
3.013
3.036
3.056
3.078
5.971
5.990
6.008
4.03
3.97
4.00
2.01
2.0
3.0
4.0
5.0
6.0
ppm (t1)
CN
NC
NH
NH
O

5

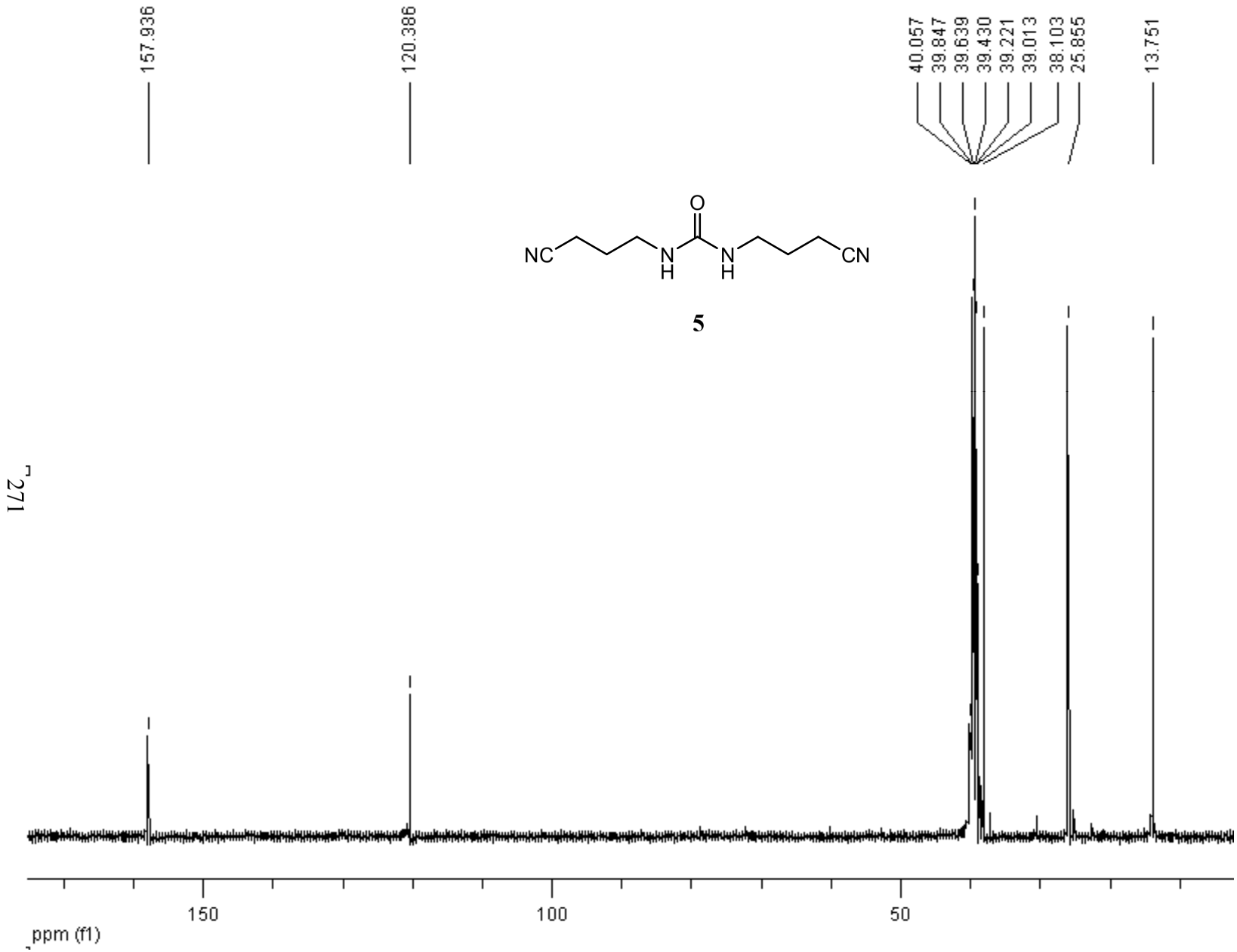
157.936
120.386
40.057
39.847
39.639
39.430
39.221
39.013
38.103
25.855
13.751
NC
N
H
O
N
H
CN
5
271
150
100
50
ppm (f1)

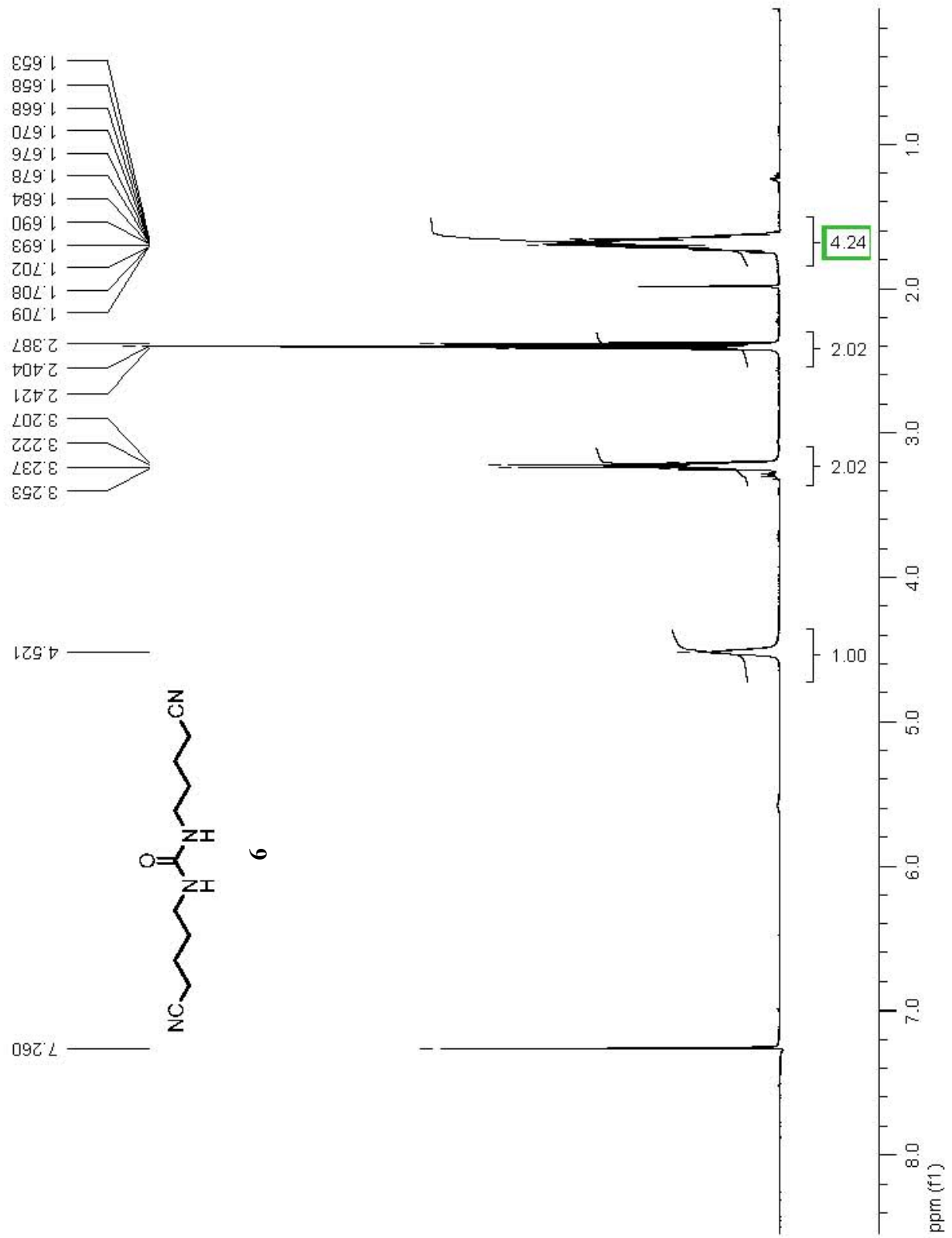
1.653
1.658
1.668
1.670
1.676
1.678
1.684
1.690
1.693
1.702
1.708
1.709
2.387
2.404
2.421
3.207
3.222
3.237
3.253
4.521
7.260
4.24
2.02
2.02
1.00
1.0
2.0
3.0
4.0
5.0
6.0
7.0
8.0
ppm (f1)
NC
CN
O
H
N
N
H
6

158.019
119.567
77.318
77.000
76.682
39.314
29.451
22.650
16.890
ppm (t1)
200
150
100
50
0
NC
CN
O
NH
NH

9

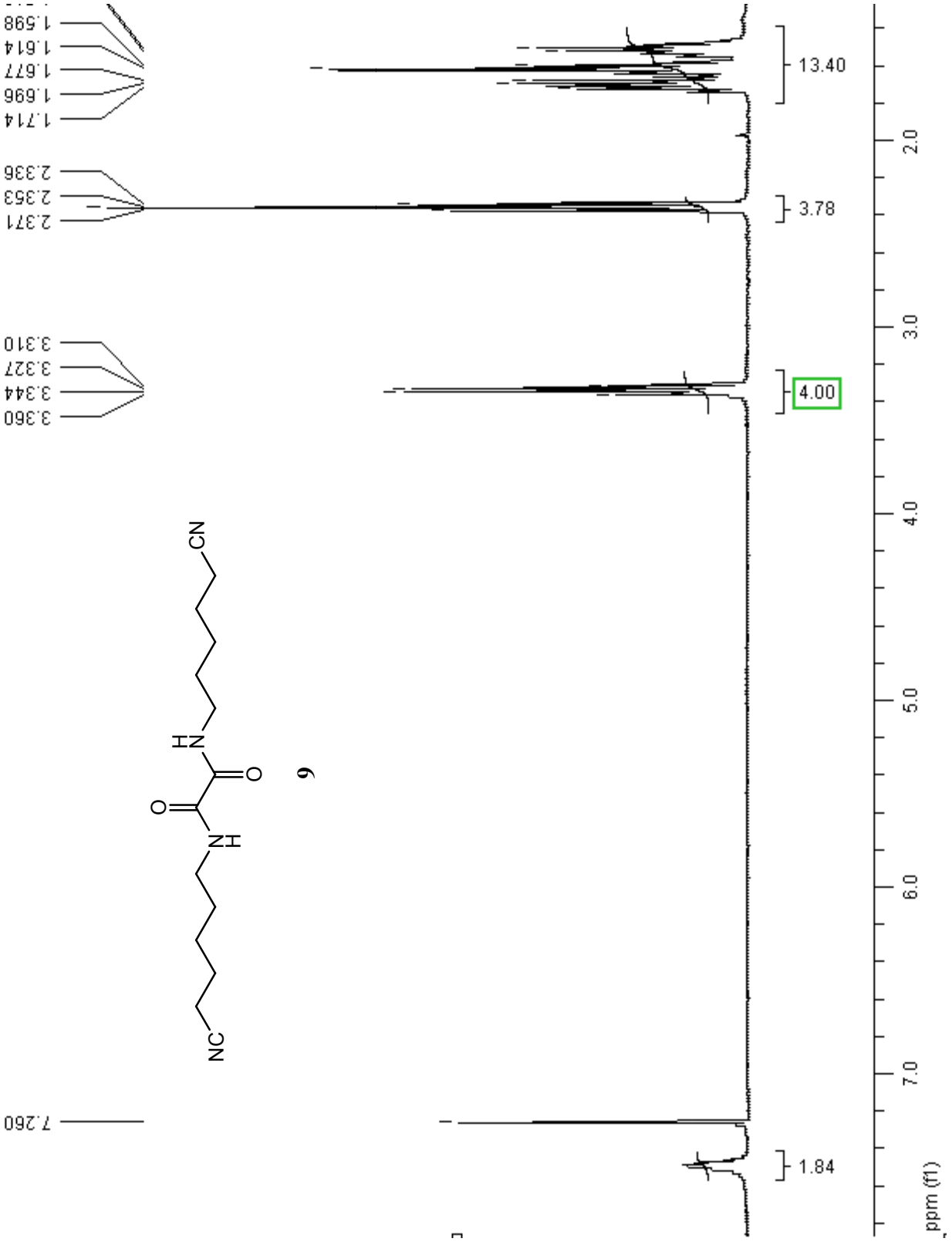
1.598
1.614
1.677
1.696
1.714
2.336
2.353
2.371
3.310
3.327
3.344
3.360
7.260
13.40
3.78
4.00
1.84
2.0
3.0
4.0
5.0
6.0
7.0
ppm (f1)
NC
CN
NH
NH
O
O
6

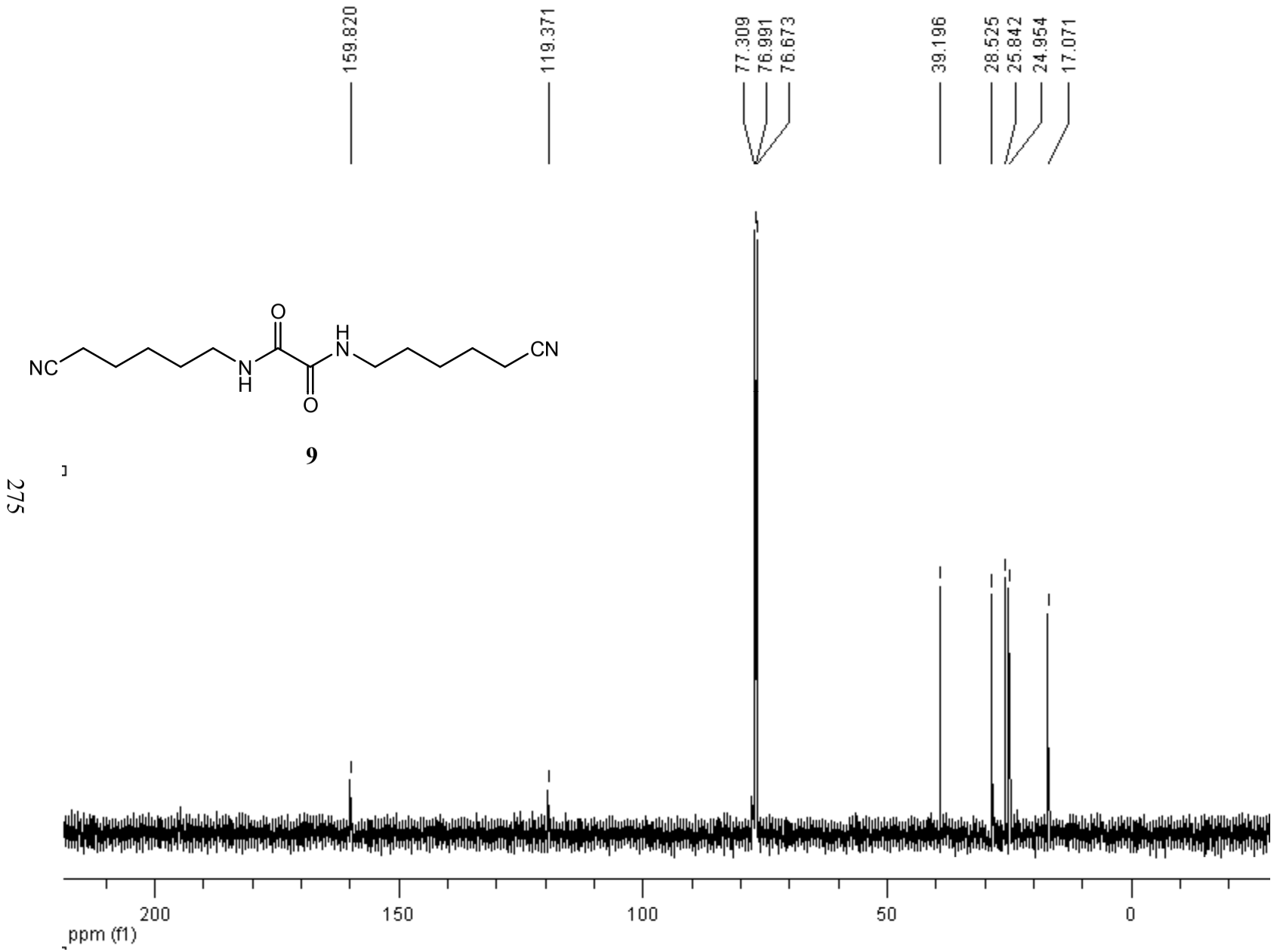
159.820
119.371
77.309
76.991
76.673
39.196
28.525
25.842
24.954
17.071
NC
N
H
O
O
H
N
CN
9
275
200
150
100
50
0
ppm (f1)

7.260
3.331
3.314
2.344
2.326
1.668
1.649
1.572
1.560
1.509
1.491
1.487
1.469
1.400
1.382
NC
CN
10
20.0
3.83
4.00
2.07
ppm (f1)

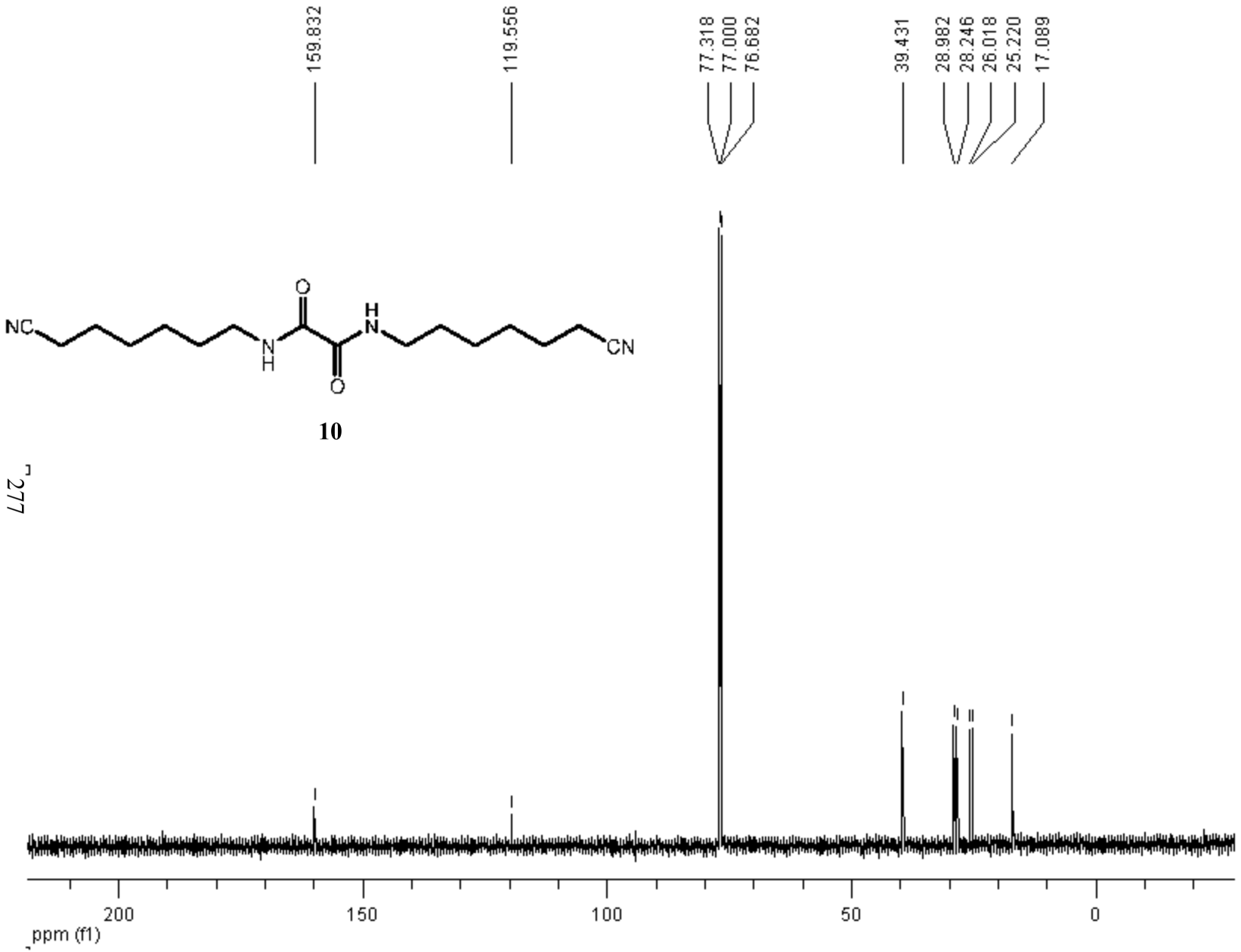
159.832
119.556
77.318
77.000
76.682
39.431
28.982
28.246
26.018
25.220
17.089
NC
O
H
N
N
H
O
CN
10
277
200
150
100
50
0
ppm (f1)

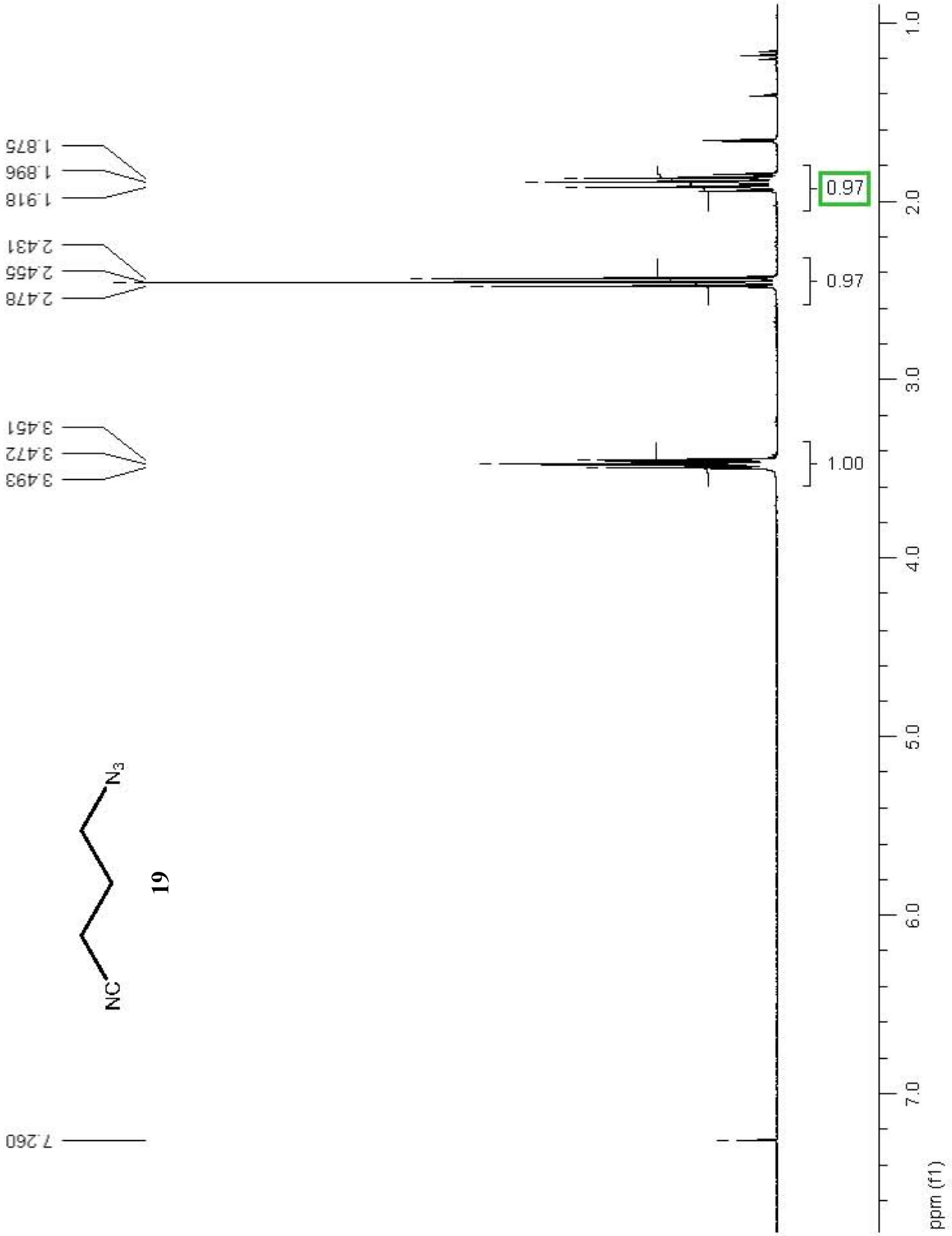
7.260
3.493
3.472
3.451
2.478
2.455
2.431
1.918
1.896
1.875
0.97
0.97
1.00
1.0
2.0
3.0
4.0
5.0
6.0
7.0
ppm (f1)
N3
NC

19

7.261
3.377
3.357
3.349
3.337
2.418
2.404
2.395
2.386
2.374
1.774
1.770
1.767
1.760
1.750
1.738
1.728
2.04
2.00
4.00
7.0
6.0
5.0
4.0
3.0
2.0
1.0
ppm (t1)
NC
N3
20

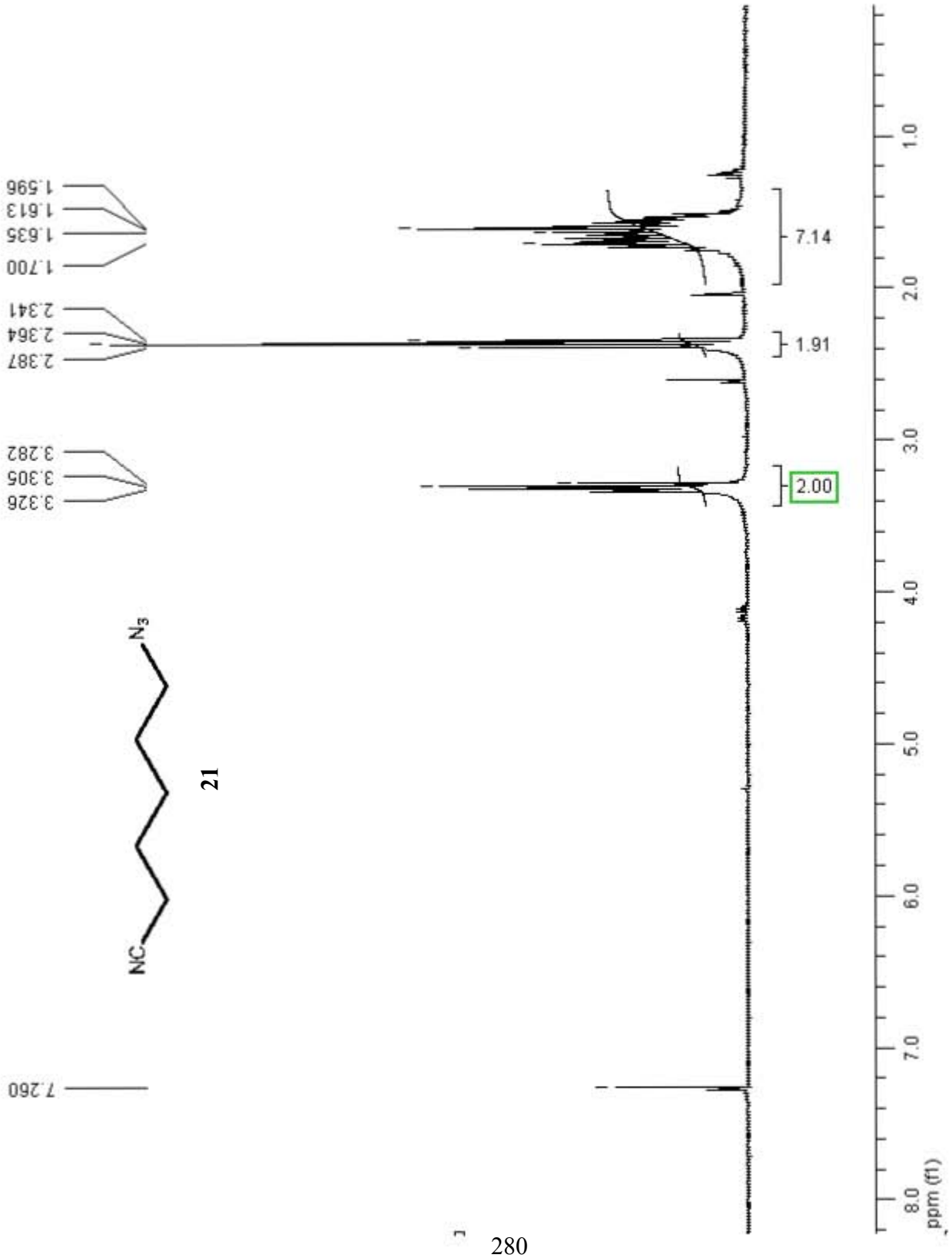
7.260
3.326
3.305
3.282
2.387
2.364
2.341
1.700
1.635
1.613
1.596
7.14
1.91
2.00
1.0
2.0
3.0
4.0
5.0
6.0
7.0
8.0
ppm (f1)
N3
NC

21

21

119.375

77.317
77.001
76.681

50.988

28.097
25.841
24.946
17.074

281

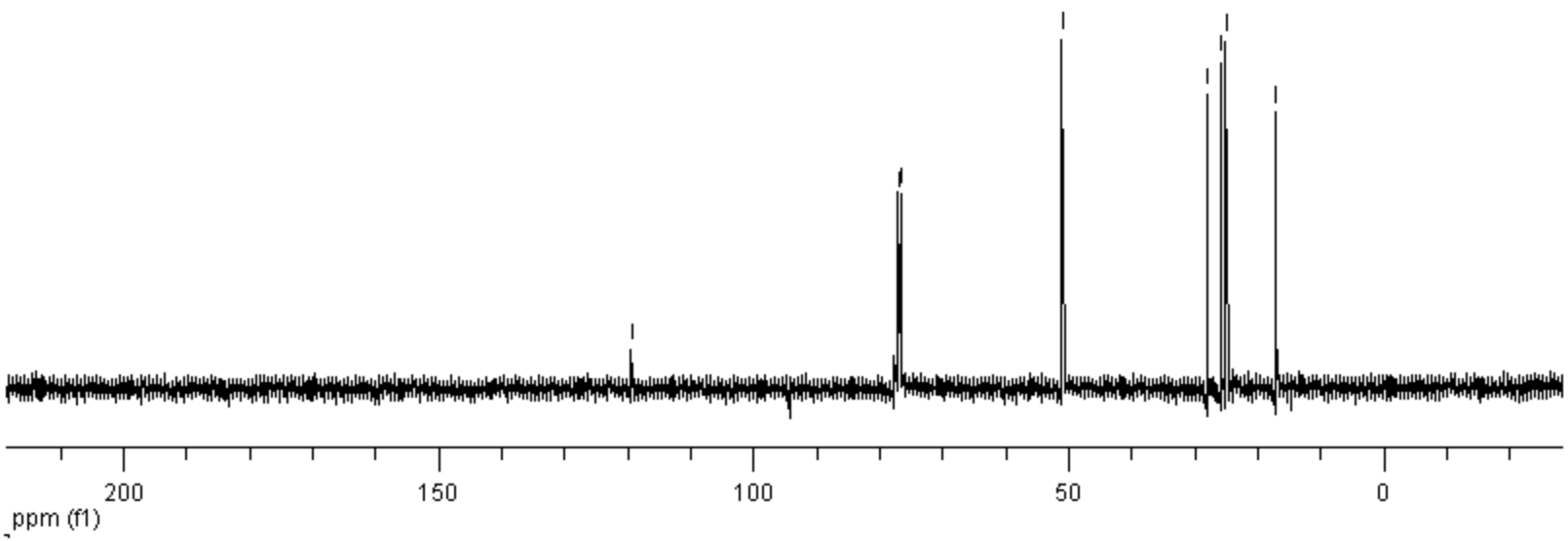

1.433
1.446
1.452
1.460
1.464
1.559
1.593
1.617
2.332
2.356
2.379
3.262
3.285
3.307
7.260
8.39
2.04
2.00
1.0
2.0
3.0
4.0
5.0
6.0
7.0
8.0
ppm (f1)
N3
NC

22

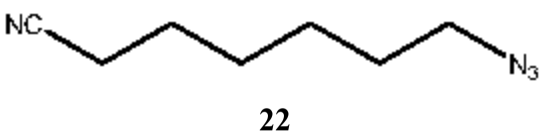

22

119.548
94.379
77.318
77.000
76.682
51.209
28.554
28.176
25.939
25.206
17.061

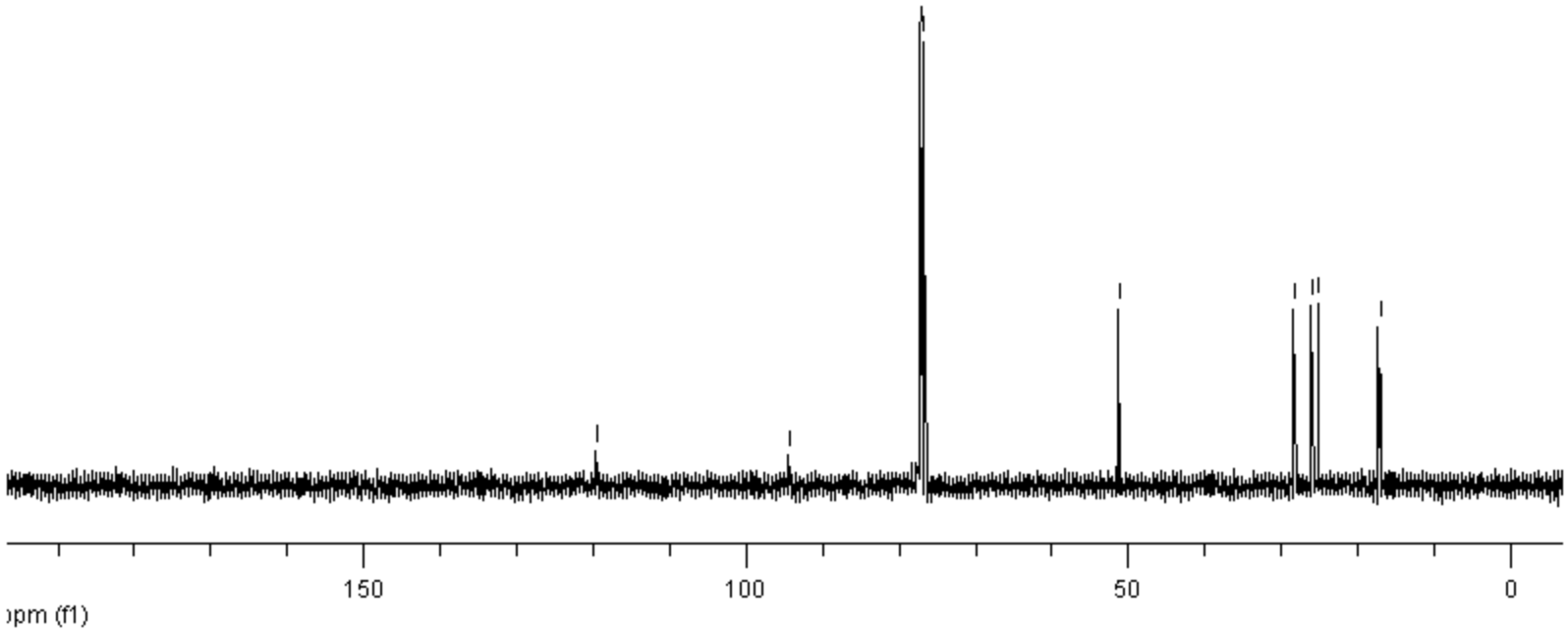

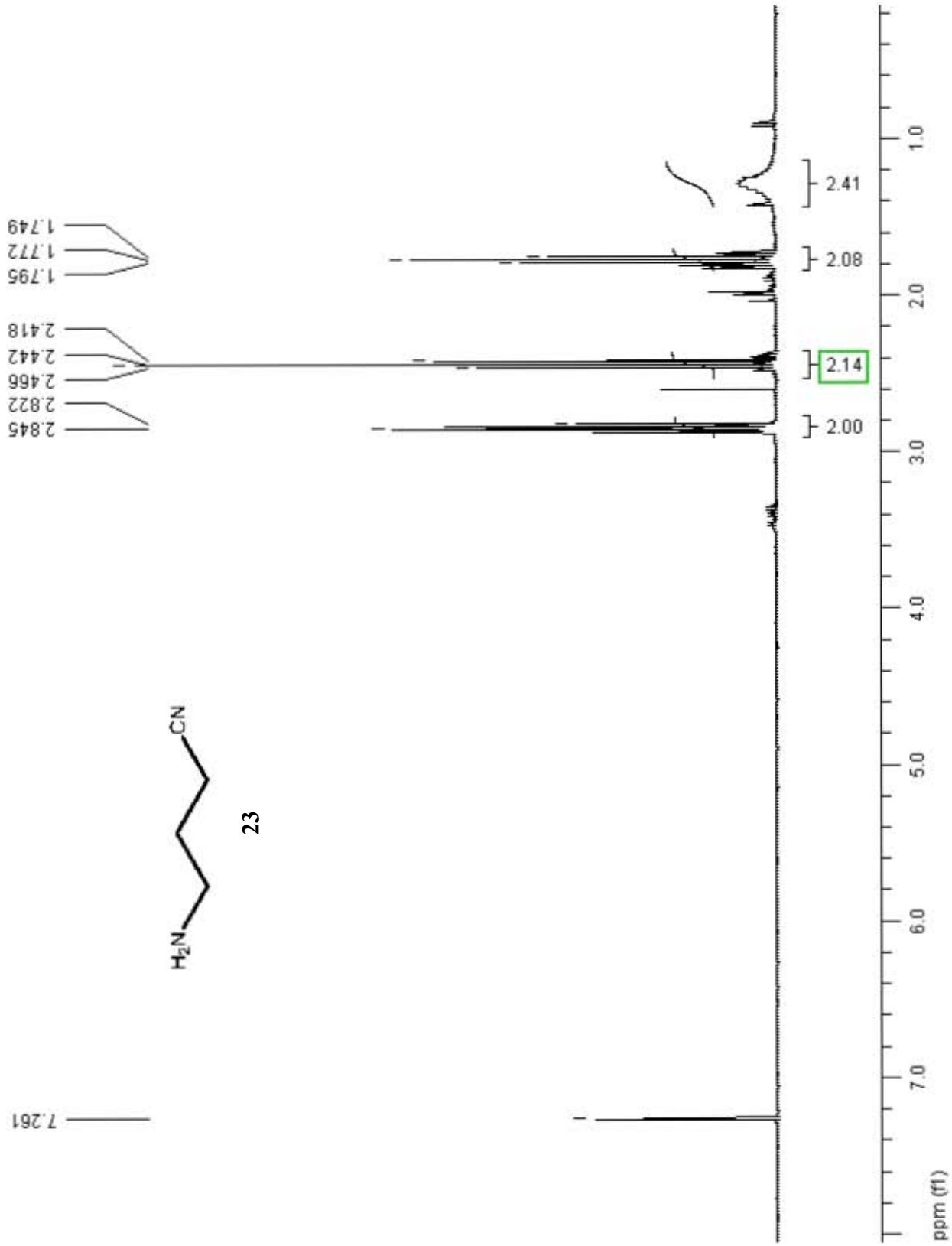
1.749
1.772
1.795
2.418
2.442
2.466
2.822
2.845
7.261
2.41
2.08
2.14
2.00
1.0
2.0
3.0
4.0
5.0
6.0
7.0
ppm (f1)
CN
H2N

23

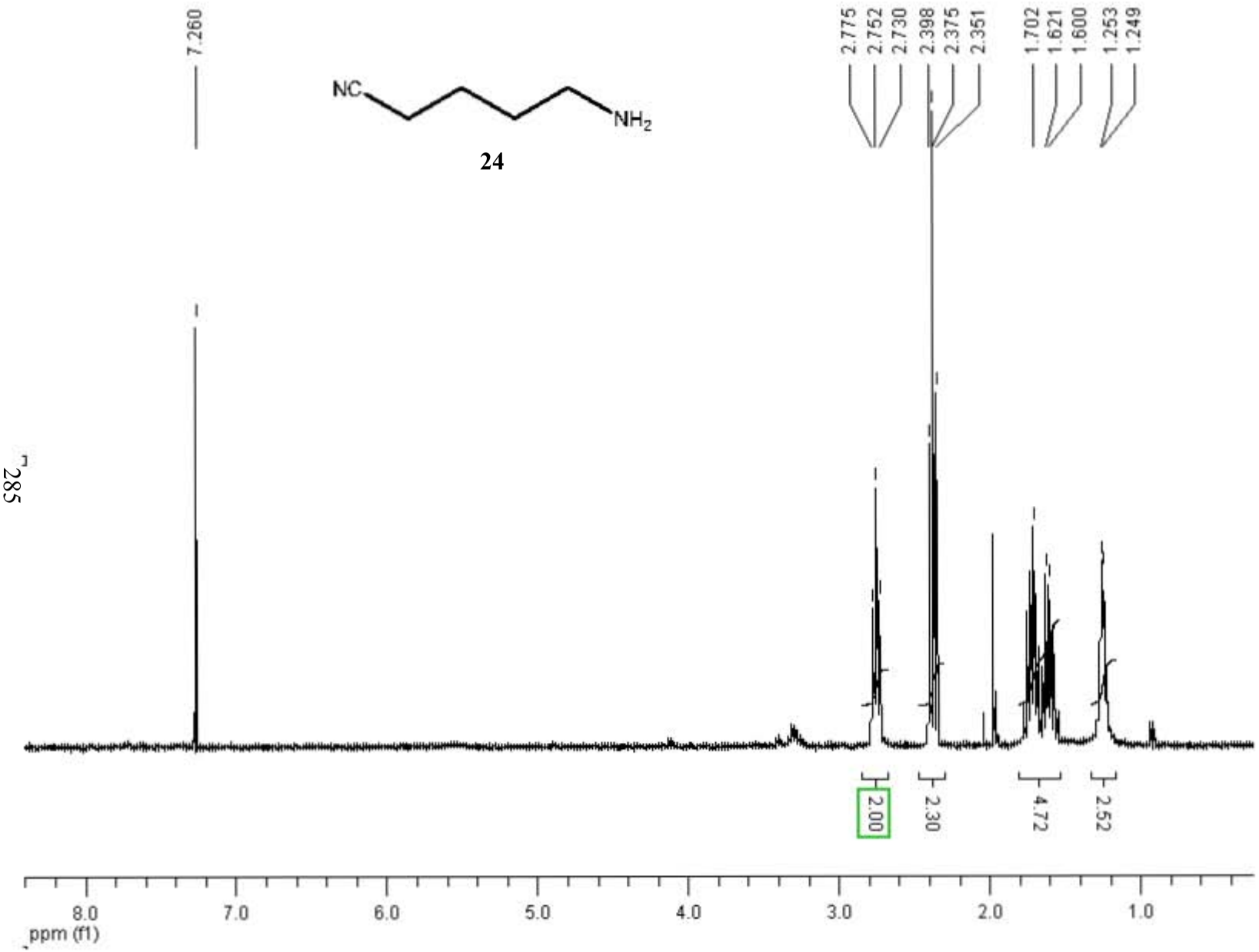
7.260
NC
NH2
24
2.775
2.752
2.730
2.398
2.375
2.351
1.702
1.621
1.600
1.253
1.249
2.00
2.30
4.72
2.52
8.0
7.0
6.0
5.0
4.0
3.0
2.0
1.0
ppm (f1)

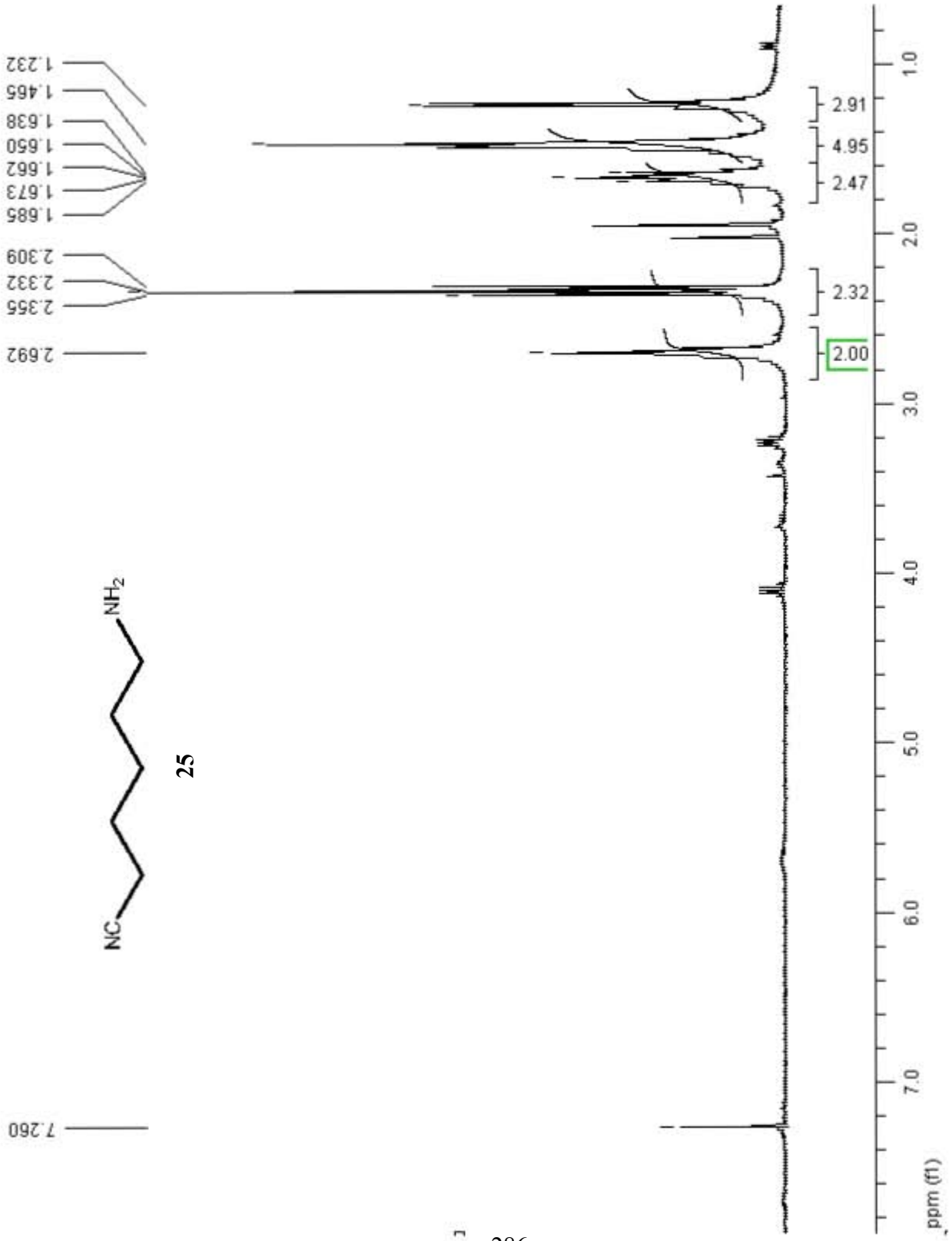
1.232
1.465
1.638
1.650
1.662
1.673
1.685
2.309
2.332
2.355
2.692
7.260
2.91
4.95
2.47
2.32
2.00
1.0
2.0
3.0
4.0
5.0
6.0
7.0
ppm (f1)
NH2
NC

25

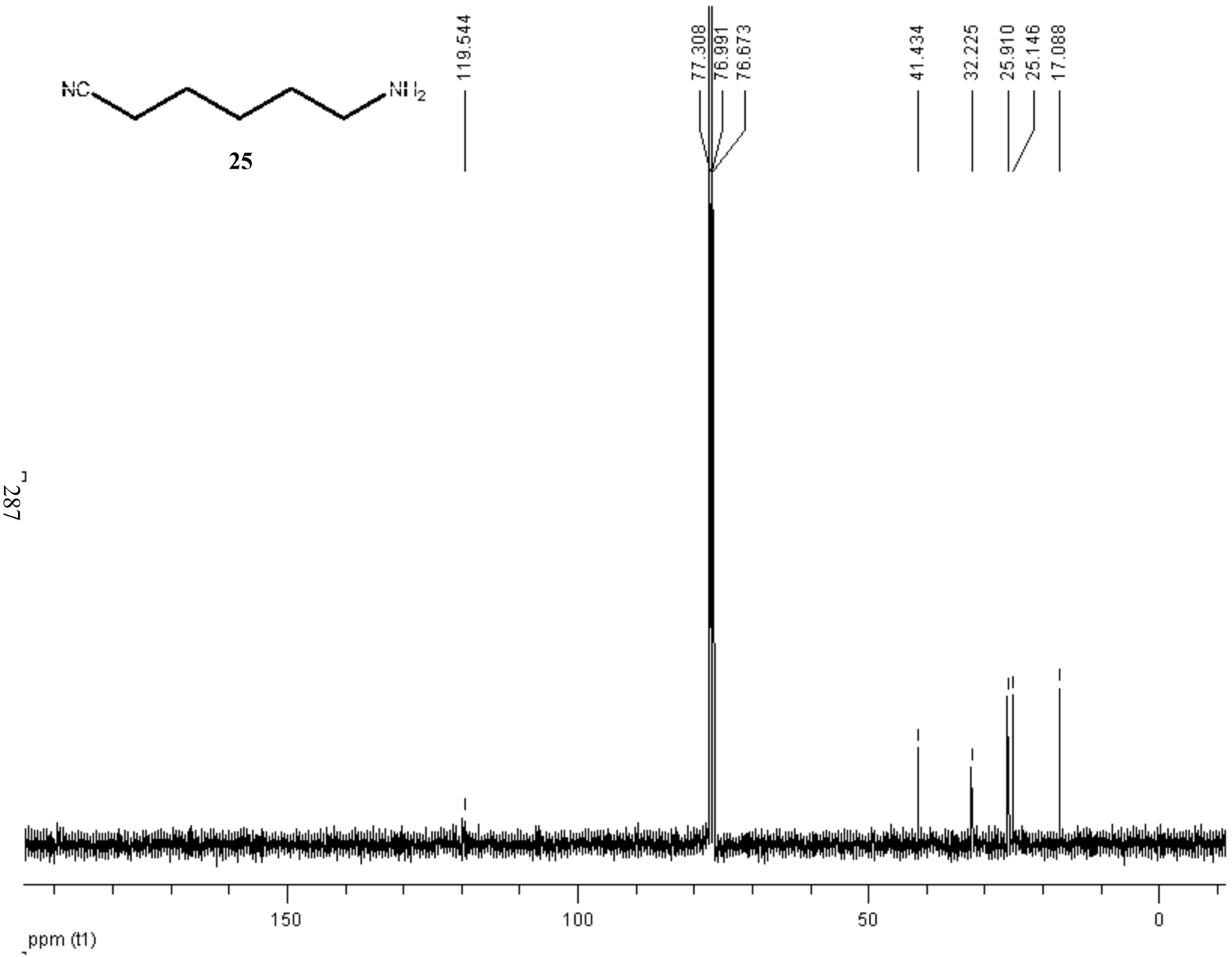
NC
NH2
25
119.544
77.308
76.991
76.673
41.434
32.225
25.910
25.146
17.088
150
100
50
0
ppm (t1)

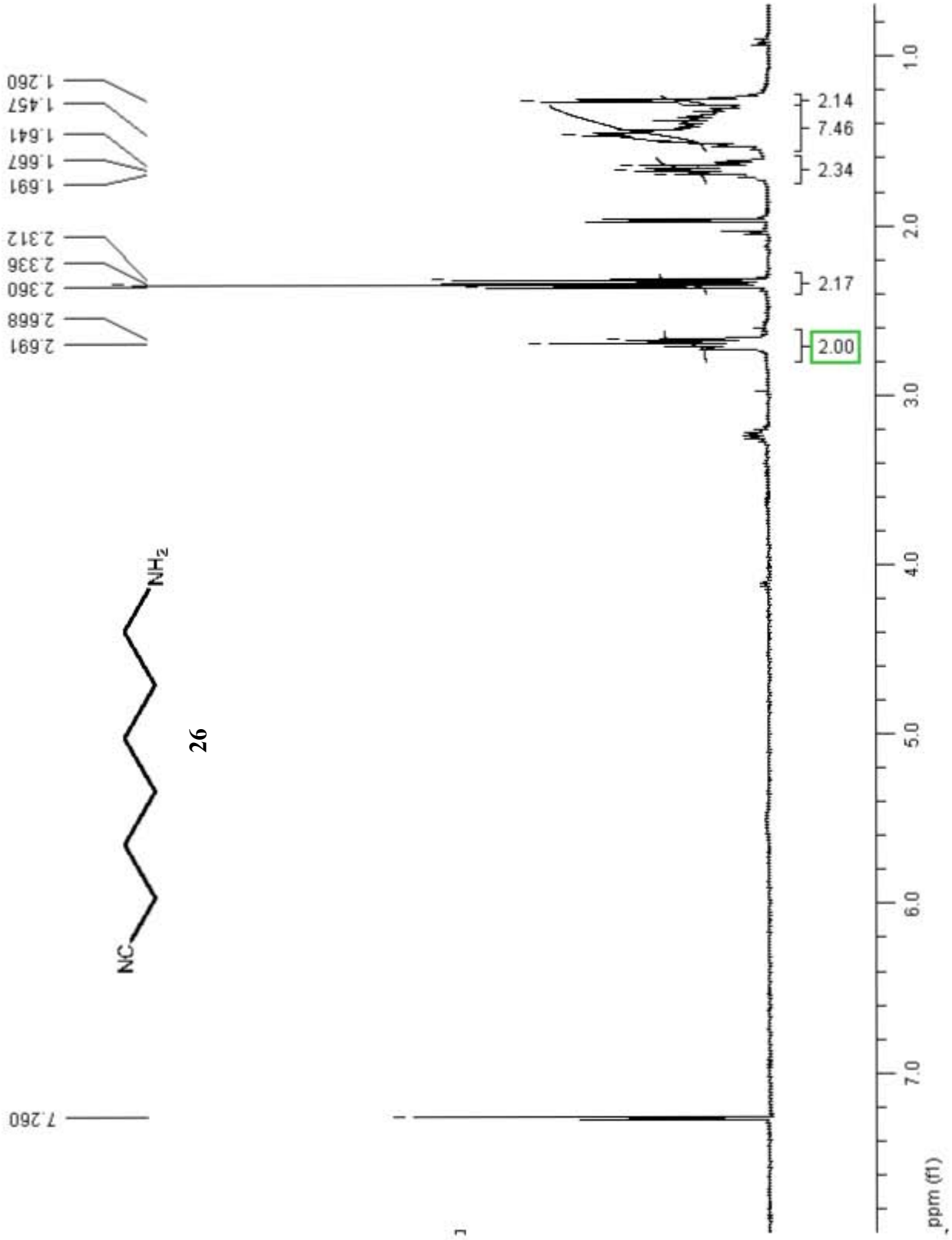
7.260
2.691
2.668
2.360
2.336
2.312
1.691
1.667
1.641
1.457
1.260
2.14
7.46
2.34
2.17
2.00
NC
NH2
26
1.0
2.0
3.0
4.0
5.0
6.0
7.0
ppm (f1)

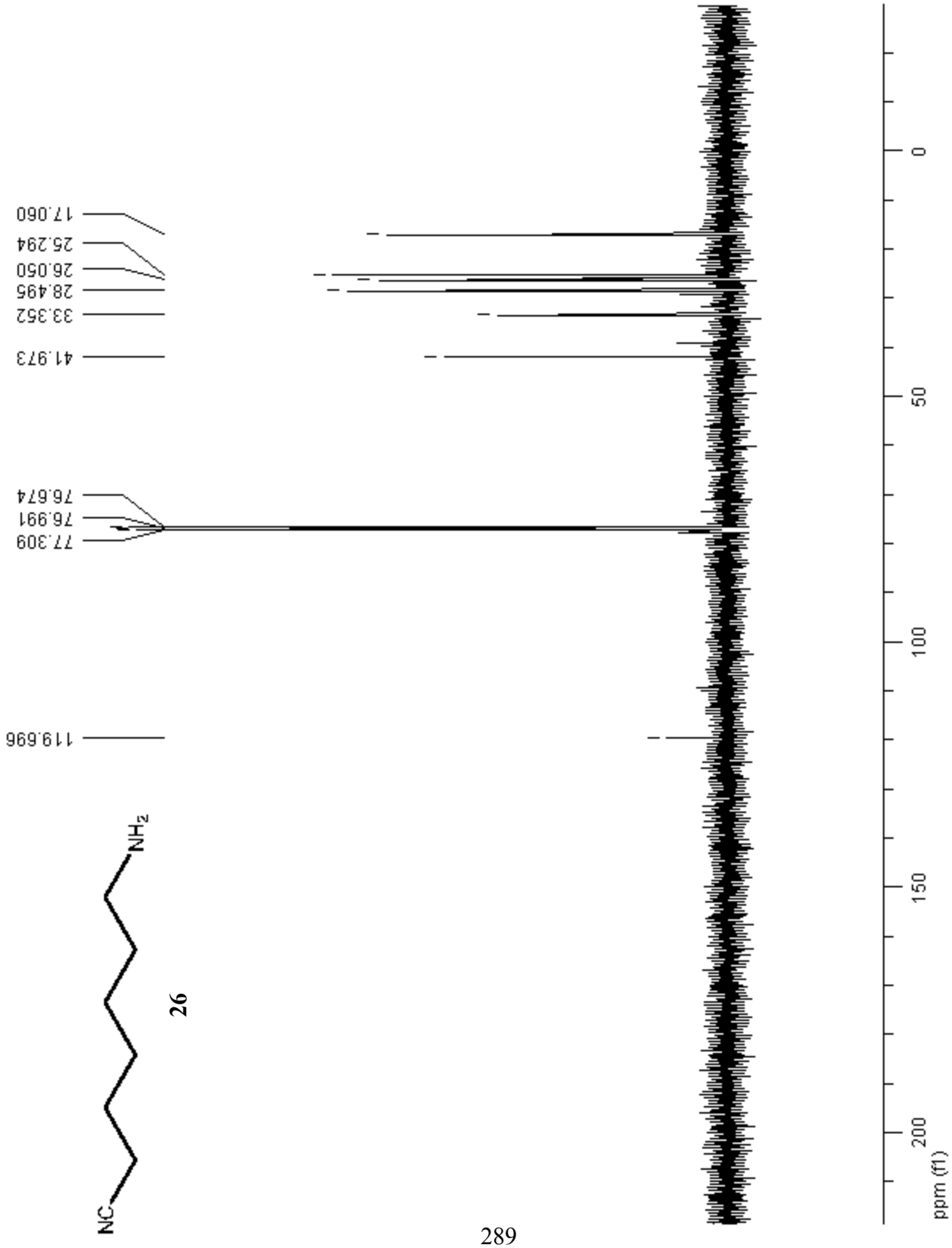
NC
NH2
26
119.696
77.309
76.991
76.674
41.973
33.352
28.495
26.050
25.294
17.060
ppm (f1)
0
50
100
150
200

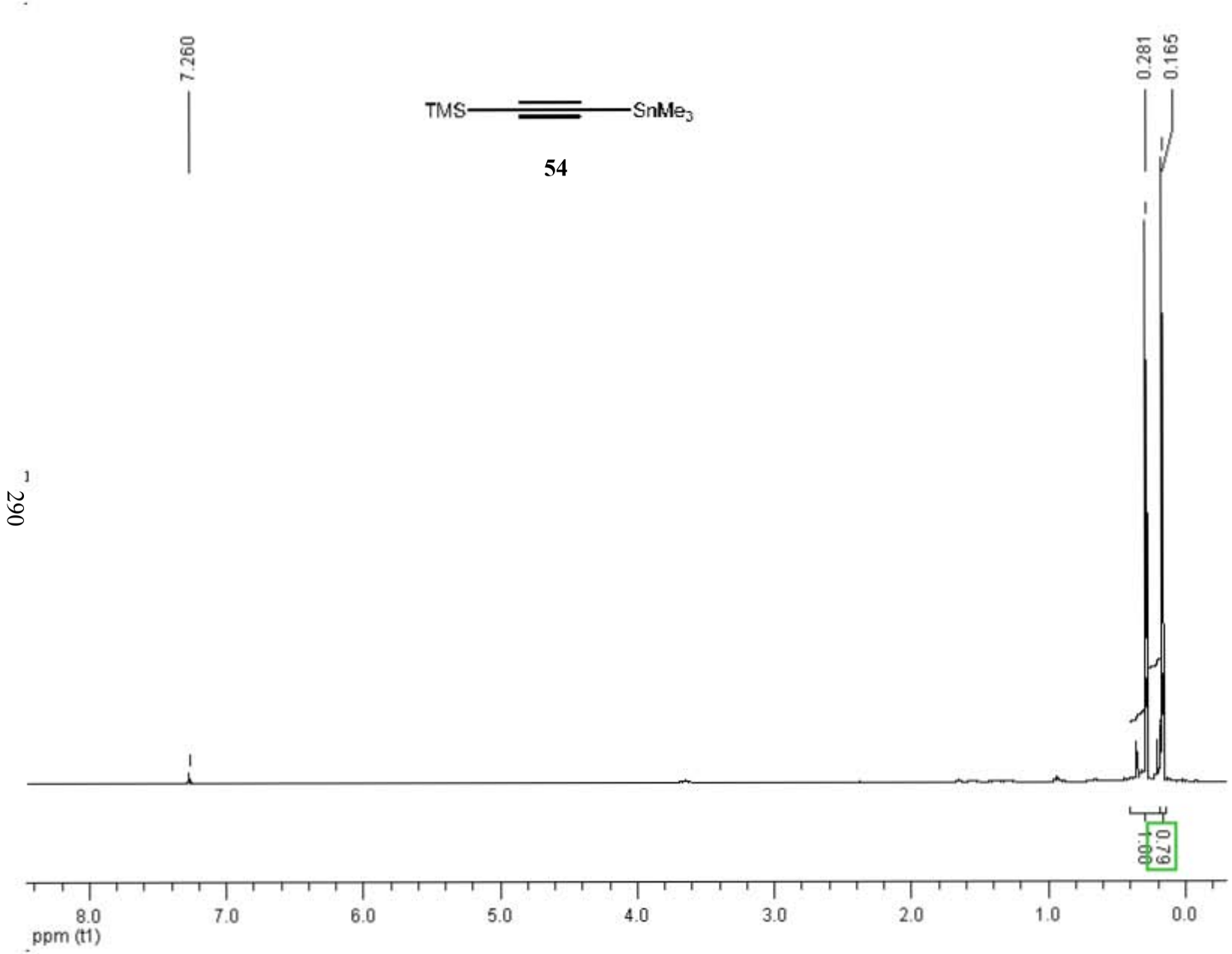

54

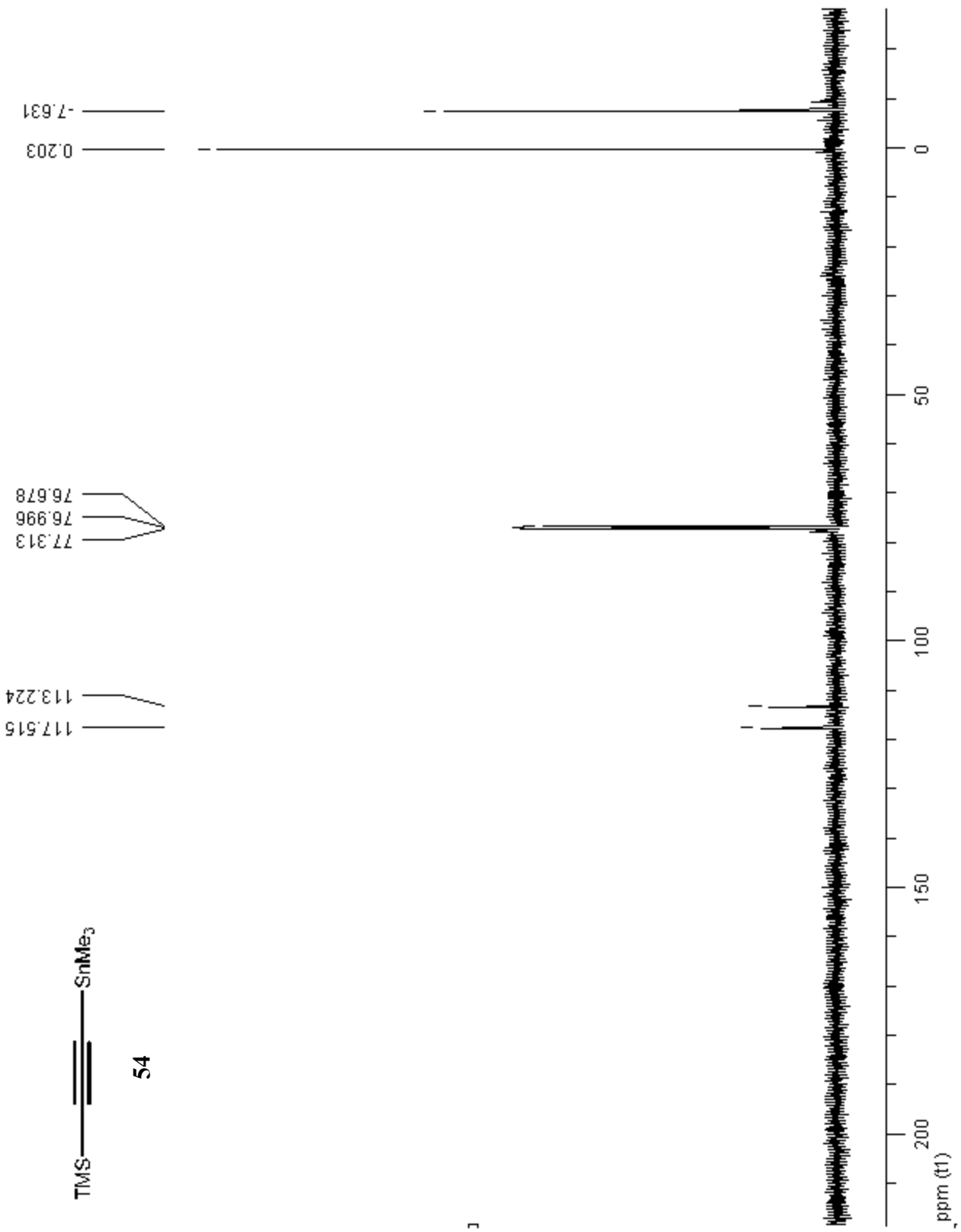
TMS
SnMe3
54
-7.631
0.203
76.678
76.996
77.313
113.224
117.515
ppm (t1)

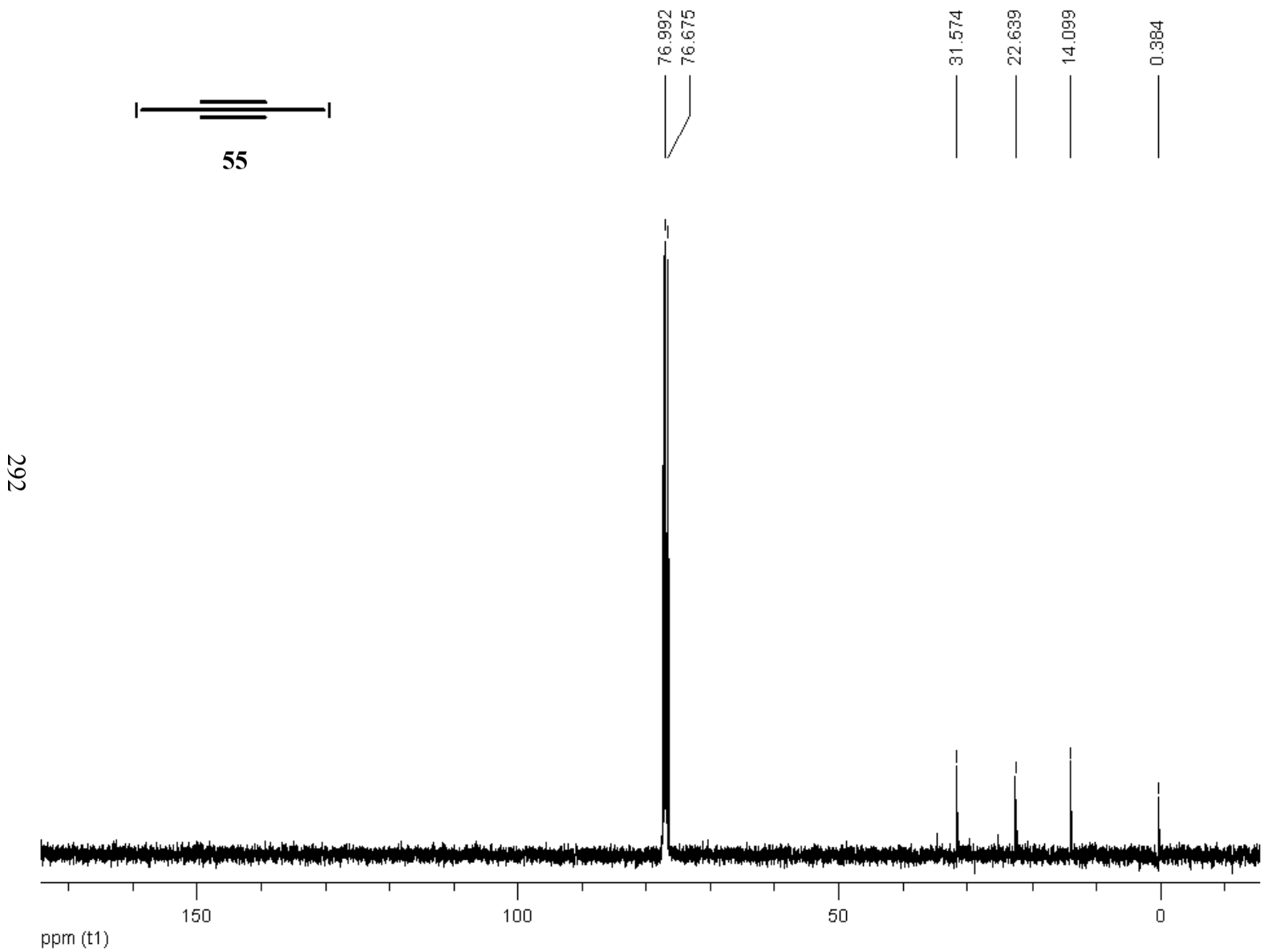
55
76.992
76.675
31.574
22.639
14.099
0.384
150
100
50
0
ppm (t1)

TMS
TMS

56

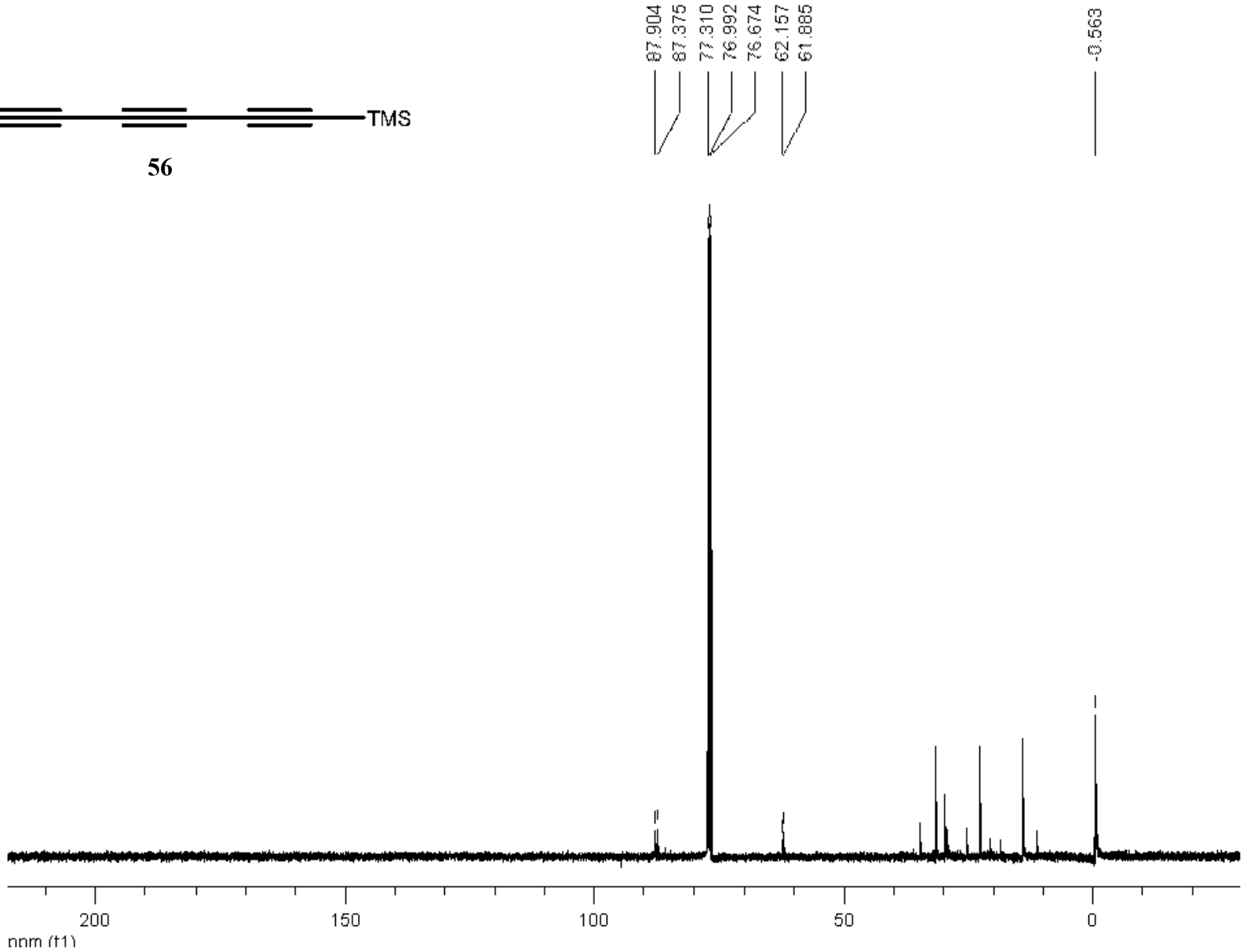
87.904
87.375
77.310
76.992
76.674
62.157
61.885
-0.563
200
150
100
50
0
ppm (t1)

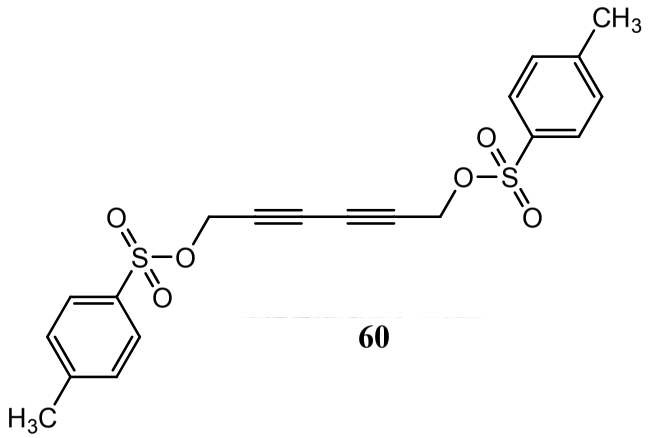
CH3
O
S
O
O
O
O
S
O
O
H3C

60

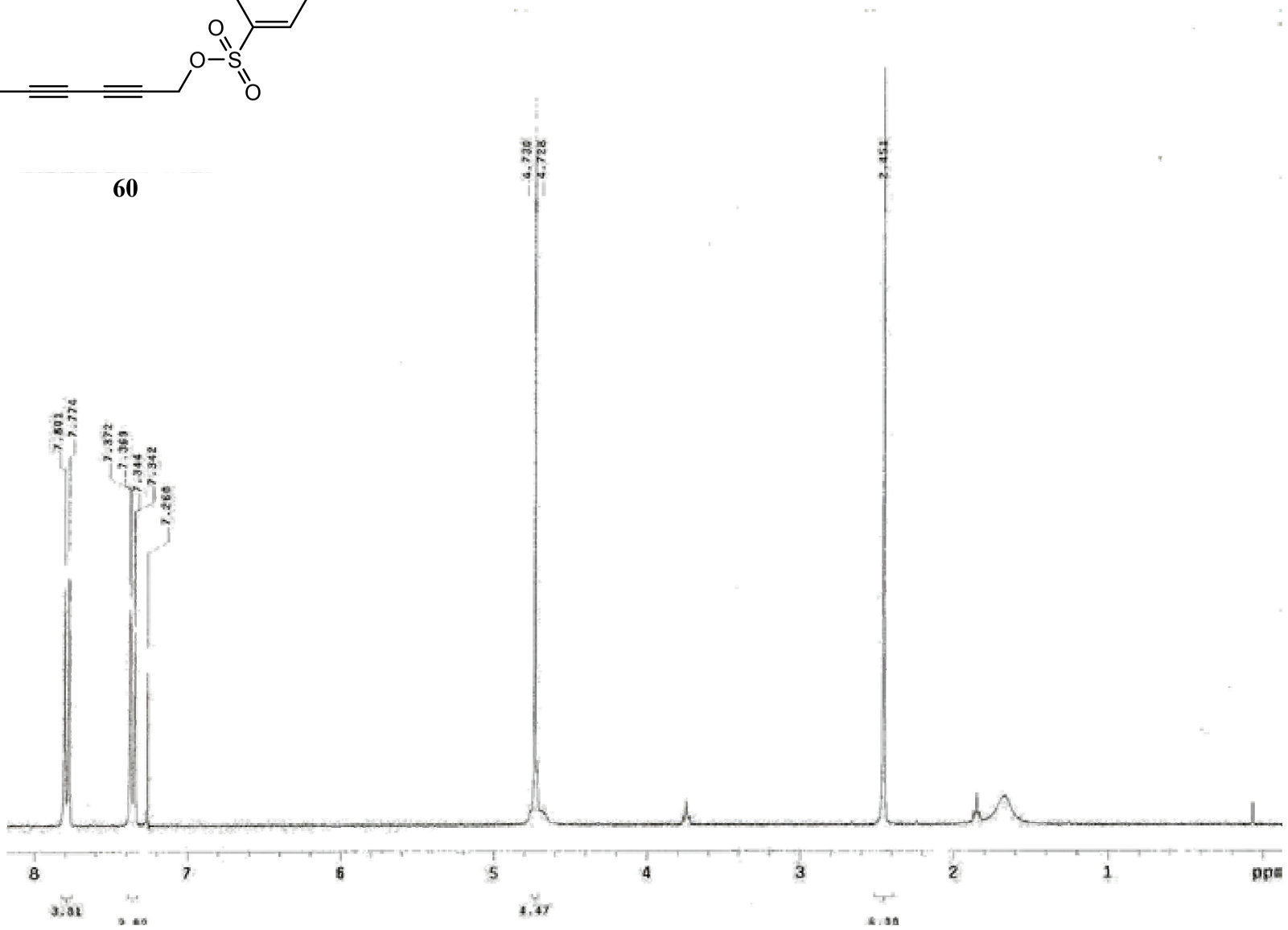
7.803
7.774
7.372
7.369
7.344
7.342
7.266
4.730
4.728
2.451
8
7
6
5
4
3
2
1
ppm
3.81
4.47


CH3
O
S
O
O
O
O
S
O
O
H3C
60
21.656
57.099
72.189
74.961
76.661
77.000
77.311
120.117
129.953
132.632
145.533
ppm
20
30
40
50
60
70
80
90
100
110
120
130
140
150
160

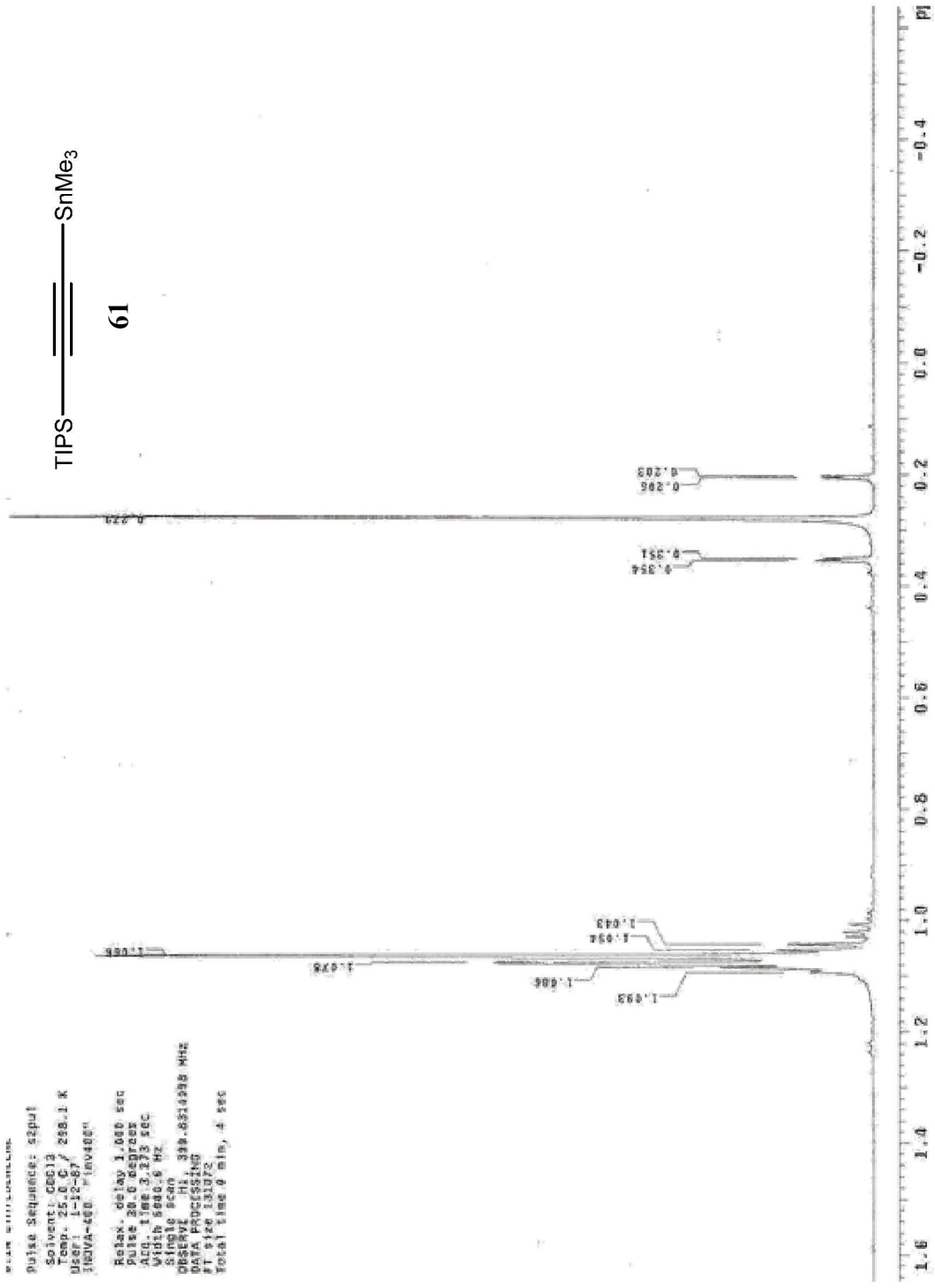
TIPS
SnMe3
61

TIPS—≡—$SnMe_3$

61

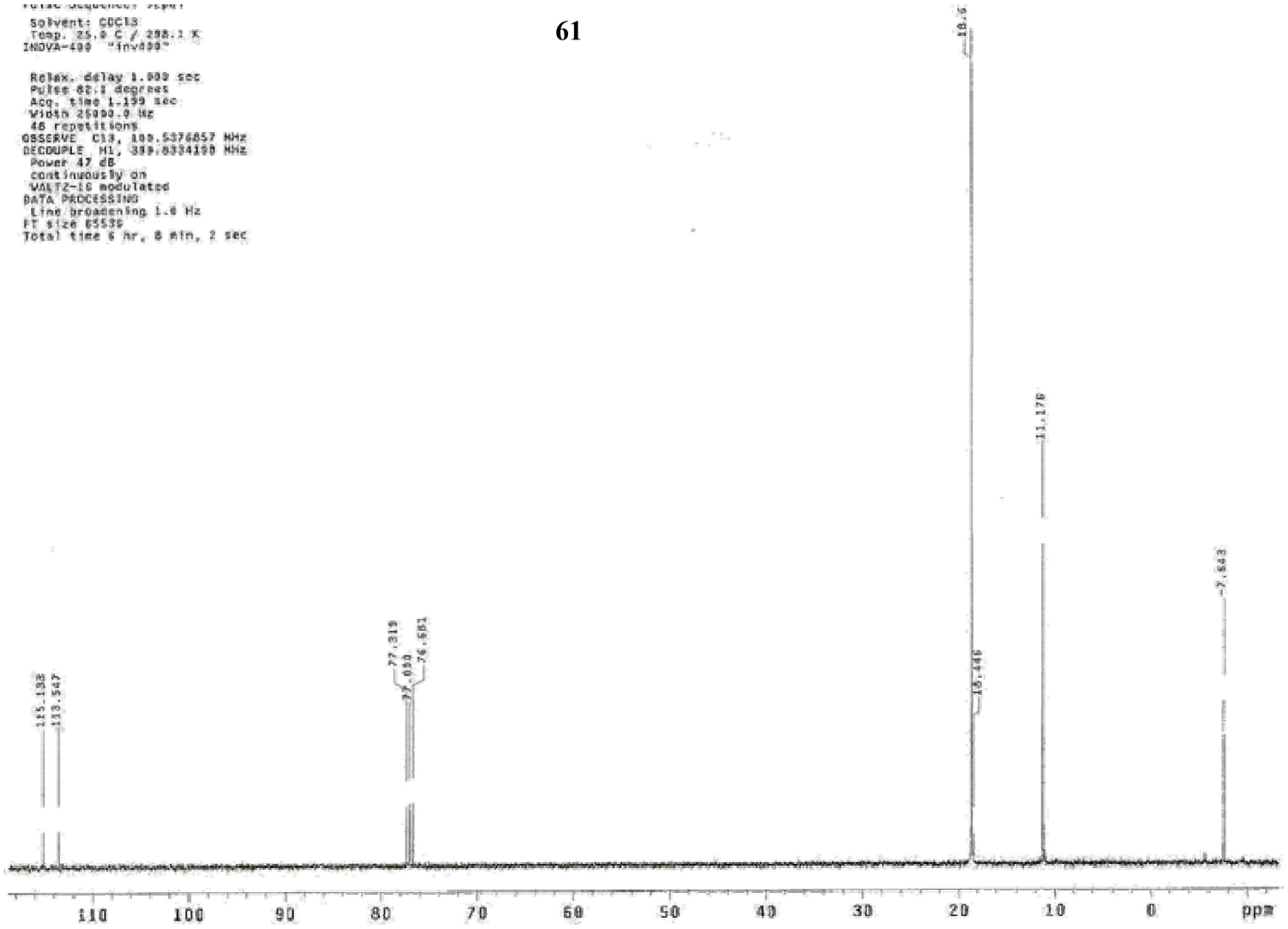

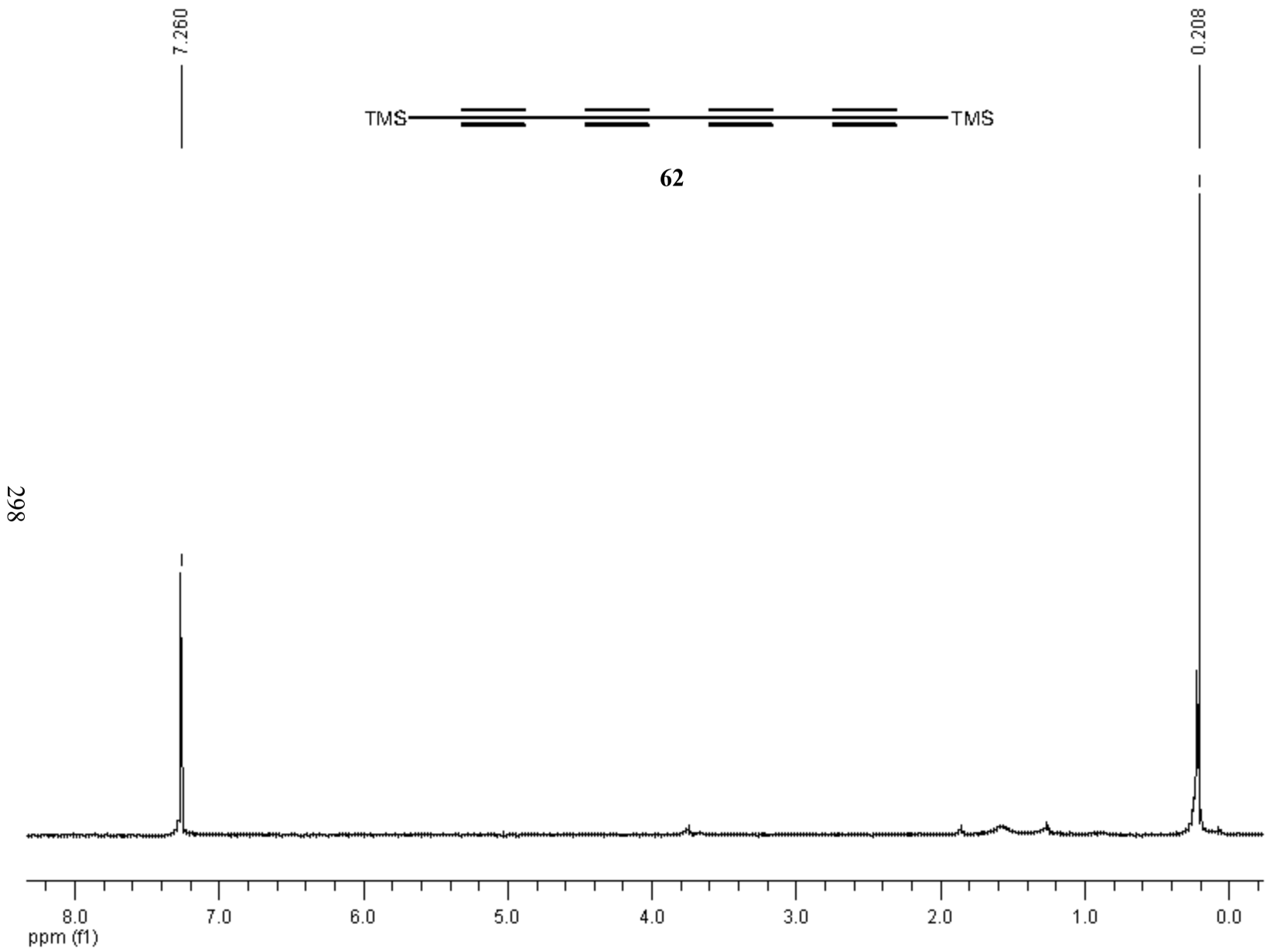

62

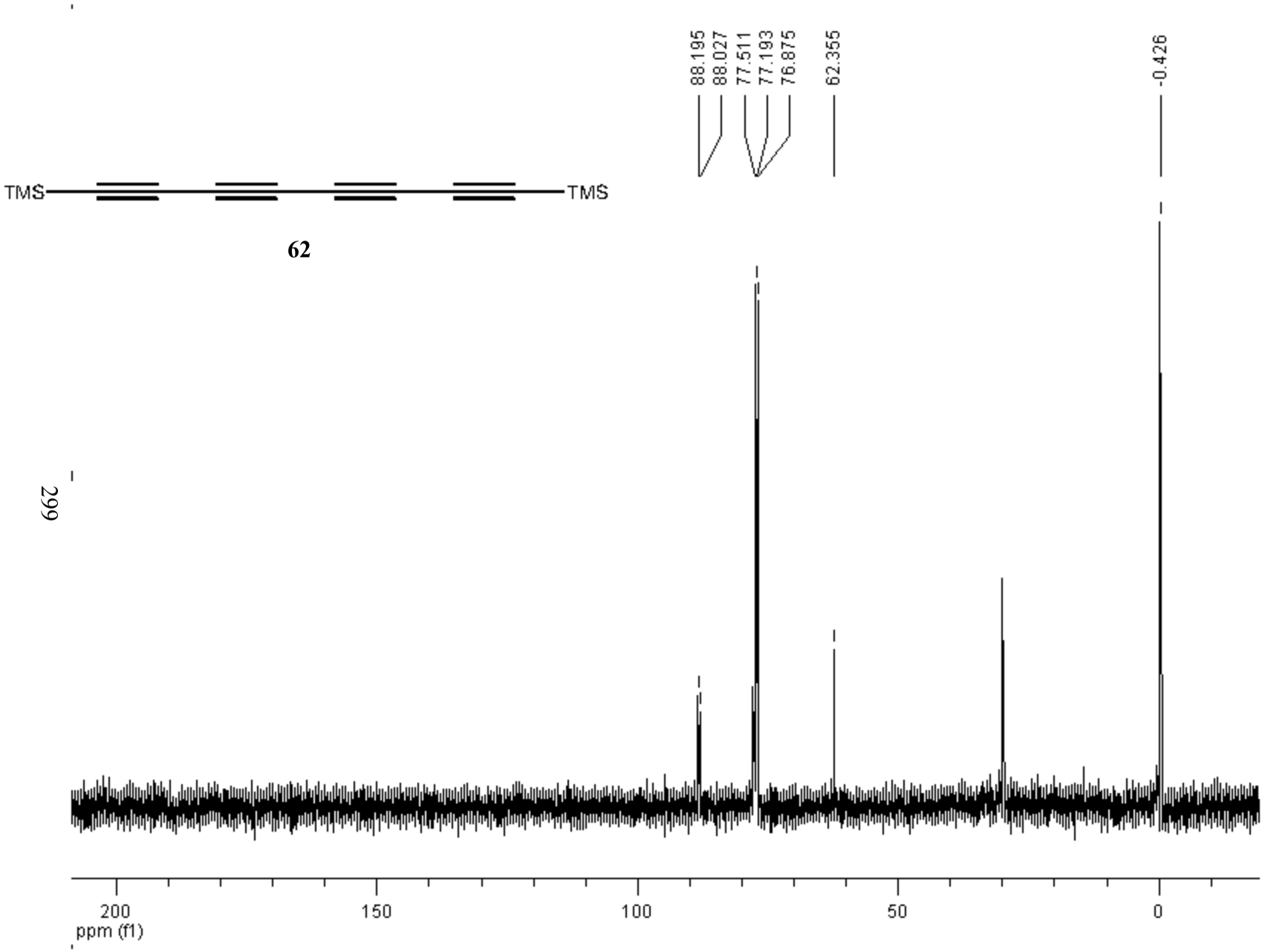
88.195
88.027
77.511
77.193
76.875
62.355
-0.426
TMS
TMS
62
299
200
150
100
50
0
ppm (f1)

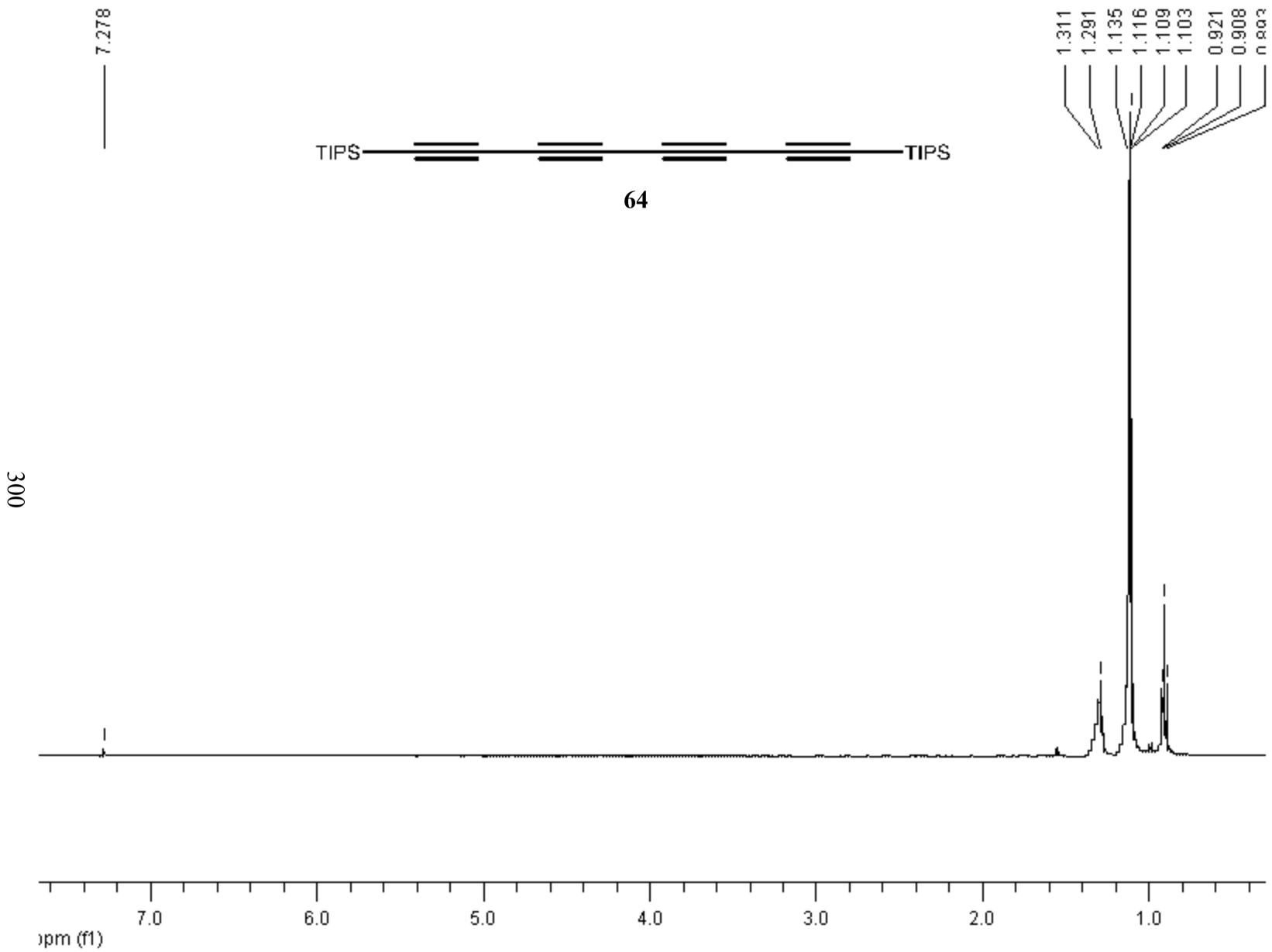
7.278
1.311
1.291
1.135
1.116
1.109
1.103
0.921
0.908
TIPS
TIPS
300
7.0
6.0
5.0
4.0
3.0
2.0
1.0
ppm (f1)

64

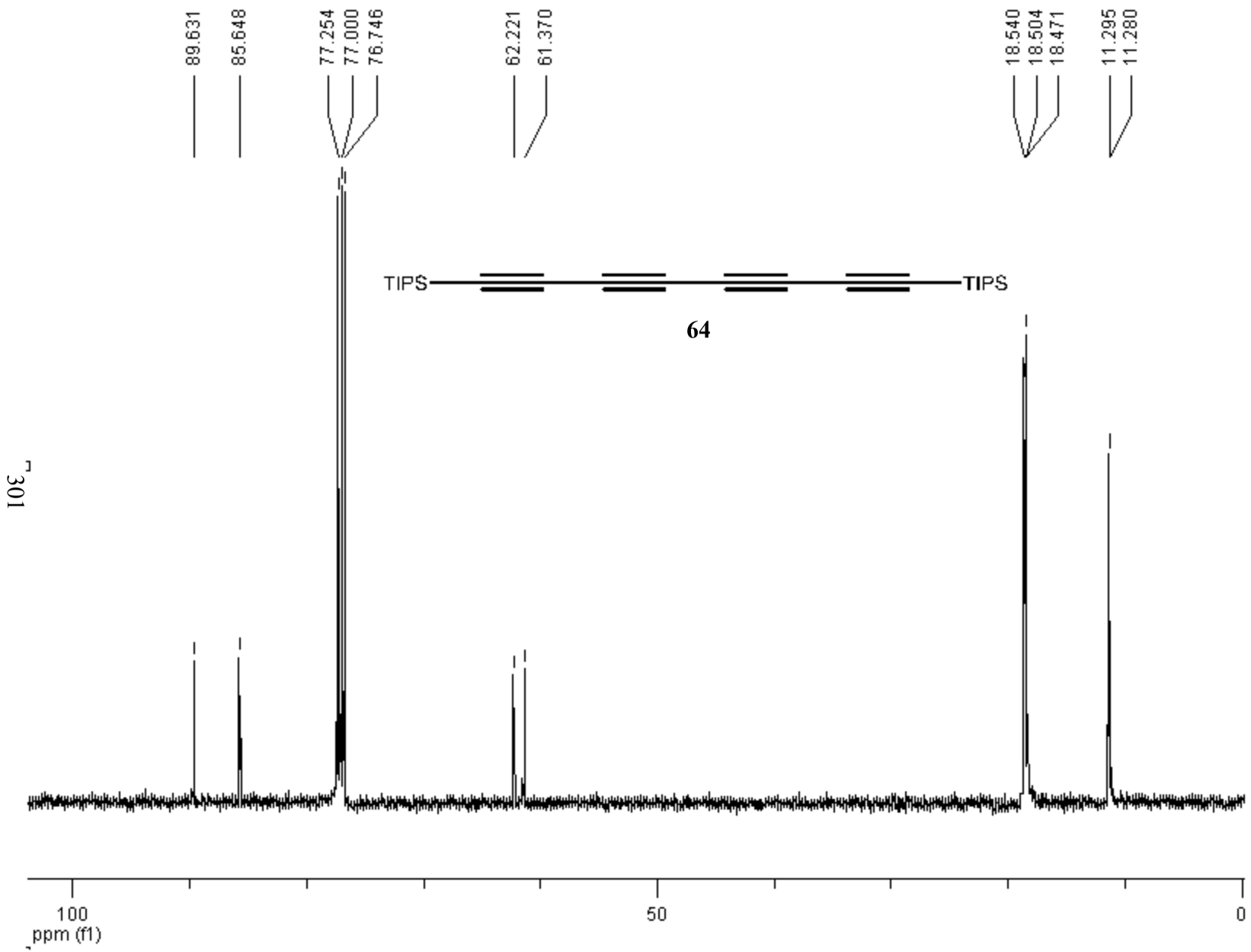
89.631
85.648
77.254
77.000
76.746
62.221
61.370
18.540
18.504
18.471
11.295
11.280
TIPS
TIPS
64
301
100
ppm (f1)
50
0

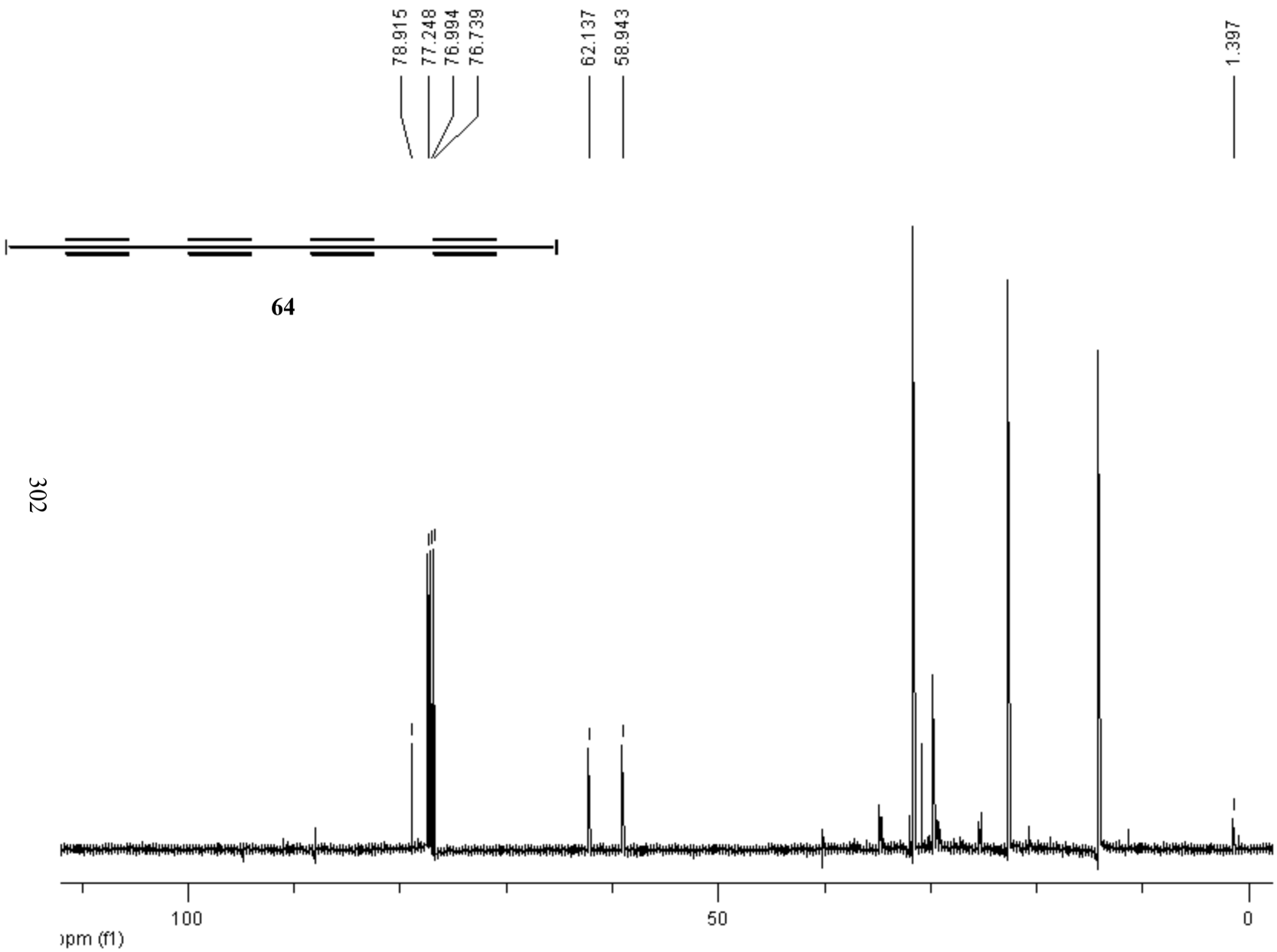
78.915
77.248
76.994
76.739
62.137
58.943
1.397
64
302
100
50
0
ppm (f1)